



# **Functional Viologens for Electrochemical Applications**

**Orielia Pria Egambaram**

Division of Natural Sciences

University of Kent

A thesis submitted for the degree of Doctor of Philosophy

April 2023

## Declaration

I, Orielia Pria Egambaram, declare that the thesis entitled "Functional Viologens for Electrochemical Applications" and all the research presented therein was generated by me, at the University of Kent between September 2019 and April 2023. I declare that I have acknowledged all contributions by others, and unless otherwise stated, all work presented is my own. This work has not been previously submitted, in part or in whole, for any other academic degree. The copyright of this degree rests with the author.

Orielia Pria Egambaram

April 2023

## Dedication

This work is dedicated to my loving parents (Ronnie & Beulah Egambaram), brother (Ithiel Egambaram), grandmother (Crocus Moodley), and late great-grand father (Pastor S.R. Paul).

To the scores of Indentured Indian laborers, my forefathers and foremothers, that journeyed to the Colony of Natal in search of a better life;

...

**I found the goose that laid the golden egg!!**

iii

## Acknowledgements

*The completion of this thesis was a collective effort ; one that would not be possible without my community. I stand at the finish line filled with the utmost gratitude for every single person that has walked this journey with me.*

*“Ubuntu Ngu’muntu Nga’bantu”*

- ❖ To the Lord who is able to do exceedingly, abundantly, and more than I could ever imagine, I praise you for the strength, favour, and the wisdom you have granted me. YOUR grace is sufficient for me.
- ❖ My immeasurable thanks to my family, my true pillars. To my parents, thank you for always believing in my dreams, for flying to the ends of the earth to be with me, and for your unending support. I would be nothing without you! To my brother, a truly wise chap. How blessed I am to have a kind, supportive, and loving brother like you. Thank you for every text, every call, and every pep talk encouraging me to keep going.
- ❖ My prayer warriors (my grandparents); Ava, Grandma, & Grandpa Pop. Your prayers and love have accompanied me and carried me through every valley and to every mountain top. Thank you!

- ❖ To my supervisors, for whom I have the utmost respect and deepest gratitude.  
To Dr Ewan Clark, thank you for every lengthy discussion trying to solve the never ending problems, enduring my “lovely” music in the lab and for not giving up on me! To Professor Jennifer Hiscock, thank you for believing in me, moulding me into a resilient scientist, and teaching me to fight for my place at the table. This journey has been exceptionally challenging, but I consider myself quite privileged to have been able to learn from you both.
- ❖ To my best friend, and “Day one”, Amaris Rennie. Thank you for going through these trenches with me, pulling me out of dark spaces and loving me harder on the days I couldn’t love myself. You are phenomenal!
- ❖ Maxwell Manana, supporting someone through a PhD journey is demanding, but you were my cheerleader on the low days, nudged me when I got too comfortable, and celebrated all my wins. I am so grateful for your love, kindness, and patience through it all.
- ❖ I am truly grateful for everyone who has been part of my journey at the University of Kent. In particular, I would like to thank the members of Lab 212, past (Harvir, Koray, and Antigoni) and present (Rebekah, and Ryan). A special thanks to Oni, my first friend in Canterbury, thank you for helping me find my feet. I’m grateful for all the good vibes and manifestations courtesy of Bexy!
- ❖ A massive thanks to the members of the Hiscock group for their support: emotionally and scientifically. I’m especially grateful for Kira Hilton who always had a listening ear for my never-ending dilemmas.

- ❖ I am also indebted to several colleagues, and friends for their technical assistance. Bini Claringbold for her assistance with the microwave and biotage, and for always having time to answer my silly questions about the equipment. Rebekah and Ryan for SEM and EDX analysis, as well as collaboration in the lab on several (random) queries.
- ❖ To Sophia Weng (MIT) and Amy Metlay (UPenn), thank you both for your kindness and patience in teaching me RDE, and EIS, respectively.
- ❖ I doubt I would have survived the pandemic and this PhD without the “*Victor Echo Echo Romeo*” gang; Uncle Pete, Aunty Shivashni and Sia Veersamy. Your love, support and encouragement has helped me find my way through this storm called PhD, especially during a global pandemic.
- ❖ My journey in STEM has been moulded by fierce, brave, and resilient women in science who have encouraged me and helped me work my way up the ladder. I would like to acknowledge Professor Patricia Forbes, Professor Lynne Pilcher, Dr Shankara Radhakrishnan, Dr Winile Mavuso, Dr Sreejarani Pillai, Dr Ntombi Mathe, Dr Cosnet Rametse, and the late Ndoni Mcunu.
- ❖ Dr Zamaswazi Tshabalala, my bravest “SHEro”, though distance separates us, I am forever indebted to you for your encouragement, and love.
- ❖ To my friends, who have become family, Catherine Tatham, Benjamin Mmari, Nontokoza Mabaso, Avania Ravinath and Justin Roberts. I’m grateful your friendship which has endured my endless frustrations, and horrid time zones.

- ❖ Thank you to Dr. A. Murray for affording me the opportunity to pursue this PhD in the United Kingdom.
- ❖ The success and completion of this work would not have been possible without the financial support granted to me by the following: Chemists Community Fund (Royal Society of Chemistry), The Division of Natural Sciences (University of Kent), and Funds for Women Graduates.
- ❖ Last, but not least, I'd like to acknowledge Floyd the FlowCell and Eloise the ElectraSyn. Although our moments together may have been filled with much frustration and desperation on my part, thanks to you I leave this PhD as the most resilient, agile, and innovative version of myself. The R&D team is quite chuffed.

***"When you pass through the deep waters, I will be with you (Orielia); and when you pass through the rivers, they will not sweep you. When you walk through the fire you will not be burned; The flames will not set you ablaze."***

***Isaiah 43:2***

## Publications

Work from this thesis, and work carried out in the duration of this Ph. D has been included in the following publication:

1. **Reductive dehalogenation of olefins by mediated phase transfer electrocatalysis** [O.Egambaram](#), J. Hiscock, and E. Clark, *Chem.Commun.*, 2023. (*In preparation*)



## Abstract

### **“Functional Viologens for Electrochemical Applications”**

Various viologen analogues were synthesized throughout the course of this doctoral work and targeted based on their electrochemical properties, stability, and solubility, and their role in energy storage and electrocatalysis was subsequently explored. Successful synthesis of each viologen was confirmed using Nuclear Magnetic Resonance (NMR) spectroscopy. Where possible, based on the stability of the molecules, electrochemical characterization was conducted. This included cyclic voltammetry (CV) and rotating disk electrode (RDE) studies which informed the decisions to pursue or abandon subsequent flow battery testing, and other applications.

This work describes a methodical approach to develop a sturdy, reliable, lab-scale rig for performance testing of Redox Flow Batteries, a potential long-term alternative for energy storage on both medium and large-scale applications. The design process and development involved systematically examining the construction and cell features and evaluating their benefits and drawbacks as to develop these technologies. Much research must be conducted on the lab scale to determine a range of performance metrics.

This work reports viologen electro-catalysts within a biphasic dichloromethane/ water system to achieve reductive dehalogenation of dihalides; a synthetically versatile route to substituted olefins in several industries including the pharmaceutical, fuel, and fine-chemical industry. The costs associated with these reactions are often exorbitant due to the use of superstoichiometric reductants, making this non-sustainable due to poor atom efficiency, and herein mediated electrosynthesis is used to develop a more efficient approach.

A range of 1,2-dibromo species are easily reduced using a simple undivided cell and inexpensive graphite electrodes in the first example of phase transfer electrocatalysis for these systems.

Beyond viologens, water-soluble flavin derivatives are potential redox active species for redox flow batteries, based on their electrochemical stability and reversibility, and herein a sulphonate-functionalized flavin was characterized, which exhibited good redox properties in acidic aqueous electrolyte making it a strong candidate for an aqueous organic redox flow battery (AORFB).

## Table of Contents

|   |       |
|---|-------|
| Declaration .....   | ii    |
| Dedication .....  | iii   |
| Acknowledgements.....                                     | iv    |
| Publications.....   | viii  |
| Abstract.....   | ix    |
| Table of Contents.....                                    | xi    |
| Abbreviations .....                                       | xviii |
| CHAPTER 1 .....   | 1     |
| 1.1 Introduction to Electrochemistry .....                | 2     |
| 1.1.1 Electrochemical theory.....                         | 3     |
| 1.2 Introduction to Redox Flow Batteries.....             | 5     |
| 1.2.1 Redox Flow Battery Fundamentals .....               | 6     |
| 1.2.2 Design and Properties of Redox Flow Batteries ..... | 11    |
| 1.3 Electrolytes .....                                    | 12    |
| 1.3.1 Electrodes.....                                     | 14    |
| 1.3.2 Membranes.....                                      | 15    |
| 1.3.3 Evolution of Redox Flow Batteries .....             | 17    |
| 1.3.4 Examples of Redox Flow Batteries .....              | 19    |

|  |    |
|--|----|
| 1.3 Introduction to Electrosynthesis.....  | 22 |
| 1.3.1 Types of Electrochemical Synthesis.....  | 24 |
| 1.3.2 Factors controlling the electrosynthetic process .....                                     | 28 |
| 1.3.3 Reactions occurring at the electrodes.....   | 33 |
| 1.3.4 Electrocatalysis .....   | 37 |
| 1.4 Viologens .....  | 38 |
| 1.4.1 Properties of viologens.....   | 38 |
| 1.4.2 Synthesis of viologens and derivatives.....  | 41 |
| 1.4.4 Applications of viologens and their derivatives .....                                      | 45 |
| 1.5 Flavins.....   | 49 |
| 1.5.1 Properties of flavins.....   | 50 |
| 1.6 Characterisation and Testing of Electroactive Species.....                                   | 52 |
| 1.6.1 Cyclic Voltammetry (CV).....   | 52 |
| 1.6.2 Rotating Disk Electrode (RDE).....   | 54 |
| 1.6.3 Galvanostatic Cycling with Potential Limitation (GCPL) (Charge and Discharge Curves) ..... | 57 |
| 1.7 Scope of the Thesis .....  | 59 |
| 1.8 References .....   | 60 |
| CHAPTER 2 .....  | 68 |
| 2.1 Introduction .....   | 69 |

|  |     |
|--|-----|
| 2.2 Synthesis of Viologens .....   | 71  |
| 2.2.1 Water-soluble Viologens.....   | 71  |
| 2.2.2 Multifunctional Viologens.....   | 78  |
| 2.3 Electrochemical characterization.....  | 82  |
| 2.3.1 Cyclic Voltammetry (CV).....   | 82  |
| 2.3.2 Rotating Disk Electrode (RDE) studies .....  | 91  |
| 2.4 Conclusions and Future Work .....  | 92  |
| 2.5 Experimental .....   | 93  |
| 2.5.1 Physical Measurements .....  | 93  |
| 2.5.2 Electrochemical Measurements.....  | 94  |
| 2.5.3 Synthesis of 1,1'-bis(2-hydroxyethyl)-[4,4'-bipyridine]-1,1'-dium (1) .....                    | 95  |
| 2.5.4 Synthesis of 1,1'-bis(2-carboxyethyl)-[4,4'-bipyridine]-1,1'-dium (2).....                     | 95  |
| 2.5.5 Synthesis of 3,3'-([4,4'-bipyridine]-1,1'-dium-1,1'-diyl)bis(propane-1-sulfonate) (4)<br>..... | 96  |
| 2.5.6 Synthesis of 1,1'-dibutyl-[4,4'-bipyridine]-1,1'-dium (5).....                                 | 96  |
| 2.5.7 Synthesis of 1,1'-bis(2-carboxylethyl-TEMPO)-[4,4'-bipyridine]-1,1'-dium (7) .....             | 97  |
| 2.5.8 Synthesis of 6-bromohexanoic-TEMPO derivative (8) .....  | 98  |
| 2.5.9 Synthesis of 1,1'-bis(2-carboxypentyl-TEMPO)-[4,4'-bipyridine]-1,1'-dium (9).....              | 98  |
| 2.6 References .....   | 99  |
| CHAPTER 3 .....  | 101 |

|  |     |
|--|-----|
| 3.1 Introduction .....                                       | 102 |
| 3.1.1 Engineering aspects of RFBs.....                       | 103 |
| 3.1.2 Viologens in Organic Redox Flow Batteries (ORFBs)..... | 104 |
| 3.2 Testing Rig Development.....                             | 107 |
| 3.2.1 $\alpha$ -generation RFB design.....                   | 107 |
| Pre-liminary flow cell results.....                          | 110 |
| Zwitterionic Preliminary RFB test.....                       | 111 |
| 3.2.2 $\beta$ -generation RFB design.....                    | 114 |
| Investigating different electrolytes .....                   | 121 |
| Oxygen permeability of tubing .....                          | 125 |
| 3.2.3 $\gamma$ -generation RFB design .....                  | 128 |
| New peristaltic pump.....                                    | 129 |
| Centrifuge tube addition .....                               | 130 |
| Symmetric Flow cell tests.....                               | 131 |
| Asymmetric System.....                                       | 134 |
| Capacity fade and electrolyte stability.....                 | 164 |
| 3.3 Conclusions .....  | 172 |
| 3.4 Future Work .....  | 173 |
| 3.5 Experimental Methodology & Materials.....                | 175 |
| 3.5.1 Materials used.....                                    | 175 |

|   |     |
|---|-----|
| 3.5.2 Physical Measurements .....                 | 175 |
| 3.5.3 Electrochemical Measurements.....           | 175 |
| 3.5.4 Flow Cell Tests.....                        | 176 |
| 3.5.5 Membrane Permeability Tests.....            | 177 |
| 3.5.6 Pre-treatment Methods.....                  | 177 |
| 3.6 References .....                              | 178 |
| CHAPTER 4 .....                                   | 181 |
| 4.1 Introduction .....                            | 182 |
| 4.1.1 Debromination of vicinal dibromides.....    | 182 |
| 4.1.2 Electrogenerated species .....              | 184 |
| 4.1.3 Phase-transfer catalysis .....              | 185 |
| 4.2 Biphasic electrocatalysis .....               | 187 |
| 4.2.1 Viologens as phase-transfer catalysts.....  | 187 |
| 4.2.2 Induction Time and Use of Br Scavenger..... | 193 |
| 4.2.3 Electrolyte composition .....               | 197 |
| 4.2.4 Scavenger Optimization .....                | 199 |
| 4.2.5 System Redesign .....                       | 202 |
| 4.2.6 Substrate Scope.....                        | 215 |
| 4.3 Conclusion .....                              | 219 |
| 4.4 Future Work .....                             | 220 |

|  |     |
|--|-----|
| 4.5 Experimental: Materials and Methods .....                            | 221 |
| 4.5.1 Materials.....   | 221 |
| 4.5.2 Synthesis of catalyst (A).....                                     | 221 |
| 4.5.3 General procedure for bromination of styrene derivatives (B):..... | 221 |
| 4.5.4 Bromination of alkene derivatives (C): .....                       | 225 |
| 4.5.5 General procedure for Electrasyn® reaction (D):.....               | 226 |
| i) Dehalogenation of 1,2-dibromo(ethyl)benzene (preliminary tests).....  | 226 |
| ii) Dehalogenation of 10 using a Br <sup>-</sup> Scavenger.....          | 227 |
| iii) Optimized conditions for dehalogenation of vic-dibromides .....     | 227 |
| Spectral data of dehalogenated compounds.....                            | 228 |
| 4.6 References .....   | 231 |
| CHAPTER 5 .....  | 234 |
| 5.1 Introduction .....   | 235 |
| 5.2 Developing Flavin Derivatives .....                                  | 238 |
| 5.2.1 Sulphonate-flavin.....   | 238 |
| 5.2.2 Water-soluble flavin derivatives .....                             | 246 |
| 5.2.3 1,3,7,8-tetramethylbenzo[g]pteridine-2,4(1H,3H)-dione (19).....    | 251 |
| 5.3 Conclusions .....  | 254 |
| 5.4 Future Work .....  | 254 |
| 5.5 Experimental Methodology & Materials.....                            | 255 |



|  |     |
|--|-----|
| 5.5.1 Materials used and Physical Measurements .....                               | 255 |
| 5.5.2 Electrochemical Measurements.....  | 255 |
| 5.5.3 Synthesis of Lumichrome .....  | 256 |
| 5.5.4 Synthesis of water soluble flavin derivatives (General procedure A) .....    | 257 |
| 5.5.5 Synthesis of 1,3,7,8-tetramethylbenzo[g]pteridine-2,4(1H,3H)-dione (19)..... | 258 |
| 5.6 References .....   | 259 |
| CHAPTER 6 .....  | 261 |
| 6.1 Conclusions .....  | 262 |
| 6.2 Future Work .....  | 263 |
| APPENDIX 1.....  | 264 |
| Additional characterization techniques.....  | 265 |
| Additional data.....   | 268 |
| Chapter 3 .....  | 268 |
| Chapter 5 .....  | 270 |
| References.....  | 271 |
| APPENDIX 2.....  | 272 |
| Additional NMR spectra .....   | 273 |
| NMR Spectra of <i>vic</i> -dibromides .....  | 274 |
| NMR Spectra of alkenes .....   | 279 |

## Abbreviations

| <b>Abbreviation</b> | <b>Definition</b>                                    |
|---------------------|--|
| <b>AEM</b>          | Anion Exchange Membrane                              |
| <b>AORFB</b>        | Aqueous Organic Redox Flow Battery                   |
| <b>BPM</b>          | Bipolar Membrane                                     |
| <b>BTMAP</b>        | Bis(3-trimethylammonio)propyl viologen tetrachloride |
| <b>CE</b>           | Coulombic Efficiency                                 |
| <b>CEM</b>          | Cation Exchange Membrane                             |
| <b>COVID</b>        | Corona Virus   |
| <b>CTC</b>          | Charge Transfer Complex                              |
| <b>CV</b>           | Cyclic Voltammetry                                   |
| <b>DC</b>           | Direct Current                                       |
| <b>DCM</b>          | Dichloromethane                                      |
| <b>DFT</b>          | Density Functional Theory                            |
| <b>DMF</b>          | Dimethylformamide                                    |
| <b>DMSO</b>         | Dimethyl Sulfoxide                                   |
| <b>ECDs</b>         | Electrochromic Devices                               |
| <b>EDX</b>          | Energy Dispersive X-Ray Analysis                     |
| <b>EIS</b>          | Electrochemical Impedance Spectroscopy               |
| <b>ESI</b>          | Electrospray Ionisation Mass Spectrometry            |
| <b>FAD</b>          | Flavin Adenine Dinucleotide                          |
| <b>FCN</b>          | Potassium Ferrocyanide                               |
| <b>FMN</b>          | Flavin Mononucleotide                                |

|                |  |
|----------------|--|
| <b>FTIR</b>    | Fourier transform Infrared Spectroscopy  |
| <b>GCPL</b>    | Galvanostatic Cycling with Potential Limitation  |
| <b>HATU</b>    | 1-[Bis(dimethylamino)methylene]-1H-1,2,3-triazolo[4,5-b]pyridinium 3-oxide hexafluorophosphate |
| <b>HOMO</b>    | Highest Occupied Molecular orbital   |
| <b>IEM</b>     | Ion Exchange Membrane  |
| <b>LSV</b>     | Linear Sweep Voltammetry   |
| <b>LUMO</b>    | Lowest Unoccupied Molecular Orbital  |
| <b>MV</b>      | Methyl Viologen  |
| <b>NMP</b>     | N-methyl-2-pyrrodione  |
| <b>NMR</b>     | Nuclear Magnetic Resonance   |
| <b>ORFB</b>    | Organic Redox Flow Battery   |
| <b>PCET</b>    | Proton-coupled electron transfer   |
| <b>PTFE</b>    | Polytetrafluoroethylene  |
| <b>QPS</b>     | Quaternary Pyridinium Salts  |
| <b>RDE</b>     | Rotating Disk Electrode  |
| <b>RFB</b>     | Redox Flow Battery   |
| <b>SEM</b>     | Scanning Electron Microscopy   |
| <b>SHE</b>     | Standard Hydrogen Electrode  |
| <b>TBA</b>     | Tetrabutylammonium   |
| <b>TEMPA</b>   | 4-amino-2,2,6,6-tetramethylpiperi- din-1-oxyl  |
| <b>TEMPO</b>   | 2,2,6,6-tetramethylpiperi- din-1-oxyl  |
| <b>TEMPTMA</b> | N,N,N-2,2,6,6-heptamethylpiperidiny l oxy-4-ammonium chloride                                  |

|             |                                  |
|-------------|----------------------------------|
| <b>THF</b>  | Tetrahydrofuran                  |
| <b>VRFB</b> | Vanadium Redox Flow Battery      |
| <b>XPS</b>  | X-ray Photoelectron Spectroscopy |

**CHAPTER 1**  
**INTRODUCTION**

---

*"The Lord will fight for you; you need only to be still."*

*Exodus 14:14*

## 1.1 Introduction to Electrochemistry

Electrochemistry is the branch of chemistry that studies the relationships between electrical energy and chemical reactions, and is one of the oldest and most interdisciplinary of all the sciences.<sup>1</sup> The foundations of electrochemistry date back to the late 18<sup>th</sup>-century where Luigi Galvani and Alessandro Volta drew correlations between the frog they were examining and electrochemical phenomena which ultimately led to the development of the “voltaic pile” by Volta.<sup>2</sup> This invention is noted as the first modern battery, and led to the move from static electricity to generated electric currents.<sup>2,3</sup> This created two main areas for further research in chemistry; the effect of electricity on chemicals, and the chemical production of electricity.

Using a “pile”, William Nicholson and Anthony Carlisle were able to electrolyze water and this led to the discovery of “water-splitting” which liberates oxygen at one pole and hydrogen at the other.<sup>2</sup> Similarly, Jons Berzelius and William Hisinger conducted experiments on the electrolysis of salts which revealed changes in pH of a solution at either pole when electrolyzing salts.<sup>4</sup>

Today, electrochemical reactions are a fundamental part of our daily lives, and electrochemistry forms the basis for several spheres of chemistry and research including, and not limited to: electrocatalysis,<sup>5</sup> electrolysis,<sup>6</sup> photoelectrochemistry,<sup>7</sup> bioelectrochemistry,<sup>8</sup> and electrochemical energy technology.<sup>9-12</sup> One of the key applications of electrochemistry is in the production of batteries, which are essential for powering a variety of portable electronic devices, such as smartphones and laptops, and other electronic devices that make our lives more convenient.<sup>1-3</sup>

### 1.1.1 Electrochemical theory

Electrochemistry studies the movement of charge, the movement of electrons in different systems, such as capacitors, and membranes, and the migration of ions in a liquid or solid solutions.<sup>1</sup> In most laboratory electrochemical systems, the movement of charge takes place at liquid/solid interfaces and the solid conductor in this set-up is known as an electrode. Depending on the movement of electrons to the electrode surface or from the electrode surface this is referred to as an anode or cathode, respectively.

In order to form a complete circuit, every electrochemical system contains at least two electrodes which are connected by an external electrical conductor and separated by an electrolyte and/or a membrane.<sup>13</sup> Electrons are able to flow from one electrode to the other through the external conductor and the circuit is completed by the movement of ions through the electrolyte. Electrolytes facilitate the movement of ions and are often dissolved salts which have dissociated into their component ions. Fundamentally, for an electrochemical reaction to occur in a galvanic cell, reduction must take place at the cathode whilst oxidation occurs simultaneously, at the anode, as classically seen in “redox” reactions, and the properties of a cell are determined by the two half-reactions. For an electrochemical cell, the redox reactions can be controlled by applying a potential difference across the electrodes. As per Faraday’s Law, the amount of species in solution that undergoes reduction or oxidation is directly proportional to the number of electrons transferred between the electrode and the solution per unit time.

- **Thermodynamics**

The cell potential,  $E_{cell}$ , is determined by the potential difference between the cathode and the anode as per **equation 1.1** :

$$E_{cell} = E_{cathode} - E_{anode} + IR_{drop} \quad \text{equation 1.1}$$

The potential of an electrochemical cell  $E_{cell}$  and the standard potential of a species ( $E^0$ ), are related to the activities of the reduced(Red)/oxidized(Ox) species by the Nernst equation (**equation 1.2**). The activities of the redox active species are usually replaced with concentrations as these are often known.

$$E_{cell} = E^0 - \frac{RT}{nF} \ln \frac{[Ox]}{[Red]} \quad \text{equation 1.2}$$

where  $E^0$  is the standard potential of a species,  $R$  is the universal gas constant,  $T$  is the temperature,  $n$  is the number of electrons transferred in the reaction of the cell, and  $F$  is Faraday's constant. The Nernst equation be used to predict how a system will respond when the concentration of redox active agents or electrode potential is changed.

The Nernst equation provides a relationship between the potential of the cell or half-cell to the concentration of the redox active species and their standard reduction potentials.<sup>1</sup> The Nernst equation can be used to determine the equilibrium cell potential,  $E_{cell eq.}$ , which can also be referred to as the open circuit or rest potential as at this point there is zero net current flow.<sup>13</sup>

As an example, assume a standard half-reaction of the reduction of ferrocenium ( $Fc^+$ ) (**equation 1.3**) which takes place under standard conditions in aqueous solutions, where  $E^0$  is the half-cell reduction potential:



The Nernst equation can be applied to this reaction as follows.



$$E = E^{0'} - \frac{RT}{nF} \ln \frac{[Fc^+]}{[Fc]} = E^{0'} + 2.3026 \frac{RT}{nF} \log_{10} \frac{[Fc^+]}{[Fc]} \quad \text{equation 1.4}$$

Where  $E^{0'}$  is the formal potential determined by the experimental conditions employed, and all other variables are consistent with **equation 1.2**.

External control of the potential can therefore be used to drive a reaction to a preferred composition (this is termed an electrolytic cell), or cell composition can be used to generate a potential (this is termed a galvanic cell).<sup>13</sup> In a galvanic cell, the positive electrode where reduction occurs is the cathode, as opposed to the electrolytic cell where the positive electrode is the anode, and *vice versa* for the anode.

In order for an electrochemical reaction to occur, a driving force must exist and in the absence of current, the potential difference between the electrodes, the *surface overpotential*, drives the reaction.<sup>13</sup> The overpotential ( $\eta$ ) is the difference between the experimentally observed potential and the theoretical potential.<sup>14</sup> The rate of mass transport and the rate of charge transfer directly influence the rate of an electrochemical reaction, and the electrode potential is the main limiting kinetic factor.<sup>1,14</sup>

## 1.2 Introduction to Redox Flow Batteries

Redox flow batteries (RFBs) have received a significant increased interest in the past few years due to the emerging energy crisis which the world at large is facing as RFBs are a potential solution for medium and large-scale energy storage, in particular with grid-scale applications.<sup>15,16</sup> At present, whilst large amounts of electrical energy are produced from intermittent renewable sources such as solar and wind energy, the development of a stable

and reliable large scale power storage is necessary in order to ensure that the supply of renewable energy to the grid will remain reliable and consistent.<sup>15,16</sup>

### 1.2.1 Redox Flow Battery Fundamentals

A typical RFB has two storage tanks containing electrolytes that are pumped across a membrane which sits between two electrodes, affording a flow of current through an external circuit, coupled with selective ion transfer across the membrane. In an ideal case, by means of size or charge exclusion, the membrane will prevent the redox species from crossing over from one tank to another whilst allowing ions of the supporting electrolyte to pass freely.<sup>17</sup> Electrolyte crossover is a phenomenon wherein the electrolyte from one reservoir crosses the membrane and ends up in the other electrolyte reservoir which may lead to the formation of insoluble complexes, electrolyte degradation, and even cell death.<sup>18</sup> The rate and extent of crossover is driven by time, concentration of active species, pressure, osmotic pressure differences, and applied current.

A typical RFB can be seen in **Figure 1.1**. As seen in the figure, a separator or membrane is responsible for facilitating the ionic transfer between the electrodes whilst impeding the mixing of the positive and negative electrolytes.<sup>19,20</sup> If the system is an undivided RFB, then no membrane or separator is required and both redox couples are dissolved in the same electrolyte solution which is contained in only one reservoir. The electrolytes are circulated between the external reservoirs and the stacks by pumps.

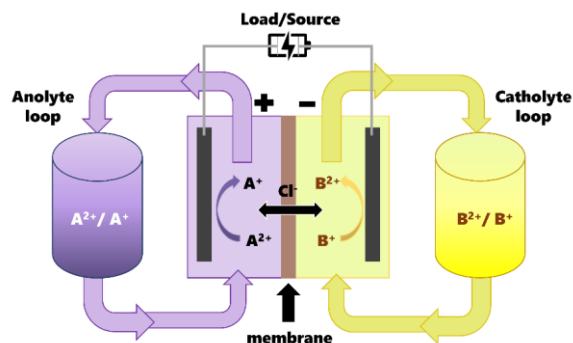


**Figure 1.1** Structure of a redox flow battery.

When the RFB is charged, the energy transferred into the system drives the redox reactions of the dissolved species which in turn stores energy in the electrolytes.<sup>19</sup> As with the battery convention, when discharging the positive electrode is the cathode whilst the negative electrode is referred to as the anode, similarly the associated energy storage solutions are referred to as the catholyte and anolyte.<sup>9</sup>

Varying the volume of an electrolyte tank, as well as changing the size of a cell stack directly affects the power and capacity of a RFB system<sup>20</sup> which is tuned for the application it is intended for: load balancing, peak shaving, power conversion, and stand-alone power system.<sup>9</sup> (*Vide supra*) This offers an added benefit as the system can swiftly alternate between charging and discharging, and then store electricity for several hours.<sup>20</sup> There are significant safety and economic factors which make RFBs a viable candidate for energy storage. These systems often utilize aqueous, non-flammable electrolytes which are recirculated throughout the cell ensuring safe battery operation.<sup>16,20</sup> Specifically, in developing countries, flow battery systems which use a shipping container form can be moved around easily, thus

forming a “mobile” energy storage device which can reduce the demand on the grid thereby assisting with issues such as rolling blackouts and load and frequency balancing.<sup>20</sup>

The primary step in developing redox active agents for RFB electrolytes involves the identification of the redox-active core. Thereafter, the core can be functionalized to tune the reduction potential and solubility accordingly.<sup>21</sup> By simply changing the chemical properties of the electrolyte one can achieve properties which are optimised for target applications. For example, in order to obtain higher energy capacity and higher volumetric energy density, one would have to increase the concentration of the active species, and this will ultimately result in the increase of current output, decreasing the occurrence of secondary reactions.<sup>19</sup>

Pushing the potential windows of each electrolyte further away from each other may be controlled by modifying redox active materials for use within RFBs by incorporating electron withdrawing groups or electron donating groups.<sup>22</sup> The use of the electron withdrawing group moves the redox potential more positive whilst the electron donating group pushes the redox potential to a more negative region. Commonly used electron withdrawing groups include nitro and sulfonic acid moieties, whilst electron donating groups are often amino and hydroxyl functional groups.<sup>17,22</sup> Due to this potential flexibility, there has been great interest in the use of organic and organometallic-based materials which can be easily manipulated to provide optimal redox potentials for a high performing RFB.<sup>17</sup>

It is important to remain within the range of stable aqueous redox potentials on order to prevent oxygen or hydrogen evolution. Computational methods can assist with the determination of the potential limits. Density Functional Theory (DFT) allows calculation of the lowest unoccupied molecular orbital (LUMO) and highest occupied molecular orbital

(HOMO)<sup>22</sup> and frontier orbital (HOMO and LUMO) energies are correlated with redox potentials.<sup>17</sup>

The cell voltage is dependent on the redox potential difference of the positive electrode/cathode and the negative electrode/anode which make up that cell.<sup>19,23</sup> The redox potential is affected by the chemical and physical conditions of the electrolytes within the RFBs and may be influenced by pH. For proton coupled reactions, change in reduction potential is linearly proportional to change in pH value.<sup>17,24</sup>

The performance of an RFB is dependent on several parameters which may be monitored to benchmark the battery's capability. Energy density is one of the main parameters and is indicative of the amount of charge that is stored in the battery.<sup>17,22</sup> The energy density with units Wh.L<sup>-1</sup>, of a RFB battery, is calculated as follows;

$$\text{Energy density} = \frac{nCFV}{\mu_v} \quad \text{equation 1.5}$$

Where  $n$  is the number of electrons that are transferred during the redox reaction,  $F$  is Faraday's constant,  $C$  is the lowest concentration of the redox-active materials in either the negolyte or catholyte,  $V$  is the battery's voltage, and  $\mu_v$  is the volume factor. The volume factor,  $\mu_v$  is calculated by [1+ (lower electrolyte concentration/higher electrolyte concentration)].<sup>22</sup> The energy density is mainly dependent on the cell voltage, electrolyte solubility, and whether single or multiple electron transfer occurs in the RFB,<sup>17,22</sup> and therefore, to ensure the optimum performance of the RFB, redox-couples selected should be highly soluble in the chosen electrolyte.<sup>17,19,24</sup> Furthermore, the aggregation of redox active species within the electrolyte tanks will remove active species from solution, changing

electrolyte concentrations and thus cell potentials per the Nernst equation, which may decrease battery performance. Modifying or engineering molecules to have higher solubility in desired electrolytes has become quite common<sup>17,25</sup> and in the case where aqueous electrolytes are used, polar functional groups and hydrogen bond donors/acceptors are frequently added to make the molecule more hydrophilic and thus increase its solubility.<sup>26-</sup><sup>28</sup> The solubility of the different redox states of the redox active species may differ, and electrochemical and analytical techniques such as cyclic voltammetry and Ultraviolet-Visible Spectroscopy (UV-Vis) may be used to assess the solubility of all redox states.<sup>15,19</sup>

Another important metric for the performance of RFBs is the power density<sup>17</sup>, measured in W/cm<sup>2</sup>, which is determined by:

$$\text{Power density} = \frac{I \times V}{S} \quad \text{equation 1.6}$$

Where I is the discharge current applied during cell cycling, V is the recorded output potential, and S is the surface area of the membrane or electrode geometric area. The power density is affected by many parameters including electrolyte conductivity, the separator's ionic conductivity, the diffusion coefficients and reaction kinetics of the redox species, cell potential, size of current collector, and battery structure/geometry.<sup>17</sup>

The Coulombic efficiency (CE) is also important in terms of evaluating the performance of the battery. This may be calculated by comparing the charge output when discharging to the charge input during charging as seen in **equation 1.7**. Highly selective exchange membranes are usually used in RFBs in order to ensure high CE.<sup>17</sup>

$$\text{Coulombic Efficiency (\%)} = \frac{\text{Discharge Capacity (C)}}{\text{Charge Capacity (C)}} \times 100 \quad \text{equation 1.7}$$

### **1.2.2 Design and Properties of Redox Flow Batteries**

The design of redox flow batteries borrows concepts and ideology from both fuel cells and batteries. Similar to a fuel cell, the chemical reaction within the system is sustained by ongoing circulation of fuel which is consumed to release energy. However, unlike a fuel cell, in RFBs the reaction taking place is reversible.<sup>17</sup>

The energy capacity of a RFB is determined by the quantity of electrolyte stored within the system, and the size of the current collectors and number of cell stacks determine the overall power of the RFB.<sup>17</sup> One of the most advantageous features of RFBs is the fact that the replacement of the electrolyte in the system allows for instantaneous recharging whilst the exhausted electroactive materials are recovered simultaneously which provides a wide range of flexibility in terms of the applications for RFBs.<sup>17</sup> Classical RFBs require reversible redox reactions to occur at electrodes, with a high potential difference, with soluble redox active species that are stable within the solvent window to avoid unwanted side reactions.<sup>19</sup>

RFBs are formed in stack or filter-press reactors which are made up of numerous cell frames containing bipolar electrodes.<sup>9</sup> The stack consists of an endplate, isolation plate, graphite plate, graphite felt, flow frames, and the membrane. The mechanical stability of the structure is governed by the end plates; the isolation plate regulates the isolation of electrical species between the half-cells and the graphite plate closes off the half cell. The distribution of electrolyte is governed by the flow frames, with the graphite felt acting as an electrode.<sup>19</sup>

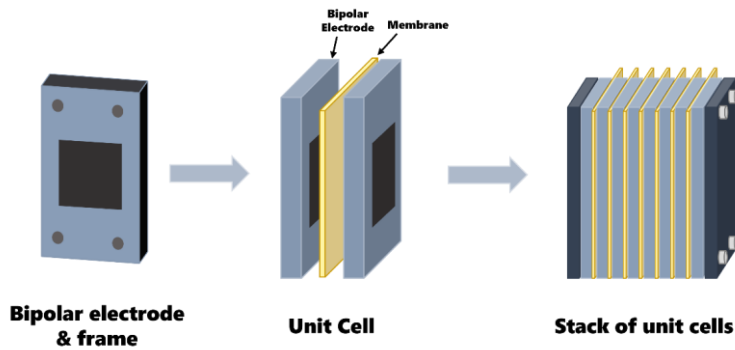


**Figure 1.2** Design of a unit cell and assembly of several unit cells to form a stack, modified from Arenas *et al.*<sup>19</sup>

The fundamental unit of an RFB is an electrochemical flow cell which has two electrolytes separated by a membrane, each contained in a separate half-cell, and several unit cells are combined to form the RFB system. As well as electrolytes and electrodes themselves, there are several additional components for RFBs which may be divided as follows;<sup>19</sup>

- *Electrolyte flow and storage* – electrolyte circuit (piping), pumps, heat exchanger, switch valves, valve actuators and electrolyte tanks.
- *Electrical connections and power conversions* – electrical circuits, power electronics, power conditioner, AC/DC rectifier, transformer, AC breaker, cooling system,
- *Control and monitoring* - sensors for: electrolyte flow rates, state of charge (SOC), temperature, pH, gas release, *etc.*; instruments for measuring stack potential and current; control system and software.

### 1.3 Electrolytes

Overall performance RFB is directly attributed to the physical and chemical properties of the electrolytes within the RFB system. An ideal electrolyte should possess the following characteristics: low viscosity, high ionic conductivity, safety when handling, good chemical



and good thermal stability, affordability & relative abundance, stability to long-term storage, high solubility of redox-active species, and easy chemical analysis to evaluate the state of charge.<sup>19</sup>

Aqueous electrolytes have one main disadvantage over non-aqueous electrolytes: the relatively narrow, pH dependent stability “window” of water which is visualised using the Pourbaix diagram of water.<sup>15</sup> As a result, it is always important to avoid water oxidation or hydrogen evolution when operating an aqueous RFB.

A co-dependent relationship exists between the electrolyte pH and the redox active species used in the system as per the Nernst equation ([equation 1.2](#)).<sup>24</sup> Certain redox couples such as ferrocyanide may have higher stability in alkaline electrolytes,<sup>29,30</sup> whilst other organic molecules such as viologens and quinones may undergo hydrolysis in alkaline electrolytes.<sup>31</sup> Therefore, it is necessary to determine the pH range within which the desired redox active species for the RFB are stable within before cycling them in the system.

Mass transport and electrolyte viscosity are directly related<sup>16,32</sup> such that lower viscosity rates allow for higher mass transport rates leading to higher energy efficiency rates.<sup>19</sup> The ionic conductivity of the electrolyte refers to the electrolyte’s ability to conduct ions, allowing a current to flow.<sup>1</sup> This is determined by the supporting electrolyte and is inversely proportional to the resistance of the cell, ultimately influencing cell potential and performance. Higher ionic conductivity is preferred as this results in lower cell resistance which equates to good cell performance.<sup>1,19</sup>

A review by the Aziz group<sup>31</sup> evaluated the lifetime of electrolytes within AORFBs, comparing the capacity fade rates from all common AORFB electrolytes. The group reported that the

extent of capacity fade was proportional to the duration of the experiment, *i.e.*, how long the system had been cycling for. Therefore, it could be concluded that capacity fade was time dependent. The authors attributed irreversible capacity fade to electrolyte leakage, or reactant crossover or reaction decomposition through various decomposition mechanisms such as Hoffman Elimination. In the case of reversible capacity fade, this was attributed to possible side reactions which may have caused unbalance in the system, and this may be corrected with time and prolonged cycling.

### 1.3.1 Electrodes

Electrodes play a crucial role in the overall RFB set-up, contributing to the long-term stability and capacity of the RFB, and therefore they should exhibit high electrochemical stability, high electrical conductivity, good mechanical stability, and rapid reaction kinetics for the redox couple to ensure good cell performance.<sup>9</sup> Other characteristics of ideal electrodes include: the ability to operate at high current densities, long cycling life, resistance to corrosion, and low electrical resistivity.<sup>19</sup> The electrode surface reactivity is dependent on the number of active sites which exist on the electrochemically active surface as well as the intrinsic rate constant of the redox couple within the system and their material properties and respective functional groups.<sup>33</sup> Therefore, by optimizing the electrode surface chemistry and the number of available active sites, the overall power density and voltage efficiency can be increased.<sup>19,33</sup>

Porous electrodes, such as graphite felt,<sup>34</sup> are often used, and these must be able to operate without any blockages, and/or parasitic surface reactions.<sup>35,36</sup> It is typical to find electrodes which are composed of graphite polymer plates in combination with porous electrode materials such as carbon felt, which are then compressed onto the surfaces.<sup>19</sup> The

performance of carbon-based electrodes may be improved by catalytic coating and varying activation treatments, which may include modifying the surface using metal oxides, non-metallic catalysts, or activation by thermal treatment or the use of acids.<sup>19,36,37</sup>

[Bipolar electrodes](#) also exist and these typically contain a carbon composite core which is flanked by activated carbon and polymer layers.<sup>38</sup> These bipolar electrodes are often used in as end electrodes within a stack to be connected due to their reversible anode and cathode sides allowing the current to flow perpendicularly to the electrode surface.<sup>19</sup> Low resistivity of the electrode is desired because this will ensure uniform current distribution and potential.

The pH of the electrolytes and the redox chemistry of the system have to be considered when choosing electrode materials as this might damage or activate the electrode surface.<sup>34,39</sup> In a recent evaluation of the next generation of aqueous RFBs, Narayan *et al.*<sup>40</sup> discussed the possible use of titanium as the negative electrode in acidic media as the metal is corrosion resistant, whilst nickel foam is a potential option for alkaline media. The use of metallic electrodes is not common as they are limited due to potential irreversible redox reactions, or dissolution of the electrodes, and they might promote water-splitting which is highly undesirable in aqueous RFBs as it worsens the battery performance. Metal electrodes are also more costly than their carbon-based counterparts.<sup>19</sup>

### **1.3.2 Membranes**

Membrane separation with a flow cell is essential to prevent crossover of species within the cell and is the only form of physical separation between the electrolytes. At the same time, high ionic conductivity of the membrane is desired to allow for the movement of charge carrier ions across the membrane. An ideal membrane should be able to keep the anolyte

and catholyte from mixing while still allowing the transport of charge carrying ions to maintain the electrical neutrality and electrolyte balance,<sup>15</sup> which decreases the internal resistance of the system and leads to good battery performance. Furthermore, properties such as ion exchange ability, ionic conductivity, ion permeability, leakage, electrolyte uptake, swelling ratio, and dimensional stability should also be monitored and evaluated over the course of use of the membrane<sup>19</sup> as the overall life of the cell depends quite significantly on the stability and longevity of the membrane.

Ion Exchange membranes (IEMs) are quite commonly used for redox flow battery research as they allow for selective transport of ion, isolating redox active species in their own reservoirs.<sup>19</sup> The biggest drawback is their cost which can be to 40% of the total cost of a RFB.

Cation exchange membranes (CEMs) are known to have better ionic conductivity, mechanical strength, and chemical stability in comparison to anion exchange membranes (AEMs).<sup>19</sup> The most commonly used cation exchange membrane is Nafion – a hydrophobic/hydrophilic two-phase structure formed of a tetrafluoroethylene( hydrophobic backbone) and sulfonate clusters which provide the hydrophilic nature. The biggest drawback to Nafion is its high cost, despite which it is still quite popular within RFB research given its high ionic conductivity, and good selectivity.<sup>15,17,19</sup>

AEMs typically conduct anions such as  $\text{OH}^-$  and  $\text{Cl}^-$ , and the membrane itself contains positive charged groups which are covalently bound to a polymer backbone.<sup>41</sup> They are commonly reported for use in systems containing organic molecules in aqueous electrolytes.<sup>16</sup>

Unfortunately, reports have indicated that AEMs may be susceptible to radical-derived degradation which limits their use in highly alkaline electrolytes.<sup>41</sup>

Electrolyte components must also be compatible with the membranes *e.g.* Winsberg *et al.*<sup>42</sup> used a cation exchange membrane with negatively charged sulfonic groups in a hybrid RFB system having previously found that the use of an anion exchange membrane lead to the precipitation of  $Zn^{2+}$  from their RFB system.

Dialysis membrane is a much cheaper option than Nafion, costing around 5-10% of the price of Nafion.<sup>15,17</sup> Pore sizes within a dialysis membrane range from 1-10 nm and the separation of molecules is purely based on size exclusion. This means that the ion selectivity may be manipulated by varying the overall size of the organic redox species which are used.<sup>17</sup> Incorporating this type of membrane into a RFB system would be a step in the right direction towards achieving a low-cost high performance system, and this has been explored previously.<sup>43</sup> Given the high cost of membranes, membrane-free systems such as zinc-manganese-oxide,<sup>44</sup> zinc-phenothiazine,<sup>45</sup> and a biphasic-electrolyte system<sup>46</sup> have been proposed and evaluated. These systems utilize microfluidic channels or immiscible electrolytes to ensure intermixing is prevented.<sup>47</sup>

### **1.3.3 Evolution of Redox Flow Batteries**

The first RFB-like cell was introduced in 1884 by Charles Renard who created a zinc-chloride battery which was used to power his airship. In 1949, the concept and initial design of a RFB was patented by Kangro,<sup>9</sup> wherein the patent stated that electrical energy could be stored within liquids through a series of electrochemical reactions which would occur at redox coupled electrodes, referring to electrodes that are located in separate reaction vessels, but

form a combined redox couple. In the device described, *"a single substance, which can appear in three or more valence states, is used as an electrochemically active substance in solution"* was passed through half cells and then into separate tanks as it was oxidized or reduced.

In this patent,  $\text{Cr}_2(\text{SO}_4)_3$  was used as the cathode and anode active material and the supporting electrolyte was 2 M sulfuric acid. It was not until the 1970s that this technology was revived by Lawrence Thaller of NASA for solar photovoltaic energy storage<sup>17</sup> which focused on the development cost-effective materials for energy storage and ultimately resulted in the development of RFBs using the  $\text{Cr}^{2+}/\text{Cr}^{3+}$  and  $\text{Fe}^{2+}/\text{Fe}^{3+}$  couples in hydrochloric acid solution.<sup>9,17</sup>

NASA pioneered the engineering of specific aspects of RFBs such as the different electrode configurations, and cost analysis.<sup>48</sup> Nevertheless, these systems had issues with electrolyte crossover and formation of Cr complexes, and so research was halted with time.<sup>19</sup> Other notable configurations were developed between 1970-1990 including a the Zn-Br RFB,<sup>20</sup> developed by Exxon which became quite popular in Japan in the 1990s when it formed part of the Moonlight project focused on the conservation of energy and the development of new energy technologies.<sup>19</sup>

In 1986, Skyllas-Kazacos and co-workers<sup>49</sup> presented an all-vanadium redox flow battery (VRFB), and this design still remains the most widely researched RFB to date with many researchers attempting to optimize the electrolyte solutions, the number of electrodes, and different membranes used.<sup>9,49</sup> The main benefit of a "same-electrolyte" system is that it minimizes the issue of electrolyte crossover and ultimately extends the lifetime of the battery.<sup>19</sup> Since its initial developments in the 1980s, extensive research has been conducted

on VRFBs by a wide array of companies<sup>49</sup> such as Kashima Kita Electric Power Corp. (Mitsubishi), Japanese Electrotechnical Lab, UniEnergy Technologies, Gildermeister AG, and Fraunhofer ICT.<sup>19</sup>

The development of RFB systems has not been without challenges, namely the limited lifetime of the RFB which directly related to operational costs.<sup>20</sup> Whilst the history of RFBs is dominated by inorganic redox active species, the high costs, and finite sources of the materials drove the research to explore organic molecules which could be engineered to achieve the desired qualities for a specific RFB system.<sup>17,20,50</sup> This led to the development of an array of RFB configurations including: organic/inorganic RFBs,<sup>51</sup> all-organic RFBs,<sup>52</sup> polymer-based organic/inorganic RFBs,<sup>43</sup> organic/halogen RFBs,<sup>53</sup> and symmetric all-organic RFBs.<sup>54</sup>

#### **1.3.4 Examples of Redox Flow Batteries**

Vanadium has been the most popular material used in RFBs as it provides high capacities and long-lifetime which is favourable.<sup>55,56</sup> However, the main drawback to this technology is the high cost of vanadium and the scarcity of the metal. Furthermore, vanadium RFBs use acidic solvents such as sulphuric acid which is highly toxic. Unfortunately, despite the major efforts made towards VRFB technology, the limitations such as solubility of redox species, high electrolyte cost, thermal precipitation of  $V^{5+}$ , and production capacity of vanadium salts, still remain.<sup>19</sup>

Therefore, the investigation into molecular engineering of organic redox active agents has gained some traction as an alternative. This affords the possibility of developing sustainable and environmentally friendly energy storage systems<sup>17</sup> containing organic molecules, which

are relatively low-cost, may allow use of safer electrolytes, have tailorable chemical and physical properties, and may be produced on scale.<sup>17,20,40</sup>

### **Aqueous Organic Redox Flow Batteries**

Despite the numerous advantages over their inorganic counterparts, ORFBs still possess limitations and areas for improvement in terms of their design and performance. These limitations include: low volumetric capacity and energy density relative to inorganic RFBs, limited operational voltage window, and the cost and performance of membranes (CEMs & AEMs).<sup>15,20</sup>

Polymer-based cells have drawn attention as they provide a means to use low cost membranes such as dialysis membranes, as exhibited by Janoschka *et al.*<sup>43</sup> in 2015. The membrane successfully separated the electrolytes from each other whilst ensuring good ionic conductivity, and notable electrolyte lifetime/stability. Alternatively, membrane-less or membrane-free RFB systems<sup>46,57</sup> have also been explored as a means to circumnavigate the high costs of membranes. In 2017, Navalporto *et al.*<sup>46</sup> reported the first membrane-less RFB system based on organic molecules instead of vanadium, which employed two immiscible electrolytes in a biphasic system.

Attempts to improve the energy density of ORFBs has been focused on increasing the solubility of the species used.<sup>20</sup> TEMPO derivatives<sup>42,58-60</sup> have been of great interest in this regard, and have often been coupled with methyl viologen (MV).<sup>54,61</sup> Liu *et al.*<sup>62</sup> developed an AORFB system comprise of MV and 4-OH-TEMPO, with NaCl as the supporting electrolyte. Due to its high water solubility (2.1 M), OH-TEMPO was chosen as the positive couple.



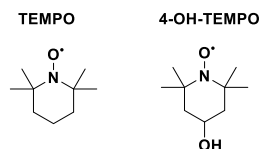


**Figure 1.3** The structures of TEMPO and 4-OH TEMPO.<sup>62</sup>

As the operation voltage window of AORFBs is limited by the water stability window, the redox pairs selected must make the most of the water stability window.<sup>15</sup> This may be achieved by using hybrid electrolyte systems or incorporating additives to stabilize the system.<sup>63</sup>

Ultimately, improving the electrolyte lifetime of ORFBs would make them more competitive against VRFBs and other inorganic configurations. This may be realized by using highly reversible redox couples that are not prone to any side reactions, and are not susceptible to conformational changes such as dealkylation or hydrolysis.<sup>20</sup> To this end, the Aziz group developed a phosphonate functionalized viologen<sup>64</sup> which cycled for 25 days without any electrolyte degradation and minimal capacity fade.

### 1.3 Introduction to Electrosynthesis

Organic electrosynthesis dates back 200 years, and a large breadth of literature regarding this topic exists.<sup>65</sup> In 1834, Michael Faraday reported a sodium acetate solution could be electrolysed to produce ethane gas,<sup>66</sup> unknowingly birthing the field of organic electrosynthesis and performing the reaction now known as the “Kolbe decarboxylation”.<sup>67</sup>

More recently, the drive towards organic electrosynthesis and/or electrocatalysis has accelerated because this approach offers a simpler, more efficient, economical, and “environmentally-friendly” approach to perform certain transformations compared to using traditional methods, particularly in the pharmaceutical, fine-chemical and fuel industries.<sup>68-</sup>

<sup>71</sup> Despite their well-established utility, traditional organic chemical methodologies suffer from numerous disadvantages such as the use of toxic solvents, costly starting materials, and multi-step reactions with often low yields.<sup>65</sup> Furthermore, these reactions tend to rely on stoichiometric reagents which increases the overall cost of synthesis.<sup>69</sup>

Organic electrosynthesis operates by transferring electrons to or from a substrate species, thereby forming a reactive intermediate which can further react to generate the desired product.<sup>69</sup> In general, all organic electrosynthesis processes may be considered to fall into four groups: direct electrolysis, mediated electrolysis, electrochemical catalysis, and ex-cell electrolysis (*vide infra*).<sup>72</sup> The formation of the activated intermediate is the key step of electrosynthesis which then allows for numerous subsequent reaction pathways, dependent upon conditions, resulting in the formation of the product.

Under electrosynthetic conditions, oxidation occurs at the anode and reduction occurs at the cathode.<sup>69</sup> The charge in the system must remain balanced and thus, as a reaction occurs

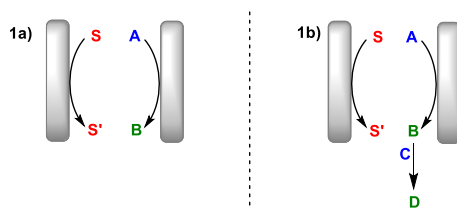
at the anode, a simultaneous reaction must occur at the cathode. This affords the possibility for pairing two different processes to occur simultaneously within the system.<sup>69</sup> In general, if only one of these reactions is desired then the paired reaction required to allow the desired transformation to occur is known as the counter reaction.

Electrosynthesis may be performed in two different modes: chronoamperometrically or chronopotentiometrically, which refers to galvanostatic and potentiostatic control, respectively.<sup>70</sup> Under galvanostatic conditions, only a working and counter electrode are required and a fixed current is passed through the system, and the applied potential increases over time.<sup>66,70,73</sup> This mode offers an easier set-up than the potentiostatic mode, with the added advantage of knowing the exact equivalents of electrons transferred, but the voltage range cannot be controlled.<sup>72</sup> During potentiostatic electrosynthesis, a fixed potential is applied to the working electrode and the current flows between the working electrode (WE) and counter electrode (CE), but a reference electrode is required to control the potential. This mode offers enhanced selectivity, but reproducibility is only ensured by using a reference electrode.<sup>72</sup> The equipment and types of electrodes used for electrosynthesis are dependent on the scale and desired outputs of the reaction and may use either two- or three-electrode equipment with varying potentiostats or galvanostats.<sup>73</sup>

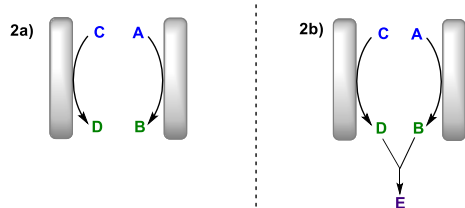
Due to its versatility, adaptability, and cost-effectiveness due to decreased quantities of reagents and solvents required, several industries and companies have embraced electrosynthetic technology.<sup>69,72</sup> Some notable electroorganic industrial processes include: the production of adiponitrile,<sup>6,72,74</sup> dimethoxylation of 4-tert-butyltoluene by BASF,<sup>6,75</sup> and the oxidation of 2-hydroxy-ethylfuran by Otsuka.<sup>6</sup>

### 1.3.1 Types of Electrochemical Synthesis

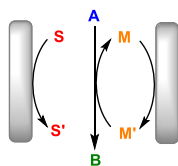
#### 1) Direct Electrochemical Reaction with solvent degradation



#### 2) Direct Electrochemical Reaction without solvent degradation



#### 3) Mediated or catalysed electrochemical reaction



#### 4) Redox combined electrochemical reaction

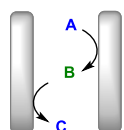


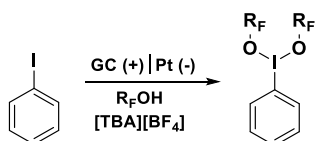
**Figure 1.4** The different types of electrochemical synthesis. S: solvent, S': solvent degradation product; A and C: reagents; B, D and E: product; M: mediator/catalyst, M': activated mediator or catalyst. Reproduced with modifications.<sup>73</sup>

As seen in **Figure 1.4**, the different types of reactions can be summarised as: 1) direct electrochemical reaction with solvent degradation as counter reaction, 2) direct

electrochemical reaction with nonsolvent degradation as counter reaction, 3) mediated or catalysed electrochemical reaction, 4) redox combined electrochemical reaction.

#### **Direct electrochemical reaction with solvent degradation**

This is the simplest kind of electrochemical reaction: the substrate is either reduced (at the cathode) or oxidized (at the anode) while the solvent is degraded at the opposite electrode surface as the counter reaction. (**Figure 1.4, 1a&b**) Radicals or unstable, reactive intermediates may react with the substrate to form a new product.<sup>73</sup> This was demonstrated by Wirth and co-workers<sup>76</sup> in the production of hypervalent iodine by oxidation of iodobenzene using fluorinated solvents used such as 1,1,1,3,3,3-hexafluoro-2-propanol (HFIP) or 2,2,2-trifluoroethanol as proton source for hydrogen evolution as the counter reaction. In this case, combining electrosynthesis with flow conditions gave an efficient method to oxidize iodoarenes to hypervalent iodine reagents, eliminating hazardous and costly chemical oxidants which are required in traditional methods.



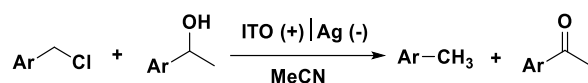
**Scheme 1.1** Direct electrochemical formation of hypervalent iodine compounds by Wirth *et al.*<sup>76</sup>

#### **Direct electrochemical reaction with non-solvent degradation**

Under direct electrosynthetic conditions, the molecules are synthesised due to an electron transfer between the electrode and the substrate in the electrolyte solution where the counter reaction is not solvent degradation. The counter reaction may be rate limiting,

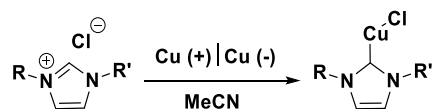
determining the rate of the main reaction or, the counter reaction may not participate in the desired reaction pathway (**Figure 1.4, 2a**).

Alternatively, the synthesis may be coupled and the products from each electrode can react further to form a new product (**Figure 1.4, 2b**). The work by Atobe *et al.*<sup>77</sup> is an example of this wherein paired electrocatalysis coupled oxidation of a ketone to an alcohol with reductive dehalogenation to form an alkane.



**Scheme 1.2** Paired electrocatalysis as reported by Atobe *et al.*<sup>77</sup>

Willans *et al.*<sup>78</sup> have used direct electrochemical synthesis without solvent degradation to synthesize metal-NHC complexes. In this work, the anode metal is oxidized to produce metal cations in solution and the imidazolium salt is reduced to the NHC on the cathode; thereafter, these products react together to form the final NHC-complex.



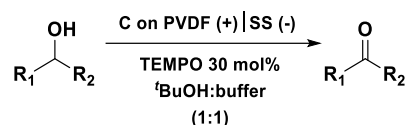
**Scheme 1.3** Formation of metal-NHC complexes as described by Willans *et al.*<sup>78</sup>

### Mediated electrochemical reaction

In this class of electrochemical process, the substrate itself is not oxidized or reduced directly on the electrode surface. Instead, a mediator or catalyst is activated at the electrode and this then goes on to oxidize or reduce the substrate, leading to the formation of a product.<sup>73</sup>

(**Figure 1.4, 3**) Mediated electrocatalysis is useful when overpotentials required for the unmediated reaction would involve working outside the solvent potential window and this

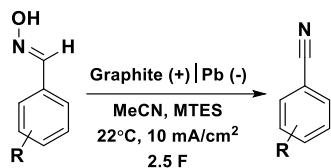
approach can prevent possible unwanted counter reactions. Furthermore, as the catalyst is regenerated electrochemically, the atom economy and efficiency of this method is enhanced in comparison to traditional methods requiring stoichiometric oxidant/reductants. Nitroxyl radicals such as 2,2,6,6-tetramethylpiperidin-1-yl)oxyl (TEMPO) are some of the most reported electrochemical mediators. For example, the TEMPO-mediated electrooxidation of alcohols has been reported previously using a continuous flow protocol<sup>79</sup> using polyvinylidene fluoride (PVDF) as the anode, coupled with a stainless steel cathode, and carried out in a buffered aqueous tert-butanol reaction medium without additional supporting electrolyte.



**Scheme 1.4** TEMPO mediated electrooxidation of alcohols by Brown and co-workers.<sup>79</sup>

#### Redox combined electrochemical reaction

This process is also known as “domino-oxidation-reduction sequence” and is often used with continuous flow methods. In this type of system, the overall transformation occurs in a sequential cascade of individual reactions, where the product generated at one electrode then reacts further on the surface of the other electrode.<sup>73</sup> (**Figure 1.4, 4**). The synthesis of nitriles from oximes *via* a nitrile-*N*-oxide demonstrates redox combined electrosynthesis.<sup>80</sup> Translating the reaction into a continuous flow protocol avoids the use of harsh reaction conditions typical of traditional methods, and increases the isolated yield for challenging substrates such as 2,6-dichlorobenzaldoxime from 40% to 63%.<sup>80,81</sup>



**Scheme 1.5** Optimized reaction conditions for the “domino oxidation-reduction sequence” as described by Waldvogel and Hartmer.<sup>80</sup>

### 1.3.2 Factors controlling the electrosynthetic process

#### Cell Design

Cell design is a critical component in the success of electrosynthetic reactions as it provides a way to control potentially parasitic counter reactions. There are three kinds of cells in common use; 1) undivided cell, 2) divided cell, and 3) undivided flow-cell.

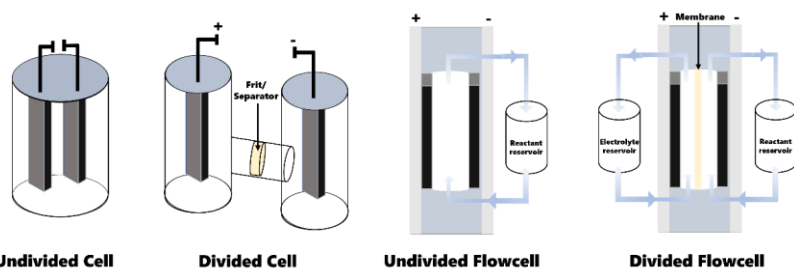


**Figure 1.5** Types of commonly used electrochemical cells.

The simplest type of electrosynthetic cell, undivided cells have both electrodes in the same reaction chamber, with both exposed to the same reaction solution and electrolyte with no physical barrier separating them.<sup>69,73</sup> The main benefits of this design is the simplicity and cheapness of its setup, relative to other more complex cell types, coupled with a relatively longer lifetime of the cell and lower internal resistance.<sup>69</sup> To lower internal resistance is preferable as this requires a smaller overpotential to drive the desired reaction.<sup>14</sup> This set-up



is often used if the reaction product is stable under electrochemical conditions, and against the counter reaction.<sup>73</sup>

In a divided cell, the cathodic and anodic reactions are separated by a membrane or a frit, often referred to as a diaphragm.<sup>69</sup> The diaphragm in the cell must allow for adequate transfer of ions between the anolyte and catholyte without the two solutions mixing, and thus the material used must be semi-permeable,<sup>14</sup> with low charge transport resistance.<sup>69</sup> Divided cells offer several benefits over undivided cells, including more facile isolation of desired products, and simpler purification of reaction mixtures.<sup>69,73</sup> This design is particularly suited to reactions wherein the product is not stable against the counter reaction, or where the desired reaction and counter reaction are incompatible.<sup>73</sup> However, higher costs arising from additional maintenance requirements and additional and more complex parts can deter the use of divided cells. The incorporation of a division between anodic and cathodic chambers also necessarily leads to an increased internal cell resistance which must be accounted for.

Undivided flow-cells, or continuous flow electrochemical reactors, employ an anode and a cathode separated by a thin spacer with flow channels cut into it, facilitating a large electrode surface area, and small inter-electrode gap which decreases the overall resistance.<sup>73</sup> Additionally, unlike batch reactors, continuous flow reactors provide a homogeneous electric field throughout the reaction solution due to the small inter-electrode gap. Flow reactors make scale-up easier as batch conditions can be replicated, producing minimal amounts of waste, and smaller quantities of solvents and reagents used. However, large-scale synthesis may require more equipment or very specialized equipment with their own attendant costs.<sup>69</sup>

### **Electrodes**

Appropriate electrode choice is critical to ensure maximum conversion and product formation. An ideal electrode possesses the following properties: physical stability under a range of reaction conditions, rapid charge transfer to substrates, a wide exploitable potential window, chemical inertness, and high conductivity.<sup>70</sup> High surface area is also desirable to facilitate increased mass transport which might otherwise limit the rate of reaction.<sup>70</sup>

Commonly used electrode materials are either carbon or metal. Carbon electrodes are typically either graphitic or glassy carbon, or boron-doped diamond (BDD). Graphitic and glassy carbon electrodes are relatively inexpensive and possess a wide potential window giving them broad general applicability. Graphite is frequently used as it is cheaper than glassy carbon and can be easily purchased, but is unfortunately less chemically stable than glassy carbon and can be prone to chemical modification over time.<sup>70</sup> BDD has been shown to offer unique selectivity, is resistant to fouling processes and is electro/chemically robust, but is more expensive than other carbon electrode types.<sup>72</sup> Metal electrodes typically provide faster electron-transfer kinetics than carbon whilst retaining relatively wide potential windows but are generally of higher cost.<sup>82</sup> Platinum and platinum alloys are a common choice as they are stable and easy to clean and may form superoxides in organic media which can further react with organic compounds at electron deficient carbon centres.<sup>70</sup> However, precious metals have a high cost associated with the metal itself and they are prone to electrode fouling caused by adsorbates like water or the supporting electrolyte.<sup>70,82</sup> Many hybrid or modified electrode materials have been developed to avoid these drawbacks or give additional properties,<sup>70</sup> such as Miller *et al.*<sup>83</sup> coating graphite with (S)-(-)-

phenylalanine methyl ester which enhanced the selectivity of the electrode when reducing 4-acetylpyridine asymmetrically.

Both working and counter electrode choice for an electrosynthesis system are similarly important, and they need not be the same material. Rather, the working electrode should be chosen to optimise conditions for the desired electrochemical transformation whilst the counter electrode should be optimised to facilitate the counter reaction. Whilst there are instances where reactions occur at the counter electrode, *e.g.* a coupled redox reaction, the major difference between working and counter electrodes is that for reductive transformations, the counter electrode may be used as a sacrificial electrode to balance the charge of the system and facilitate ion exchange. As such, aluminium, magnesium, and zinc are common choices for counter electrode as they are easily oxidized, providing a low potential counter reaction and reducing the necessary applied potential to drive the desired electrochemical process.<sup>70</sup> Sacrificial electrodes may also enhance reactivity by forming Lewis acidic species (*e.g.*  $\text{Zn}^{2+}$ ) *in situ*.<sup>84</sup> However, the stoichiometric consumption of the electrode does introduce additional costs and maintenance issues.

Reference electrodes are used when accurate information about the cell potential is required – they are therefore employed in potentiostatic electrosynthesis and may be aqueous or organic depending on the nature of the system.

### **Solvents**

Electrochemical reactions, just as traditional synthesis methods, can be heavily impacted by the choice of solvent which can affect intermediate stability and reagent solubility, leading to different reaction pathways.<sup>14,73</sup> Additionally, in electrochemical synthesis, the following

factors must also be considered when choosing a solvent: solvent electrochemical window, promotion of counter reaction, stabilisation of intermediates, and inherent resistance (conductivity).<sup>73</sup>

The electrochemical window is the range of potentials in which the solvent is stable towards oxidation or reduction, and this can be dependent on the electrode material, electrolyte species and concentration. Ultimately, the solvent should be able to dissolve the reagents and electrolyte, whilst remaining sufficiently stable during the reaction.<sup>85</sup>

However, in the case of "Direct electrochemical reaction with solvent degradation", the stability of the solvent is less of a concern. Protic solvents are often a good choice for solvent degradation as they can be reduced to hydrogen as the counter reaction.<sup>73</sup>

Polar, protic solvents offer lower resistance and thus higher conductivity and usually dissolve electrolytes better than non-polar and aprotic solvents and therefore they are commonly used in electrochemistry. Protic acidic solvents such as sulfuric and acetic acid have been used as they can dissolve both organic and inorganic compounds, but their incompatibility with certain organic compounds and highly corrosive nature make them a less popular choice.<sup>14</sup> Water may be used as a solvent for electrolysis provided that it is compatible with the reaction mechanism, however, the use of water is limited because many organic species have little to no solubility in water.

If excess protons are detrimental to the desired reaction then aprotic solvents such as acetonitrile (MeCN), tetrahydrofuran (THF), *N,N*-dimethylformamide (DMF), and dichloromethane (DCM) are good solvents of choice.<sup>14,73</sup> The most popular aprotic solvent

is MeCN because of its large electrochemical window and high conductivity for electrolyte solutions, and thus it has been used for both reductions or oxidations.<sup>14</sup>

### **Electrolytes**

In most electrochemical reactions, a supporting electrolyte is required to decrease the resistance of the system and so lower the potential which must be applied to the system to achieve a given current; excessively high potentials can lead to unwanted side reactions. The degree to which the resistance is lowered is dependent on the concentration and nature of the electrolyte.<sup>70,73</sup> Additionally, the electrolyte coats the surface of the electrode leading to the formation of a “double layer” which affects the diffusion of the substrates and ultimately influences the reactivity.<sup>85</sup> Supporting electrolytes are chosen based on solubility, chemical compatibility, and dissociation within the reaction solvent.<sup>14</sup>

Tetraalkylammonium (*e.g.* tetrabutylammonium (TBA)) salts have good solubility in organic solvents and are the most commonly employed electrolyte in organic synthesis,<sup>14,73</sup> but they can also react with electrogenerated intermediates or coordinate with the metal centres of electrocatalysts.<sup>70</sup> Alkali metal salts are also used which may have simple halides ( $\text{Br}^-$ ,  $\text{Cl}^-$ ) or complex ions such as  $\text{PF}_6^-$ ,  $\text{BF}_4^-$ , and  $\text{ClO}_4^-$  as the counteranion.<sup>73</sup> Based on the nature of the counter anion, the solubility for a given cation can vary: *e.g.* tetrabutylammonium perchlorate and tetrabutylammonium tetrafluoroborate are less soluble in organic solvents than tetrabutylammonium triflate.<sup>14</sup>

#### **1.3.3 Reactions occurring at the electrodes**

Typical reactions at the anode include direct oxidation, cleavage, substitution, and addition.<sup>69,70,75</sup> In organic solvents, anodic oxidations can occur by reaction between the

electrolyte and the dissolved substrate which adds the functional group from the solvent on to the organic substrate.<sup>75</sup> Through anodic oxidation, the C-H bonds in aromatic compounds may be replaced with functional groups such as acetate and acetamide.<sup>69,75</sup> Anodic substitutions may typically occur in both saturated and unsaturated organic molecules.

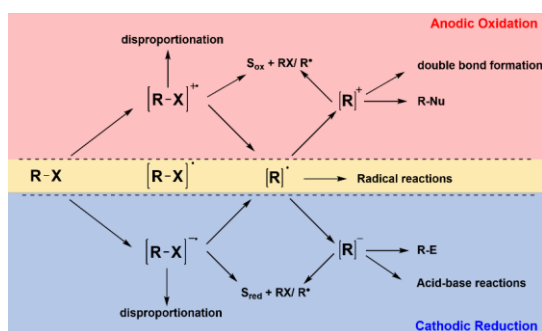
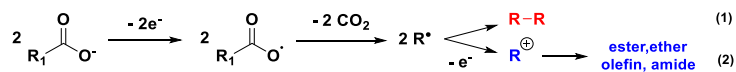


**Figure 1.6** Possible reaction pathways occurring at the electrodes. Reproduced with permission from Lam and Leech.<sup>14</sup>

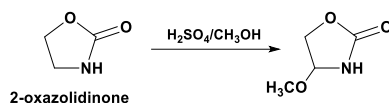
Anodic decarboxylation, known as the Kolbe reaction, has been thoroughly explored in the literature. This involves a one-electron oxidation which leads to decarboxylation thereby producing a carboxy radical; in the event of R being an alkyl group a resultant alkyl radical (R•) is formed.<sup>86</sup> (**Scheme 1.6-1**) Kolbe electrolysis is commonly used for the synthesis of R-R homodimers,<sup>69,75,86</sup> and this has become a convenient means to access alkyl radicals using various carboxylic acids.<sup>66</sup> If the electrode material, current density, and additives are controlled then further oxidation to a carbocation may occur which can undergo solvolysis and/or rearrange to form amides, esters, ethers, and olefins. When this occurs, it is referred to as non-Kolbe electrolysis.<sup>75</sup> (**Scheme 1.6-2**)



**Scheme 1.6** Oxidative carboxylation via 1) Kolbe Electrolysis and 2) Non-Kolbe Electrolysis.

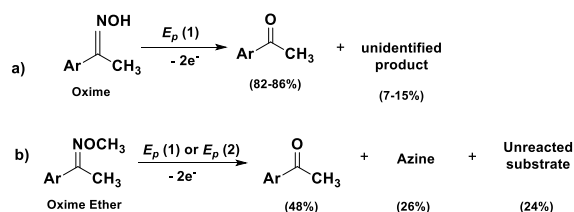
The conversion of *p*-methoxytoluene to *p*-anisaldehyde is one of the best known direct oxidation reactions occurring at the anode.<sup>75</sup> At the anode, the toluene molecules undergo acetalization, forming dimethylacetal intermediates in the presence of methanol, which may be hydrolysed to form the desired product of *p*-anisaldehyde.<sup>75</sup>

Using a boron doped diamond electrode or graphite electrode, Saravanan *et al.*<sup>87</sup> (**Scheme 1.7**) showed that methoxymethyl ether functionality may be added to 2-oxazolidinones.<sup>69,70,87</sup>



**Scheme 1.7** Methoxylation of a 2-oxazolidinone as reported by Saravanan *et al.*<sup>87</sup>

Using platinum anodes, hydrazones and alcohols may undergo electrochemical oxidation to introduce C=N bonds and form azines and oximes,<sup>88</sup> for example giving acetophenone from the electrolysis of oxime in acetonitrile (or methanol) at a Pt anode at both redox potentials (**Scheme 1.8**) However, when the electrolysis of oxime ether was carried out on a Pt anode acetophenone and azine were produced at the first oxidation potential, and only acetophenone at the second one.

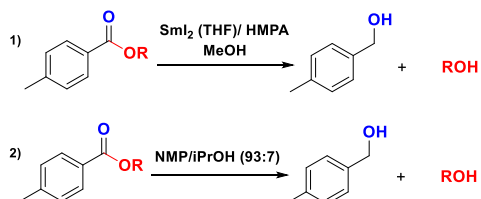


**Scheme 1.8** Electrochemical oxidation of organic compounds with C-N double bonds.<sup>88</sup>

Reactions at the cathode may also be used to form desired products, and this occurs most commonly by means of reductive cleavage,<sup>69</sup> typically of R-X bonds where X is an

electroactive leaving group such as a pseudohalide. This occurs when an electron is transferred from the electrode surface to the LUMO of the organic compound, leading to the formation of activated radical anion  $RX^{\cdot-}$ ,<sup>75</sup> which may then react with another species present or be further reduced to a carbanion,  $R^-$ . Cathodic cleavages have applications in analytical, synthetic, and environmental fields.<sup>75</sup>

The position of the halogen, electrode surface, and molecular structure can all affect the overall mechanism of these reactions,<sup>75</sup> which may be exploited to the benefit of synthetic chemists. For example, Marko and Lam<sup>89</sup> showed, seen in **Scheme 1.9**, that it is possible to chemoselectively cleave different groups on the same molecule by controlling the potential applied to the cell, a phenomenon which has been termed “electrochemoselectivity”. Given that the reduction potential of the ester will differ based on the nature and number of substituents on the aromatic ring, an appropriate potential can be applied to selectively deprotect certain functional groups.



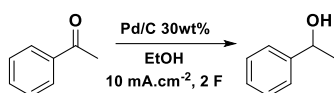
**Scheme 1.9** Chemoselective deprotection using: 1) Samarium Iodide and Hexamethylphosphoramide and/or, 2) electrolysis.<sup>89</sup>

A common side/counter reaction in the presence of water or alcohol is the formation of hydrogen gas due to proton reduction at the cathode. This may be exploited using the hydrogen for electrochemical hydrogenation under mild conditions as an alternative to conventional catalytic hydrogenation.<sup>69</sup> It has been reported that this occurs *via* a multistep



mechanism: initially adsorbed hydrogen is formed on the metal surface, the organic compound is then adsorbed to the surface, and then electrocatalytic hydrogenation occurs.<sup>75</sup>

The two-electron reduction of acetophenone to 1-phenyl-ethanol by Sáez *et al.*<sup>90</sup> has several applications in the fine chemicals and pharmaceutical industry, and using a Pd/C 30 wt% in the presence of ethanol, the group reported 90% selectivity when applying 10 mA/cm<sup>2</sup> current density and 2 F charge.<sup>90</sup>



**Scheme 1.10** Electrocatalytic hydrogenation of acetophenone.<sup>90</sup>

### 1.3.4 Electrocatalysis

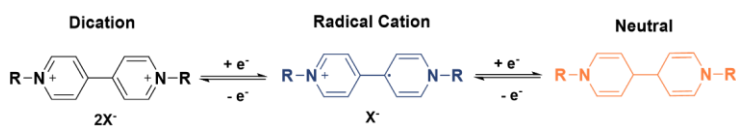
During an electrocatalytic reaction, a mediator or catalyst is used to oxidize or reduce a substrate in solution rather than direct reduction or oxidation of the substrate at the electrode surface, and the catalyst or mediator is then regenerated electrochemically.<sup>91</sup>

**(Figure 1.4, 3)**

Electrocatalysts can be classified into two categories based on their role during electrochemical reaction.<sup>71</sup> The first category refers to catalysts that accelerate redox reactions, relative to a non-mediated system, by facilitating electron transfer events between electrodes and substrates. Electrocatalysts in the second category shuttle electrons and chemical information to the substrates, allowing the catalyst to control the reactivity and selectivity of the reaction.

## 1.4 Viologens

Viologens are a type of quaternary pyridinium salts (QPS) which contain conjugated multi/bi-pyridyl groups and have an array of properties, such as their 3 stable states as seen in **Scheme 1.11**, that make them ideal for electrochromic and energy applications.<sup>92</sup> The name “Viologen” was given by Michaelis in 1932 primarily to QPSs which are derived from 4'4'-bipyridine which generate a dark purple colour as a result of the first reduction of the dication to a radical cation state. To date viologens have been used in electrochromic displays, memory devices, transistors, and used as antibacterial agents, electrodes within supercapacitors and batteries, and as sensitizers for solar cells.<sup>92</sup>



**Scheme 1.11** The three stable redox states of viologens.

### 1.4.1 Properties of viologens

Some of the key features of viologens are:<sup>92</sup>

- Three reductive states of viologens (dication, radical cation, and neutral) which are all thermodynamically stable. (**Scheme 1.11**) The conversion of the viologen between these three states occurs in a sequential manner and can be performed at easily accessible potentials.
- The radical-cation of the viologen is dark blue or purple in colour and can remain in this relatively stable phase formed by one-electron reversible reduction, making them electrochromic.

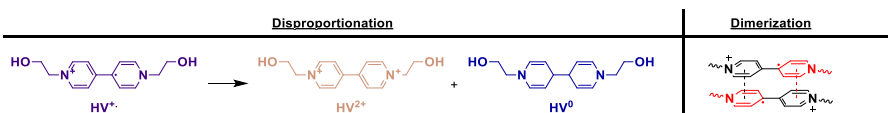
- Viologens form strong intermolecular  $\pi$ - $\pi$  interactions with other species and so easily form host-guest complexes *via* self-assembly.
- Related to their propensity for  $\pi$ - $\pi$  interactions, viologens can act as strong electron acceptors to form viologen/electron-donor based charge transfer complexes.
- The properties of viologens may be easily manipulated by integrating viologens with other materials *via* covalent or coordination bonding,
- As cationic materials, viologen properties may be tuned by choice of anion.

Various properties of viologens such as redox potentials, ion conductivity, and UV-Vis absorption bands may be easily altered *e.g.* the change in the substituent groups at nitrogen such as methyl, ethyl, and phenyl leads to alterations in the properties mentioned above.<sup>92</sup>

Viologens are well studied for various reasons and some of the earliest literature dates back to the 1970s. Originally, viologens were investigated as redox indicators in several biological studies due to their highly reversible, low cathodic redox potential.<sup>93</sup> The continued high interest in viologens is mainly due to their tunability of nitrogen substituents, stable redox states, and their useful electron-accepting capabilities.<sup>55</sup> For example, viologens may serve as replacements for metal-based electronic devices which would reduce manufacturing costs whilst avoiding the toxicity of the materials currently in use.<sup>55,92</sup>

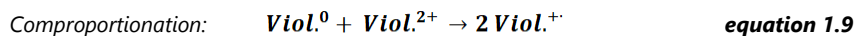
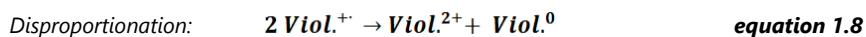
The dication ( $\text{Viol}^{2+}$ ) is the most stable state and is typically colourless unless involved in charge transfer complexes with the counter anion.<sup>55,92,94</sup> The dication can be reduced to the highly coloured radical cation ( $\text{Viol}^{\cdot+}$ ), which is reasonably stable due to the delocalization of electrons across the  $\pi$ -system of the bipyridyl rings and the substituents. The first reduction step is highly reversible; this step may be cycled repeatedly without unwanted side

reactions,<sup>93</sup> however, the second reduction is much less reversible and usually results in the formation of an uncharged, insoluble species which may be as a result of dimerization.<sup>92,93</sup>



**Scheme 1.12** Disproportionation and dimerization of viologens.

Viologen redox and electrochromic properties are electrolyte and solvent dependent because viologens can undergo disproportionation and comproportionation (**Equation 1.8** and **1.9**, respectively) reactions depending on their environment. These reactions may be favourable or undesirable depending on the application of the particular viologen.<sup>93</sup>



Typically, two monocationic viologen radicals ( $\text{Viol.}^{\cdot+}$ ) can dimerize to form a stable charge transfer complex which may disproportionate to form the neutral ( $\text{Viol.}^0$ ) and dication viologen ( $\text{Viol.}^{2+}$ ).<sup>31</sup>

Similarly, by comproportionation, the neutral viologen can react with the dicationic viologen to form an undesirable dimerized viologen. Dimerization may also be influenced by the presence of bulky substituents which hinder the formation of the aggregate or dimerized form.<sup>55,56,92</sup> Additionally, the interaction with ionic electrolytes also controls the formation of the dimerized viologen through hydrogen bonding and kinetics.<sup>95</sup>

Certain hydrophilic substituents have shown to improve the solubility of viologens in water, which has direct benefit to the field of organic redox flow batteries (ORFBs).<sup>92</sup>

The influence of different alkyl viologens in poly(ethylene oxide) medium, on the ionic conductivity, was investigated by H. Ohno and H. Satoh.<sup>96</sup> The study revealed that shorter alkyl chain lengths results in higher ionic conductivities thus indicating direct dependence between the alkyl chain length and the ionic conductivity.<sup>92,96</sup>

Methyl viologen (MV), a herbicide commonly known as “paraquat”, is the simplest viologen.<sup>97</sup> It has 2 redox transitions ( $MV^{2+}/MV^+$  and  $MV^+/MV^0$ ) and can both dimerize easily due to  $\pi$ - $\pi$  interactions and disproportionate to form  $MV^{2+}$  and  $MV^0$ . Like other viologens, it undergoes profound colour changes as it moves from one oxidation state to another - methyl viologen is colourless in the dicationic state, forms a deep violet-blue colour in the radical cation state, and ultimately adopts a yellow-brown colour as the final neutral species.<sup>55,97</sup>

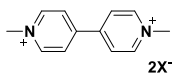


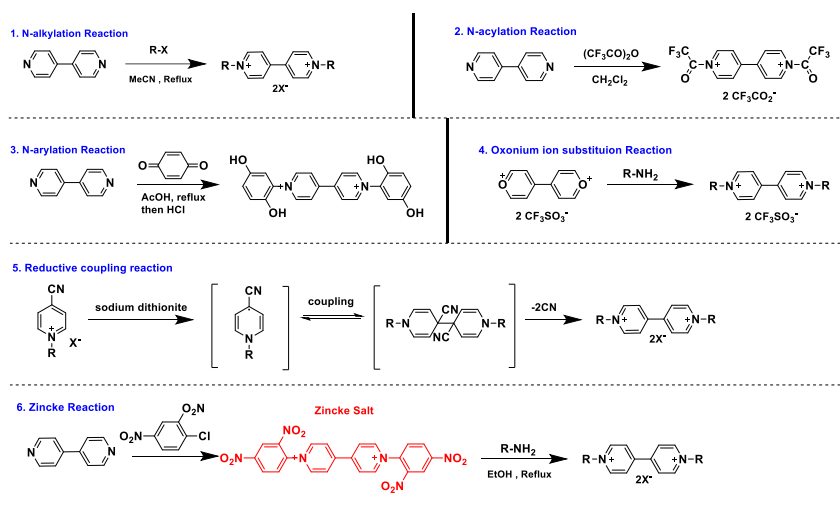
**Figure 1.7** Structure of methyl viologen (MV).

Thermodynamic properties of viologens such as solubility and crystallization may be manipulated by changing the nature of the counter anion of the viologen. Halides are usually soluble in protic solvents such as water and methanol. Alternatively, viologens with anions such as  $BF_4^-$  and  $PF_6^-$  are soluble in aprotic solvents such as DMF and MeCN.

#### 1.4.2 Synthesis of viologens and derivatives

Several synthesis methods are known to prepare viologens, including substitution reactions, N-acylation reactions, and most commonly *via* the Zincke reaction.<sup>55,92</sup> The basicity of the

nitrogen atoms on the rings allows for easy synthesis of substituted viologens *via* an  $S_N2$  mechanism. (Scheme 1.13)



**Scheme 1.13** Synthesis route for viologens and their derivatives.

- **N-Alkylation of 4,4'-bipyridines:** Nucleophilic substitution between bipyridine and alkyl halides in polar aprotic solvents like DMF, results in the non-selective N-alkylation of bipyridine, producing a symmetrical viologen.<sup>92,98</sup> This method is the most convenient synthetic method, providing high yields of the desired viologen and diverse array of viologens may be obtained by simply changing the type of halogenated alkanes which are used.<sup>92</sup> These substituted alkyls may be further categorized into 2 groups; those with terminal functional group substituted alkyl chain and different-length alkyl chain.

- **N-acylation substitution:** Highly reactive acyl N-substituted viologens are produced by this method wherein pyridinium compounds are reacted with a powerful acylating agent.<sup>92</sup>

- **N-arylation substitution of 4,4'-bipyridines:** Quinone-based compounds are reacted with 4,4'-bipyridines producing hydroquinone N-substituted viologens which are desirable for applications such as energy storage and electrochromism.<sup>92</sup>
- **Oxonium ion substitution reactions:** Primary amines react with pyrrillium ions which ring-open and then close again to form the target QPS.<sup>92</sup> This process may also be used for the synthesis of phosphaviologens.<sup>98</sup>
- **Reductive coupling reaction:** Reduction of 4-cyanopyridine-based quaternary pyridinium salts with sodium dithionite forms radical intermediates which self-dimerize and eliminate cyanide to form the desired viologen. This method was first used in 1964 by Kosower *et al.*<sup>99</sup> and has since been used frequently due to its convenience.<sup>92</sup>
- **The Zincke Reaction:** This reaction is a preferred synthetic route because it is a means to produce new viologen structures, and unlike alkyl substitution which produces non-conjugated products, the Zincke reaction produces fully conjugated viologens. This reaction involves the formation of a Zincke salt which is then reacted with an aromatic primary amine to produce an aryl-bipyridinium salt.<sup>92,98</sup>

### 1.4.3 Types of viologens and derivatives

- **Extended viologens**

To synthesize extended viologens, conjugate multi-pyridinium salts, viologen units containing a spacer/bridging group between each pyridinium ring, are used. These salts may be bridged with aromatic rings, heterocyclic rings, and double or triple bonds. Extended viologens can be further expanded to include fused viologens, and cyclic viologens.<sup>92,100</sup> Extended viologens can only be formed if the multi-pyridinium quaternary salts, viologens

with spacer groups such as indoles or aromatic rings, are able to form stable radical or cationic compounds, and this is based on the conjugation of the multi-pyridinium quaternary salts.

Extended viologens offer enhanced properties compared to regular viologens, and this includes increased stabilization of the radical species due to spatial delocalization of the lone electron through the extended  $\pi$ -conjugation.<sup>101</sup>

- **Fused viologens**

Fused viologens may be considered as a sub-set of extended viologens.<sup>92</sup> There are two different types of fused viologens, classified by the type of bridging between the two quaternary centres: 1) acene- or benzene- ring- and 2) heterocyclic-ring-fused viologens. Fused viologens are targeted as they permit the modulation of the electron affinity of the viologen by extension and/or tuning of the viologen  $\pi$ -system. Heterocyclic-ring-fused viologens can incorporate a range of heteroatoms including phosphoryl groups, germanium, or silicon atoms as bridges between the two QPSs. (Figure 1.8-2)

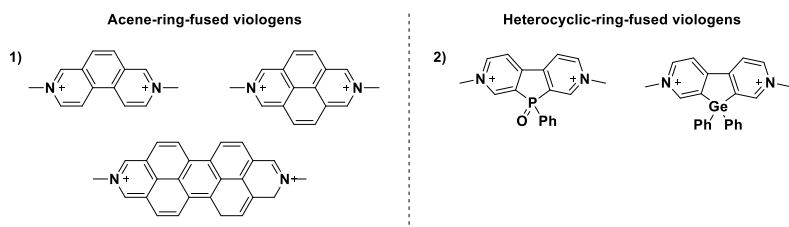


**Figure 1.8** Examples of extended viologens.

- **Macrocyclic viologens**

Viologens may be incorporated into cyclophanes or cages, which are synthesized from pyridines using chlorinated hydrocarbons as ditopic linkers. Viologen cyclophanes have



been thoroughly researched by Stoddart *et al.*<sup>102</sup> since 1994, who studied their formation of inclusion complexes and supramolecular chemistry. The group reported that the uptake of organic molecules can be modulated by controlling the redox state of the viologen.

- **Polyviologens**

Polyviologens are polymers containing viologens and viologen-like structures<sup>92</sup> and they are known to exhibit unique properties such as good mechanical properties, higher stability, and higher solvation than convention viologens. There have been several polyvinyl developed which are separated into 2 main groups: linear polyvinyl and cross-linked species. Given their enhanced properties over their regular counterparts, polyviologens have been used in an array of applications such as electrochromic devices,<sup>98,103,104</sup> RFBs,<sup>43</sup> and supercapacitors.<sup>105,106</sup>

- **Viologen-based polyionic liquid gels**

Polyionic liquids are favourable for electrochromic devices due to properties such as wide operating potential window, high boiling point, non-flammability, and good ionic conductivity.<sup>98</sup> Another favourable aspect of these liquids is the fact that they have properties of both ionic liquids and polymers and can play a dual role of ions and solvents.

#### **1.4.4 Applications of viologens and their derivatives**

The electron transfer properties, varying solubility of different redox states, and localized conjugation, among other properties, make viologens and viologen derivatives attractive for use in numerous applications.<sup>55,92,94,98</sup> To date, viologens and their derivatives have been incorporated in several fields including energy storage,<sup>22,58,107</sup> supercapacitors,<sup>105,106</sup> electrochromism,<sup>98</sup> molecular machines,<sup>102,108</sup> memory devices,<sup>109,110</sup> and biochemistry.<sup>111</sup>

**Organic Redox Flow Batteries (ORFBs)**

Viologens offer a sustainable approach to redox flow batteries because these carbon-based, organic molecules can replace Vanadium as the redox active species. This minimizes costs and replaces toxic, hazardous electrolytes such as sulphuric acid with aqueous NaCl solutions.

Janoschka and co-workers<sup>54</sup> developed a single, combi-molecule consisting of a viologen unit with a TEMPO radical called VIOTEMP, to serve as the anode and cathode within a water based RFB, operating at pH 4. The battery was able to be cycled reversibly and the same material was successfully used for both electrodes. One drawback to this system was the loss of capacity which was influenced by the solubility.

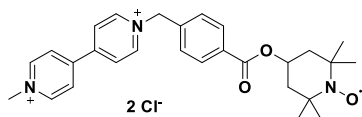


**Figure 1.9** Structure of VIOTEMP and counterion.<sup>54</sup>

In 2016 the same group reported a high-capacity AORFB consisting of a TEMPO derivative, *N,N,N,2,2,6,6*-heptamethylpiperidinyloxy-4-ammonium chloride (TEMPTMA) and MV.<sup>61</sup> The addition of the trimethylammonium substituent of TEMPO increased the solubility from 2.1 M to 2.3 M in water, and increased the cell voltage from 1.25 V for the MV/4-OH TEMPO couple<sup>62</sup> to 1.4 V for this couple.

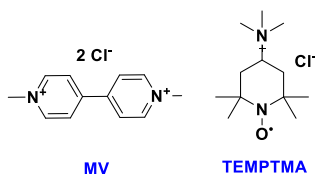


**Figure 1.10** Structures of MV and TEMPTMA.<sup>61</sup>

Viologens have also been reported in other AORFBs and have been used with these couples: (ferrocenylmethyl)trimethylammonium chloride,<sup>112-114</sup> ferrocene derivatives,<sup>115</sup> potassium ferrocyanide,<sup>116</sup> potassium iodide,<sup>117,118</sup> bromine,<sup>63</sup> and TEMPO derivatives.<sup>43,52,119,120</sup> The water soluble ferrocene derivatives are an attractive choice as a redox couple due to their low-cost, earth abundance and use of water rather than acidic electrolytes for the RFB system.<sup>55</sup> Furthermore, the reversible reaction between  $\text{Fe}^{2+}$  and  $\text{Fe}^{3+}$  is favourable in AORFBs because of the excellent thermal and electrochemical stability of this redox couple, which is why ferrocyanide is also considered as a redox couple for RFBs containing viologens.<sup>29,92</sup> TEMPO and TEMPO-derivatives have worked well as a redox couple due to their rapid charge transfer kinetics, high water solubility (~5.7 M), and excellent structural stability.<sup>121</sup>

### **Electrochromic Devices**

Electrochromism is the phenomenon whereby a material can change their colour in a reversible manner when they are stimulated electrochemically, and thus electrochromic devices (ECDs) contain electroactive species that change colour when they undergo redox reactions.<sup>94</sup> Viologen-based ECDs are favourable due to the switching which occurs at low potentials to yield an array of different colours which may be altered depending on the substituent added as well as the counter anion. As such, viologens are frequently incorporated into ECDs with varying configurations<sup>98</sup> including viologen-based inorganic composites,<sup>122,123</sup> viologen-based organic composites,<sup>124,125</sup> viologen-based polymer composites,<sup>104</sup> and viologen-based graphene composites.<sup>126</sup> The extended conjugation of  $\pi$ -extended viologens is advantageous for ECDs because it allows faster colour-switching and re-oxidation of the viologen<sup>124,125</sup> which is a desirable trait for ECDs.

An ECD containing a MV-graphene quantum dot was reported to have high thermal stability, good stability, and favourable switching performance in comparison to other devices not containing viologen-based nanocomposites.<sup>126</sup> Pande and co-workers<sup>127</sup> explored 1-hexyl-1'-nonafluorohexyl viologens (HERFVs), containing either hexafluorophosphate ( $\text{PF}_6^-$ ) or bis(trifluoromethane)sulfonimide (TFSI) as a counter ion, for their use in electrochromic devices such as transmissive windows and eye wear. The group reported that the optical contrast, coloration efficiency, and switching speed of both viologen based ionic liquids were dependent on the nature of the anion, and that due to the smaller anion  $[\text{HERV}][\text{PF}_6]_2$  experienced faster bleaching than  $[\text{HERV}][\text{TFSI}]_2$ .

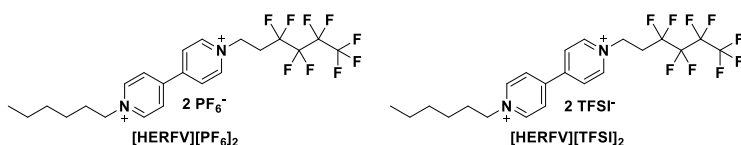


**Figure 1.11** Structure of 1-hexyl-1'-nonafluorohexyl viologens (HERFV) with hexafluorophosphate ( $\text{PF}_6^-$ ) and bis(trifluoromethane)sulfonimide (TFSI) as a counter ion.<sup>127</sup>

### Energy Storage and Conversion: Supercapacitors

Supercapacitors are new kinds of energy storage devices which lie between conventional rechargeable batteries and capacitors, storing electrical energy rather than chemical energy like batteries.<sup>92,128</sup> These devices allow for rapid charge and discharge, coupled with good cycle stability and ultrahigh power density, superior to batteries, making them suitable for use in wearable electronic devices, back-up power supply, or energy storage.<sup>128</sup> Polyviologens have often been of interest for supercapacitors<sup>55,92</sup> due to their excellent electron-accepting ability and reversible electrochemical redox behaviour which has led to their use as an electronic memory device and all-solid-state supercapacitor with superior non-volatile re-writable memory behaviour and high volumetric capacitance.<sup>105</sup>

Small-molecular viologens are preferred over bulky, conjugated viologens, within the electrolyte of the supercapacitor, for use as the redox couple.<sup>92</sup> The first stimulus-responsive micro-supercapacitor(SR-MSC) device was reported by Feng and Zhuang *et al.*<sup>106</sup> in 2016, containing polyvinyl alcohol/LiCl with MV as the electrolyte.

### 1.5 Flavins

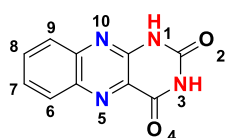


**Figure 1.12** Diagram of a labelled flavin base.

Flavins and Flavinium salts are a family of organic compounds structurally related riboflavin, a naturally occurring vitamin (Vitamin B2), found in several food products including milk, eggs, vegetables, and various meats. Flavins are considered to be highly versatile in terms of their electroactivity<sup>17</sup> and many derivatives of flavins are known such as: flavin mononucleotide (FMN), Flavin adenine dinucleotide (FAD), isoalloxazine, and alloxazine. These are biologically important molecules and FAD and FMN are common cofactors in enzyme catalysis.<sup>129</sup>

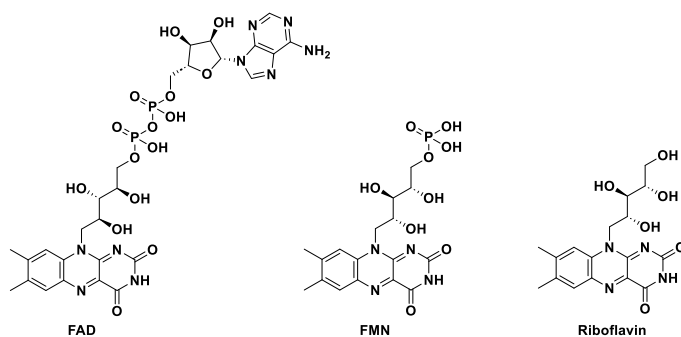
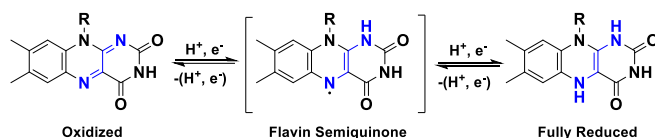


**Figure 1.13** Structures of FAD, FMN and Riboflavin.

All three molecules in **Figure 1.13** have methyl groups at the C7 and C8 positions, but the side chains at the N10 position differs for each flavin.<sup>130</sup> The isoalloxazine core makes up the electroactive part of the molecule and the substituents at N10 are responsible for apoprotein-cofactor binding and specificity.<sup>130,131</sup>

### 1.5.1 Properties of flavins

Flavins can undergo a reversible two-electron reduction which typically occurs by means of proton coupled electron transfer (PCET), and have a reduction potential of about 200 mV which greatly vary in different flavoproteins, mainly due to the protein environment that the flavin is in.<sup>131</sup> Originally, PCET referred to the transfer of a proton and electron simultaneously during an elementary step in reactions such as the comproportionation reaction of Ruthenium<sup>4+/3+</sup>.<sup>132</sup> However, more recently, PCET reactions have described reactions and half reactions wherein both electrons and protons are transferred, and this is not dependent on the mechanism of the reaction.<sup>133</sup> Flavins have three redox states, oxidized, singly reduced/semiquinone, and fully reduced, and all of which have three corresponding protonation states.<sup>131,134</sup> Given their 3 redox states, flavins can participate in redox reactions as either one-electron, or two-electron mediators, such as flavoenzymes which can transfer single electrons, hydrogen atoms or hydride ions in biological systems. In addition to their different redox states, flavins can exist in charge-transfer states where partial charge is transferred between the states, giving rise to different colours.



**Scheme 1.14** The oxidized, semiquinone and reduced forms of a flavin.

The reactivity of flavins, their stability, solubility,  $pK_a$  and redox potential can be influenced by the substituents at the C7, C8, N1, N3, and N5 positions.<sup>130,131,135</sup> The addition of electron withdrawing groups at these positions is known to increase the reduction potential of the flavin, making it more negative, and increase the flavins reactivity towards nucleophiles.<sup>135</sup>

### **1.5.2 Applications of flavins and their derivatives**

The use of flavins has been reported in a wide array of applications including photosensitizers,<sup>136</sup> photoreceptors in plants<sup>137</sup> and bacteria,<sup>138</sup> and photocatalysts.<sup>139</sup> In 1981, Otto and co-workers,<sup>140</sup> reported the use of flavin derivatives with an "altered absorption spectrum" , indicating the photoreceptor capabilities of flavins.<sup>141</sup> Numerous studies suggest that flavins have photochemical properties, which are influenced by the interaction of the sidechain with isoalloxazine nucleus,<sup>142</sup> therefore, they can act as efficient photosensitizers,<sup>136</sup> and participate in photobiological functions and reactions.<sup>141,143,144</sup> These properties also make flavins potential candidates for RFBs, however, very few examples exist in the literature.<sup>28,145-147</sup>

## 1.6 Characterisation and Testing of Electroactive Species

### 1.6.1 Cyclic Voltammetry (CV)

Cyclic voltammetry is an electrochemical method of investigating the reduction and oxidation processes of redox active species, and a technique which can be used to study electron-transfer initiated chemical reactions like catalysis.<sup>148</sup> A typical cyclic voltammetry experiment consists of three electrodes (reference, counter, and working electrode) which are placed into a solution containing an analyte and supporting electrolyte which carries the current between the electrodes. The supporting electrolyte used must be redox stable for the conditions within the experiment, and before the experiment, it should be sparged sufficiently to prevent unwanted redox processes. During the experiment, a varying potential is applied between the working and counter electrodes and a cyclic voltammogram is a plot of the measured current response against the applied potential. A reference has a defined equilibrium potential against which the potential of the other electrodes can be measured. The applied potential across the electrodes induces redox processes in the analyte which cause changes in current. **Figure 1.14** shows the annotated voltammogram of the reversible reduction and oxidation of 1 mM Potassium ferrocyanide (FCN). As the potential is scanned negatively from point **A** to point **B**, and FCN loses an electron and is oxidized, producing ferricyanide (FCN<sup>+</sup>), causing an increase in current. As the concentration of FCN<sup>+</sup> increases at the electrode surface the current response reaches a peak current known as the anodic current,  $i_{p,a}$ , and then falls as all FCN in the vicinity of the electrode is consumed. Due to diffusion, the concentration of the oxidized species at the electrode surface decreases as the potential is scanned negatively, towards point **B**.



When the switching potential is reached (**B**) the scan direction is reversed and now the potential is scanned positively while FCN<sup>+</sup> is being reduced to FCN. The peak current recorded is called the cathodic current,  $i_{p,c}$ .<sup>148</sup>

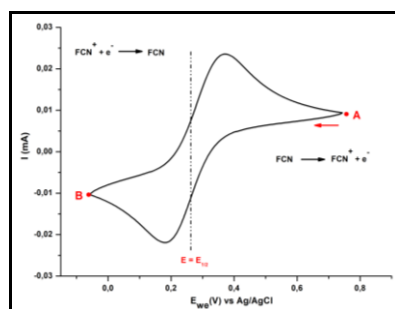


**Figure 1.14** Voltammogram of 1 mM FCN in 1 M NaCl. (Scan rate: 100 mV·s<sup>-1</sup>)

In a cyclic voltammogram, the cathodic and anodic peaks separation is based on the diffusion rates of analyte to the electrodes and therefore, the solution must not be stirred to allow diffusion to control the movement of electrons and analyte ions in the electrolyte. When a single electron transfer process is electrochemically and chemically reversible, the difference between the peak potentials ( $\Delta E_p$ ) is 57 mV. Mechanistically, this value is derived from various electrochemical reactions, including the Nernst equation, and this is due to the independent relationship between the scan rate, concentration of analyte and the peak potential.<sup>149</sup> Chemical reversibility refers to an analyte that is stable when reduced and subsequently reoxidized. Electrochemical reversibility describes fast electron transfer kinetics between the analyte and the electrode.

The scan rate controls how fast the applied potential is changed and this has a direct impact on the size of the diffusion layer at the electrode surface. For an electrochemically reversible electron transfer process wherein the redox active species are freely diffusing, the Randles-

Sevick equation (**equation 1.10**) describes the relationship between the peak current ( $i_p$ ), in Amps, and the square root of the scan rate,  $\nu$ , in volts per second.

$$i_p = 0.466nFAC^0 \left( \frac{nF\nu D_0}{RT} \right)^{\frac{1}{2}} \quad \text{equation 1.10}$$

where  $n$  is the number of electrons transferred in the redox event,  $F$  is Faraday's constant ( $C.mol^{-1}$ ),  $A$  ( $cm^2$ ) is the electrode surface area (usually treated as the geometric surface area),  $C^0$  ( $mol.cm^{-3}$ ) is the bulk concentration of the analyte,  $D_0$  ( $cm^2.s^{-1}$ ) is the diffusion coefficient of the oxidized analyte,  $R$  is the universal gas constant ( $J.(mol.K^{-1})$ ), and  $T$  is the absolute temperature (K). A linear relationship between the current and square root of the scan rate indicates that the process is electrochemically reversible and the species are freely diffusing.<sup>148</sup>

### 1.6.2 Rotating Disk Electrode (RDE)

A Rotating Disk Electrode (RDE) study is a popular hydrodynamic method that is used to determine kinetic parameters such as the Diffusion coefficient ( $D$ ) of redox active species being investigated.<sup>150,151</sup> The experimental set-up is similar to CV, consisting of three electrodes, except that a rotating working electrode is used rather than a stationary one.<sup>152</sup> During an RDE voltammetry experiment, the rotation rate of the working electrode is held constant as the potential is swept linearly at a constant sweep rate, and the voltammogram obtained for this experiment is a plot of electrode potential (x-axis) versus the current response (y-axis). The potential range for the experiment is usually set from 200 mV above the standard electrode potential to 200 mV after the reduction potential.

At the start of the experiment, the electrolyte solution would only contain the oxidized form of the redox active species ( $A^{2+}$ ). The rotating working electrode is placed in the solution, and the experiment is started at a redox potential that is more positive than the standard redox potential of A.<sup>153</sup> Initially, given the lack of species available to oxidize and the low reduction potential, little or no current response will be observed, however, as the applied potential reaches the reduction potential of A, a cathodic current response is observed and increases as A is reduced and the potential is swept beyond the reduction potential. The maximum current value, the "limiting current" ( $i_{LC}$ ), is reached when the potential at the working electrode is negative enough to reduce all  $A^{2+}$  ions that reach the surface of the electrode. The cathodic current response observed is due to the electrons flowing from the surface of the electrode into the solution, and this rate is limited by the rate of oxidation at the electrode surface.<sup>152,153</sup> If the current is limited by the rate of movement of ions to the electrode surface, this is considered as mass transport limited and with a rotating electrode, the rate of mass transport can be related to the rotation rate of the WE. Therefore, faster rotation speeds facilitate higher movement of ions in solutions which results in an increase in the limiting current.

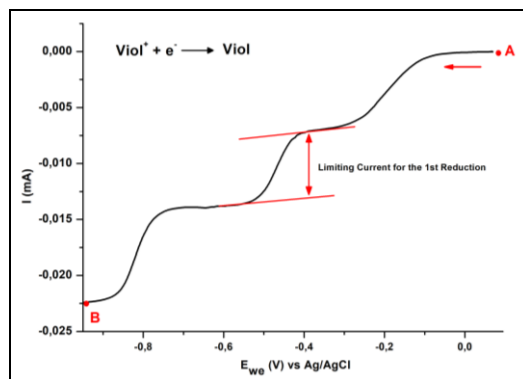


**Figure 1.15** Labeled voltammogram from a typical RDE experiment.

Levich and Koutecky-Levich analysis are often performed on rotating electrode data. In a Levich study, the voltammogram obtained is a function of the square root of the rotation rate (x-axis) versus the currents measured.<sup>154</sup> The Diffusion coefficient of  $A^{2+}$  can be determined from the slope of this plot, using the Levich equation:

$$I_L = (0.620)nFAD_3^2\omega_2^{\frac{1}{2}}\nu_6^{-1}C \quad \text{equation 1.11}$$

where  $I_L$  is the Levich current (A),  $n$  is the number of moles of electrons transferred in the half reaction (number),  $F$  is the Faraday constant (C/mol),  $A$  is the electrode area ( $\text{cm}^2$ ),  $D$  is the diffusion coefficient ( $\text{cm}^2\cdot\text{s}^{-1}$ ),  $\omega$  is the angular rotation rate of the electrode ( $\text{rad}\cdot\text{s}^{-1}$ ),  $\nu$  is the kinematic viscosity ( $\text{cm}^2\cdot\text{s}^{-1}$ ),  $C$  is the analyte concentration ( $\text{mol}\cdot\text{cm}^{-3}$ ). In this form of the equation, the constant with a value of 0.620 has units of  $\text{rad}^{-1/2}$ .

A Koutecky-Levich plot is a plot of the reciprocal current (y-axis), which is taken at different potentials versus the square root of the rotation rate.<sup>154</sup> In this work, a Levich study was performed to determine the diffusion coefficient of different molecules synthesized. Further kinetic studies were beyond the scope of this research.

### 1.6.3 Galvanostatic Cycling with Potential Limitation (GCPL) (Charge and Discharge Curves)

Galvanostatic cycling with potential limitation (GCPL) is a battery testing technique that measures the output capacity of an assembled system as a function of a fixed charge and discharge current. GCPL is the most commonly and widely used electrochemical technique for studying the behaviour of batteries, flow cells, and supercapacitors.<sup>155</sup> This method provides information about the materials and system overall performance, capacity, coulombic efficiency, and the electrolyte lifetime.

The capacity of the system relates to the amount of energy the system holds and can be expressed in Ah.L<sup>-1</sup> or C. The theoretical capacity of the system is dependent on the concentration of redox-active species in solution and the volume of the electrolyte, and this can be calculated by:

$$Q = nCVF \quad \text{equation 1.12}$$

With  $Q$  the capacity in C or mAh contained by a volume  $V$  in L<sup>-1</sup> of electrolyte with a concentration  $C$  in mol.L<sup>-1</sup> of active species involving  $n$  electrons, and  $F$  the Faraday constant in C.mol<sup>-1</sup>.

The Coulombic efficiency (CE) is an important metric to classify the performance of the system and is determined by relating the discharge capacity to the charge capacity of a corresponding cycle. CE may be affected by parasitic side reactions such as water splitting, electrolyte degradation, operational temperature, and the solubility of the ions in solution at different redox states. CE can be calculated by [equation 1.7](#).

During a typical GCPL experiment for RFBs, the system is cycled under inert atmosphere conditions at a specified flowrate. The voltage range for the cycling experiment is set beforehand and is dependent on the reduction potentials of the redox active species utilized in the system. To evaluate the performance of a system, the system can be cycled at different current densities, and the output capacity and coulombic efficiency at each current density can be compared. A typical GCPL curve is shown in **Figure 1.15** wherein species  $[A]^{2+}$  undergoes a reduction during the charge cycle which proceeds in the direction of A until it reaches the charging potential limit (point B), set at 1.1 V.

Having reduced all available  $[A]^{2+}$  the potential is then switched, and the system begins discharging, proceeding in the direction of C. During the discharge cycle,  $[A]^+$  is oxidized back to  $[A]^{2+}$  until it reaches the discharging potential limit (point D), set at 0.3 V. The overpotential, E, represents the additional voltage required to drive the charge and discharge processes due to internal resistance of the cell. In this example, CE is calculated by the following:  $CE_{[A]} = |Q_D/Q_B| \times 100$ .

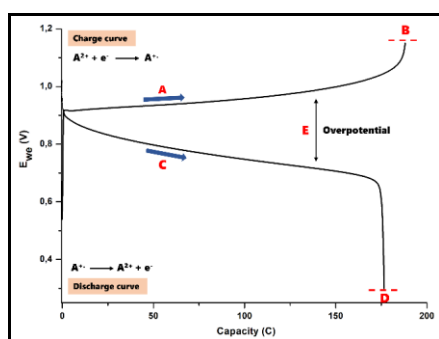


**Figure 1.16** A labelled GCPL curve showing the cell potential as a function of capacity.

## 1.7 Scope of the Thesis

Viologens show promise for their use in varying electrochemical applications such as energy storage devices like flow batteries and electrocatalysis. Viologens offer added value due to their unique electrochemical properties and varying solubility at different redox states, and this served as the basis for this work. The 2<sup>nd</sup> chapter explored the different electrochemical properties of synthesized viologens, which gave way to the further electrochemical testing of a selected viologen in a redox flow battery system. Using a stable, water-soluble viologen, the development of a reliable, lab-scale testing rig for an AORFB was investigated in Chapter 3. Given their various stable redox states, viologens have previously been investigated catalysts, and the work in Chapter 4 seeks to expand on the use of a viologen within a biphasic electrosynthetic systems. Similarly, flavins present themselves as a unique class of organic molecules which show promise in electrochemical applications such as redox flow batteries. The final chapter evaluates different flavin derivatives and their respective electrochemical properties.

## 1.8 References

- 1 W. R. Browne, *Electrochemistry*, Oxford University Press, 2018.
- 2 A. Overview and J. T. Stock, 1989, 1–17.
- 3 A. Shukla and T. Prem Kumar, *Isr. J. Chem.*, 2021, **61**, 120–151.
- 4 H. M. Leicester, *The historical background of chemistry*, Courier Corporation, 1971.
- 5 R. Francke and R. D. Little, *Chem. Soc. Rev.*, 2014, **43**, 2492–2521.
- 6 S. Möhle, M. Zirbes, E. Rodrigo, T. Gieshoff, A. Wiebe and S. R. Waldvogel, *Angew. Chemie - Int. Ed.*, 2018, **57**, 6018–6041.
- 7 M. M. Khan, S. A. Ansari, D. Pradhan, D. H. Han, J. Lee and M. H. Cho, *Ind. Eng. Chem. Res.*, 2014, **53**, 9754–9763.
- 8 E. Frackowiak, K. Fic, M. Meller and G. Lota, *ChemSusChem*, 2012, **5**, 1181–1185.
- 9 J. Noack, N. Roznyatovskaya, T. Herr and P. Fischer, *Angew. Chemie - Int. Ed.*, 2015, **54**, 9776–9809.
- 10 Y. Chen, S. A. Freunberger, Z. Peng, O. Fontaine and P. G. Bruce, *Nat. Chem.*, 2013, **5**, 489–494.
- 11 A. Z. Weber, M. M. Mench, J. P. Meyers, P. N. Ross, J. T. Gostick and Q. Liu, *J. Appl. Electrochem.*, 2011, **41**, 1137–1164.
- 12 D. Bryans, V. Amstutz, H. H. Girault and L. E. A. Berlouis, *Batteries*, 2018, **4**, 54.
- 13 J. Newman, N. P. Balsara and M. Moshinsky, *Electrochemical systems*, John Wiley & Sons, 2021, vol. 13.
- 14 M. C. Leech and K. Lam, *Nat. Rev. Chem.*, 2022, **6**, 275–286.
- 15 H. Chen, G. Cong and Y. C. Lu, *J. Energy Chem.*, 2018, **27**, 1304–1325.
- 16 P. Leung, A. A. Shah, L. Sanz, C. Flox, J. R. Morante, Q. Xu, M. R. Mohamed, C. Ponce de León and F. C. Walsh, *J. Power Sources*, 2017, **360**, 243–283.
- 17 Y. Ding, C. Zhang, L. Zhang, Y. Zhou and G. Yu, *Chem. Soc. Rev.*, 2018, **47**, 69–103.
- 18 M. L. Perry, J. D. Saraidaridis and R. M. Darling, *Curr. Opin. Electrochem.*, 2020, **21**, 311–318.
- 19 L. F. Arenas, C. Ponce de León and F. C. Walsh, *J. Energy Storage*, 2017, **11**, 119–153.
- 20 J. Winsberg, T. Hagemann, T. Janoschka, M. D. Hager and U. S. Schubert, *Angew. Chemie - Int. Ed.*, 2017, **56**, 686–711.
- 21 B. Lee, Y. Ko, G. Kwon, S. Lee, K. Ku, J. Kim and K. Kang, *Joule*, 2018, **2**, 61–75.
- 22 V. Singh, S. Kim, J. Kang and H. R. Byon, *Nano Res.*, 2019, **12**, 1988–2001.
- 23 N. S. Sinclair, R. F. Savinell and J. S. Wainright, *MRS Energy Sustain.*, 2022, **9**, 387–391.



- 24 J. Asenjo-Pascual, I. Salmeron-Sanchez, J. R. Avilés-Moreno, P. Mauleón, P. Mazur and P. Ocón, *Batteries*, 2022, **8**, 193.
- 25 R. P. Fornari, M. Mesta, J. Hjelm, T. Vegge and P. de Silva, *ACS Mater. Lett.*, 2020, **2**, 239–246.
- 26 Z. Huang, C. W. M. Kay, B. Kuttich, D. Rauber, T. Kraus, H. Li, S. Kim and R. Chen, *Nano Energy*, 2020, **69**, 104464.
- 27 Y. Liu, Q. Chen, P. Sun, Y. Li, Z. Yang and T. Xu, *Mater. Today Energy*, 2021, **20**, 100634.
- 28 A. Hollas, X. Wei, V. Murugesan, Z. Nie, B. Li, D. Reed, J. Liu, V. Sprenkle and W. Wang, *Nat. Energy*, 2018, **3**, 508–514.
- 29 J. Luo, A. Sam, B. Hu, C. DeBruler, X. Wei, W. Wang and T. L. Liu, *Nano Energy*, 2017, **42**, 215–221.
- 30 J. Luo, B. Hu, C. Debruler, Y. Bi, Y. Zhao, B. Yuan, M. Hu, W. Wu and T. L. Liu, *Joule*, 2019, **3**, 149–163.
- 31 D. G. Kwabi, Y. Ji and M. J. Aziz, *Chem. Rev.*, 2020, **120**, 6467–6489.
- 32 T. Xuan and L. Wang, *Energy Storage Mater.*, 2022, **48**, 263–282.
- 33 A. Forner-Cuenca and F. R. Brushett, *Curr. Opin. Electrochem.*, 2019, **18**, 113–122.
- 34 L. F. Castañeda, F. C. Walsh, J. L. Nava and C. Ponce de León, *Electrochim. Acta*, 2017, **258**, 1115–1139.
- 35 G. Qiu, C. R. Dennison, K. W. Knehr, E. C. Kumbur and Y. Sun, *J. Power Sources*, 2012, **219**, 223–234.
- 36 B. Sun and M. Skyllas-Kazacos, *Electrochim. Acta*, 1992, **37**, 1253–1260.
- 37 E. M. Hammer, B. Berger and L. Komsijska, *Int. J. Renew. Energy Dev.*, 2014, **3**, 7–12.
- 38 D. Zhang, Q. Liu and Y. Li, *Design of flow battery*, Elsevier B.V., 2014.
- 39 A. Hassan and T. Tzedakis, *J. Energy Storage*, 2019, **26**, 100967.
- 40 S. R. Narayan, A. Nirmalchandar, A. Murali, B. Yang, L. Hooper-Burkhardt, S. Krishnamoorthy and G. K. S. Prakash, *Curr. Opin. Electrochem.*, 2019.
- 41 J. R. Varcoe, P. Atanassov, D. R. Dekel, A. M. Herring, M. A. Hickner, P. A. Kohl, A. R. Kucernak, W. E. Mustain, K. Nijmeijer, K. Scott, T. Xu and L. Zhuang, *Energy Environ. Sci.*, 2014, **7**, 3135–3191.
- 42 J. Winsberg, C. Stolze, A. Schwenke, S. Muench, M. D. Hager and U. S. Schubert, *ACS Energy Lett.*, 2017, **2**, 411–416.
- 43 T. Janoschka, N. Martin, U. Martin, C. Friebe, S. Morgenstern, H. Hiller, M. D. Hager and U. S. Schubert, *Nature*, 2015, **527**, 78–81.
- 44 G. Li, W. Chen, H. Zhang, Y. Gong, F. Shi, J. Wang, R. Zhang, G. Chen, Y. Jin, T. Wu, Z.

- Tang and Y. Cui, *Adv. Energy Mater.*, 2020, **10**, 1–10.
- 45 J. Chai, A. Lashgari, A. E. Eisenhart, X. Wang, T. L. Beck and J. J. Jiang, *ACS Mater. Lett.*, 2021, **3**, 337–343.
- 46 P. Navalpotro, J. Palma, M. Anderson and R. Marcilla, *Angew. Chemie - Int. Ed.*, 2017, **56**, 12460–12465.
- 47 S. V. Venkatesan, K. Karan, S. R. Larter and V. Thangadurai, *Sustain. Energy Fuels*, 2020, **4**, 2149–2152.
- 48 L. H. Thaller, in *9th Intersociety energy conversion engineering conference.*, 1974, pp. 924–928.
- 49 M. Skyllas-Kazacos, M. H. Chakrabarti, S. A. Hajimolana, F. S. Mjalli and M. Saleem, *J. Electrochem. Soc.*, 2011, **158**, R55.
- 50 Z. Rhodes, J. R. Cabrera-Pardo, M. Li, S. D. Minteer, P. Leung, T. Martin, Q. Xu, C. Flox, M. R. Mohamad, J. Palma, A. Rodchanarowan, X. Zhu, W. W. Xing, A. A. Shah, Z. Li, Y. C. Lu, E. Sánchez-Díez, E. Ventosa, M. Guarnieri, A. Trovò, C. Flox, R. Marcilla, F. Soavi, P. Mazur, E. Aranzabe and R. Ferret, *Appl. Energy*, 2021, **32**, 101–112.
- 51 Y. Xu, Y. Wen, J. Cheng, G. Cao and Y. Yang, *Electrochem. commun.*, 2009, **11**, 1422–1424.
- 52 Y. Liu, M. A. Goulet, L. Tong, Y. Liu, Y. Ji, L. Wu, R. G. Gordon, M. J. Aziz, Z. Yang and T. Xu, *Chem*, 2019, **5**, 1861–1870.
- 53 B. Huskinson, M. P. Marshak, C. Suh, S. Er, M. R. Gerhardt, C. J. Galvin, X. Chen, A. Aspuru-Guzik, R. G. Gordon and M. J. Aziz, *Nature*, 2014, **505**, 195–198.
- 54 T. Janoschka, C. Friebe, M. D. Hager, N. Martin and U. S. Schubert, *ChemistryOpen*, 2017, **6**, 216–220.
- 55 L. Striipe and T. Baumgartner, *Chem. - A Eur. J.*, 2017, **23**, 16924–16940.
- 56 S. Gentil, D. Reynard and H. H. Girault, *Curr. Opin. Electrochem.*, 2020, **21**, 7–13.
- 57 P. Navalpotro, C. Trujillo, I. Montes, C. M. S. S. Neves, J. Palma, M. G. Freire, J. A. P. Coutinho, R. Marcilla, Z. Rhodes, J. R. Cabrera-Pardo, M. Li, S. D. Minteer, W. Duan, R. S. Vemuri, J. D. Milshtein, S. Laramie, R. D. Dmello, J. Huang, L. Zhang, D. Hu, M. Vijayakumar, W. Wang, J. Liu, R. M. Darling, L. Thompson, K. Smith, J. S. Moore, F. R. Brushett, X. Wei, P. Navalpotro, C. Trujillo, I. Montes, C. M. S. S. Neves, J. Palma, M. G. Freire, J. A. P. Coutinho, R. Marcilla, G. Li, W. Chen, H. Zhang, Y. Gong, F. Shi, J. Wang, R. Zhang, G. Chen, Y. Jin, T. Wu, Z. Tang, Y. Cui, J. Chai, A. Lashgari, A. E. Eisenhart, X. Wang, T. L. Beck, J. J. Jiang, S. V. Venkatesan, K. Karan, S. R. Larter and V. Thangadurai, *Energy Storage Mater.*, 2020, **26**, 400–407.
- 58 J. Luo, B. Hu, C. Debruler and T. L. Liu, *Angew. Chemie - Int. Ed.*, 2018, **57**, 231–235.
- 59 J. Cao, F. Ding, H. Chen, H. Wang, W. Wang, Z. Chen and J. Xu, *J. Power Sources*, 2019, **423**, 316–322.

- 60 A. Orita, M. G. Verde, M. Sakai and Y. S. Meng, *J. Power Sources*, 2016, **321**, 126–134.
- 61 T. Janoschka, N. Martin, M. D. Hager and U. S. Schubert, *Angew. Chemie - Int. Ed.*, 2016, **55**, 14427–14430.
- 62 T. Liu, X. Wei, Z. Nie, V. Sprenkle and W. Wang, *Adv. Energy Mater.*, 2016, **6**, 1501449.
- 63 W. Liu, Y. Liu, H. Zhang, C. Xie, L. Shi, Y. G. Zhou and X. Li, *Chem. Commun.*, 2019, **55**, 4801–4804.
- 64 S. Jin, E. M. Fell, L. Vina-Lopez, Y. Jing, P. W. Michalak, R. G. Gordon and M. J. Aziz, *Adv. Energy Mater.*, 2020, **10**, 1–10.
- 65 D. Pletcher, *Electrochem. commun.*, 2018, **88**, 1–4.
- 66 M. Yan, Y. Kawamata and P. S. Baran, *Chem. Rev.*, 2017, **117**, 13230–13319.
- 67 N. Sbei, S. Aslam and N. Ahmed, *React. Chem. Eng.*, 2021, **6**, 1342–1366.
- 68 A. Dey, T. B. Gunnoe and V. R. Stamenkovic, *ACS Catal.*, 2020, **10**, 13156–13158.
- 69 M. C. Leech, A. D. Garcia, A. Petti, A. P. Dobbs and K. Lam, *React. Chem. Eng.*, 2020, **5**, 977–990.
- 70 E. C. R. R. McKenzie, S. Hosseini, A. G. C. C. Petro, K. K. Rudman, B. H. R. R. Gerroll, M. S. Mubarak, L. A. Baker and R. D. Little, *Chem. Rev.*, 2021, **122**, 3292–3335.
- 71 L. F. T. Novaes, J. Liu, Y. Shen, L. Lu, J. M. Meinhardt and S. Lin, *Chem. Soc. Rev.*, 2021, **50**, 7941–8002.
- 72 D. Pollok and S. R. Waldvogel, *Chem. Sci.*, 2020, **11**, 12386–12400.
- 73 C. Schotten, T. P. Nicholls, R. A. Bourne, N. Kapur, B. N. Nguyen and C. E. Willans, *Green Chem.*, 2020, **22**, 3358–3375.
- 74 M. M. Baizer, *J. Electrochem. Soc.*, 1964, **111**, 215.
- 75 D. S. P. Cardoso, B. Šljukić, D. M. F. Santos and C. A. C. Sequeira, *Org. Process Res. Dev.*, 2017, **21**, 1213–1226.
- 76 M. Elsherbini, B. Winterson, H. Alharbi, A. A. Folgueiras-Amador, C. Génot, T. Wirth, A. A. Folgueiras-Amador, C. Génot and T. Wirth, *Angew. Chemie Int. Ed.*, 2019, **58**, 9811–9815.
- 77 F. Amemiya, D. Horii, T. Fuchigami and M. Atobe, *J. Electrochem. Soc.*, 2008, **155**, E162.
- 78 B. R. M. Lake, E. K. Bullough, T. J. Williams, A. C. Whitwood, M. A. Little and C. E. Willans, *Chem. Commun.*, 2012, **48**, 4887–4889.
- 79 J. T. Hill-Cousins, J. Kuleshova, R. A. Green, P. R. Birkin, D. Pletcher, T. J. Underwood, S. G. Leach and R. C. D. Brown, *ChemSusChem*, 2012, **5**, 326–331.
- 80 M. F. Hartmer and S. R. Waldvogel, *Chem. Commun.*, 2015, **51**, 16346–16348.
- 81 C. Gütz, A. Stenglein and S. R. Waldvogel, *Org. Process Res. Dev.*, 2017, **21**, 771–778.

- 82 D. M. Heard and A. J. J. Lennox, *Angew. Chemie*, 2020, **132**, 19026–19044.
- 83 B. F. Watkins, J. R. Behling, E. Kariv and L. L. Miller, *J. Am. Chem. Soc.*, 1975, **97**, 3549–3550.
- 84 Y. Li, L. Wen and W. Guo, *Chem. Soc. Rev.*, 2023, **52**, 1168–1188.
- 85 C. Kingston, M. D. Palkowitz, Y. Takahira, J. C. Vantourout, B. K. Peters, Y. Kawamata and P. S. Baran, *Acc. Chem. Res.*, 2020, **53**, 72–83.
- 86 M. C. Leech and K. Lam, *Acc. Chem. Res.*, 2020, **53**, 121–134.
- 87 K. R. Saravanan, V. Selvamani, K. Kulangiappar, D. Velayutham and V. Suryanarayanan, *Electrochem. commun.*, 2013, **28**, 31–33.
- 88 Y. Shusterman-Honger and J. Y. Becker, *J. Electroanal. Chem.*, 2015, **740**, 105–113.
- 89 K. Lam and I. E. Markó, *Org. Lett.*, 2009, **11**, 2752–2755.
- 90 A. Sáez, V. García-García, J. Solla-Gullón, A. Aldaz and V. Montiel, *Electrochim. Acta*, 2013, **91**, 69–74.
- 91 S. Srinivasan, H. Wroblowa and J. O. M. Bockris, in *Advances in Catalysis*, eds. D. D. Eley, H. Pines and P. B. B. T.-A. in C. Weisz, Academic Press, 1967, vol. 17, pp. 351–418.
- 92 J. Ding, C. Zheng, L. Wang, C. Lu, B. Zhang, Y. Chen, M. Li, G. Zhai and X. Zhuang, *J. Mater. Chem. A*, 2019, **7**, 23337–23360.
- 93 C. L. Bird and A. T. Kuhn, *Chem. Soc. Rev.*, 1981, **10**, 49–82.
- 94 R. J. Mortimer, *Electrochim. Acta*, 1999, **44**, 2971–2981.
- 95 F. André, P. Hapiot and C. Lagrost, *Phys. Chem. Chem. Phys.*, 2010, **12**, 7506–7512.
- 96 H. Ohno and H. Satoh, *J. Electroanal. Chem.*, 1993, **360**, 27–37.
- 97 C. Gao, Q. Huang, Q. Lan, Y. Feng, F. Tang, M. P. M. Hoi, J. Zhang, S. M. Y. Lee and R. Wang, *Nat. Commun.*, 2018, **9**, 2967.
- 98 K. Madasamy, D. Velayutham, V. Suryanarayanan, M. Kathiresan and K. C. Ho, *J. Mater. Chem. C*, 2019, **7**, 4622–4637.
- 99 E. M. Kosower and J. L. Cotter, *J. Am. Chem. Soc.*, 1964, **86**, 5524–5527.
- 100 S. Yu, J. Ying and A. Tian, *Chempluschem*, 2022, **87**, e202200171.
- 101 V. Madhu, A. K. Kanakati and S. K. Das, *New J. Chem.*, 2020, **44**, 10781–10785.
- 102 I. C. Gibbs-Hall, N. A. Vermeulen, E. J. Dale, J. J. Henkelis, A. K. Blackburn, J. C. Barnes and J. F. Stoddart, *J. Am. Chem. Soc.*, 2015, **137**, 15640–15643.
- 103 H. C. Lu, S. Y. Kao, H. F. Yu, T. H. Chang, C. W. Kung and K. C. Ho, *ACS Appl. Mater. Interfaces*, 2016, **8**, 30351–30361.
- 104 S. Y. Kao, H. C. Lu, C. W. Kung, H. W. Chen, T. H. Chang and K. C. Ho, *ACS Appl.*

- Mater. Interfaces*, 2016, **8**, 4175–4184.
- 105 L. Wang, S. Sun, Y. He, N. He, F. Zhang, Y. Yao, B. Zhang, X. Zhuang and Y. Chen, *Eur. Polym. J.*, 2018, **98**, 125–136.
- 106 P. Zhang, F. Zhu, F. Wang, J. Wang, R. Dong, X. Zhuang, O. G. Schmidt and X. Feng, *Adv. Mater.*, 2017, **29**, 1604491.
- 107 M. Kathiresan, B. Ambrose, N. Angulakshmi, D. E. Mathew, D. Sujatha and A. M. Stephan, *J. Mater. Chem. A*, 2021, **9**, 27215–27233.
- 108 L. Zhu, H. Yan, X. J. Wang and Y. Zhao, *J. Org. Chem.*, 2012, **77**, 10168–10175.
- 109 R. Kumar, R. G. Pillai, N. Pekas, Y. Wu and R. L. McCreery, *J. Am. Chem. Soc.*, 2012, **134**, 14869–14876.
- 110 H. J. Yen, C. L. Tsai, S. H. Chen and G. S. Liou, *Macromol. Rapid Commun.*, 2017, **38**, 1600715.
- 111 T. Wu, K. D. Moeller, Y. Liu, Q. Chen, P. Sun, Y. Li, Z. Yang, T. Xu, J. Broggi, T. Terme, P. Vanelle, D. Pletcher, M. C. Leech, A. D. Garcia, A. Petti, A. P. Dobbs, K. Lam, D. S. P. Cardoso, B. Šljukić, D. M. F. Santos, C. A. C. Sequeira, B. C. Patterson, J. K. Hurst, D. L. Cain, C. McLaughlin, J. J. Molloy, C. Carpenter-Warren, N. A. Anderson, A. J. B. Watson, Z. Qi, W. Li, Y. Niu, E. Benassi, B. Qian, N. Fu, G. S. Sauer, S. Lin, A. G. Wills, D. L. Poole, C. M. Alder, M. Reid, H. R. Stephen, C. Schotten, T. P. Nicholls, M. Woodward, R. A. Bourne, N. Kapur, C. E. Willans, J. Hao, L. Yuan, C. Ye, D. Chao, K. Davey, Z. Guo, S. Z. Qiao, D. M. Heard, A. J. J. Lennox, A. Dey, T. B. Gunnoe, V. R. Stamenkovic, C. D. S. Philippa B. Cranwell\*, Andrew T. Russell\*, C. C. Based, D. Zhang, L. Hou, Q. Zhang, J. He, H. Feng, Diering, Maxson & Mitchell and Freeman, *React. Chem. Eng.*, 2017, **97**, 1213–1226.
- 112 B. Hu, C. DeBruler, Z. Rhodes and T. L. Liu, *J. Am. Chem. Soc.*, 2017, **139**, 1207–1214.
- 113 C. DeBruler, B. Hu, J. Moss, X. Liu, J. Luo, Y. Sun and T. L. Liu, *Chem*, 2017, **3**, 961–978.
- 114 J. Huang, Z. Yang, V. Murugesan, E. Walter, A. Hollas, B. Pan, R. S. Assary, I. A. Shkrob, X. Wei and Z. Zhang, *ACS Energy Lett.*, 2018, **3**, 2533–2538.
- 115 E. S. Beh, D. De Porcellinis, R. L. Gracia, K. T. Xia, R. G. Gordon and M. J. Aziz, *ACS Energy Lett.*, 2017, **2**, 639–644.
- 116 Z. Yan, R. J. Wycisk, A. S. Metlay, L. Xiao, Y. Yoon, P. N. Pintauro and T. E. Mallouk, *ACS Cent. Sci.*, 2021, **7**, 1028–1035.
- 117 J. B. Gerken, A. Stamoulis, S. E. Suh, N. D. Fischer, Y. J. Kim, I. A. Guzei and S. S. Stahl, *Chem. Commun.*, 2020, **56**, 1199–1202.
- 118 C. Debruler, B. Hu, J. Moss, J. Luo and T. L. Liu, *ACS Energy Lett.*, 2018, **3**, 663–668.
- 119 B. Hu, Y. Tang, J. Luo, G. Grove, Y. Guo and T. L. Liu, *Chem. Commun.*, 2018, **54**, 6871–6874.
- 120 T. Hagemann, J. Winsberg, M. Grube, I. Nischang, T. Janoschka, N. Martin, M. D.

- Hager and U. S. Schubert, *J. Power Sources*, 2018, **378**, 546–554.
- 121 W. Zhou, W. Liu, M. Qin, Z. Chen, J. Xu, J. Cao and J. Li, *RSC Adv.*, 2020, **10**, 21839–21844.
- 122 Y. Alesanco, J. Palenzuela, R. Tena-Zaera, G. Cabañero, H. Grande, B. Herbig, A. Schmitt, M. Schott, U. Posset, A. Guerfi, M. Dontigny, K. Zaghbi and A. Viñuales, *Sol. Energy Mater. Sol. Cells*, 2016, **157**, 624–635.
- 123 P. Y. Chen, C. S. Chen and T. H. Yeh, *J. Appl. Polym. Sci.*, 2014, **131**, 40485.
- 124 C. Reus, M. Stolar, J. Vanderkley, J. Nebauer and T. Baumgartner, *J. Am. Chem. Soc.*, 2015, **137**, 11710–11717.
- 125 R. Sydam, A. Ghosh and M. Deepa, *Org. Electron.*, 2015, **17**, 33–43.
- 126 E. Hwang, S. Seo, S. Bak, H. H. Lee, M. Min and H. H. Lee, *Adv. Mater.*, 2014, **26**, 5129–5136.
- 127 G. K. Pande, N. Kim, J. H. Choi, G. Balamurugan, H. C. Moon and J. S. Park, *Sol. Energy Mater. Sol. Cells*, 2019, **197**, 25–31.
- 128 W. Raza, F. Ali, N. Raza, Y. Luo, K. H. Kim, J. Yang, S. Kumar, A. Mehmood and E. E. Kwon, *Nano Energy*, 2018, **52**, 441–473.
- 129 X. L. Li and Y. Fu, *J. Mol. Struct. THEOCHEM*, 2008, **856**, 112–118.
- 130 A. Kormányos, M. S. Hossain, G. Ghadimkhani, J. J. Johnson, C. Janáky, N. R. de Tacconi, F. W. Foss, Y. Paz and K. Rajeshwar, *Chem. - A Eur. J.*, 2016, **22**, 9209–9217.
- 131 E. Silva and A. M. Edwards, *Flavins: photochemistry and photobiology*, Royal Society of Chemistry, 2006, vol. 6.
- 132 D. R. Weinberg, C. J. Gagliardi, J. F. Hull, C. F. Murphy, C. A. Kent, B. C. Westlake, A. Paul, D. H. Ess, D. G. McCafferty and T. J. Meyer, *Chem. Rev.*, 2012, **112**, 4016–4093.
- 133 J. M. Mayer, *Annu. Rev. Phys. Chem.*, 2004, **55**, 363–390.
- 134 S. L. J. Tan, J. M. Kan and R. D. Webster, *J. Phys. Chem. B*, 2013, **117**, 13755–13766.
- 135 W. S. Li, N. Zhang and L. M. Sayre, *Tetrahedron*, 2001, **57**, 4507–4522.
- 136 J. Y. D'Aoust, W. G. Martin, J. Giroux and H. Schneider, *Photochem. Photobiol.*, 1980, **31**, 471–474.
- 137 W. R. Briggs, *Flavins, Photochem. Photobiol.*, 2006, 183–216.
- 138 A. Losi, *Flavin Photochem. Photobiol.*, 2006, **6**, 223–276.
- 139 P. R. D. Murray, J. H. Cox, N. D. N. D. Chiappini, C. B. Roos, E. A. Mcloughlin, B. G. Hejna, S. T. Nguyen, H. H. Ripberger, J. M. Ganley, E. Tsui, N. Y. Shin, B. Koronkiewicz, G. Qiu and R. R. Knowles, *Chem. Rev.*, 2021, **122**, 2017–2291.
- 140 M. K. Otto, M. Jayaram, R. M. Hamilton and M. Delbruck, *Proc. Natl. Acad. Sci.*, 1981, **78**, 266–269.

- 141 B. J. Fritz, S. Kasai and K. Matsui, *Photochem. Photobiol.*, 1987, **45**, 113–117.
- 142 B. J. Fritz, K. Matsui, S. Kasai and A. Yoshimura, *Photochem. Photobiol.*, 1987, **45**, 539–541.
- 143 K. Hoenes, U. Wenzel, B. Spellerberg and M. Hessling, *Photochem. Photobiol.*, 2020, **96**, 156–169.
- 144 A. Niemz, J. Imbriglio and V. M. Rotello, *J. Am. Chem. Soc.*, 1997, **119**, 887–892.
- 145 K. Lin, R. Gómez-Bombarelli, E. S. Beh, L. Tong, Q. Chen, A. Valle, A. Aspuru-Guzik, M. J. Aziz and R. G. Gordon, *Nat. Energy*, 2016, **1**, 1–8.
- 146 G. Kwon, S. Lee, J. Hwang, H. S. Shim, B. Lee, M. H. Lee, Y. Ko, S. K. Jung, K. Ku, J. Hong and K. Kang, *Joule*, 2018, **2**, 1771–1782.
- 147 A. Orita, M. G. Verde, M. Sakai and Y. S. Meng, *Nat. Commun.*, 2016, **7**, 1–8.
- 148 N. Elgrishi, K. J. Rountree, B. D. McCarthy, E. S. Rountree, T. T. Eisenhart and J. L. Dempsey, *J. Chem. Educ.*, 2018, **95**, 197–206.
- 149 J.-M. Savéant, *Elements of molecular and biomolecular electrochemistry: an electrochemical approach to electron transfer chemistry*, John Wiley & Sons, 2006.
- 150 F. Dalton, *Electrochem. Soc. Interface*, 2016, **25**, 50.
- 151 Z. Galus, C. Olson, H. Y. Lee and R. N. Adams, *Anal. Chem.*, 1962, **34**, 164–166.
- 152 P. Kissinger and W. R. Heineman, *Laboratory Techniques in Electroanalytical Chemistry, revised and expanded*, CRC press, 2018.
- 153 C. G. Zoski, J. Leddy, A. J. Bard, L. R. Faulkner and H. S. White, *Electrochemical methods: fundamentals and applications, student solutions manual*, JOHN WILEY, 2021.
- 154 S. Treimer, A. Tang and D. C. Johnson, *Electroanalysis*, 2002, **14**, 165–171.
- 155 BioLogic, EC-Lab – Application Note Protocols for studying intercalation electrodes materials. Galvanostatic cycling/potential limitations (GCPL), <https://www.biologic.net/documents/gitt-electrochemistry-battery-application-note-1/>.

**CHAPTER 2**

**VIOLOGENS :**

**FUNCTIONAL DESIGN AND CHARACTERIZATION**

---

*"My grace is sufficient for you, for My power is made perfect in weakness."*

*2 Corinthians 12:9*

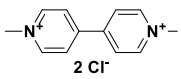
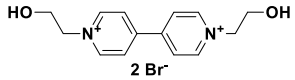
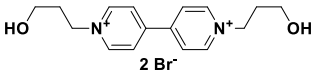
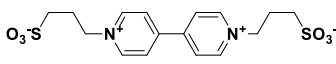
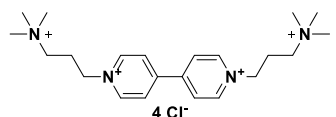


## 2.1 Introduction

Viologens have been extensively functionalized in literature<sup>1-3</sup> to achieve properties that are in line with the desired application, such as AORFBs. (**Table 2.1**) A suitable viologen for an AORFB should possess good solubility (~2 M) in aqueous electrolytes, be bulky enough to prevent crossover, exhibit stable electrochemical reversibility and be chemically stable to withstand potential degradation.

The nature of the alkyl chain and alkyl chain length have been explored by several groups<sup>4-8</sup> as these can also influence the redox potentials, ion conductivity, and solubility of the viologens. The solubility of viologens in aqueous media improves when hydrophilic substituents such as hydroxyl and sulphonic acid groups are added.<sup>1</sup>

**Table 2.1** Summary of redox potentials (vs Ag/AgCl) of previously synthesized viologens.\*

|   | 1 <sup>st</sup> Reduction (V) | 2 <sup>nd</sup> Reduction (V) | Ref. |
|---|-------------------------------|-------------------------------|------|
| <br>2 Cl <sup>-</sup>              | -0.65                         | -1.06                         | 15   |
| <br>2 Br <sup>-</sup>              | -0.59                         | -0.99                         | 7    |
| <br>2 Br <sup>-</sup>              | -0.63                         |                               | 9    |
| <br>2 SO <sub>3</sub> <sup>-</sup> | -0.63                         |                               | 5    |
| <br>4 Cl <sup>-</sup>              | -0.58                         |                               | 4    |

\*All reduction potentials converted and represented Ag/AgCl.

For example, the work by Liu *et al.*<sup>9</sup> has shown that the alkyl-chain length between the viologen core and hydroxyl group substituent (**Figure 2.1**) has significant influence on the electrochemical properties of viologens.

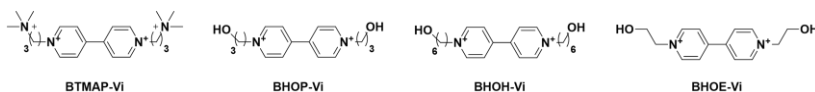


**Figure 2.1** Viologen derivatives which have been previously synthesized.<sup>9</sup>

For example, comparing BHOP-Vi to BHOE-Vi: <sup>9</sup>

- BHOP-Vi exhibited the highest solubility in water (2.69 M).
- The Highest Occupied Molecular orbital (HOMO)-Lowest unoccupied molecular orbital (LUMO) gaps of the hydroxylated viologens are narrower than BTMAP-Vi, and this due to an elevated LUMO energy.
- The LUMO energy increases with an increase in chain length which affects the electronic distribution of the viologen, subsequently influencing the electrochemical properties.

**Table 2.1** shows the different properties of viologen derivatives which were screened in the work by Liu and co-workers.<sup>9</sup>

| Viologen        | $D$<br>( $\text{cm}^2 \cdot \text{s}^{-1}$ ) | $k_0$<br>( $\text{cm} \cdot \text{s}^{-1}$ ) | $E_{1/2}$<br>(V vs SHE) | HOMO<br>(eV) | LUMO<br>(eV) |
|-----------------|--|--|-------------------------|--------------|--------------|
| <b>BTMAP-Vi</b> | $3.07 \times 10^{-6}$                        | $6.86 \times 10^{-3}$                        | - 0.369                 | -9.10        | -3.89        |
| <b>BHOE-Vi</b>  | $5.78 \times 10^{-6}$                        | $1.09 \times 10^{-2}$                        | - 0.408                 | -8.31        | -3.81        |
| <b>BHOP-Vi</b>  | $5.26 \times 10^{-6}$                        | $1.12 \times 10^{-2}$                        | - 0.433                 | -8.07        | -3.76        |
| <b>BHOH-Vi</b>  | $4.35 \times 10^{-6}$                        | $1.28 \times 10^{-2}$                        | - 0.452                 | -7.74        | -3.72        |

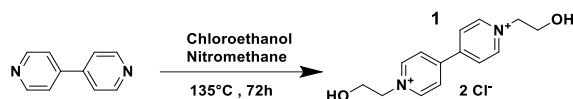
$D$  = Diffusion Coefficient.  $k_0$  = electron transfer rate constant, and  $E_{1/2}$  = reduction potential.

## 2.2 Synthesis of Viologens

### 2.2.1 Water-soluble Viologens

Water soluble viologens offer a means to create more affordable RFBs by eliminating costly materials such as Vanadium, commonly used in commercial RFBs.<sup>10</sup> However, crossover and agglomeration are issues commonly faced when using viologens in RFB systems.<sup>11–13</sup> The incorporation of a hydroxy group into viologen should increase their solubility in water, and furthermore, water-soluble viologens would allow inexpensive and safer electrolytes (NaCl/KOH), rather than sulphuric acid which is the necessary electrolyte for VRFBs.

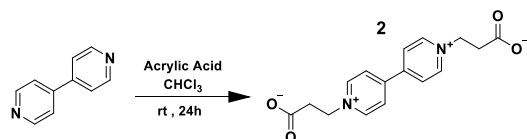
The synthesis of bis(2-hydroxyethyl)viologen has been reported in literature, synthesized by alkylation of 4,4'-bipyridine with bromoethanol in acetonitrile,<sup>14</sup> and this served as a starting point for the synthesis of the first water-soluble viologen. In a previous study by the Murray group, nitromethane was used as the solvent of choice due to previously observed faster conversion when chloroethanol was used.



**Scheme 2.1** Synthesis of 1,1'-bis(2-hydroxyethyl)-[4,4'-bipyridine]-1,1'-dium (**1**).

Initial synthesis attempts at 115 -120 °C had poor yields and the reaction would often need to run for 96 h to afford the product. Synthetic optimization revealed that higher temperature (135 °C) and a more concentrated solution of chloroethanol and bipyridine yielded large quantities (~80 % yield) of product, **1**, as a light brown powder, under shorter reaction time (72 h).

To further explore the application of viologens containing water-soluble groups, a zwitterionic viologen, compound **2** (Scheme 2.2) was successfully synthesized by N-alkylation of 4,4'-bipyridine using acrylic acid to afford a white powder in fair yield (56 %).



**Scheme 2.2** Synthesis of 1,1'-bis(2-carboxyethyl)-[4,4'-bipyridine]-1,1'-dium (**2**).

Having successfully isolated two different water-soluble viologens containing a hydroxy- and carboxy-functionality respectively, efforts were directed towards the incorporation of different functional group: trimethyl-ammonium. One of the most stable viologen derivatives synthesized by the Aziz group is bis(3-trimethylammonio)propyl viologen tetrachloride (BTMAP-Vi)<sup>4,6</sup> which was initially used as the negative couple in a neutral pH AORFB coupled with bis((3-trimethylammonio)propyl)-ferrocene dichloride (BTMAP-Fc), shown in **Figure 2.2**.

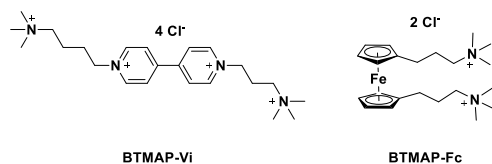
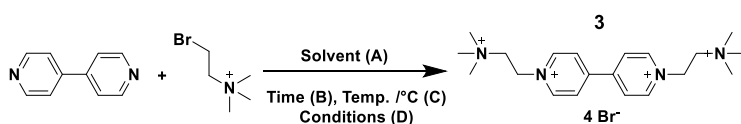


**Figure 2.2** Chemical structures of BTMAP-Vi and BTMAP-Fc as synthesized by Aziz *et al.*<sup>4</sup>

The incorporation of the trimethyl amino group on the viologen increased the solubility to 2M in water as compared to the 0.5 - 0.75 M for MV in an AORFB,<sup>10,15,16</sup> and prevented dimerization by increasing coulombic repulsion and resulted in a cell voltage of 0.748 V with minimal reactant crossover.

Further success of BTMAP was reported by the group in 2019 when it was used as a positive redox couple in an AORFB at neutral pH.<sup>6</sup> Despite the success of BTMAP-Vi, at the time, there were no reports of the ethyl analogue of this compound in literature. Another member of the research group was currently using “bromocholine bromide” for their own synthesis, and this motivated the synthesis of the ethyl analogue as per **Scheme 2.3**.



**Scheme 2.3** Synthesis of 1,1'-bis(2-(trimethylammonio)ethyl)-[4,4'-bipyridine]-1,1'-dium (3).

Initially, the synthesis was carried out in DMSO and in air, unlike the conditions used by the Aziz group,<sup>4</sup> as these had previously worked for another group member for the alkylation of flavin derivatives. The initial synthesis attempt was unsuccessful, and no product could not be isolated after concentration of the reaction mixture. Unfortunately, it seemed that the product had been lost upon standing overnight. The synthesis was repeated using dimethylformamide (DMF), consistent with the work by the Aziz group,<sup>4</sup> and after 24 h a solid was evident in the reaction flask. However, due to the hygroscopic nature of the product, it could not be isolated successfully. A final synthesis was attempted in dimethyl sulfoxide (DMSO) under inert conditions. Within the first hour, the reaction mixture changed colour from colourless to yellow, without any visible trace of solid in the flask. MeCN was added in excess *via* canula, resulting in the formation of a mustard-yellow solid and the product was dried under high-vac. **Table 2.2** details the different synthetic attempts for this molecule.

**Table 2.2** Synthesis conditions for 1,1'-bis(2-(trimethylammonio)ethyl)-[4,4'-bipyridine]-1,1'-dium (**3**).

| Solvent (A) | Temp. / °C (B) | Time / hours (C) | Conditions (D)                    | Outcome   |
|-------------|----------------|------------------|-----------------------------------|---|
| DMSO        | 100            | 24               | Stirring in oxygen atmosphere     | Unsuccessful. Product not isolated. Reaction mixture runs through filter paper and cannot be retrieved.       |
| DMF         | 100            | 72               | Stirring in oxygen atmosphere     | Unsuccessful. Product not isolated. Product is hygroscopic and was lost due to exposure to oxygen atmosphere. |
| DMSO        | 100            | 24               | Inert atmosphere – N <sub>2</sub> | Partially successful. A product was isolated from this reaction but decomposed upon standing.                 |

The <sup>1</sup>H NMR spectrum (**Figure 2.3**) of this material from the final synthesis attempt in DMSO shows that the product did not form successfully. The large peaks at 2.08 and 2.73 ppm correspond to MeCN and DMSO, and the integration of the other smaller peaks observed in the aliphatic region does not correlate to the structure of **3**, and therefore it is probable that the 2 peaks in the aromatic region (8.57 ppm and 9.07 ppm) are indicative of the starting material, 4,4'-bipyridine.

The synthesis of an ethyl analogue of BTMAP-Vi was attempted, but unfortunately was consistently unsuccessful. Thus, other viologens were targeted instead and focus of the work was directed to synthesis of other viologens.

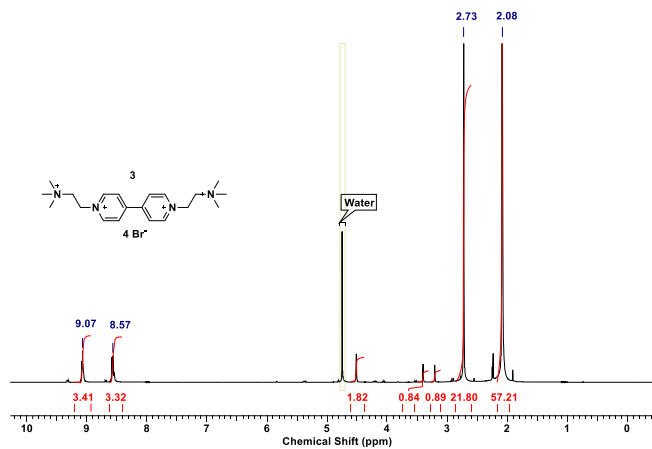
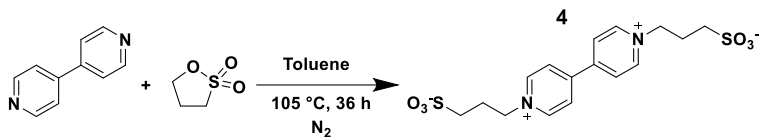


**Figure 2.3**  $^1\text{H}$  NMR spectrum of the isolated product from the final synthesis attempt of compound **3**, recorded in  $\text{D}_2\text{O}$  at 298.15 K.

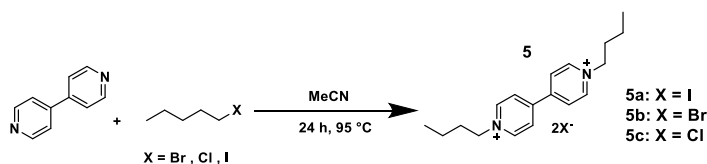
Similarly to BTMAP-Vi, sulphonate functionalization of viologens has been used to prevent dimerization due to enhanced coulombic repulsion by the water-soluble, sulphonate substituents.<sup>9</sup> This knowledge led to the synthesis of 3,3'-([4,4'-bipyridine]-1,1'-diium-1,1'-diyl)bis(propane-1-sulfonate) (**4**), shown in **Scheme 2.4**, which was carried out with ease using a standard  $\text{S}_{\text{N}}2$  alkylation; the product was obtained in high yield (89.4 %) and was characterized without further purification. The  $^1\text{H}$  NMR spectrum of **4** corresponds with literature values<sup>5,17</sup> and shows the distinct splitting pattern for the propane sulphonate chain, confirming the formation of the disubstituted product.



**Scheme 2.4** Synthesis of 3,3'-([4,4'-bipyridine]-1,1'-diium-1,1'-diyl)bis(propyl)bis(propyl sulfonate) (**4**).

The aim was to test this viologen as a negative couple in an AORFB owing to its high-water solubility, approximately (~2.5 M), coupled to potassium ferrocyanide as this had not been reported in literature. Unfortunately, at this point, lab work was interrupted by a 7 month gap due to COVID-19 and in this time, the system proposed was published by Yan *et al.*<sup>17</sup> This work was therefore terminated at this time.

Unlike the viologens discussed in this PhD, compound **5**, shown in **Scheme 2.5**, was not synthesized with the intention of using it in an AORFB but rather, used as a biphasic electrocatalyst.



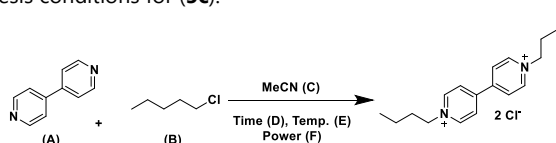
**Scheme 2.5** Synthesis of 1,1'-dibutyl-[4,4'-bipyridine]-1,1'-diium (**5**).

The synthetic route was straightforward, using an alkyl halide as the alkylating agent under mild reflux conditions. The first synthesis attempt was on the iodide salt of this viologen, (**5a**), and this product was obtained in high yield (73 %) as a pure red powder after filtration and washing. The bromide derivative, (**5b**), was synthesised in a similar manner, and was also obtained in high yield (83 %). However, the change in counter anion resulted in the formation of a yellow fine powder, rather than red as for **5a**, indicating a change in the degree of interaction between anion and cation. Several attempts were made to synthesize the chloride derivative, **5c**, of this viologen. Unlike the iodide and bromide, synthesis of the dichloride is reported to require the use of a microwave<sup>18</sup> due to slow reaction kinetics and poor conversion to product under reflux conditions.



After the first two unsuccessful synthesis attempts using the microwave (**Table 2.3 -Run 1&2**), a ramp time was included in the method to allow the equipment to reach the desired temperature for the reaction, before starting the reaction. This marginally improved the outcome but only yielded a monosubstituted product (**Table 2.3 - Run 3**).

**Table 2.3** Synthesis conditions for (5c).



| Run            | (A) / mmol | (B) / mL | (C) / mL | (D) / min. | (E) / °C | (F) / W | Outcome   |
|----------------|------------|----------|----------|------------|----------|---------|---|
| 1              | 6.45       | 3.33     | 10.0     | 5          | 90       | 80      | Unsuccessful.<br>No product formed.   |
| 2              | 3.2        | 1.0      | 5.0      | 15         | 90       | 80      | Unsuccessful.<br>No product formed.   |
| 3 <sup>a</sup> | 6.46       | 5.0      | 7.0      | 25         | 120      | 80      | Unsuccessful.<br>Only mono-substituted product                              |
| 4 <sup>a</sup> | 19.2       | 10.0     | 15.0     | 45         | 130      | 80      | Unsuccessful.<br>Starting material did not fully dissolve.                  |
| 5 <sup>b</sup> | 12.8       | 8.0      | 8.0      | 45         | 130      | 80      | Unsuccessful.<br>Lid exploded off microwave tube. Product lost as a result. |
| 6 <sup>b</sup> | 3.64       | 1.04     | 8.0      | 45         | 130      | 80      | Successful.   |

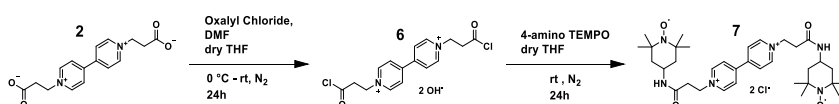
<sup>a</sup> Ramp time was increased to 10 minutes. <sup>b</sup> 15 minutes ramp time.

Upscaling the reaction was also unsuccessful as this resulted in issues with fully dissolving the starting material. (**Run 4**) Increasing the reaction time seemed to be the obvious next step to improve conversion but build-up of pressure in the microwave tube caused the reaction to explode in the reactor, causing product to be lost.

Using the same reaction conditions as **Run 5**, a repeat attempt was made using a smaller scale and ultimately, this reaction was successful, giving the product as a fine brown powder, obtained in very low yield (24%). <sup>1</sup>H NMR showed traces of mono- and di-substituted product. Unfortunately, during drying of the product moisture was taken in which resulted in a loss of product. No further synthesis attempts were made, and this drew a close to the synthesis of water-soluble viologens.

### 2.2.2 Multifunctional Viologens

Whilst water-soluble viologens target the issue of precipitation and aggregation of species within RFBs, crossover, an equally detrimental artefact, still exists. Symmetrical RFB systems are advantageous as this minimizes any crossover issues because the contents of both the anode and cathode of the battery contain the same redox active species, and they ideally remain balanced over long-term cycling. Inspired by the work of Janoschka and co-workers,<sup>19</sup> and to approach and potentially overcome problems with crossover and cross contamination, the synthesis of a novel "viotempa-viologen" molecule covalently linked to a 4-amino-2,2,6,6-tetramethylpiperidin-1-oxyl (TEMPO) moiety, was attempted in a 2-step synthetic process as seen in **Scheme 2.6**. Both components of this molecule are soluble in aqueous systems, making them ideal candidates for this application, and it was hoped that this solubility would be retained in the final molecule.



**Scheme 2.6** Synthesis of 1,1'-bis(2-carbonylethyl-TEMPO)-[4,4'-bipyridine]-1,1'-dium (**7**).

On characterisation, however, it was found that the initial  $^1\text{H}$  NMR results had been misleading in confirming the formation of the desired product. Fourier transform Infrared Spectroscopy (FTIR) analysis was used to test for presence of the amide group which should be present if **7** had been successfully synthesized. However, a comparison of the FTIR spectra of **2** (black curve) and **6** (red curve) (**Figure 2.4**) showed minimal change pertaining to the strong band at  $1702\text{ cm}^{-1}$  which is indicative of the C=O stretching of a carboxylic acid. It is most likely that the acid chloride either had not formed or was hydrolysed *in situ* by wet solvent; no acid halide C-O stretch (typically centred between  $1815\text{-}1785\text{ cm}^{-1}$ ) was observed.

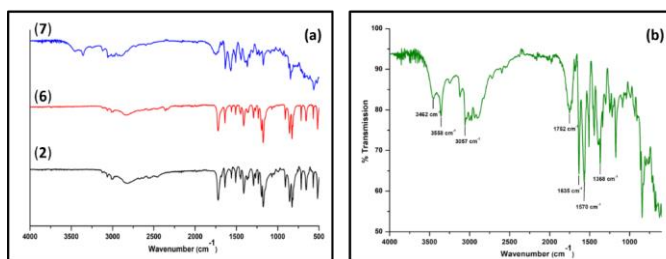


**Figure 2.4** a) FTIR spectra of precursors (**6** and **7**) and **2**; b) FTIR spectrum of **2**.

No conclusive identification could be made from the Electrospray Ionisation Mass Spectrometry (ESI+ MS). No fragments corresponding to the final product were observed in the ES+ screen. (**Figure 2.5**) The total molecular weight of the "viotempa-viologen" is  $609.83\text{ g}\cdot\text{mol}^{-1}$  and expected peaks were at; 304.2, 304.7. No flow battery testing was conducted on this product given that the ES+ MS showed only the presence of starting materials. These findings led to the belief that compound **7** was not formed.

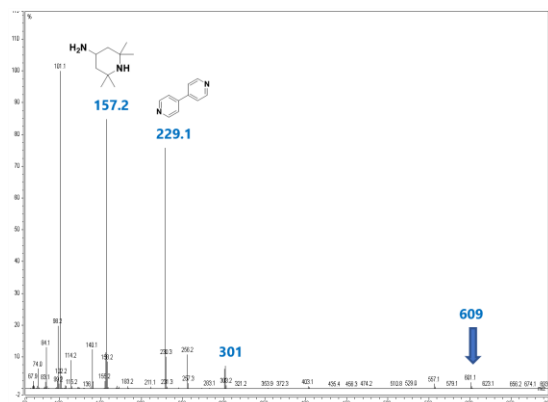
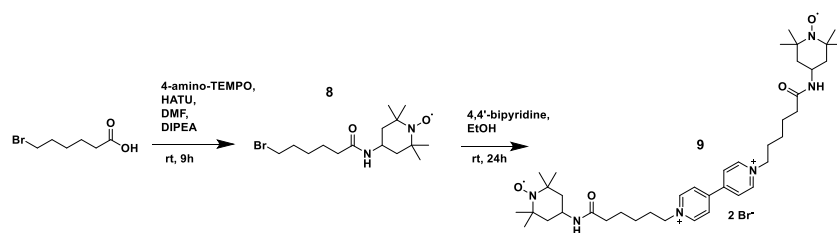


**Figure 2.5** ESI-MS+ of **7** confirming the presence of starting materials rather than fragments from the desired product.

Following the unsuccessful synthesis of **7**, a different approach was employed to synthesize a similar molecule. Several examples of conjugate redox active molecules are present in literature, and there seemed to be an ever-growing success when using co-polymer backbones to synthesize these molecules.<sup>16,19–21</sup> Compound **9**, shown in **Scheme 2.7**, was chosen as a target because it would contain the simple viologen core, flanked by an extended alkyl chain terminated by a TEMPO derivative. Furthermore, 6-bromohexanoic acid is a relatively inexpensive precursor that can easily be bound to 4-amino TEMPO using 1-[Bis(dimethylamino)methylene]-1H-1,2,3-triazolo[4,5-b]pyridinium 3-oxide hexafluorophosphate (HATU).<sup>22</sup> Overall, this approach seemed like a cost-effective, feasible means to synthesize a conjugated molecule for possible use in an AORFB.



**Scheme 2.7** Synthesis of 1,1'-bis(2-carboxypentyl-TEMPO)-[4,4'-bipyridine]-1,1'-dium (**9**).

Hydrazine hydrate was added to the NMR sample to reduce TEMPO to TEMPOH to obtain a clean diamagnetic spectrum, however, due to the paramagnetic nature of the compound, the  $^1\text{H}$  NMR was difficult to interpret. Given the lack of success with the NMR, ES+ MS was used next, and this confirmed the formation of the **8** with peaks for  $[\text{M} + \text{Br}]$  at 347, 348, and 349 as expected due to the  $^{79}\text{Br}$  and  $^{81}\text{Br}$  isotopes which are shown in **Figure 2.6**.

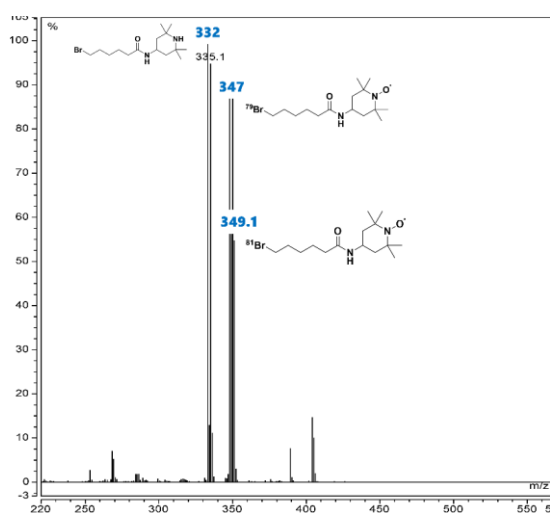


**Figure 2.6** ESI-MS+ of **8** confirming the formation of the desired product.

The peak at 332 is likely due to the loss of the terminal oxygen radical ( $\text{O}^\cdot$ ) which was on TEMPO. The final product **9** obtained was a red residue in fair yield: 0.44g, 0.51 mmol, ~58%. The solubility in water and 1M NaCl solution was quite poor at room temperature, at < 0.05 M. The solubility was increased slightly by heating the solution to 60 °C, but reprecipitation occurred rapidly on cooling. The product was analysed by  $^1\text{H}$  NMR in DMSO but showed evidence of the mono-substituted product.

## 2.3 Electrochemical characterization

The electrochemical characterization of certain viologens has been previously documented in the literature,<sup>5,7,9,14,17</sup> given the versatility of viologen derivatives. The redox potentials of viologens are tunable based on their counter anions and as such, viologens synthesized in this work were characterized electrochemically, and where applicable, the results were compared to literature.

### 2.3.1 Cyclic Voltammetry (CV)

Being a quick and simple analytical technique, cyclic voltammetry provided initial insight into the electrochemical properties of synthesized viologens, allowing a means to determine their feasibility for use in AORFBs.

#### Water-soluble Viologens

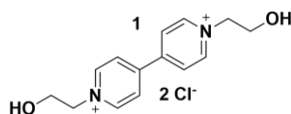
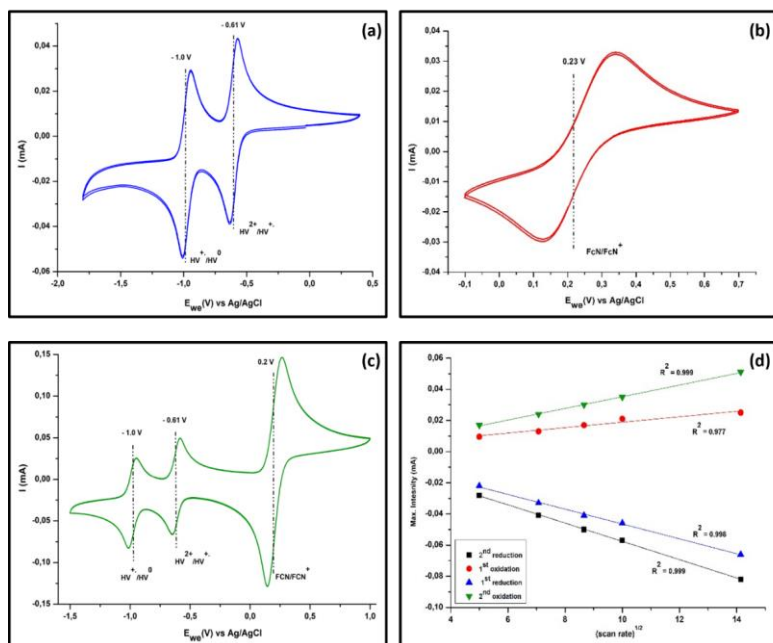


**Figure 2.7** Structure of compound **1**.

Compound **1** showed high solubility, both in water and 0.1 M NaCl solution, and its electrochemical properties were studied using cyclic voltammetry (CV). The voltammogram of **1** (**Figure 2.8a**) shows two oxidation and reduction peaks as expected,<sup>6,10</sup> with the first reduction at -0.70 V vs Ag/AgCl which correlates to the reduction from  $[1]^{2+}$  to  $[1]^+$ , forming the radical cation, followed by the second reduction from  $[1]^+$  to  $[1]^0$ , at -1.095 V. In addition to the redox process taking place, distinct colour changes were evident; the solution changed colour from very faint brown to purple as **1** was reduced sequentially.

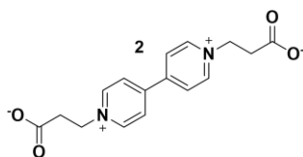
Two equivalents of Potassium Ferrocyanide (FCN) were added to the mixture to test the coupled electrochemical properties of the **1**-FCN couple and determine whether this was feasible for use in an AORFB.

As seen from **Figure 2.8c**, during CV study of the system at 200 mV/s, the system remains reversible when **1** and FCN are dissolved in 1 M NaCl. The peak separation for the two reduction steps of the viologen is approximately 58 mV which confirms that the redox event is both chemically and electrochemically reversible.<sup>23</sup> When **1** is paired with the FCN/FCN<sup>+</sup> redox couple, at pH 7, the resulting AORFB would have a cell voltage of 0.81 V for the first reduction ( $[1]^{2+}/[1]^+$ ) and 1.2 V for the second reduction ( $[1]^+/[1]^0$ ). This is in accord with previous reports about RFBs utilizing viologens.<sup>6,14</sup> The peak currents of the first reduction step showed a linear relationship with the square root of the scan rate which confirms that both redox couples are reversible and exhibit diffusion controlled behaviour.<sup>14,19</sup> The chemical and electrochemical reversibility of the system, good theoretical voltage, and diffusion controlled behaviour shows promise for battery applications because this implies that the redox species will be able to freely diffuse during charge and discharge of the battery, which is necessary for good operation of the flowcell.



**Figure 2.8** a) Cyclic voltammogram of **1** with half-wave potentials ( $E_{1/2}$ ) (supporting electrolyte: 1 M NaCl); b) Cyclic voltammogram of FCN (supporting electrolyte: 1 M NaCl); c) Cyclic voltammogram of coupled with 2 equivalents of FCN (supporting electrolyte: 1 M NaCl); d) maximum peak currents vs the square root of the scan rate.

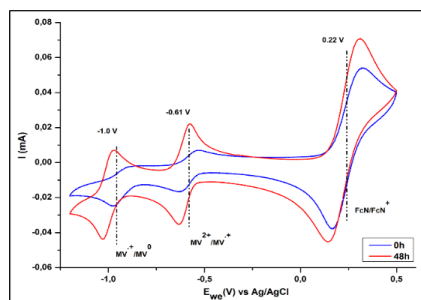
Compound **2** was originally synthesized as the precursor for **6**, and so as a precursor, the electrochemical properties of **2** were not initially investigated.



**Figure 2.9** Structure of compound **2**.

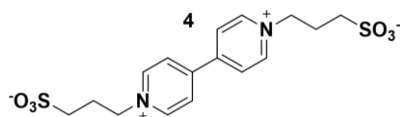


To ensure results were directly comparable with those from **1**, **2** and FCN were analysed together by cyclic voltammetry in 1M NaCl. Initially the second reduction,  $[2]^0$  to  $[2]^-$  was irreversible, however, after 48 h the same sample was re-analysed with CV and the results revealed that both reductions were then found to be reversible (**Figure 2.10**). The half wave potentials were recorded at -1.0 V and -0.6 V for the second ( $[2]^0/[2]^-$ ) and first ( $[2]^-/[2]^0$ ) reductions, respectively. There was an overall potential difference of 1.2 V between the second reduction of **2** and the FCN redox couple, which is comparable with those previously obtained in this work using compound **1**. In addition to the change in electrochemical properties, a colour change from colourless to a pale purple colour was also observed after 48 hours. Sluggish formation of a solid was observed which was due to the mixing of **2** and FCN and the nature of the kinetic barrier to rapid viologen-FCN complex formation is unclear. Unfortunately, we did not investigate this further.



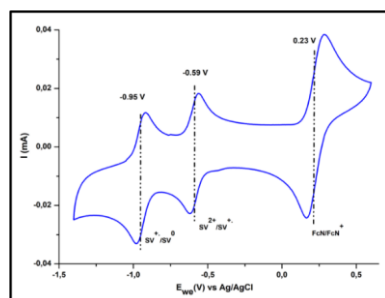
**Figure 2.10** Cyclic voltammogram of **2** and FCN with half-wave potentials ( $E_{1/2}$ ) (supporting electrolyte: 1M NaCl).

Compound **4** was characterized with the intention of coupling **4** with FCN for use in AORFB, however, this was done before the onset of COVID-19 and the discovery of the work by Yan *et al.*<sup>17</sup> As such, CV data is included in this chapter, but no flow cell testing was carried out on this compound.



**Figure 2.11** Structure of compound **4**.

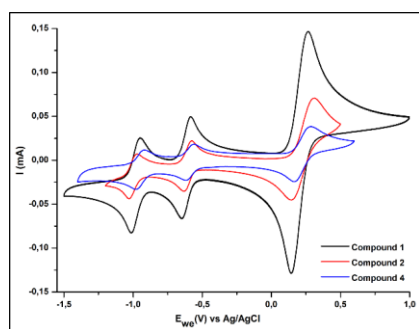
Compound **4** shows two reduction waves at  $E_{1/2} = -0.59$  and  $-0.95$  V, corresponding to the first and second reduction, respectively, and the electrochemically reversible behaviour of **4** was confirmed by CV. Unlike with **2**, there was no evidence of solid after the addition of 2 equivalents of FCN to the CV solution, which was then analysed by CV and confirmed that compound **4** had retained its electrochemical properties (**Figure 2.12**). There was a potential difference of 0.82 V between the first reduction,  $[4]^0/[4]^-$ , and FCN, and for the second reduction ( $[4]^-/[4]^{2-}$ ), a potential difference of 1.18 V was recorded between this redox event and the peak correlating to FCN. These values are quite like the values which were observed for the couple between **1**/FCN, 1.2 V.



**Figure 2.12** Cyclic voltammogram of **4** and FCN with half-wave potentials ( $E_{1/2}$ ) (supporting electrolyte: 1M NaCl).

During the course of this project, work was published on an AORFB using **4** and FCN<sup>17</sup> using a bipolar membrane to enable the use of electrolytes with different pH values. Therein, 1 M H<sub>2</sub>SO<sub>4</sub> (pH 0) was used as the electrolyte containing **4** whilst 2 M KOH (pH 14) was used for FCN.

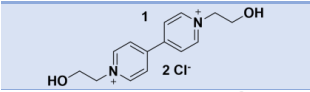
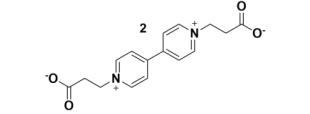
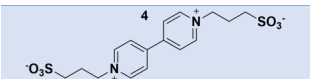
Under these conditions, a potential difference of 0.88 V between the first reduction ( $4^{2+}/4^{+}$ ) and FCN was reported. When the pH of the viologen supporting electrolyte was changed to a more alkaline nature (pH 14) and the CV was repeated, the potential difference remained the same, and therefore, it was concluded that the formal potential and electrochemical behaviour of the **4** couple is unaffected by pH.



**Figure 2.13** Cyclic voltammograms of **1**, **2**, and **4** (supporting electrolyte: 1M NaCl; scan rate =  $250 \text{ mV}\cdot\text{s}^{-1}$ ).

The data displayed in **Figure 2.13** and **Table 2.4** compares the electrochemical properties, as obtained from CV, of three water-soluble viologens synthesized in this work (**1**, **2**, and **4**). All three viologens show reversible electrochemical behaviour in aqueous electrolytes (1 M NaCl) with good solubility ( $> 1.5 \text{ M}$ ) which shows promise for their use in AORFBS.

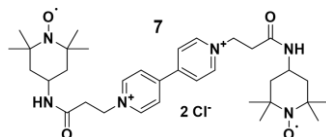
**Table 2.4** Redox potentials for synthesized viologens in 1 M NaCl. Scan rate=250 mV.s<sup>-1</sup>

| Viologen  | E <sub>1/2</sub> (V) vs Ag/AgCl<br>(First Reduction) | E <sub>1/2</sub> (V) vs Ag/AgCl<br>(Second Reduction) |
|---|--|---|
| <br>1<br>2 Cl <sup>-</sup> | -0.70 V  | 1.09 V  |
| <br>2<br>2 Cl <sup>-</sup> | -0.6 V   | -1.0 V  |
| <br>4<br>2 Cl <sup>-</sup> | - 0.59 V   | - 0.95 V  |

As compound **5** was synthesized with the intention of being used as a catalyst rather than redox active species in an AORFB, the cyclic voltammetry results for **5** are discussed in Chapter 4 of this work.

#### Multifunctional Viologens

Based on initial <sup>1</sup>H NMR data, crude putative compound **7** was analysed using CV with a supporting electrolyte of 1M NaCl and the results are shown in **Figure 2.15**.

**Figure 2.14** Structure of compound **7**.

The voltammogram of **7** (**Figure 2.15b**) shows two reversible redox peaks, with reduction potentials at -0.63 V vs Ag/AgCl, and -1.0 V, for the first and second reduction respectively. The results show a potential difference of 1.34 V between the redox peak corresponding to TEMPO and the first reduction, and an overall potential difference of 1.71 V to the second reduction. As expected, TEMPO (**Figure 2.15a**) exhibited a reduction peak centred around

0.70 V.<sup>7,19</sup> Unfortunately, based on MS analysis and FTIR, it was found that the promising CV results were due to a mixture of the starting materials, not the formation of covalently linked **7**. Nevertheless, these results are comparable with literature reports on viologen-TEMPO systems,<sup>7,16,19</sup> and show promise for further developments of a conjugated molecule containing both redox couples.

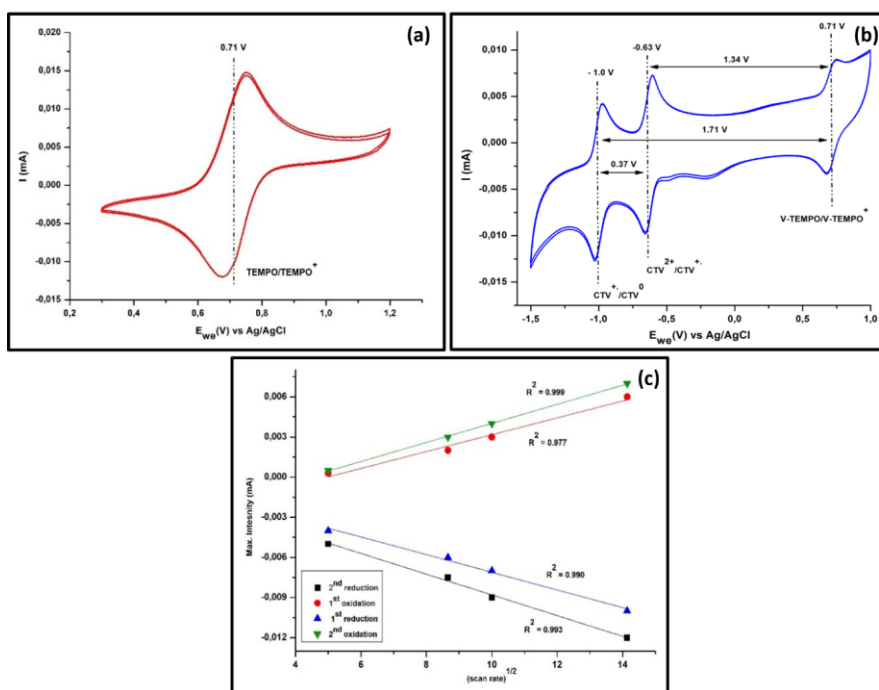


**Figure 2.15** a) Cyclic voltammogram of 4-amino-TEMPO (supporting electrolyte: 1M NaCl); b) Cyclic voltammogram of **4** with half-wave potential ( $E_{1/2}$ ) provided in parentheses (supporting electrolyte: 1M NaCl); c) maximum peak currents vs the square root of the scan rate.

Compound **9** was designed with the hope that it might bear similar electrochemical results to VIOTEMP,<sup>19</sup> but have improved results to **7**. Unfortunately, <sup>1</sup>H NMR indicated that the desired product had not been isolated but was rather the mono-substituted form of this

compound. Regardless of this outcome, CV analysis was carried out to see if the coupling had had any effect on the redox properties of the TEMPO moiety. Compound **9** was obtained as a red residue which had poor apparent solubility in 1 M NaCl. Therefore, to produce a solution of sufficient concentration for CV analysis, a solution of 1M NaCl, containing **9**, was heated to 60 °C and stirred for 10 minutes before running CV analysis.

CV analysis of **9** revealed clear reduction and oxidation peaks for TEMPO with  $E_{1/2}$  at 0.66 V, in accordance with previous literature reports.<sup>16,19</sup> Unfortunately, unlike VIOTEMP, which had a reversible peak for the first reduction, no visible reversible electrochemical behaviour was observed for the viologen portion of **9**. We suspect that the presence of the alkyl chain linker is responsible for the decreased solubility, which may affect the reversibility of the reduction given that the process is usually controlled by the diffusion of the molecules into the supporting electrolyte.<sup>16,19</sup>

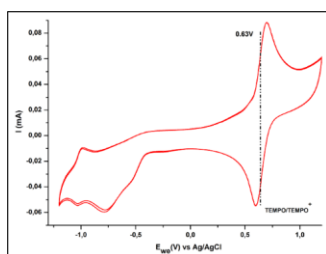


**Figure 2.16** Cyclic voltammogram of **9** with half-wave potential ( $E_{1/2}$ ) (supporting electrolyte: 1M NaCl).

Given the lack of success with regards to solubility and stability observed in most of the compounds synthesized, 1,1'-bis(2-hydroxyethyl)-[4,4'-bipyridine]-1,1'-diium (**1**) was selected for further optimization in the development of an AORFB.

### 2.3.2 Rotating Disk Electrode (RDE) studies

Following the initial electrochemical characterization using CV, RDE studies were performed to evaluate the reduction kinetics of compound **1** and **5** which were selected for further study. The voltage was swept negatively from 0.0 V to -1.0 V for **1** and from -0.2 V to -1.8 V for **5**, and the voltammograms were collected over a range of rotation rates.

The electrochemical kinetics of **1** were measured by linear sweep voltammetry (LSV), using 1 M NaCl as the electrolyte solution, and **Figure 2.17** shows the average data obtained from these experiments, which were run in triplicates; the results are consistent with literature.<sup>9,14</sup> It is believed that the first plateau observed between -0.2 V to -0.4 V is due to surface adsorption of **1** on the surface of the working electrode given that this occurs at a lower potential than that of the first electron reduction (-0.7 V), eliminating the possibility of it being attributed to the first reduction. This is in accordance with findings from other groups working on a similar molecule.<sup>14</sup> Therefore, the second and third plateaus observed correspond to the first and second electron reduction, respectively. Using **equation 1.11**, the diffusion coefficient ( $D$ ) of **1** was determined from the Levich plot of limiting current versus the square root of the rotation rate and had a value of  $5.02 \times 10^{-6} \text{ cm}^2/\text{s}$ .

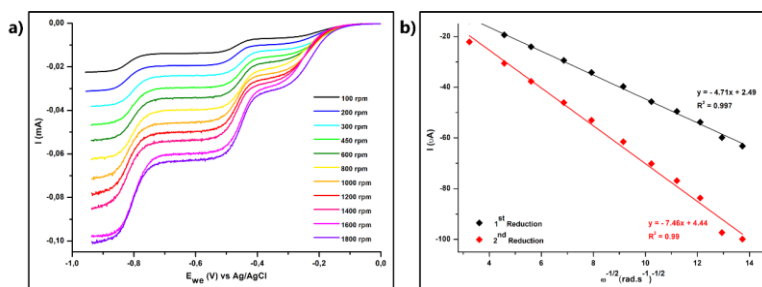


**Figure 2.17** Rotating Disk electrode experiment on **1** (1 mM in 1 M NaCl). a) Current vs potential at different rotation rate with potential sweep of 5 mV/s; b) Levich-plot of limiting current versus square root of rotation rate.

Thereafter, the electrochemical kinetics of **5b** were measured by linear sweep voltammetry (LSV), using MeCN as the electrolyte solution, and tetrabutylammonium hexafluorophosphate [(TBA)(PF<sub>6</sub>)] (2 mM) as the supporting electrolyte. **Figure 2.18** shows the average data obtained from these experiments, which were run in triplicates, and the results are consistent with literature. Using **equation 1.11**, the diffusion coefficient (*D*) of **5** was determined from the Levich plot of limiting current versus the square root of the rotation rate and had a value of  $2.27 \times 10^{-8} \text{ cm}^2/\text{s}$ .

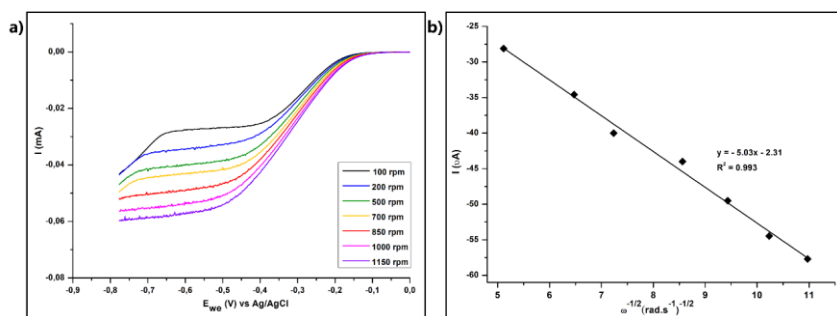


**Figure 2.18** Rotating Disk electrode experiment on **5b** (1 mM in MeCN with 2mM [(TBA)(PF<sub>6</sub>))] as supporting electrolyte). a) Current vs potential at different rotation rate with potential sweep of 5 mV/s; b) Levich-plot of limiting current versus square root of rotation rate.

## 2.4 Conclusions and Future Work

In this chapter, the reports of synthesis of an array of 4,4'-bipyridinium-based compounds with different substituents has been presented, coupled with investigation of their physical and electrochemical properties. The synthesis of bulky, conjugated molecules (**7** and **9**) was not successful during this work, but the results obtained indicate that the synthetic route can be optimized, and this might lead to the development of a stable, conjugated molecule for use in AORFBs as both the anolyte and catholyte material.



As hoped, all successfully synthesized viologens were soluble in aqueous electrolytes such as NaCl. Compound **1** showed the most promise for further optimization in an AORFB. The viologen's redox events are both chemically and electrochemically reversible in NaCl, at neutral pH. Furthermore, when coupled with FCN the overall system has a potential difference of 1.2 V which is comparable with current AORFB systems.<sup>9,14</sup>

From the results above, these viologens show promise for further use in varied electrochemical applications such as AORFBS (**1** & **4**), electrochromic devices (**2**), and as electrocatalysts (**5b**). Further work in this project will be focused on the optimization of use of these viologens in varied applications. This will include the optimization of testing protocol and equipment for symmetric and asymmetric AORFBS. In addition, the electrocatalytic work will focus on the use of **5a** and **5b** as a biphasic electrocatalyst with the aim to optimize a known reaction.

## 2.5 Experimental

### 2.5.1 Physical Measurements

All reagents used were purchased from several commercial suppliers and were used without further purification. <sup>1</sup>H and <sup>13</sup>C NMR (400 MHz) spectra were recorded on a Bruker AV2-400 instrument. All chemical shifts are given in ppm with respect to residual solvent peaks. Coupling constants (J values) are quoted to one decimal place with values given in Hertz (Hz). Mass spectroscopy was conducted on a MSQ Plus single quadrupole mass spectrometer. Fourier Transform Infra-Red (FTIR) spectra were recorded on an IRAffinity-1S Fourier Transform Infrared Spectrophotometer with a germanium-coated diamond tip and bands are reported in cm<sup>-1</sup>.

### 2.5.2 Electrochemical Measurements

Cyclic voltammetry experiments were carried out on a BioLogic VSP-3 potentiostat using a three-electrode system comprising a glassy carbon working electrode, a platinum wire counter electrode, and a Ag/AgCl reference electrode which was stored in 3M KCl solution. The working electrode was polished using microfibre pads by fine polishing with 6  $\mu\text{m}$  diamond polish, 1  $\mu\text{m}$  diamond polish, and 0.05  $\mu\text{m}$  alumina polish, then rinsed with deionized water and air dried before use.

CV solutions were prepared by dissolving the compound of interest (10 mg) in 0.1 M NaCl solution which was prepared in bulk. Solutions were purged using  $\text{N}_2$  gas and then CV was run at varying scan rates. Where viologen/anolyte mixed studies were performed, these were first performed on only the viologen and then, following the addition of anolyte material (FCN or TEMPO), the solution was purged again with  $\text{N}_2$  and then mixed studies run.

Rotating-disc electrode (RDE) experiments were conducted using a Metrohm Autolab RDE (AUT.RDE.S) instrument equipped with an Ultra Trace carbon working electrode, a Ag/AgCl reference electrode (pre-soaked in 3M KCl solution) and a platinum wire counter electrode. Linear sweep voltammetry (LSV) scans were recorded at a scan rate of 5  $\text{mV}\cdot\text{s}^{-1}$  from 0.0 V to -1.5 V vs. SHE, with rotational speed between 100-1500 rpm. Three scans were recorded and averaged to ensure reproducible results at each rotation rate. A Levich plot was constructed of the limited current versus the square root of the rotation speed, and the diffusion coefficient was calculated from the linear slope of the plot according to the Levich equation:  $i = 0.62nFAcD^{2/3}\nu^{-1/6}\omega^{1/2}$ , where  $n = 1$ , Faraday's constant  $F = 96485 \text{ C}\cdot\text{mol}^{-1}$ , electrode area  $A = 0.196 \text{ cm}^2$ , molar concentration  $c = 1 \times 10^{-6} \text{ mol}\cdot\text{cm}^{-3}$ , the kinematic

viscosity  $\nu = 9.56 \times 10^{-3} \text{ cm}^2 \cdot \text{s}^{-1}$  (1 M NaCl aqueous solution),  $\nu = 4.2 \times 10^{-3} \text{ cm}^2 \cdot \text{s}^{-1}$  (0.1 M [TBA][PF<sub>6</sub>] in MeCN), and D represents the diffusion coefficient.

### 2.5.3 Synthesis of 1,1'-bis(2-hydroxyethyl)-[4,4'-bipyridine]-1,1'-dium (1)

In a 100 mL flask, 4, 4'-bipyridine (2.834 g, 15 mmol) and chloroethanol (3.077 mL, 46 mmol) were dissolved in nitromethane (35 mL). The reaction mixture was refluxed at 135 °C for 72 hours. The brown precipitate obtained was vacuum filtered and washed with a solution of ethanol: methanol (1:1) and a small amount of nitromethane (15mL). The product was dried under a flow of warm air to give compound **1** as a pale brown powder. (5.83 g, yield=77.43%).

**<sup>1</sup>H NMR** (300 MHz, 298.15 K; D<sub>2</sub>O)  $\delta_{\text{H}} = 3.98$  (4H, t,  $J = 10$  Hz, CH<sub>2</sub>), 4.34 (3H, s, CH<sub>3</sub>), 8.43 (4H, d,  $J = 7$  Hz, Ar-H), 8.98 (4H, d,  $J = 7$  Hz, Ar-H) ppm.

### 2.5.4 Synthesis of 1,1'-bis(2-carboxyethyl)-[4,4'-bipyridine]-1,1'-dium (2)

4, 4'-bipyridine (0.14 g, 0.896 mmol) was dissolved in chloroform (12 mL). Acrylic acid (0.92mL, 0.0134 mol) was added to the reaction mixture which was then left to stir at room temperature for 24 hours. A mixture of acetone:hydrochloric acid (2 M) (6:1) was added to the mixture. The resulting precipitate was then filtered and washed with acetone (15 mL) and methanol (15 mL) and dried to give compound **2** as a white powder (0.15 g, yield=56 %). **<sup>1</sup>H NMR** (300 MHz, 298.15 K; D<sub>2</sub>O)  $\delta_{\text{H}} = 3.10$  (4H, t,  $J = 12$  Hz, CH<sub>2</sub>), 4.88 (4H, t,  $J = 12$  Hz, CH<sub>2</sub>), 8.43 (4H, d,  $J = 7$  Hz, Ar-H), 9.08 (4H, d,  $J = 7$  Hz, Ar-H) ppm.

### 2.5.5 Synthesis of 3,3'-([4,4'-bipyridine]-1,1'-diium-1,1'-diyl)bis(propane-1-sulfonate) (4)

In a 100 mL flask, 4, 4'-bipyridine (0.254 g, 1.6 mmol) was dissolved in toluene (20 mL) and stirred for 5 minutes under N<sub>2</sub>. Propyl sultone (0.5 mL, 4.8 mmol) was added to the mixture which was then stirred at 105 °C for 36 hours. Resultant white precipitate was vacuum filtered and washed with acetonitrile (50 mL). The product was dried under a flow of warm air to give compound **4** as a white powder (0.57 g, yield=89.4%). **<sup>1</sup>H NMR** (300 MHz, 298.15 K; D<sub>2</sub>O) δ<sub>H</sub> = 2.46 (4H, t, *J* = 7.3 Hz, 7.3 Hz, CH<sub>2</sub>), 2.96 (4H, t, *J* = 7.2 Hz, 7.2 Hz, CH<sub>2</sub>), 4.82 (4H, t, *J* = 7.4 Hz, 7.4 Hz, CH<sub>2</sub>), 8.5 (4H, d, *J* = 6.8 Hz, Ar-H), 9.08 (4H, d, *J* = 6.8 Hz, Ar-H) ppm.

### 2.5.6 Synthesis of 1,1'-dibutyl-[4,4'-bipyridine]-1,1'-diium (5)

4,4'-bipyridine (3.00 g, 0.020 mol) was dissolved in acetonitrile (20 mL). Butyl Halide (0.08 mol) was added to the reaction mixture, which was then left to stir, under reflux at 95 °C, for 24 hours. The reaction mixture was filtered, and resultant precipitate was washed with acetonitrile (50 mL), then dried to give a solid. Spectral data were consistent with literature values.<sup>18,24</sup>

#### 2.5.6.1 Preparation of 5a:

Prepared by general procedure A, yield = 1.15 g, 2.19 mmol, 73 %. The final dried product obtained was a reddish-orange powder, compound **5a**. NMR was found to match previously published values.<sup>24</sup> **<sup>1</sup>H NMR** (300 MHz, 298.15 K; D<sub>2</sub>O) δ<sub>H</sub> = 0.95 (6H, t, *J* = 7.4 Hz, CH<sub>3</sub>), 1.37 - 1.43 (4H, m, CH<sub>2</sub>), 2.02 - 2.09 (4H, m, CH<sub>2</sub>), 4.71-4.73 (4H, m, CH<sub>2</sub>), 8.52 (4H, dd, *J* = 6.8 Hz, Ar-H) ppm, 9.08 (4H, d, *J* = 7 Hz, Ar-H) ppm.

#### 2.5.7.2 Preparation of 5b:

Prepared by general procedure A, yield = 6.74 g, 16 mmol, 83 %. The final dried product obtained was a yellow powder, compound **5b**. NMR was found to match previously published values.<sup>24</sup> **<sup>1</sup>H NMR** (300 MHz, 298.15 K; D<sub>2</sub>O)  $\delta_{\text{H}}$  = 0.95 (6H, t,  $J$  = 7.4 Hz, CH<sub>3</sub>), 1.38 (4H, m, CH<sub>2</sub>), 2.05 (4H, m, CH<sub>2</sub>), 4.71 (4H, m, CH<sub>2</sub>), 8.52 (4H, dd,  $J$  = 6.8 Hz, Ar-H) ppm, 9.08 (4H, d,  $J$  = 7 Hz, Ar-H) ppm.

#### 2.5.7.2 Preparation of 5c:

Prepared by general procedure A but was carried out in a microwave rather than by reflux. The final dried product was not the desired compound.

#### 2.5.7 Synthesis of 1,1'-bis(2-carbonylethyl-TEMPO)-[4,4'-bipyridine]-1,1'-dium (7)

Compound **2** (0.202 g, 0.72 mmol) was added to an N<sub>2</sub> purged flask, 10 mL of dry THF was added to the flask. Oxalyl chloride (0.16 mL, 1.866 mmol) was dissolved in 10 mL of dry THF. The mixture containing viologen was cooled to 0 °C, thereafter the solution containing oxalyl chloride was added dropwise under N<sub>2</sub> with constant stirring. A drop of DMF was added to the reaction mixture whilst at 0 °C. The reaction was left to proceed for 24h and allowed to warm to ambient temperature. A pale yellow powder was isolated, **6**. **<sup>1</sup>H NMR** (300 MHz, 298.15 K; D<sub>2</sub>O)  $\delta_{\text{H}}$  = 3.14 (4H, t,  $J$  = 6 Hz, CH<sub>2</sub>), 4.92 (4H, m, CH<sub>2</sub>), 8.48 (4H, d,  $J$  = 7 Hz, Ar-H), 9.12 (4H, d,  $J$  = 7 Hz, Ar-H) ppm. FTIR:  $\tilde{\nu}_{\text{max}}$  = 2837.29, 1722.43, 1193.94, 1177, 856, 827, 815 cm<sup>-1</sup>.

Compound **6** (0.101 g, 0.295 mmol) was dissolved in 10 mL dry THF and N<sub>2</sub> was passed over the solution. Thereafter 4-amino,2,2,6,6-tetramethylpiperidinoxy free radical (0.201 g, 1.18 mmol) was added to the solution in a single portion. The reaction proceeded under inert conditions at room temperature for 24h.

The precipitate isolated by filtration and washed with diethyl ether (20 mL) giving the putative final product, **7**, as a peach powder (0.02 g, yield=11 %). **<sup>1</sup>H NMR** (300 MHz; D<sub>2</sub>O)  $\delta_{\text{H}}$  = 1.10 (24H, s, CH<sub>3</sub>), 1.73-1.48 (8H, m, CH<sub>2</sub>), 2.89 (4H, t,  $J$  = 6 Hz, CH<sub>2</sub>), 8.43 (4H, d,  $J$  = 7 Hz, Ar-H), 9.00 (4H, d,  $J$  = 7 Hz, Ar-H) ppm. FTIR:  $\tilde{\nu}_{\text{max}}$  = 3358.07, 3057, 3003, 2976, 1752, 1636, 1570 cm<sup>-1</sup>.

### 2.5.8 Synthesis of 6-bromohexanoic-TEMPO derivative (**8**)

In a 100 mL flask, 6-bromohexanoic acid (0.522 g, 2.68 mmol) was dissolved in dimethylformamide (30 mL) and cooled to 0 °C. *N, N'*-Diisopropylethylamine (1.33 mL, 7.68 mmol) and 4-amino-TEMPO (0.45 g, 2.62 mmol) were added to the reaction mixture. After an additional 10 minutes of stirring, HATU (0.963 g, 4.09 mmol) was added and the reaction mixture then warmed to room temperature; the mixture was stirred for a further 9h. Ethyl acetate (25 mL) was added to the reaction mixture which was then washed with aqueous NaHCO<sub>3</sub> (20 mL), brine (20 mL), and finally water (3x 60 mL). The solution was concentrated to remove excess solvent to give a yellow "sludge." (Mass was not accurately determined but estimated to be 0.3 g) Interpretation of the <sup>1</sup>H NMR was attempted, however, due to paramagnetic peak broadening, peak assignment was not possible. Due to the paramagnetic nature of the compound <sup>1</sup>H NMR was difficult to interpret. HRMS *m/z* (ESI+) Found 347.13 and 349.13 [M + Br]<sup>+</sup>, C<sub>15</sub>H<sub>28</sub>BrN<sub>2</sub>O<sub>2</sub> requires 347.13, 349.13 and 348.14.

### 2.5.9 Synthesis of 1,1'-bis(2-carboxypentyl-TEMPO)-[4,4'-bipyridine]-1,1'-dium (**9**)

Compound **8** (~0.3 g, 0.86 mmol) was dissolved in ethanol (7mL) and the flask was purged with N<sub>2</sub>. 4, 4'-bipyridine (0.05 g, 0.29 mmol) was added to the solution. The mixture was stirred at 80 °C under reflux under N<sub>2</sub> for 24h. The mixture was then concentrated, and the red-orange residue (compound **9**) obtained was washed with hexane (10 mL) and diethyl

ether (3x 30 mL). Due to the paramagnetic nature of the compound, the  $^1\text{H}$  NMR was difficult to interpret, and it was suspected that the addition of hydrazine hydrate reduced the viologen. Hydrazine hydrate - added to NMR sample to reduce TEMPO to TEMPOL in order to obtain a clean diamagnetic spectrum.

## 2.6 References

- 1 J. Ding, C. Zheng, L. Wang, C. Lu, B. Zhang, Y. Chen, M. Li, G. Zhai and X. Zhuang, *J. Mater. Chem. A*, 2019, **7**, 23337–23360.
- 2 J. Winsberg, T. Hagemann, T. Janoschka, M. D. Hager and U. S. Schubert, *Angew. Chemie - Int. Ed.*, 2017, **56**, 686–711.
- 3 M. H. Chakrabarti, R. A. W. Dryfe and E. P. L. Roberts, *J. Chem. Soc. Pakistan*, 2007, **29**, 294–300.
- 4 E. S. Beh, D. De Porcellinis, R. L. Gracia, K. T. Xia, R. G. Gordon and M. J. Aziz, *ACS Energy Lett.*, 2017, **2**, 639–644.
- 5 C. Debruler, B. Hu, J. Moss, J. Luo and T. L. Liu, *ACS Energy Lett.*, 2018, **3**, 663–668.
- 6 Y. Liu, M. A. Goulet, L. Tong, Y. Liu, Y. Ji, L. Wu, R. G. Gordon, M. J. Aziz, Z. Yang and T. Xu, *Chem*, 2019, **5**, 1861–1870.
- 7 B. Hu, Y. Tang, J. Luo, G. Grove, Y. Guo and T. L. Liu, *Chem. Commun.*, 2018, **54**, 6871–6874.
- 8 S. Liu, M. Zhou, T. Ma, J. Liu, Q. Zhang, Z. Tao and J. Liang, *Chinese Chem. Lett.*, 2020, **31**, 1690–1693.
- 9 Y. Liu, Y. Li, P. Zuo, Q. Chen, G. Tang, P. Sun, Z. Yang and T. Xu, *ChemSusChem*, 2020, **13**, 2245–2249.
- 10 B. Hu, C. DeBruler, Z. Rhodes and T. L. Liu, *J. Am. Chem. Soc.*, 2017, **139**, 1207–1214.
- 11 H. Ohno and H. Satoh, *J. Electroanal. Chem.*, 1993, **360**, 27–37.
- 12 S. Zhang, X. Li and D. Chu, *Electrochim. Acta*, 2016, **190**, 737–743.
- 13 D. Zhang, Q. Liu and Y. Li, *Design of flow battery*, Elsevier B.V., 2014.
- 14 W. Liu, Y. Liu, H. Zhang, C. Xie, L. Shi, Y. G. Zhou and X. Li, *Chem. Commun.*, 2019, **55**, 4801–4804.
- 15 T. Liu, X. Wei, Z. Nie, V. Sprenkle and W. Wang, *Adv. Energy Mater.*, 2016, **6**, 1501449.
- 16 T. Janoschka, N. Martin, M. D. Hager and U. S. Schubert, *Angew. Chemie - Int. Ed.*, 2016, **55**, 14427–14430.
- 17 Z. Yan, R. J. Wycisk, A. S. Metlay, L. Xiao, Y. Yoon, P. N. Pintauro and T. E. Mallouk, *ACS Cent. Sci.*, 2021, **7**, 1028–1035.
- 18 M. O. Liu, I. M. Chen and J. L. Lin, *Mater. Lett.*, 2007, **61**, 5227–5231.
- 19 T. Janoschka, C. Friebe, M. D. Hager, N. Martin and U. S. Schubert, *ChemistryOpen*, 2017, **6**, 216–220.
- 20 T. Hagemann, J. Winsberg, M. Grube, I. Nischang, T. Janoschka, N. Martin, M. D. Hager and U. S. Schubert, *J. Power Sources*, 2018, **378**, 546–554.

| Chapter 2 : Viologen Synthesis & Characterization

- 21 T. Janoschka, N. Martin, U. Martin, C. Friebe, S. Morgenstern, H. Hiller, M. D. Hager and U. S. Schubert, *Nature*, 2015, **527**, 78–81.
- 22 E. Valeur and M. Bradley, *Chem. Soc. Rev.*, 2009, **38**, 606–631.
- 23 N. Elgrishi, K. J. Rountree, B. D. McCarthy, E. S. Rountree, T. T. Eisenhart and J. L. Dempsey, *J. Chem. Educ.*, 2018, **95**, 197–206.
- 24 D. Zhang, L. Hou, Q. Zhang, J. He, H. Feng, F. Würthner, X. Yang and B. Wu, *Chem. Eur. J.*, 2020, **26**, 1414–1421



## CHAPTER 3

### OPTIMIZATION OF TESTING RIG FOR AORFBS

---

*"... Your heavenly Father knows you have need for all of these things."*

*Matthew 6:32b*

### 3.1 Introduction

Great strides have been made to implement the use of RFBs into large-scale applications.<sup>1</sup>

In general, these RFBs are able to provide stored energy and could therefore offer the following support: uninterruptible power supply in case of main power failure; support systems for renewable energy installations such as wind and solar; and providing load levelling function to store surplus energy during non-peak times.<sup>2</sup>

China has aggressively addressed the issue of energy storage through projects like the “Hubei Zaoyang project” launched by the China National and Development Reform Commission (NRDC). In 2019, the Hubei project went online, and this saw VRBs with energy capacities of 3 MW/12MWh being integrated into the Chinese grid-system.<sup>3</sup> As of September 2022, Rongke Power in Dalian, China, is home to the world's biggest flow battery - a vanadium flow battery with a current capacity of 100 MW/400 MWh which will eventually be expanded to 200 MW/800 MWh.<sup>4</sup> The overarching aim of this project is to perform peak-shaving by supplying stored energy during peak demand times, and off-setting the variability caused by the wind and solar energy supply in Dalian. The station's VRFBs will be charged by the solar and wind systems to store chemical energy and then at peak grid load the chemical energy will be converted into electrical energy and transmitted to consumers through Dalian's power grid.

In 2023, the need for energy storage is undeniable and Bloomberg NEF forecasts that an additional 28 GW station energy storage installations will be developed by the end of 2023, and despite the rising costs of raw materials and components throughout 2022, the energy storage market is predicted to double by the end of 2023.<sup>5</sup>

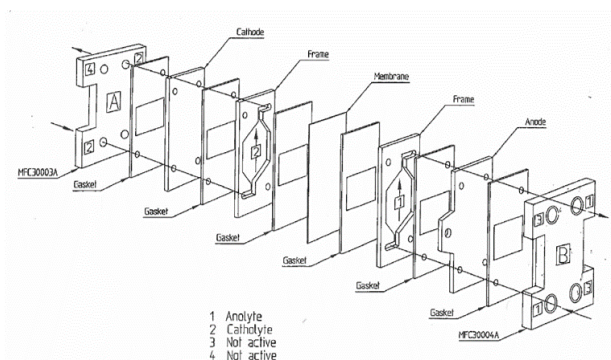
There has been limited material published in the academic literature on the principles of electrochemical engineering for these systems, particularly the use of specific materials for the design of a lab-scale testing rig. This inconsistency may lead to further issues such as unsuccessful scale-up of the technology, low-efficiency of the system, and costly manufacturing.<sup>6</sup> Cell-design, electrode structure, reaction environment, and operating conditions are all crucial parameters which must also be considered when focusing on the development of a sustainable RFB.

Given the overarching aim of RFBs is to enhance sustainability initiatives and improve our dependence on green energy, careful consideration must then be taken into the design of said energy storage system. When looking at the “Twelve Principles for Green Energy Storage in Grid Applications” it is clear that design of energy storage systems plays a crucial role in ensuring that future technology has a long-lasting positive impact on the environment.<sup>7</sup> In particular, “Principle #11 Minimize the Environmental Impact Per Unit of Energy Service for Material Production and Processing” is relevant given the negative environmental burden associated with the processing of vanadium, in particular, vanadium redox flow batteries (VRFBs).

### **3.1.1 Engineering aspects of RFBs**

Of research done over the last three decades involving the development of RFBs, most research has been focused on optimizing the redox active agents used in these RFBs to improve their performance. Information regarding the testing protocol of these lab-scale RFBs is scarce. It is important to note the differences between large-scale RFBs and their lab-based counterparts which are used for research and testing purposes. For research purposes, a lab-scale single unit cell is often used for testing.

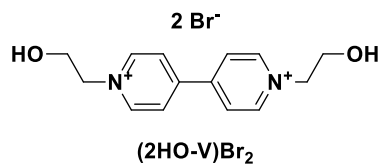
To upscale, e.g. in grid scale applications, several (larger) unit cells are connected in a filter-press reactor orientation to form a stack.<sup>6</sup> The performance of these unit cells such as the rate of redox reactions (charging or discharging), and the stack voltage is thus governed by principles of electrochemical engineering.



**Figure 3.1** Figure of lab-scale flow cell assembly obtained from user manual.

### 3.1.2 Viologens in Organic Redox Flow Batteries (ORFBs)

In early 2019, Liu *et al.*<sup>8</sup> reported a RFB system with a stable neutral hydroxy-substituted viologen anode coupled to  $\text{Br}_2$  at the cathode: the hydroxyl substituted viologen gave a significant increase in solubility to all redox states of the viologen. On the positive side, the  $\text{Br}^-/\text{Br}_2$  redox couple was used due to the high solubility of  $\text{Br}^-$  and  $\text{Br}_3^-$ , as well as the exceptional electrochemical properties such as high redox potential.<sup>8</sup>

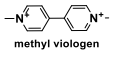
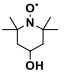
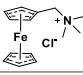
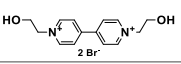
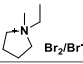
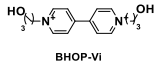
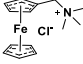
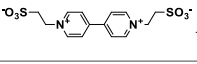
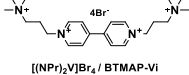
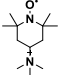
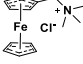
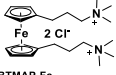
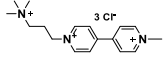
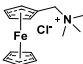


**Figure 3.2** Structure of neutral viologen used the work of Liu *et al.*<sup>8</sup>

The battery exhibited high energy density of 95.1 Wh/L, and energy efficiency of 83.4%, observed at a current density of 40 mA/cm<sup>2</sup>. The group reported that the use of a complexing agent, 1-ethyl-1-methylpyrrolidinium bromide [MEP]Br prevented the precipitation of Br<sub>2</sub> by forming water soluble [MEP]-Br<sub>3</sub> which allowed the use of a porous polyolefin membrane with high conductivity rather than the use of a more expensive, selective, ion exchange membrane.<sup>8</sup>

Motivated by the molecules in **Table 3.1** we were inspired to consider the development of symmetrical RFB systems and redox-active compounds suitable for long-term use in RFBs. These compounds should ideally be water-soluble, bulky enough to prevent crossover within the system, and exhibit long-term stability over many cycles with minimal capacity losses. Given the toxicity of bromine, and the need for additives to prevent Br<sub>2</sub> deposition from solution, we considered ways to develop a similar system without the use of toxic compounds. We hypothesized that the development of a relatively bulky, symmetrical, water soluble viologen would mitigate issues such as crossover and insolubility issues often experienced with AORFBs.<sup>8</sup>

**Table 3.1** Viologen derivatives and corresponding positive couples used in AORFBs.

| Neg. couple<br>(Viologen Derivatives)   | Pos. couple   | Conc.<br>(M) | Cell potential<br>(V) | Capacity Fade rate             |         | Year |
|---|---|--------------|-----------------------|--------------------------------|---------|------|
|   |   |              |                       | %/cycle                        | % / day |      |
| <br>methyl viologen  | <br>4-OH TEMPO                       | 0.5          | 1.25                  | 0.1 % /cycle<br>27.5 % /day    |         | 2015 |
|   |                                      | 0.5          | 1.05                  | 0.01 % /cycle<br>0.22 % /day   |         | 2017 |
| <br>2 Br <sup>-</sup>  | <br>Br <sub>2</sub> /Br <sup>-</sup> | 0.5          |                       | -                              |         | 2019 |
| <br>BHOP-VI  |                                      | 2.0          | 1.02                  | 0.055 % /cycle<br>2.82 % /day  |         | 2020 |
| <br>SO <sub>3</sub> <sup>-</sup>   | I <sub>3</sub> /I <sup>-</sup>  | 0.5          | 1.0                   | 0.01 % /cycle<br>0.45 % /day   |         | 2018 |
|   | K <sub>4</sub> [Fe(CN) <sub>6</sub> ]   | 0.1          | 1.6                   | -                              |         | 2021 |
| <br>4Br <sup>-</sup><br>[(NPr) <sub>2</sub> V]Br <sub>4</sub> / BTMAP-VI |                                      | 0.5          | 1.38                  | 0.005 % /cycle<br>0.2 % /day   |         | 2018 |
|   |                                    | 0.5          | 1.32                  | 0.01 % /cycle<br>0.5 % /day    |         | 2017 |
|   | <br>BTMAP-Fc                       | 1.3          | 0.75                  | 0.0057 % /cycle<br>0.01 % /day |         | 2017 |
| <br>3 Cl <sup>-</sup><br>[(Me)(NPr)V]Cl <sub>3</sub>                   |                                    | 0.5          | 1.38                  | 0.18 % /cycle<br>0.88 % /day   |         | 2017 |

A stable testing rig was necessary to evaluate the compounds and conditions for such a system, but no such equipment existed within the department. As such, the focus of the work was developing a sturdy and reliable lab-scale testing rig, using as the redox active agents the viologens discussed in the previous chapter ([Chapter 2](#)). These viologens were chosen due to their physical and electrochemical properties including good solubility in aqueous electrolytes, chemical and electrochemical stability and reversibility, and favourable redox potential window, which make them suitable for AORFB application.

### 3.2 Testing Rig Development

Initial lab-scale RFB tests were performed using compound **1** given its high solubility in aqueous electrolytes, and its electrochemical and chemical reversibility and stability. Based on CV analysis of **1** with FCN, the potential difference between the two couples was found to be 1.2 V, comparable with current AORFBs.<sup>8</sup> Unless otherwise stated, flow cells discussed in this chapter were operated using **1** as the negative couple, and FCN as the positive couple.

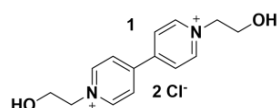


**Figure 3.3** Structure of compound **1**.

#### 3.2.1 $\alpha$ -generation RFB design

The “ $\alpha$ -generation” of the RFB battery design employed the use of a standard lab based microflow cell, sourced from ElectroCell, Denmark, which was used without any further modifications. This design had been used by previous members of the Murray research group for lab scale flow cell testing for energy storage systems. In this design, Masterflex® transfer tubing was used to carry the electrolytes, whilst 100 mL conical flasks, sealed with rubber septa were used as reservoirs. The return (inlet) channel for electrolytes was provided by 21G stainless steel needles, whilst the outlet channel, which carried electrolyte from the flow cell to the electrolyte reservoir, was terminated by a thicker 18G needle.

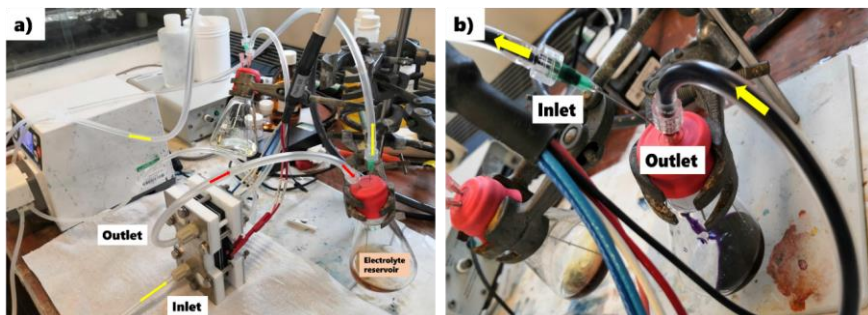


**Figure 3.4** a)  $\alpha$ -generation RFB design using needles for inlet and outlet from electrolyte reservoir. b) Close-up of  $\alpha$ -generation design. Direction of electrolyte flow indicated by yellow arrows.

At this stage, no static tests were run to confirm the flow rate of the peristaltic pump with the  $\alpha$ -generation transfer and peristaltic tubing configuration which had been established by former members of the Murray research group. For this design, the flow rate was maintained at  $30 \text{ mL}\cdot\text{min}^{-1}$  for all experiments. At the outset, this design seemed to be functional as the electrolyte was cycled between the reservoir and the flow cell with ease, and the rubber septa allowed easy purging of the system to place it under an inert atmosphere. However, after multiple runs and upon further investigation, it became apparent that there were several problematic design features .

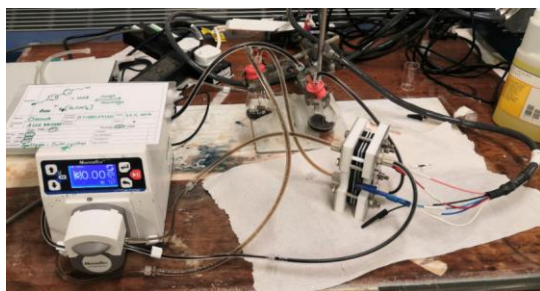


**Figure 3.5** Overall set-up of RFB including the peristaltic pump.



Some of the initial problems observed were as follows: the length of tubing used was excessive; leaking of electrolyte at flow cell joints; leaking of electrolyte at tubing joints; and blockage of tubing and/or needles. The current transfer tubing in use was clear C-flex tubing with an inner diameter of 0.125", outer diameter of 0.25" and a maximum flow rate of 480 mL.min<sup>-1</sup>. The corresponding peristaltic tubing used was Masterflex® peroxide-cured silicone tubing which had an inner diameter of 0.063" and maximum flow rate of 130 mL.min<sup>-1</sup>. The use of excessively long transfer tubing meant that large volumes of electrolyte were required for use to both fill the tubes and cell and ensure sufficient residual volume in the reservoir to avoid air locks. Large volumes of electrolyte correlate directly to larger quantities of redox active agents for a given concentration which ultimately translates to higher overall costs to testing due to the cost of starting materials and solvents, as well as time required to synthesise sufficient quantities of electrolyte.

On several occasions, leaking was observed at the joints between the transfer tubing and peristaltic tubing, as well as the inlet and outlet joints for the flow cell. In the case of the tubing joints, this was due to formation of hairline cracks in these joints which would worsen over the course of the experiments. However, the main flaw identified in this design was the use of needles to connect the electrolyte reservoir and flow cell. Every time the system was run, precipitation around the needles and within the needles was observed which led to further blockages in the transfer and peristaltic tubing and then had a knock-on effect on the flow of the electrolyte. It was suspected that this was due to the limited solubility of [1]<sup>+</sup> which was exacerbated by the use of needles.



**Figure 3.6** Blockage of tubing fitting due to precipitation.

**Figure 3.6** clearly shows the solid within the fitting connecting the transfer tubing to the peristaltic tubing. There is also some precipitation on the exterior of the fitting, as highlighted by the yellow arrow on the figure, likely due to a hairline crack in the fitting allowing some of the electrolyte to leak out and eventually precipitate. The reason for the frequency of cracks in these fittings is unknown, but it was decided that these should be replaced with other fittings for further tests.

#### ***Pre-liminary flow cell results***

Preliminary studies were conducted using this design and the data for the “best” run is shown below. To evaluate the flow cell performance of **1**, a symmetrical flow cell was set-up with **1** (0.1 M) as the negative couple, FCN (0.2 M) as the positive couple, and 1.0 M NaCl was used as the supporting electrolyte which was cycled through the system at  $30 \text{ mL}\cdot\text{min}^{-1}$ . The flow cell was constructed using a fumasep® FAA-3-PE-30 anion exchange membrane (AEM) which was used without any pre-treatment, and the cell was run between 0.1- 2.0 V at a current density of 20 mA. **Figure 3.7** shows voltage profiles of the charging/discharging process and there’s clear evidence of substantial capacity fade was observed during the 4.7 hours (20 cycles) of operation.

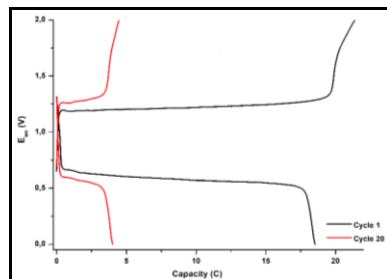


**Figure 3.7** Voltage profile of 1st and 20th cycle of **1** and FCN (electrolyte: 1 M NaCl).

The system stopped running due to precipitation issues with solid observed within the fittings of the tubing, and aggregation visible at both inlets. The maximum charge capacity recorded was 21.3 C with a corresponding discharge capacity of 18.5 C, and over 20 cycles there was total loss of 14.5 C over the course of this run. The expected theoretical capacity, as per **equation 1.12**, for this system is 111 C, and it is clear that these results are both much lower than expected and additionally, inferior to those previously published on a similar viologen system.<sup>8</sup> Given the extent of precipitation observed during this flow cell test, it was concluded that the loss of redox active material was the primary factor for the low capacity obtained. However, these preliminary results confirmed that the system showed some promise for further development as a symmetrical AORFB.

#### **Zwitterionic Preliminary RFB test**

The zwitterionic viologen, **2**, was investigated to further explore the application of viologens containing water-soluble groups. Inspired by the work of Liu and co-workers,<sup>9</sup> this zwitterionic viologen was synthesized because it would have an anionic charged redox state with substantial hydrogen bonding capacity which would ensure high water solubility which is desirable.

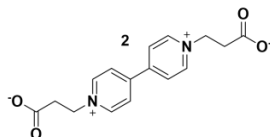


**Figure 3.8** Structure of **2**.

Given the promising initial electrochemical data obtained from CV studies, **2**, was studied in both symmetrical and asymmetrical set-ups in the flow cell, using 1M NaCl supporting electrolyte and FCN as the catholyte. Both cases exhibited issues with precipitation and aggregation due to the poor solubility of the carboxy viologen above 6 mM. Additionally, it was observed that the addition of FCN to a stirred solution of **2** in NaCl resulted in the formation of a precipitate which made an asymmetrical set-up more favourable than a symmetrical one to avoid the formation of precipitate between both species.

To mitigate the solubility issue, solutions containing **2** were heated to 40 °C before being circulated through the flow cell in the expectation that the poor solubility was a kinetic artefact of dissolution rates. This was successful whilst the solution remained warm, but upon cooling it was found that the viologen would precipitate from solution and aggregation was observed in the tubing of the flow cell.

The flow cell was run for 20 cycles at a flow rate of 30 ml.min<sup>-1</sup> with a fumasep® F-930 PFSA cation exchange membrane (CEM), with **Figure 3.9** showing the voltage profiles of the charging/discharging process and the successful operation of the asymmetric cell between 0.1 and 2.0 V at a current density of 2 mA/cm<sup>2</sup>. Electrolyte degradation and loss of capacity were observed over the duration of the study, and these are mainly attributed to issues with precipitation, ultimately limiting the system to a total run time of 3 hours and 39 minutes.

The system was able to reach a maximum charge capacity of 110.6 C but only discharged to 37.95 C in the first cycle, and the capacity faded by 21.25 C to result in a final discharge capacity of 16.8 C. Given that the theoretical capacity for this system is ~111 C, it is evident that this system performed quite poorly.

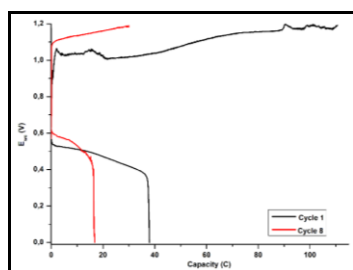
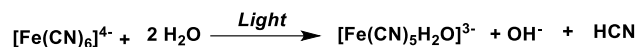


**Figure 3.9** Voltage profile of 1st and 8th cycle of 2 and FCN (electrolyte: 1M NaCl).

Ferro/ferricyanide mixtures are considered to be stable and as such are commonly used in RFBs, but there has been extensive research by several groups<sup>10-12</sup> concerning the stability of ferrocyanide electrolytes. Reber *et al.*<sup>10</sup> evaluated the effect of light and air exposure on different ferrocyanides with sodium, potassium, ammonium, or lithium cations. The group reaffirmed former reports on the photolysis of ferrocyanide, and additionally reported a larger pH increase, stronger yellow discoloration, and more pronounced formation of the oxidized anion in comparison to samples stored in the dark. Subsequently, samples that were stored in the dark showed a smaller pH change, and less discoloration which indicates a higher stability of ferrocyanide at near-neutral pH when stored in the dark is in accordance with the work of the Aziz group.<sup>13</sup> It is also known that the ferro/ferricyanide couple may undergo degradation over the course of cycling which can lead to the formation of Prussian Blue, a polymeric mixed valence Fe<sup>II</sup>/Fe<sup>III</sup> compound.<sup>12</sup>



**Scheme 3.1** Mechanism of photolysis as described by Reber *et al.*<sup>10</sup>

Based on the literature,<sup>10,11</sup> it is postulated that the formation of Prussian Blue is observed due to the loss of cyanide ligands driven by an excess of  $\text{OH}^-$  ions which may lead to irreversible electrolyte chemical decomposition. Since Prussian blue has low solubility in aqueous solutions, this may have contributed to the precipitation issues observed.



**Scheme 3.2** Formation of insoluble Prussian Blue.<sup>10</sup>

### 3.2.2 $\beta$ -generation RFB design

Given these observations, the system was redesigned to eliminate the use of needles and complex fittings. It was hoped that by removing these points of failure that the electrolyte could be circulated more easily throughout the system with few to no issues of impeded flow due to precipitation. To replace the needles, a new electrolyte reservoir design was required, and in this case 15 mL falcon tubes were chosen as the electrolyte reservoirs.

Transfer tube fittings were attached to the bottom of the falcon tube to enable a secure connection to transfer tubing and sealed in place using several layers of epoxy resin glue to serve as the outlet channels, carrying the electrolyte to the flow cell. An inlet hole was drilled approximately 1.5 cm from the top of the falcon tube and a second fitting sealed in place in the same way, allowing transfer tubing to be fastened securely to the reservoir.

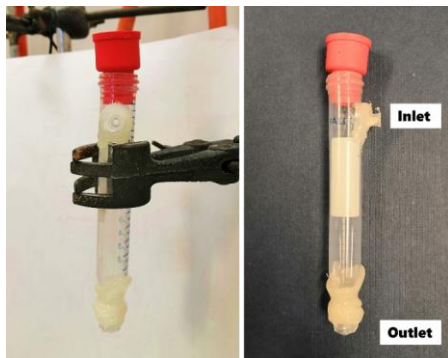


**Figure 3.10** The  $\beta$ -Generation design for the electrolyte reservoir.

A benefit of this design was that the lids of the falcon tubes could easily be replaced with an appropriately sized septum to facilitate low effort purging of the electrolyte liquid using a  $N_2$  filled balloon. Additionally, the compact electrolyte tank reduced the amount of air, and thus oxygen, present in the electrolyte reservoir during cell assembly, ensuring that purging of the electrolyte was more efficient and rapid. At this time, no other features of the design such as tubing, pump, or membrane were changed.

Using the new  $\beta$ -Generation flow cell design, further flow cell testing was conducted using similar parameters as to those previously used; a 1:2 ratio between **1** and FCN, 1.0 M NaCl as supporting electrolyte, the same AEM, and a symmetrical cell configuration. The flow rate was increased from  $30 \text{ mL}\cdot\text{min}^{-1}$  to  $42 \text{ mL}\cdot\text{min}^{-1}$  to mitigate the issue of aggregation by minimizing the time available for any solids to remain at the interfaces such as the inlet and outlet fittings and the membrane: carbon-felt interface.

**Table 3.2** Parameters used for flow cell testing.<sup>a</sup>

|                  | Concentration<br>(mol.dm <sup>-3</sup> ) |       |        | Current (mA) |           | Voltage<br>Cut-Off<br>(V) | Theoretical<br>Capacity<br>(C) | Max.<br>Discharge<br>Capacity<br>(C) |
|------------------|--|-------|--------|--------------|-----------|---------------------------|--------------------------------|--------------------------------------|
|                  | [1]                                      | [FCN] | [NaCl] | Charge       | Discharge |                           |                                |                                      |
| β1               | 0.1                                      | 0.2   | 1.0    | 40           | 20        | -                         | 231.56                         |                                      |
| β2               | 0.1                                      | 0.2   | 1.0    | 20           | 20        | -                         | 231.56                         | 187.6                                |
| β3               | 0.1                                      | 0.2   | 1.0    | 20           | 20        | 1.4                       | 231.56                         | 75.04                                |
| β4               | 0.175                                    | 0.35  | 1.0    | 20           | 20        | 1.4                       | 211                            | 121                                  |
| β4 <sup>b</sup>  | 0.175                                    | 0.35  | 1.0    | 80           | 20        | 1.4;<br>1.55;<br>1.65     | 211                            | 175.4                                |
| β5               | 0.175                                    | 0.35  | 1.0    | 60           | 30        | 1.65; 1.3                 | 211                            | 146.31                               |
| β5a <sup>c</sup> | 0.175                                    | 0.35  | 1.0    | 70           | 30        | 1.30                      | 211                            | 39.4                                 |
| β6               | 0.2                                      | 0.4   | 1.5    | 60           | 30        | 1.4                       | 241.21                         | -                                    |
| β6a <sup>c</sup> | 0.2                                      | 0.4   | 1.5    | 80           | 40        | 1.3                       | 241.21                         | 140                                  |
| β7               | 0.175                                    | 0.35  | 1.5    | 80           | 20        | 1.4;<br>1.55              | 211                            | 136.4                                |
| β7a <sup>c</sup> | 0.175                                    | 0.35  | 1.5    | 80           | 40        | 1.65                      | 211                            | 57                                   |

<sup>a</sup>All runs were completed with a symmetrical configuration with a flow rate of 42 mL.min<sup>-1</sup>; <sup>b</sup>Voltage cut-off reset multiple times within the same run to prevent aggregation caused due to irreversible redox event ;

<sup>c</sup>Runs restarted due to system dying and/or technical issues



An initial flow cell-test (**Run  $\beta$ 1**) was set up replicating the conditions of the best run from the  $\alpha$ -generation design to compare the efficacy of the  $\beta$ -generation design. **Figure 3.11** shows the charge and discharge profiles for **Run  $\beta$ 1** wherein the system was charged at 40 mA and discharged at 20 mA without a voltage cut-off.

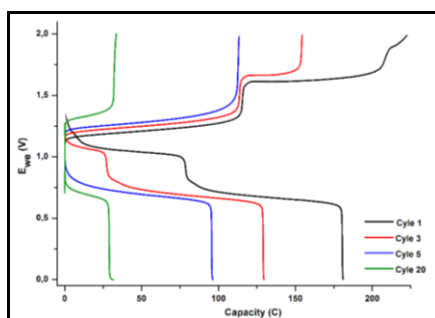


**Figure 3.11** Galvanostatic cycling of **Run  $\beta$ 1** containing: 0.1 M **1** and 0.2 M FCN in 1 M NaCl as anolyte (15 mL) and catholyte (15 mL).

As evidenced by the two distinct charge/discharge plateaus seen in **Figure 3.11** for the first 4 cycles, the system proceeded to the 2<sup>nd</sup> electron reduction of **1** for both the charge and discharge. However, from cycle 5 onwards, only the 1<sup>st</sup> electron reduction was utilized in both the charge and discharge cycles which correlates to the single plateau observed. Given that there was no voltage cut-off set for this system, the transition from a 2e<sup>-</sup> reduction to a 1e<sup>-</sup> may be attributed to a change in the chemical composition of the electrolyte which only allowed access to the first electron reduction. Furthermore, there appeared to be a large decrease in capacity observed between the 1<sup>st</sup> and 2<sup>nd</sup> charge cycle. Prolonged cycling of the battery improved the coulombic efficiency from 68 % to 95 %, observed between cycle 3 and cycle 5, nevertheless, the observed capacity for the highest discharge cycle was only 180C, 51 C lower than the theoretical capacity.

Given the disparities in the charge cycles, the subsequent [Run  \$\beta 2\$](#)  was set up with similar conditions except for the charging current which was set lower at 20 mA. It is well known that the kinetics of redox processes are crucial for optimum battery performance because slow diffusion of the redox active agents in use could restrict the potential current density thus requiring larger overpotentials.<sup>14</sup> Given the possible solubility variations for the different redox states of **1**, a lower charging current would therefore accommodate for the slower redox kinetics, allowing better interaction between the species in solution and the surface of the electrode. As seen in **Run  $\beta 1$** , the system underwent a  $2e^-$  reduction during the 1<sup>st</sup> four cycles, discharging to a maximum value of 231.56 C.

These results (Run  $\beta 1$  &  $\beta 2$ ) gave insight into the overall stability of the system, revealing that in the absence of a voltage cut-off the system would continue to charge and discharge in an unbalanced manner, leading to rapid electrolyte degradation, capacity fade, and eventual cell death.

The significant loss of capacity over time may be due to the limited solubility of the neutral form of the viologen arising from the second reduction resulting in a loss of active material in the system and creating an imbalance in the internal charge of the system. Similar issues were encountered by Liu *et al.*<sup>15</sup> in their 0.1M BHOH-Vi/FcNCl neutral AORFB which precipitated when charged. Herein, the group attributed the precipitation to the decreased solubility of the radical cation,  $[1]^+$ . After 60 cycles and marked capacity fade, 20 mL of water was added to their viologen electrolyte which aided the solubility of the radical viologen, increasing the concentration of active species in the electrolyte. This ultimately increased the discharge capacity by almost 3-fold.

From [Run  \$\beta 3\$](#)  onwards, a voltage cut-off was implemented to limit electrolyte degradation due to precipitation of the neutral,  $[1]^0$  and radical cation,  $[1]^+$ , redox states of **1** when the system progressed to the second reduction. Run  $\beta 2$  and  $\beta 3$  were identical except for the voltage cut-off.

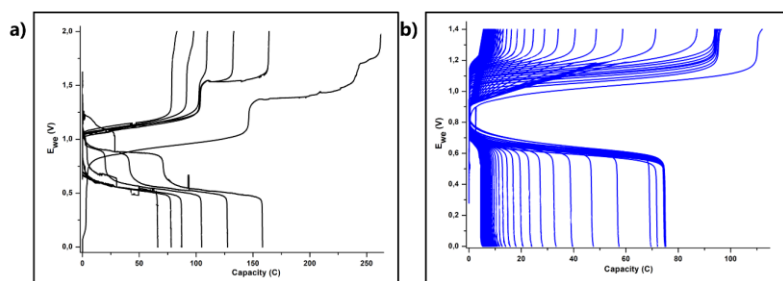


**Figure 3.12** Galvanostatic cycling data of a) **Run  $\beta 2$**  and b) **Run  $\beta 3$** .

The results (**Run  $\beta 3$** ) clearly show that the use of a voltage cut-off limited the maximum charge voltage to 1.4 V, thereby preventing the 2<sup>nd</sup> electron reduction from taking place. In doing so, the battery maintained a discharge capacity at approximately 70 C for 8 cycles. However, by limiting the system to the 1<sup>st</sup> electron reduction, the value of the maximum discharge capacity decreased substantially from 187 C to 79 C, and the system maintained a stable capacity for 8 cycles which was an improvement from previous runs which had not exhibited any capacity stability during cycling.

Given the large capacity losses and low capacity obtained previously, the concentration of **1** and FCN were increased in hopes of increasing the maximum discharge capacity and, in the event of capacity fade, that this would occur over an extended period allowing for longer monitoring of the system. As such, in [Run  \$\beta 4\$](#) , the concentration of **1** was 0.175 M, and the concentration of FCN was 0.35 M with a consistent voltage cut-off of 1.4 V.

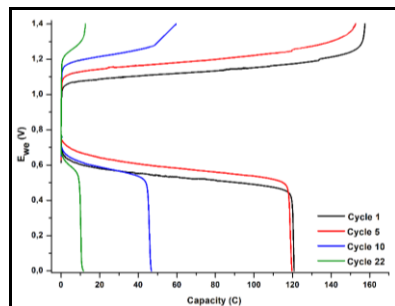


**Figure 3.13** Galvanostatic cycling of **Run  $\beta 4$**  containing: 0.175 M **1** and 0.35 M FCN in 1 M NaCl as anolyte (15 mL) and catholyte (15 mL).  $42 \text{ mL}\cdot\text{min}^{-1}$  flow rate,  $2 \text{ mA}\cdot\text{cm}^{-2}$  charge/discharge current.

As expected, the 1.4 V voltage cut-off limited the transition to the second electron reduction ( $[1]^{+}/[1]^0$ ) as evident by the results in **Figure 3.13** which show only one charge and discharge plateau. In addition, the system maintained capacity at approximately 121 C between cycle 1 to cycle 5. In line with our predictions, increasing the concentration of **1** and FCN had increased the maximum discharge capacity which, despite being lower than the theoretical capacity for this run, was 50 C larger than the previous run at lower concentration. Unfortunately, the overall Coulombic Efficiency was not promising, as seen by the substantial capacity decay of 72 C observed between cycle 5 and cycle 10, and the system was only able to run for 22 cycles. During this experiment, the pH of the electrolytes was monitored, and the results are captured in the table below. Despite starting at a neutral pH, this changes drastically over the course of 22 cycles. The change in pH may be attributed to water splitting or electrolyte degradation, both of which may release free  $\text{OH}^-$  ions.

Whilst most viologen derivatives are stable at neutral or near-neutral pH, FCN is frequently used in RFBs within the pH range of 10–14,<sup>11,16</sup> and therefore, degradation of FCN may account for the pH change.

**Table 3.3** pH of electrolytes during galvanostatic cycling of [Run  \$\beta\$ 4](#).

|          | Initial | Cycle 1 | Cycle 6 | Cycle 10 | Final |
|----------|---------|---------|---------|----------|-------|
| Oxidized | 7.7     | 4.4     | 6.2     | 7.3      | 8.2   |
| Reduced  | 7.7     | 12.7    | 13.4    | 13.2     | 12.5  |

In the subsequent runs ( $\beta$ 5 –  $\beta$ 7), the voltage cut-off, concentration of redox active agents, and applied current were varied to evaluate the effect of these parameters on the flow battery system. During [Run  \$\beta\$ 5](#) the applied charge current was double that of the discharge current, and the initial voltage cut-off was 1.65 V, however, the system only reached a maximum discharge capacity of 146 C which decayed rapidly over the 14 cycles that the system ran for. Given literature reports<sup>17</sup> wherein the concentration of the supporting electrolyte was varied, [Run  \$\beta\$ 6](#) and [Run  \$\beta\$ 7](#) were run with a supporting electrolyte concentration of 1.5 M NaCl. Unfortunately, unlike the work of Hagemann *et al.*<sup>17</sup> the use of a 1.5 M NaCl did not improve the performance of the battery with [Run  \$\beta\$ 6](#) cutting out in the first discharge cycle. The attempt to restart this run at 80 mA charge and discharge capacity resulted in a rapidly decaying system that ran for 19 h with large overpotentials, likely due to a large internal resistance which may have been aggravated by the high concentration of redox species with limited solubility. Decreasing the concentration in [Run  \$\beta\$ 7](#) had no marked difference on the systems performance as capacity fade persisted and the observed capacity remained lower than the theoretical.

#### ***Investigating different electrolytes***

AORFBs have been reported in various electrolytes, and the nature of the electrolyte is known to affect the ionic conductivity and thus internal resistance of the cell, which ultimately impacts on the battery performance.<sup>18-20</sup>

NaCl had been selected as the initial electrolyte of choice due to its low cost and toxicity, and ease of access, and because the publication which provided the inspiration for this work had used NaCl as the supporting electrolyte.<sup>8</sup> Given the issues seen regarding the stability and solubility of the redox active agents used (**1** and FCN), additional flow cell tests in different supporting electrolytes were run using the  $\beta$ -generation RFB design to determine if the NaCl electrolyte was the limiting factor.

**Table 3.4** Effect of change of nature of electrolyte on battery testing performance.<sup>a</sup>

| Run          | Concentration<br>(mol.dm <sup>-3</sup> ) |       | Current<br>(mA) |           | Voltage<br>Cut-Off<br>(V) | Theoretical<br>Capacity<br>(C) | Max.<br>Discharge<br>Capacity<br>(C) |       |
|--------------|--|-------|-----------------|-----------|---------------------------|--------------------------------|--------------------------------------|-------|
|              | [1]                                      | [FCN] | Charge          | Discharge |                           |                                |                                      |       |
| $\beta 8^b$  | KCl                                      | 0.175 | 0.35            | 80        | 20                        | 1.65;<br>1.4                   | 211                                  | 173   |
| $\beta 9$    |  | 0.2   | 0.4             | 80        | 20                        | 1.4                            | 260                                  | 140.4 |
| $\beta 10$   |  | 0.2   | 0.4             | 80        | 40                        | 1.4                            | 260                                  | 126.2 |
| $\beta 11^b$ | NH <sub>4</sub> Cl                       | 0.175 | 0.35            | 80        | 20                        | 1.4;<br>1.55                   | 211                                  | 124   |
| $\beta 12$   | KCl :<br>NH <sub>4</sub> Cl              | 0.175 | 0.35            | 80        | 20                        | 1.65                           | 211                                  | 86.4  |

<sup>a</sup>All runs were completed with a symmetrical configuration with supporting electrolyte concentration of 1.0 (mol.dm<sup>-3</sup>). Flow rate = 42 mL.min<sup>-1</sup>. <sup>b</sup>Voltage cut-off reset multiple times within the same run to prevent aggregation caused due to irreversible redox event.

Three attempts were made to run the system using KCl as the supporting electrolyte. Unfortunately, these repeats were marred, leaks at the pump caused by perforation of the peristaltic tubing, which resulted in capacity fade and even the complete loss of electrolyte for run  **$\beta 10$** . **Run  $\beta 8$**  had better cycling data than  **$\beta 9$**  as the system consistently retained higher discharge capacities despite only having run for a total of 22 cycles.

The capacity fade per cycle for [Run β8](#) occurred at a consistent rate of 4 C per cycle whilst capacity fade in run 9 was quite sporadic, fading greatly quite early on. This may indicate that the higher concentration of **1** was less favoured in a symmetrical system when KCl is used as the supporting electrolyte which could be a result of the solubility limitations of both redox species, particularly the neutral and radical cation redox states of **1**.

Only one flow cell test was conducted using NH<sub>4</sub>Cl as the supporting electrolyte ([Run β11](#)), which ran for a 28 hours and 22 minutes to a total of 100 cycles. The system finally stopped when the capacity was depleted. The initial voltage cut-off of 1.4 V was too low, and this was seen in the first charge cycle, thereafter, the cut-off was adjusted to 1.55 V and the system seemed to charge better which correlated to an increase in discharge capacity.

Comparison of the cycling data for these runs, as seen below, reveals that **run β9** had greater internal resistance as deduced by the larger overpotential required. Regrettably, a large capacity decrease was observed in both cases with **run β8** exhibiting a total loss of 97 C in comparison to a 123 C loss of capacity for **run β9**. Overall, neither KCl nor NH<sub>4</sub>Cl could "outperform" a comparative flow test in NaCl ([Run β4<sup>b</sup>](#)) which recorded higher discharge capacities over the duration of the run and had improved stability as a capacity of 175 C was retained for 8 cycles.

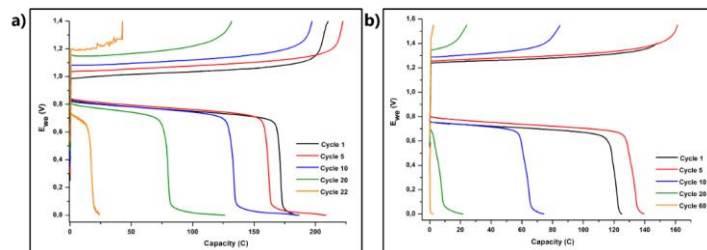


**Figure 3.14** Galvanostatic cycling results for symmetrical cells containing: 0.175 M **1** and 0.35 M FCN in a) 1 M KCl (**Run  $\beta$ 8**), and b) 1 M  $\text{NH}_4\text{Cl}$  (**Run  $\beta$ 9**), as supporting electrolyte (15 mL).

These pre-liminary results indicated that the use of a mixed electrolyte system was not conducive to good performance of the battery as seen by **Run  $\beta$ 12** which only ran for a total of 21 hours and during this time the capacity decreased from 78.4 C to 0.8 C on the 20<sup>th</sup> cycle. Furthermore, the internal resistance of the system was quite high which is reflected in the overpotentials seen in the cycling data, and may be indicative of corrosion of the electrode and the formation of a double layer on the electrode surface which will further impede the capacity.

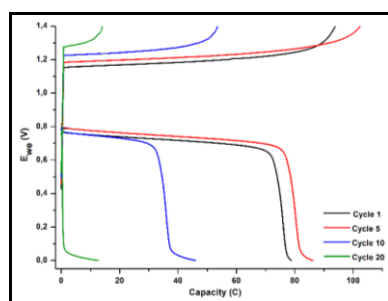


**Figure 3.15** Galvanostatic cycling results for a symmetrical cell containing: 0.175 M **1** and 0.35 M FCN in 1 M KCl : 1 M  $\text{NH}_4\text{Cl}$  (**Run  $\beta$ 12**), as supporting electrolyte (15 mL).



The results obtained by these experiments are merely preliminary, however, and the limitations seen during testing of the different electrolytes were likely affected by other factors given that the reactor design was not yet optimized. The effect of the solubility of **1** cannot be ignored when evaluating these systems as the solubility of the different redox states has not been fully studied. Furthermore, no work was done to compare the solubility of **1** in different electrolytes such as KCl and NH<sub>4</sub>Cl.

#### ***Oxygen permeability of tubing***

Throughout the course of as the flow cell testing, the lack of reproducible results was a recurring issue. Even when all parameters were kept constant, there were often large discrepancies between the results obtained for otherwise identical runs.

In most cases, this was attributed to variation in experimental conditions such as laboratory temperature, and even unfavourable electrochemical changes of compounds during testing. Up until this point, the oxygen permeability of the tubing had not been considered. Given the lack of peristaltic pump and thus inability to conduct further flow cells tests, this was an ideal time to investigate other potential sources of failure, and so the permeability of the current transfer and peristaltic tubing to oxygen was tested.

Within the research group, a control experiment was set-up using a solution of 1 M vanadium (II) sulphate generated by reduction of vanadyl sulphate by zinc metal under Schlenk conditions. A static, closed-loop system was constructed using the  $\beta$ -generation electrolyte reservoirs with the inlet and outlet linked together, as shown in **Figure 3.16**.

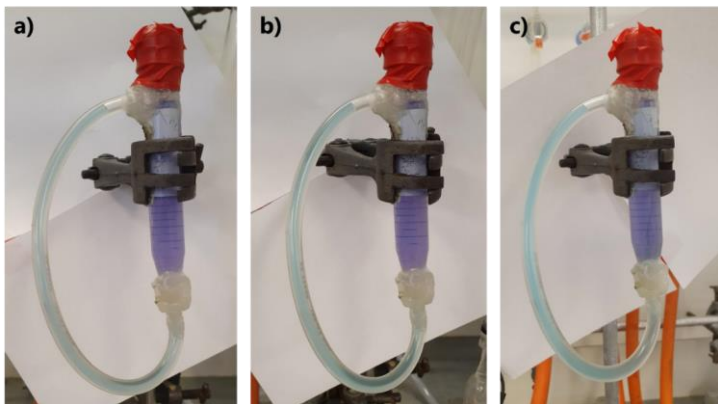


**Figure 3.16** Static closed-loop test of transfer tubing with V(II) electrolyte at a) 1 hour ; b) 24 hours and c) 96 hours.

Approximately 15 mL of V(II) electrolyte under inert atmosphere was placed in the reservoir which was then sealed and monitored over a 96h period. The differently coloured redox states of vanadium are well-known, which enabled this simplistic, yet effective test, to determine where, if at all, oxygen might be entering the system. At the onset, the electrolyte in both the reservoir and the tubing loop maintained the purple colour characteristic of  $V^{2+}$  ions which is as expected as the rate of diffusion into the system was expected to be low. As seen in **Figure 3.16** despite the slow diffusion rate, a distinct colour change is present in the tubing loop, but not in the bulk reservoir nor specifically around the joints. This colour change from purple to blueish-green indicates a change in redox state from  $V^{2+}$  to  $V^{3+}/V^{4+}$  as a result of oxidation, and as this occurs throughout the transfer tubing, it must be due to the permeation of oxygen through the tubing itself.

The results from this test provided significant insight into the lack of reproducibility in results that had plagued the research group but confirmed that the connectors and septum were not points of weakness in the design.

An additional experiment, seen in **Figure 3.17**, using the V(II) electrolyte was performed on a full loop of tubing, incorporating peristaltic tubing as well as the transfer tubing. The set-up was monitored over a period of 48 hours and, as seen in the figure above, there was definite colour change observed in both the transfer tubing, as expected from the previous results, and the peristaltic tubing, indicating that this was also permeable to oxygen.

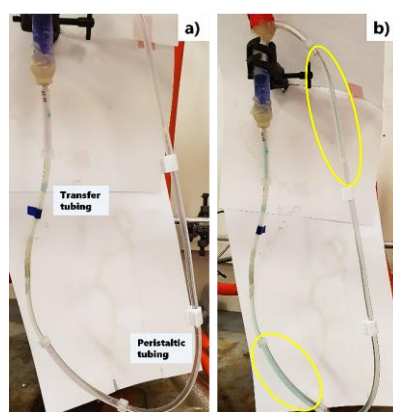


**Figure 3.17** Oxygen permeability test on full loop including transfer tubing and peristaltic tubing at ; a) 5 hours and b) 48 hours.

The effects caused by tubing selection are seldom discussed in the literature. This critical, yet often overlooked design feature could have substantial effects on the success of the flow cell testing. In the case where lab-scale flow cell tests are performed outside a glove box or equivalent inert environment, it is important to ensure that the tubing used is not only chemically resistant, but also sufficiently impermeable to oxygen to prevent premature cell death.

### 3.2.3 $\gamma$ -generation RFB design

The discovery of the oxygen permeability of the transfer and peristaltic tubing, in conjunction with the purchase of the new pumps, gave rise to a complete overhaul of the design. Several key factors had been identified that were clearly hindering the success in testing the flow battery system. The tubing used for the flow cell experiment was unfortunately oxygen permeable and, given the significant length of tubing used, this further increased the possibility of electrolyte degradation during cell cycling. Therefore, the transfer tubing was replaced with Masterflex® Polytetrafluoroethylene (PTFE) Transfer Tubing, and the peristaltic tubing was replaced with FDA Viton tubing, . both sets of tubing being far less permeable to oxygen. However, the new Teflon transfer tubing was far more rigid than the tubing previously used, and this required additional modification to the overall design.

The  $\beta$ -design falcon tubes had served relatively well as electrolyte reservoirs, but prolonged usage had led to additional issues. On a few occasions, electrolyte had been seen leaking from the joints on the tubing, or through cracks in the epoxy glue. In one instance, a hairline crack had formed at the inlet fitting and traversed the side of the falcon tube, leading to loss of electrolyte which ultimately resulted in the “death” of a run. A new design for the electrolyte reservoirs was therefore required. 150 mL Schott Duran bottles were identified as an ideal replacement for the  $\beta$ -reservoirs. These bottles are made of borosilicate glass which ensures high chemical stability, thermal resistance, and facilitates easy sterilization. A key feature of these bottles is their polypropylene screwcap which allows a good seal, and which is easy to modify to form inlets and outlets. Three holes were drilled into each lid which were fitted with an appropriately sized septum to serve as inlet, outlet, and purging channels for the electrolyte.



**Figure 3.18** New lid design for  $\gamma$ -generation RFB design.

***New peristaltic pump***

The failed pump was replaced with an L100-1E precision pump with a 4-channel pump head with a flow rate range of  $0.0002 - 380 \text{ mL}\cdot\text{min}^{-1}$  which was based on the tubing size. When assembling the new testing rig several factors needed to be considered. Firstly, the rigidity of the Teflon transfer tubing meant that the reservoirs needed to be in a fixed position close to the pump, and close enough to the flow cell that the electrolyte could be circulated with ease. Originally, the pump was placed at the same height as the electrolyte tanks which affected electrolyte cycling because there was often an issue getting the electrolyte to flow when the cell was first connected. To combat this issue, the pump was elevated, and the reservoirs were placed directly under the pump head.

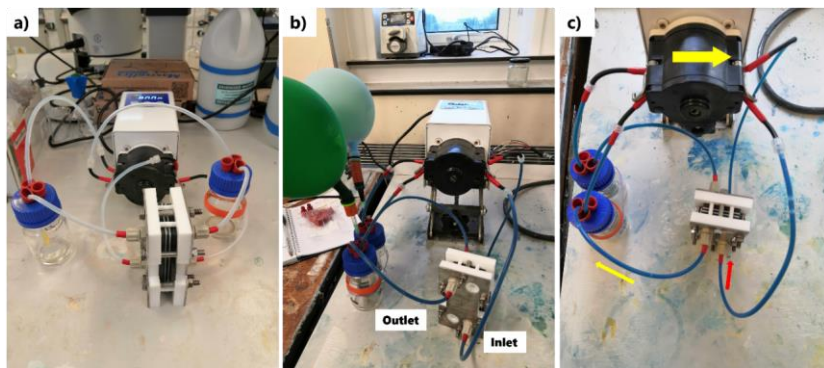


**Figure 3.19**  $\gamma$ -generation RFB design with a) pump and reservoirs at the same height.; b) elevated pump.; c) Elevated pump with indication of the direction of electrolyte flow.

Stability and durability testing of the  $\gamma$ -generation RFB design was conducted using a commercial vanadium electrolyte and a cation exchange membrane (CEM) to use the well-known redox states of vanadium to ensure simple and early detection of any mechanical issues with the testing system. Overall, the system worked well; the electrolyte flowed seamlessly through the flow cell, no leaks were observed at the fittings, and at the flow cell joints. Upon closer inspection, it was observed that there was a very minor leak in the system which was observed due to the formation of  $N_2$  bubbles within the electrolyte from the balloon used to maintain the inert atmosphere, indicating the need to maintain a gentle positive pressure of inert atmosphere.

#### ***Centrifuge tube addition***

The presence of oxygen in the system is detrimental in the long-run and thus it was necessary to address this before beginning with actual flow cell tests. A 50 mL centrifuge tube was added into the Schott bottle to minimize available oxygen by reducing the total effective volume of the reservoir. In this way, the electrolyte would be contained in a smaller space and thus a smaller volume of air which needed to be purged. Moreover, the bulk of the inner tube meant that a tighter seal was formed between the rim of the centrifuge tube and the inner rim of the lid, reducing leaks through this route.

Ultimately, this afforded a means to purge the electrolytes efficiently and safeguard against any oxygen entering the system.

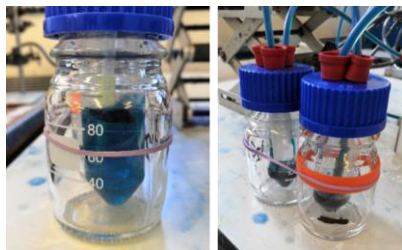


**Figure 3.20** Addition of centrifuge tube into Schott bottle for  $\gamma$ -generation RFB design.

### ***Symmetric Flow cell tests***

Having constructed a sturdier flow cell testing rig with suitable tubing, the next step was to rerun previous experiments and compare the results. As mentioned, reproducibility had been an issue and thus there had been difficulty in obtaining a full data set with comparative results.

Still maintaining the use of an AEM, a symmetrical system using 0.175 M **1**, and 0.35 M FCN in 1.0 M NaCl as supporting electrolyte was set up (**Run  $\gamma$ 1**) to give direct comparison to [Run  \$\beta\$ 4](#). The system was charged and discharged at 20 mA, and a voltage cut-off of 1.65 V was applied, whilst the electrolytes were cycled at 50 mL.min<sup>-1</sup>. The relatively low charging current was to permit an initial screening of this system using the updated testing rig where electron transfer rates could be neglected as a contribution.

**Figure 3.21** shows the charge and discharge profiles for this system. The decrease in capacity is quite stark. Additionally, all charge sequences exhibit a faint second plateau indicating the transition to the second reduction of **1**, however, all discharge sequences only exhibit one plateau. Coulombic efficiency for this run was erratic with a marked increase in efficiency after the first cycle, followed by a sharp decrease in the 11<sup>th</sup> cycle.

During this run precipitation was observed at the inlet on the “reduced” side which resulted in a blockage which may account for the significant capacity loss which was observed. The lack of active redox agents in the system would result in an imbalance and thus capacity fade.

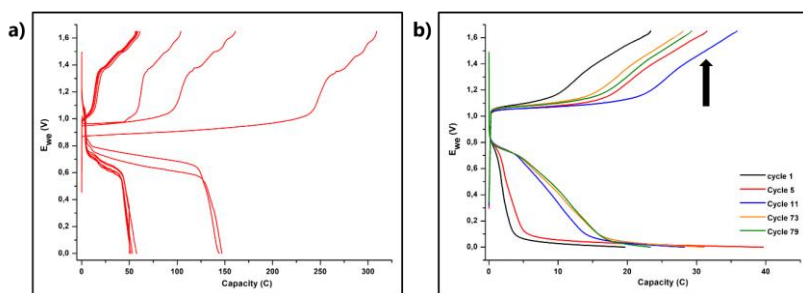


**Figure 3.21** a) Cycling data for all cycles at 20 mA for Run  $\gamma 1$ .; b) Cycling data from selected cycles for Run  $\gamma 1$  at 30 mA.

The blockage was removed, and the electrolytes were purged with  $N_2$ . Purely out of interest, the system was restarted at higher current density (30 mA) and the flow rate was adjusted to  $60 \text{ mL}\cdot\text{min}^{-1}$  whilst the voltage cut-off of 1.65 V was maintained. Surprisingly, the system ran for almost 40 hours although there was still capacity fade, and the overall capacity was quite low (20 C). Despite the failure of this run due to the precipitation issues, the overpotential for this run was lower than what was observed previously implying that the improved testing rig design had reduced the internal resistance of the flow cell, though the mechanism for this is not understood. It is likely that the precipitation is due to an irreversible chemical reaction occurring between the different redox states of **1** and FCN, thereby consuming available species in each electrolyte reservoir, decreasing the capacity, and potentially blocking the membrane.



Despite the new system design, the solubility of the redox species may still pose a risk to the long-term stability and thus success of the redox flow battery.

To mitigate the issue regarding solubility, the concentration of the redox active agents was decreased and additionally, a lower voltage cut-off was set at 1.4 V to inhibit the second reduction of **1**. A mixed electrolyte containing 0.1 M **1**, and 0.2 M FCN in 1.0 M NaCl was cycled at 60 mL.min<sup>-1</sup> (**Run γ2**). The system was charged at 30 mA and discharged at 20 mA. Again, the low charging currents were selected as this was still an early screening of the γ-generation design.

Furthermore, the difference in charge and discharge current was inspired by previous observations wherein the system had been unable to discharge fully at currents higher than 20 mA. In spite of that, the cycling data for this run was quite peculiar, because there was a very large charge cycle (238 C) which corresponded to a substantially lower discharge cycle (72 C) which was followed by persistent capacity fade all totalling 9 hours. Post-mortem electrolyte analysis revealed a notable increase in pH in one of the electrolytes to from pH 7 to pH 10.5, whilst the other electrolyte remained at pH 7. Previous speculation regarding the pH increase was that the permeability of the transfer and peristaltic tubing had allowed an influx of oxygen into the system which may have driven the increase in pH. The exposure to oxygen which subsequently leads to electrolyte degradation and decomposition of redox active species has previously been discussed in literature.<sup>14,21,22</sup> Further discussion regarding possible mechanisms of degradation and decomposition are discussed at a later stage (*vide infra*). However, it is worth noting that no visible precipitation was observed during this run.

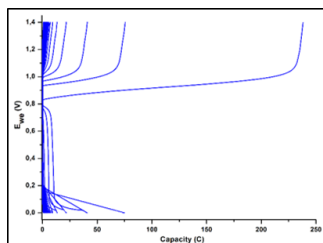


**Figure 3.22** Galvanostatic cycling data for **Run  $\gamma$ 2**.

### ***Asymmetric System***

Given the recurring precipitation issues when using the mixed electrolyte containing **1** and FCN, the question as to the solubility of the different redox states of **1** became more pertinent. Until this point, the solubility of the different redox states had not been investigated. CV analysis had shown that the reductions of **1** are chemically reversible in aqueous electrolytes, but this might not necessarily be the case; a) at higher concentrations, and b) in the presence of FCN.

Frequently, research groups using viologens in AORFBs limit the system to prevent the formation of the insoluble neutral form of the viologen which results in a loss of active material, translating into loss of capacity for the system.<sup>15,23–25</sup> However, in a previous symmetrical AORFB, the use of 1-ethyl-1-methylpyrrolidinium bromide (MEP), suppressed the precipitation of the (2HO-V)Br<sub>2</sub>-Br<sub>2</sub> complex and increased the stability of (2HO-V)Br<sub>2</sub>/Br<sub>2</sub>.<sup>8</sup> This made the second reduction of the viologen accessible without suffering the risk of precipitation, and enhanced the stability of the AORFB which was able to cycle for 200 cycles without any capacity decay.

It was observed that on mixing of the combined **1**/FCN electrolyte, a colour change was seen, and viologens are known to form charge transfer complexes in weakly polar media.<sup>26,27</sup>

A literature search showed that charge transfer complex formation between dibutyl viologen and ferrocyanide ion is known.<sup>27</sup> In aqueous solutions under ultraviolet light ( $\lambda \leq 350$  nm), these species form a 1:1 charge transfer complex which formed reversible photochromic complexes that decomposed in the dark. A similar charge-transfer complex was reported involving a non-symmetrical viologen and ferrocyanide,<sup>26</sup> which showed that electron withdrawing substituents lead to the viologen becoming more prone to reduction by ferrocyanide anions.

It thus seemed likely the capacity loss within the symmetrical system was due to the formation of a charge-transfer complex between **1** and FCN in some combination of the available redox states with different solubility than the individual components. This would thus cause the blockages which were frequently observed, and this competing side reaction account for the consistent capacity loss experienced with each experiment. Despite the high solubility (<6 M) of the dication state of **1** in 1 M NaCl, the solubility of the other redox states has not been quantified, and therefore it is possible, indeed likely, that the radical cation and neutral forms of **1** are less soluble than the dication, and during the charging and discharging process the formation of these species may result in the formation of insoluble product. Given these observations, it was decided to investigate unsymmetrical RFB electrolyte systems to limit these parasitic side reactions which may consume the redox active agents and cause substantial capacity loss.

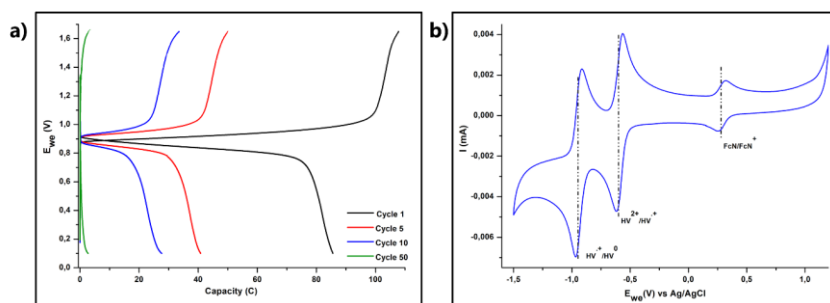
**Table 3.5** Conditions for asymmetrical flow cell testing.<sup>a</sup>

|    | Concentration<br>(mol.dm <sup>-3</sup> ) |       |        | Current (mA) |           | Voltage<br>Cut-Off<br>(V) | Theoretical<br>Capacity<br>(C) | Max.<br>Discharge<br>Capacity<br>(C) |
|----|--|-------|--------|--------------|-----------|---------------------------|--------------------------------|--------------------------------------|
|    | [1]                                      | [FCN] | [NaCl] | Charge       | Discharge |                           |                                |                                      |
| γ3 | 0.1                                      | 0.2   | 1.0    | 10           | 5         | 0.1 – 1.65                | 231.56                         | 106                                  |
| γ4 | 0.1                                      | 0.1   | 1.0    | 10           | 5         | 0.1 – 1.65                | 231.56                         | -                                    |

<sup>a</sup> Flow rate = 70 mL.min<sup>-1</sup> for all runs.

Using the γ-generation RFB design, an asymmetrical flow cell test was set-up with 0.1 M **1** in 1 M NaCl (negolyte), and 0.2 M FCN in 1 M NaCl (posolyte) (**Run γ3**), and the system was charged at 10 mA and discharged at 5 mA with a voltage cut-off of 1.65 V based on previous experiments and literature reports.<sup>8,15</sup> Lower operating currents were selected as this was an initial screening run and the kinetic and electron transfer relationship between the redox active agents and the electrode surface were still unknown.

The system ran for a total of 4 days and 8 hours before the capacity was depleted resulting in cell death. Nevertheless, this run was quite promising due to the low overpotentials observed, and subsequently low internal resistance evidenced in the cycling data, shown in

**Figure 3.23.**

**Figure 3.23** a) Cycling data of selected cycles for **Run γ3** ; b) Post-cycling CV analysis of viologen electrolyte revealing evidence of FCN crossover.s

Despite the maximum discharge capacity being 126 C lower than theoretical capacity, the coulombic efficiency of this run remained above 80% for the duration and the increase in internal resistance was quite gradual. The selected voltage cut-off set between 0.1 V – 1.65 V appeared to work in favour of battery longevity, and this may be attributed to the fact that only the first electron reduction was utilized, potentially minimizing the formation of insoluble products which would reduce the concentration of redox active species in solution. Post cycling analysis of the electrolytes indicated that there was crossover of ferrocyanide ions.

Limiting the system to the 1<sup>st</sup> reduction of the viologen,  $HV^{2+}$  to  $HV^+$ , seemed the most appropriate step based on the literature and previous issues with precipitation which may have been caused by the insoluble neutral viologen. With this measure in place, there was no need to have excess FCN in the system and the concentration of the FCN electrolyte was decreased to 0.1 M; all other parameters were kept constant ([Run  \$\gamma\$ 4](#)). **Figure 3.24** shows the full charge and discharge profile for the run  $\gamma$ 4 which contained 0.1 M **1** as negative electrolyte and 0.1 M FCN as positive electrolyte.

Despite charging to 200 C in the first cycle, the system only discharged to a maximum discharge of 10 C, and continued to run poorly thereafter, eventually dying after 9 hours. Unlike the previous flow test where crossover was most likely the largest cause of capacity fade, post cycling analysis revealed that there was no crossover of ferrocyanide ions, but there was increase in the pH of the viologen electrolyte which recorded a final pH value of 11. Therefore, given the stark difference between the cycling data of Run  $\gamma$ 3 and  $\gamma$ 4, it may be that an excess of FCN ions is necessary in order for the flow cell to cycle properly without low capacity and rapid death.

Alternatively, given the physical evidence of a fouled AEM, the poor performance observed may be related to blockage of the membrane or issues with the electrodes and/or current collectors such as fouling.

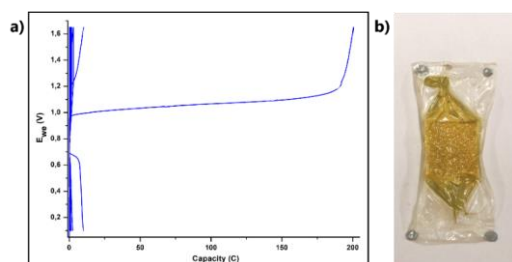


**Figure 3.24** a) Cycling data for **Run γ4**. ; b) Fouled AEM from **Run γ4**.

#### **Membrane fouling - Testing CEM**

Despite the lack of reproducible flow cell behaviour, there was one consistent factor observed: the fouling of the membrane. Previous literature reports evaluating different AEMs when using viologens in AORFBs found that fumasep® FAA-3-PE-30 AEM (a non-reinforced AEM highly stable in basic and acidic environments, with low resistance and high anion selectivity) exhibited the lowest electric cell resistance and best performance parameters such as CE and EE.<sup>17</sup> Nevertheless, during these experiments and regardless of analyte concentration and/or cycling duration, the membrane seemed to foul easily as evidenced by the permanent discolouration of membranes shown in **Figure 3.25**.

After rinsing the membranes with deionized water for five minutes the colour was not removed, and this indicates semi-permanent inclusion of FCN and Cl.



**Figure 3.25** Evidence of fouling on AEMs used in FCN-based cell tests.

An ideal membrane in an RFB has five main characteristics, two of which focus on the conductivity and selectivity of charge carriers and redox active agents, respectively.<sup>1,6,20,28</sup> The membrane used needs to be applicable for the particular redox couple in use which will minimize issues with crossover and ionic conductivity. The use of porous polyolefin membranes<sup>8,15</sup> has also been reported by other groups working with viologens and there was no mention of membrane fouling in these reports. In systems using ferrocyanide derivatives, cation exchange membranes (CEMs) are commonly employed in RFBs as this allows their counter cations ( $K^+$ ,  $Ca^+$ ,  $NH_4^+$ ) to be conducted easily.<sup>10,11,16,22</sup> Given the poor performance, lack of reproducible results and crossover of FCN after other issues were eliminated, the choice of membrane was next to be questioned. Since FCN incorporation into the AEM was observed, a cation exchange membrane was next investigated.

**Table 3.6** Testing conditions using CEM.<sup>a</sup>

|     | Concentration<br>(mol.dm <sup>-3</sup> ) |       |        | Current (mA) |           | Voltage<br>Cut-Off<br>(V) | Theoretical<br>Capacity<br>(C) | Max.<br>Discharge<br>Capacity<br>(C) |
|-----|--|-------|--------|--------------|-----------|---------------------------|--------------------------------|--------------------------------------|
|     | [1]                                      | [FCN] | [NaCl] | Charge       | Discharge |                           |                                |                                      |
| γ5  | 0.1                                      | 0.1   | 1.0    | 10           | 10        | 0.3 – 1.6                 | 173                            | -                                    |
| γ5a | 0.1                                      | 0.1   | 1.0    | 10           | 2         | 0.3 – 1.6                 | 173                            | 38.5                                 |
| γ6  | 0.05                                     | 0.05  | 1.0    | 10           | 10        | 0.2 – 1.3                 | 231.56                         | -                                    |
| γ6a | 0.05                                     | 0.05  | 1.0    | 5            | 5         | 0.1 – 1.65                | 211                            | 0.3                                  |

<sup>a</sup> Flow rate = 60 mL.min<sup>-1</sup> for all runs.

Maintaining the voltage cut-off of 1.6 V which had previously limited the system to the 1<sup>st</sup> reduction of the viologen, [1]<sup>2+</sup> to [1]<sup>+</sup>, a 1:1 ratio between **1** and FCN was employed for the first run using the CEM ([Run γ5](#)). Unfortunately, when cycling was attempted the system seemed to “surge” and cut-off within seconds. The exact reason for this is unclear but it may be attributed to poor contact with the electrodes, or a high internal resistance. The electrolytes were returned to their reservoirs, resparged with N<sub>2</sub> for 10 minutes and then cycled as per the conditions for [Run γ5a](#). The system seemed to favour the lower discharge current as it was able to cycle for a total of 18 hours, however, the discharge capacities obtained were consistently lower than 7 C.

Given the failure of the first attempt (Run γ5 and γ5a), a second flow cycling test was set up at half the concentration of viologen and FCN with the initial voltage cut off set at 0.2 - 1.3 V ([Run γ6](#)). The solubility of the redox states of **1** was still unknown and this may have contributed to the failure of the previous run. Regrettably, the system did not discharge properly, and given the large overpotentials observed, there was a high internal resistance. Overall, it was only able to charge for one cycle.



Given the poor discharge and inability to cycle properly under these conditions, the system was restarted under different conditions ([Run y6](#)). Herein, the voltage cut-off was reset at 0.1-1.65 volts and the charge and discharge currents were set to 5 mA to determine whether the system performance was limited due to sluggish kinetics which were influenced by the CEM. After resetting the voltage cut off, the discharge capacity seemed to increase but the value was still incredibly low (0.8 C) in comparison to the theoretical discharge of 231 C. Post cycling analysis was conducted on the electrolytes and it was found that **1** had crossed the membrane into the ferrocyanide reservoir. In addition, the pH of both electrolytes had changed; the pH of the viologen electrolyte had increased from 6.1 to 10.3, and pH of the ferrocyanide electrolyte decreased from 8.3 to 5.6.

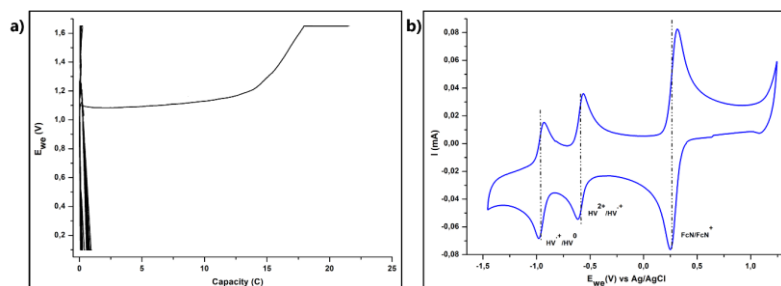


**Figure 3.26** a) Cycling data of selected cycles for [Run y6](#) ; b) Post-cycling CV analysis of viologen electrolyte revealing evidence of FCN crossover.

These runs indicated that the performance of this battery was not enhanced using the CEM, and issues such as crossover and pH fluctuations were still evident. Given the outcome, there was no obvious reason why the CEM should be used instead of the AEM and , as such, future testing reverted to the use of the AEM.

### **Cleaning protocol**

During earlier studies, the flow cell was taken apart between each flow cell test and washed using copious hot water. In cases where Prussian blue had formed, a weak solution (~ 1 M) of sodium hydroxide was used to remove any stubborn stains. Up to this point, no additional protocol was in place for cleaning of the current collectors. Given the poor discharge results obtained, the purity and cleanliness of the surface of the current collectors were considered as possible sources of problems. On several occasions, solid was observed on the surface of the current collectors after washing, and so a new basic cleaning protocol was established for the current collectors. The current collectors used in this work were porous graphite plates procured as part of the flow cell design and were used without any further modifications. As a porous material, graphite is susceptible to the adsorption of species on its surface<sup>29</sup> and this is consistent with reports by Hageman *et al.*<sup>17</sup> who used the same flow cell in their work. Acid treatment of graphite is commonly used to pre-treat the graphite surface and enhance the stability and performance of the battery.<sup>30</sup>

Additionally, acid treatment has been known to aid in the removal of adsorbed species on the surface of the graphite and as such, cleaning with mild acid solution was selected as the cleaning protocol in this work. Each current collector was sonicated for 20 minutes in ~1.5 M HCl. The initial round of cleaning with acid resulted in the formation of a deep blue-green acid solution which confirmed surface contamination and affirmed the need for consistent cleaning with acid. Therefore, the current collectors were washed with acid twice more with fresh acid on each round.

After the third round of acid wash when it was found that the acid solution no longer changed colour, the current collectors were rinsed with deionized water, sonicated for 20 minutes in the deionised water, and thereafter the current collectors were left to air dry.

**Figure 3.27** shows the evidence of efflorescence on the current collectors as well as the micrographs from scanning electron microscopy (SEM) and corresponding Energy Dispersive X-Ray Analysis (EDX) spectrum for each current collector. This confirmed that the surface contamination on the current collectors was mostly from  $\text{Na}^+$ ,  $\text{Cl}^-$  and  $\text{K}^+$  ions which were from the supporting electrolyte and the counter ion of the ferrocyanide, respectively. Adsorption of  $\text{NaCl}$  on graphite surface has been reported and is even exploited in the sphere of desalination.<sup>31</sup> It is possible that the alkaline conditions which emerged during certain runs altered the graphite surface, rendering it more susceptible to adsorption of  $\text{Na}^+$  and  $\text{K}^+$  ions which would attach on the surface defects.<sup>32</sup> Electrochemical ageing of current collectors has been reported previously and the enhanced porosity of the surface was attributed to  $\text{CO}_2$  and  $\text{CO}$  gas evolution due to severe over oxidation of the graphite, and it was concluded that the electrolyte flow rate, charging current and voltage cut-off for a system should be selected to prevent and limit corrosion and side reactions.<sup>33</sup>

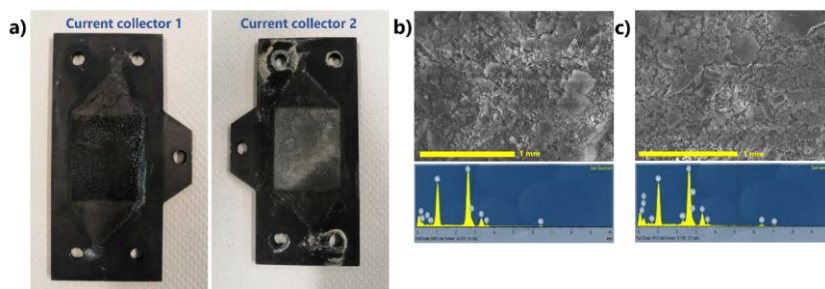


**Figure 3.27** a) Current collectors before cleaning; ; b) SEM micrograph of current collector 1 with corresponding EDX spectrum; ; c) SEM micrograph of current collector 2 with corresponding EDX spectrum.

***Pre-treatment : Membrane and/or graphite felt***

Electrodes and membranes are key components of redox flow batteries and despite commercially available electrodes and membranes being designed for electrochemical flow cell use, pre-treatment of both electrodes and membranes is commonly mentioned in literature<sup>29,34,35</sup> to optimise their performance. In the case of carbon felt electrodes, three different treatment methods are commonly used: thermal treatment, acid treatment, and electrochemical ageing. Thermal treatment has been reported to reduce the overall oxygen (O<sub>2</sub>) content from 25% to 19% in graphitized felts and from 30% to 19% for carbonised felts,<sup>30</sup> with the same study reporting that soaking in sulfuric acid increased the electrochemical performance of the felts. Another report using a range of anthraquinones as electrolytes stated that thermal treatment in air at 550 °C for 3 h led to the best electrochemical performance of graphite felt in comparison to 4 other samples which were pre-treated using a variation of acid and thermal treatments, and calcination.<sup>36</sup> The superior electrochemical performance was attributed to the reduced surface of the graphite which became smoother after "air-heat treatment". During treatment, the carbon fibres lattice parameters such as average crystallite width and thickness were decreased, and this "exfoliated" the outer layer of the fibre which increased the catalytic activity of the felts.

XPS results from this work<sup>36</sup> showed increased content of C-OH functional groups leading to improved electron-transfer capability and catalytic performance of the felt which thus enhanced the redox reaction with the electrolyte.

Membrane modification methods vary depending on the nature of the membrane in use, with typical pre-treatment methods including electrolyte soaking, oxidation polymerization, and electrodeposition.<sup>37</sup>

An investigation on the effect of pre-treatment of Nafion membranes on the performance of a VRFB revealed that “wet-treated” Nafion pre-treatment was the best choice for practical VRFB application. This process was less costly than alternatives and the resultant RFBs were more efficient because water and acid pre-treatment of the Nafion membranes swells the micro needle structure of the membrane and therefore increases proton conductivity, and membrane area, in comparison to the “as-received” dry membranes.<sup>35</sup>

Broadly speaking, pre-treatment of AEMs typically involves the exchange of the current anion, as provided by commercial suppliers, to the anion of choice for the AORFB. Hageman *et al.*<sup>17</sup> evaluated the performance of four different AEMS in an AORFB, including the fumasep® FAA-3-PE-30 AEM used in this work, where the Br<sup>-</sup> anion was exchanged for Cl<sup>-</sup> by soaking the membrane in 0.5 M NaCl at 25 °C for 24 hours.

A set of four experiments was designed to evaluate the effect of pre-treatment of membrane and/or electrode on the performance of the viologen-based RFB (see **Figure 3.28**). For these experiments, charge and discharge currents, flow rate, volume of electrolytes, electrolyte concentrations, and supporting electrolyte concentration were kept constant whilst the treatment status of the membrane and graphite felts were varied to allow a direct comparison on the effect of pre-treatment on battery performance.

To ensure experimental integrity, an initial screening experiment (**Run γ7**) was set-up, incorporating the constant parameters of flow rate (70 mL.min<sup>-1</sup>) and electrolyte volume (20 mL), and additionally, the membrane and felt used were untreated. The charge and discharge currents were set at 10 mA and 5 mA, respectively, and the corresponding voltage cut-off was set between 0.5 – 1.05 V.

Initial screening results had revealed that at lower currents ( $\leq 20$  mA) the battery could not discharge above 1 C and stopped after 2 cycles corresponding to 6 hours run time. Guided by these results and literature<sup>14,17</sup> regarding the relationship between current density and battery performance, higher charging currents appeared attractive as these catered to the reaction kinetics and diffusion limitations of the system whilst minimizing the possibility of parasitic side reactions by decreasing the time taken per charge and discharge cycle. In theory, this would allow the system to cycle correctly with consistent charge and discharge cycles, in comparison to charging at lower currents.

Hence, all tests were performed at a fixed charge and discharge currents, 60mA and 50 mA, respectively. The constant parameters were as follows: flow rate of 70 mL.min<sup>-1</sup>, 20 mL electrolyte volume, 0.1 M **1** coupled with 0.2 M FCN in 1 M NaCl giving a corresponding theoretical capacity of ~193 C. Where felt treatment is mentioned, graphite felts were treated in air at 200 °C for 24 hours; membrane treatment refers to soaking the membrane in 1.0 M NaCl for 24 hours.



**Figure 3.28** Matrix of pre-treatment methods

The first pre-treatment evaluation flow cell test was conducted on a system without any pre-treatment on the AEM and the felt ([Run y8](#)). With these parameters, the system ran for a total of 4 hours and 36 minutes but only achieved a maximum discharge capacity of 31 C which faded at a rate of 0.019 C/minute, resulting in a final discharge capacity of 26 C. The initial voltage cut-off was set from 0.2 – 1.05 V, but it was evident that the charge cycle was hampered by this cut-off. Therefore, after cycle 3, the voltage cut-off was reset to 1.3 V which increased the charge capacity from 41 C in the third cycle to 78 C in the fourth cycle. Post-cycling CV analysis showed very minor traces of FCN crossover into the viologen electrolyte, and the final pH values of the electrolytes were recorded at 11.7 and 6.8 for **1** and FCN, respectively. The capacity and overall performance of this system is quite poor as the recorded capacity values are substantially lower than the theoretical capacity of 193 C. Electrochemical impedance spectroscopy (EIS) showed that the recorded internal resistance increased from 1.53  $\Omega$  before cycling to 3.1  $\Omega$  after cycling for 8 hours which is comparable with values recorded in literature.<sup>17,38</sup> (**Appendix 1, Figure A1.2**) These EIS results provided a benchmark for future experiments as the cell performance and nature of pre-treatment per experiment could be linked to the internal resistance and this would dictate which method improved the system holistically.





Unfortunately, blocking of the membrane channels was not confirmed analytically, however, SEM analysis of a pre-treated membrane is discussed [below](#).

In [Run y10](#) wherein the performance of a flow cell containing a treated AEM, and thermal treated graphite felt were tested, the system only charged to a maximum capacity of 70 C and could not discharge beyond 0.3 C, and ultimately the system stopped running after 35 minutes. These values are significantly lower than the expected values, and even previously recorded values in this work. The change in internal resistance recorded was 3  $\Omega$  (Initial - 5  $\Omega$ ; Final - 8  $\Omega$ ) but given that the system only ran for 35 minutes, it is evident that this increase would have been much larger should the system have run longer. Notably, the initial internal resistance was, at 5.0  $\Omega$ , the highest initial internal resistance recorded in this data set. These results are a clear indicator that the pre-treatment of the AEM hinders the performance of this system, and this may be due to blocked membrane channels which would inhibit the movement of charge carriers across the membrane, preventing proper charging and discharging of the system.

At higher current densities (60 mA), the system would not discharge properly and so the system was restarted at lower charge and discharge currents of 10 mA, and 5 mA, respectively. The lower currents improved the system and evidence of this can be seen in the flow cell data wherein the system was able to charge. Unfortunately, the results obtained are still flawed as there is a very large first charge cycle, 250 C, followed by poor discharge and ultimately premature cell death, and the highest discharge capacity recorded was 53 C, substantially lower than the theoretical value of 196 C. Post-cycling CV confirmed crossover of FCN which likely attributed to cell death as **1** and FCN may have formed an insoluble complex, decreasing the concentration of active species in the electrolyte.

**Table 3.7** shows the influence of pre-treatment on the internal resistance of the RFB.

|                                  | Re (Z) (Ohm) |       | $\Delta Z$ (Ohm) | $\Delta Z$ (Ohm)/min |
|----------------------------------|--------------|-------|------------------|----------------------|
|                                  | Initial      | Final |                  |                      |
| <b>Run <math>\gamma</math>8</b>  | 1.53         | 3.1   | 1.57             | 0.005                |
| <b>Run <math>\gamma</math>9</b>  | 3.17         | 27.2  | 24.03            | 0.18                 |
| <b>Run <math>\gamma</math>10</b> | 5.0          | 8.27  | 3.27             | 0.09                 |

On a positive note, the combination of a thermally treated graphite felt coupled with an untreated AEM (**Run  $\gamma$ 11**) led to improved battery cycling data as the system cycled for 28 cycles which spanned 6 hours and 54 minutes and was able to maintain capacity at 33.3 C for the first four cycles. Despite the low value for the maximum discharge capacity in comparison to the theoretical of 193 C, the system was able to maintain a CE greater than 70% throughout this run. Large capacity fade was observed over the course of the run, and this is attributed to the large fluctuation in pH in the system, with the final pH of the viologen electrolyte reaching 11.6 and ferrocyanide electrolyte reaching 5.4. Post cycling analysis revealed crossover of potassium ferrocyanide to the viologen electrolyte and, additionally,  $^1\text{H}$  NMR analysis (**Appendix 1, Figure A1.5**) showed that de-alkylation of the viologen, albeit to a minor degree, had occurred which may have been a result of Hoffman elimination.<sup>39</sup> Further details regarding possible mechanisms of dealkylation and the corresponding products are discussed [below](#). The internal resistance increased from 2.2  $\Omega$  to 4.7  $\Omega$  over approximately 7 hours, corresponding to an increase internal resistance rate of 0.006  $\Omega$ /minute, making the rate of internal increase comparable to **Run  $\gamma$ 8**, and superior to **Run  $\gamma$ 9** and  **$\gamma$ 10**.

When considering the overall performance, including the stability, and internal resistance, **Run  $\gamma 11$**  is the best run in this data set identifying pre-treatment of graphite to be a key parameter upon which performance is contingent.

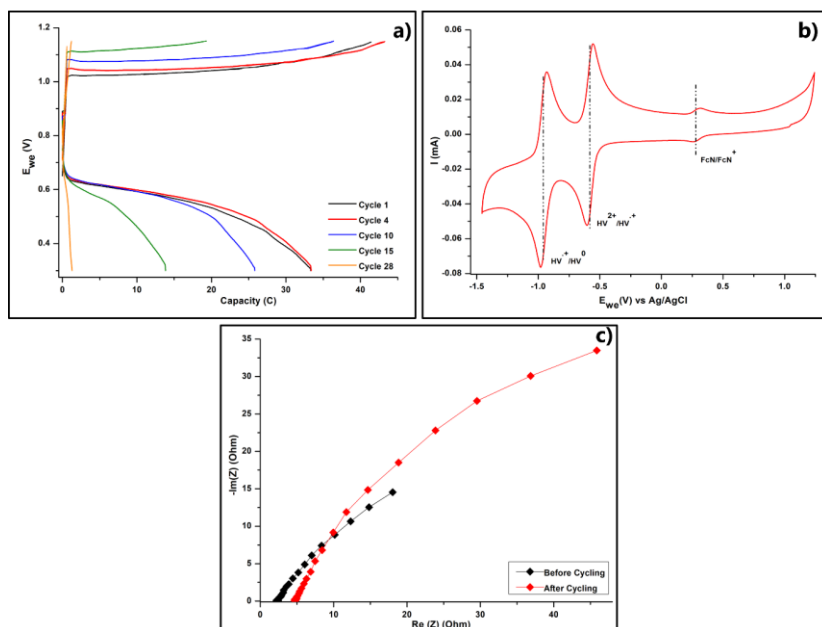


**Figure 3.30** a) Cycling data of selected cycles for **Run  $\gamma 11$**  ; b) Post-cycling CV analysis of viologen electrolyte revealing evidence of FCN crossover. ; c) EIS curves for **Run  $\gamma 11$** .

Having established that the use of a thermally treated felt and an untreated AEM gave best results for cell cycling at neutral pH, investigation then turned to optimisation of the supporting electrolyte (**Run  $\gamma 12$** ). In related literature work using the same AEM, 1.5 M NaCl was reported as the electrolyte concentration with the lowest internal cell resistance.<sup>17</sup> A flow-cell run was therefore set-up using 1.5 M NaCl as the supporting electrolyte with a thermally treated graphite felt and untreated AEM, and all other parameters such as charge/discharge currents, voltage cut-offs and flow rate were maintained as per previous

experiments (**Run  $\gamma$ 8 -11**). The system ran for a total of one day 22 hours and 19 minutes and showed rapid capacity decay for the first 26 cycles before stabilising at cycle 27 at a capacity of approximately 28 C, where it remained till cycle 100, as seen in **Figure 3.31a**. The CE over cycles 27-100 was approximately 98%. Suspecting that the capacity fade was in part due to poor electron transfer kinetics, the system was restarted with the lower charge and discharge currents of 30 mA. (**Figure 3.31b**)

After restarting, the system stabilised at 37 C, noticeably greater than the 28 C seen in the initial cycling and ran for a total of 39 cycles with a CE of 98%. At this point, these results were the most stable battery cycling results obtained throughout the course of this work. The stability of both electrolytes was confirmed by CV analysis post cycling which also revealed that there had been a minor degree of ferrocyanide crossover. (**Figure 3.31c**) Additionally, the pH had fluctuated with the viologen electrolyte becoming more basic (9.8) and the ferrocyanide electrolyte becoming less basic (5.8).

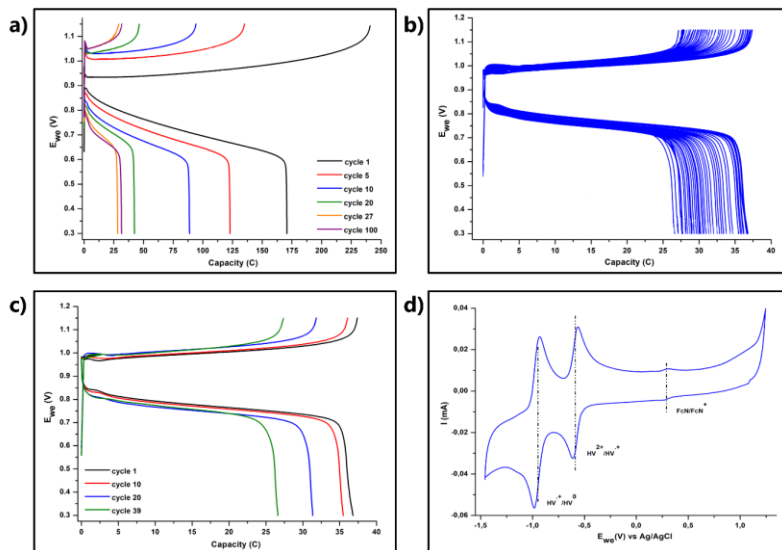


**Figure 3.31** Galvanostatic cycling of **Run γ12** containing : 0.1 M **1** and 0.2 M FCN in 1.5 M NaCl as anolyte (20 mL) and catholyte (20 mL). 70 mL.min<sup>-1</sup> flow rate, 60 mA charge, and 60 mA discharge current. a) Selected cycles of **Run γ12** ; b) All cycles of **Run γ12a** ; c) Selected cycles of **Run γ12a** and d) Post-cycling CV of viologen electrolyte.

The viologen electrolyte was analysed by <sup>1</sup>H NMR post-cycling, and **Figure 3.32** confirms a marked degree of dealkylation which is discussed further [below](#). The aromatic region of the NMR spectrum (**Figure 3.32b**) shows the formation of new peaks indicating the degradation of the viologen electrolyte by dealkylation.

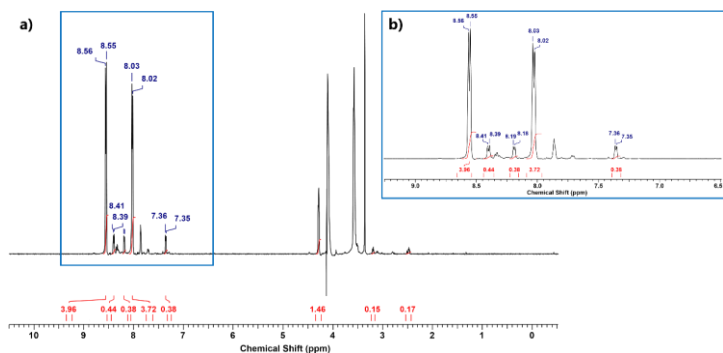


**Figure 3.32** a) Full  $^1\text{H}$  NMR spectrum of **Run  $\gamma$ 12** viologen electrolyte post-cycling; b) Inset of aromatic region of  $^1\text{H}$  NMR spectrum.

Cycling data from the previous experiment indicated that the system stabilized at significantly lower capacity than expected, and it was postulated that this might have occurred because of two possible reasons. Firstly, irreversible adsorption and loss of redox active species resulting in a stable final concentration of species and secondly, reversible adsorption of species onto the carbon felt and membrane to produce a buffered lower final concentration. To test the first postulation, a cell cycle test was run at lower concentration of **1** and FCN (**Run  $\gamma$ 13**). An asymmetrical system was assembled consisting of 0.025 M **1** in 1.5 M NaCl as the negative electrolyte and 0.05 M FCN in 1.5 M NaCl as the positive electrolyte and was charged and discharged at 30 mA with a voltage cut-off between 0.3 – 1.150 V, cycled at 70 mL $\cdot$ min $^{-1}$ . The charge and discharge currents were scaled to accommodate for the lower concentration of redox active species but the flow rate, voltage cut-off and concentration of NaCl was maintained to ensure that there were still grounds for comparison between the results.

The system exhibited major capacity fade, and an overall poor charge-discharge capacity, running for only 2 hours and 14 minutes and only achieving a maximum discharge capacity of 24 C despite having charged to 90 C. Ultimately, the system did not stabilize under these conditions, and it ran until the capacity was depleted.

To further probe the system, the electrolytes were returned to their reservoirs, resparged with N<sub>2</sub> and then the system was restarted several times at lower currents; 2.5, 5.0 and 10 mA. None of these attempts were successful as the system could not charge and discharge properly. At the lowest current, 2.5 mA, the system ran for 5 hours and 30 minutes but only achieved a maximum discharge capacity of 1.2 C. Unfortunately, each cycle attempt on this system fell very far short of the theoretical value of 97 C, and the system did not stabilize as expected which indicates that the previous stabilization observed in **Run y12** can-not be attributed to reversible adsorption to the surface but was likely due to irreversible adsorption or equivalent decay process which created a stable final concentration, and it may not be possible to replicate this phenomenon. Despite the lower concentration of redox active species, CV analysis of the electrolytes revealed crossover of FCN, and this may be attributed to the long cycle time (~12 hours) due to several restarts at different currents. At this point, it was suspected that crossover was time-dependent rather than a concentration and cycling artefact. Under these conditions, dealkylation of **1** was confirmed by <sup>1</sup>H NMR (**Appendix 1, Figure A1.6**) and this may be associated with the large pH fluctuation observed: the pH of the final solutions was 11.9 and 2.8 for **1** and FCN, respectively. Overall, this system exhibited the lowest internal resistance (1.4 Ω) within this dataset, and this increased slightly to a final internal resistance of 3.7 Ω.

Given that **Run  $\gamma$ 12** was the most successful run to date, this run needed to be repeated to confirm reproducibility of these results. Therefore, **Run  $\gamma$ 14** was set up using 1.5 M NaCl supporting electrolyte with 0.1 M **1** and 0.2 M FCN and all other parameters were maintained. The cycling data for this system was quite remarkable: the system ran for a total of 51 hours with a total capacity loss of 46 C which equates to 0.13% capacity loss per minute and 0.47% capacity loss per cycle.

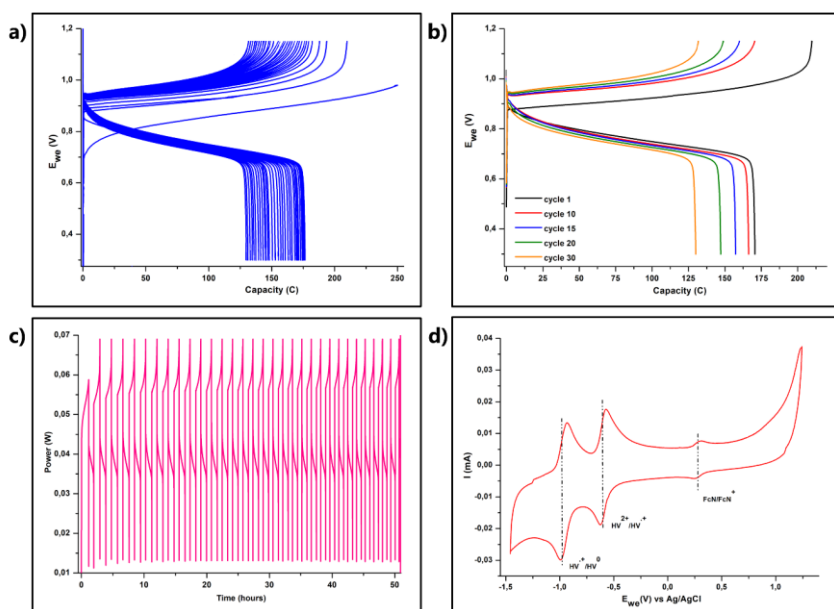


**Figure 3.33** a) Full cycle profile for **Run  $\gamma$ 14**. ; b) Cycling data of selected cycles for Run  $\gamma$ 14. c) Time versus power for **Run  $\gamma$ 14**. ; d) Post-cycling CV analysis of viologen electrolyte revealing evidence of FCN crossover.

The maximum discharge was 177 C which is 91.4 % of the theoretical capacity of 193 C, comparable with the maximum of 172 C which was recorded for **Run  $\gamma$ 12**. The success of this ran may be attributed to the low internal resistance recorded which increased from 0.53



$\Omega$  to 1.2  $\Omega$  during this run, and it should be noted that this was lower than the internal resistance recorded for **Run  $\gamma$ 12**.

One factor which may also account for this is that the temperature in the lab was 18°C, 10°C higher than when **Run  $\gamma$ 12** was done previously, and so the effect of system temperature on cell function cannot be discounted. Post-cycling analysis was comparable with previous results and was consistent for the crossover of FCN into the viologen reservoir, and dealkylation of the viologen which were confirmed by CV and  $^1\text{H}$  NMR, respectively. There was also a large change in the pH; final pH of **1** and FCN were 12.5 and 9.1, respectively.

Ultimately the effect of pre-treatment was clear from the difference in the discharge capacity and lifetime of the different flow-cell tests. These results are summarized in **Table 3.8**, and it is clear that **Run  $\gamma$ 12** and  **$\gamma$ 14** produced the best results in terms of maximum discharge capacity.

**Table 3.8** Summary of results obtained from pre-treatment tests.

|               | Concentration<br>(mol.dm <sup>-3</sup> ) |       |        | Current<br>(mA)     |                   | Voltage<br>Cut-Off<br>(V) | Q <sup>a</sup><br>(C) | Max.<br>Discharge<br>Capacity<br>(C) |
|---------------|--|-------|--------|---------------------|-------------------|---------------------------|-----------------------|--------------------------------------|
|               | [1]                                      | [FCN] | [NaCl] | Charge              | Discharge         |                           |                       |                                      |
|               | $\gamma 7^b$                             | 0.1   | 0.2    | 1.0                 | 10                | 5                         | 0.5 – 1.05; 1.3       | 193                                  |
| $\gamma 8^b$  | 0.1                                      | 0.2   | 1.0    | 60                  | 50                | 0.2 -1.05; 1.3            | 193                   | 31                                   |
| $\gamma 9$    | 0.1                                      | 0.2   | 1.0    | 60                  | 50                | 0.2 - 1.3                 | 193                   | 27.5                                 |
| $\gamma 10$   | 0.1                                      | 0.2   | 1.0    | 60                  | 50                | 0.2 - 1.15                | 193                   | 0,3                                  |
| $\gamma 11$   | 0.1                                      | 0.2   | 1.0    | 60                  | 50                | 0.2 - 1.15                | 193                   | 33.3                                 |
| $\gamma 12$   | 0.1                                      | 0.2   | 1.5    | 60                  | 50 ; 30           | 0.3 - 1.15                | 193                   | 171.7                                |
| $\gamma 13^c$ | 0.025                                    | 0.05  | 1.5    | 30 ;10 ;5 ;<br>;2.5 | 30;10 ;5 ;<br>2.5 | 0.3 - 1.15                | 96.5                  | 23.5                                 |
| $\gamma 14$   | 0.1                                      | 0.2   | 1.5    | 60                  | 50                | 0.3 - 1.15                | 193                   | 176.5                                |

<sup>a</sup>Theoretical capacity of the system calculated by  $Q = nCF$ ; <sup>b</sup>Voltage cut-off reset multiple times within the same run to prevent aggregation caused due to irreversible redox event; <sup>c</sup>System resparged and restarted at different charge and discharge currents.

#### Membrane permeability : Osmotic Chamber vs Flow cell

Given the recurring issue with crossover in the system, a simple set of experiments were established to evaluate the permeability of the AEM under static and dynamic conditions. Static tests were carried out in a home-made osmotic chamber comprised of two 50 mL electrolyte tanks which were separated by the AEM and sealed using a custom-made O-ring compression joint.

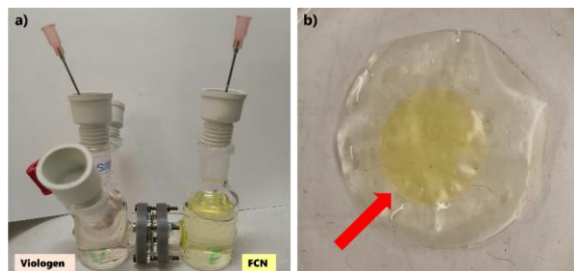


**Figure 3.34:** a) Osmotic chamber for static AEM permeability tests. ; b) Untreated AEM after 48h in the static osmotic chamber.

In both cases, one electrolyte tank contained 0.1 M **1** in 1 M NaCl and the other tank contained 0.2 M FCN with 1 M NaCl supporting electrolyte. Two static tests were conducted: the first using an untreated AEM, and the second test with an AEM which was soaked in 1 M NaCl for 24h, as for membrane pre-treatment. For dynamic tests, the flow cell was assembled under standard conditions, one electrolyte reservoir was filled with 1 M NaCl, and the other reservoir contained a solution of 0.2 M FCN which was made up with 1 M NaCl supporting electrolyte. The system was cycled without current at  $70 \text{ mL}\cdot\text{min}^{-1}$  for 48 hours.

To test the effect of applied current on crossover, a dynamic flow cell test was assembled under standard conditions, one electrolyte reservoir was filled with 1 M NaCl, and the other reservoir contained a solution of 0.2 M FCN which was made up with 1M NaCl supporting electrolyte which was cycled at  $70 \text{ mL}\cdot\text{min}^{-1}$

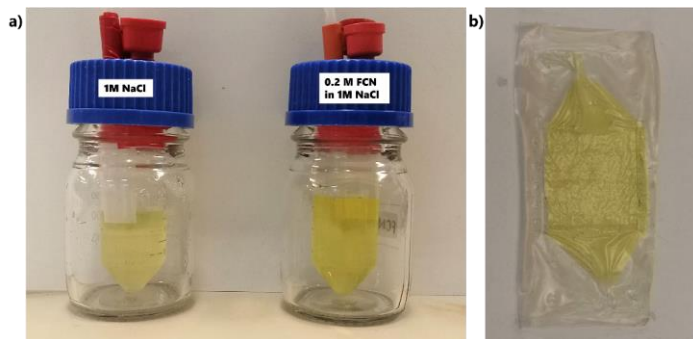


**Figure 3.35** Electrolytes after 48h dynamic flow cell test on membrane permeability.; b) Membrane obtained from the flow cell after this test.

Both static tests using the treated and untreated AEM revealed that no FCN crossover had taken place as confirmed by CV after 48 hours, but membrane fouling/staining was observed in both tests. For the untreated AEM, the pH of the FCN electrolyte remained constant at a value of 8.4, however, there was a minor increase from 5.8 to 6.4 in the pH of **1**. However, in comparison to the static test with the treated AEM, the increase in pH was observed for both electrolytes with a final pH value of 7.1 and 8.8 for the viologen (**1**) and FCN, respectively. Despite the increase in pH,  $^1\text{H}$  NMR confirmed that no degradation of **1** had occurred in either the treated or untreated static tests.

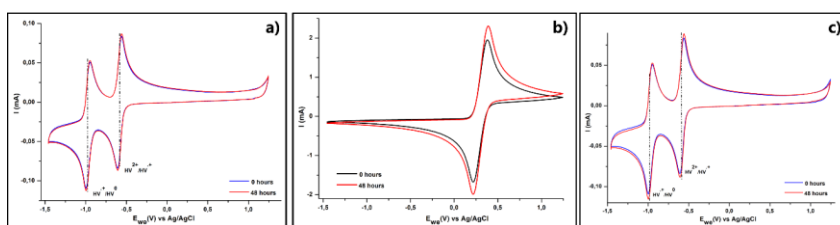


**Figure 3.36** Cyclic voltammograms of electrolytes from the osmotic chamber. a) CV of viologen electrolyte after the static test containing the untreated AEM.; b) CV of FCN as reference.; c) CV of viologen electrolyte after the static test containing the treated AEM.

Scanning Electron Microscopy (SEM) and X-ray energy dispersive spectra (EDX) was run on the membranes after 48 hours and **Figure 3.37** shows a comparison between the different AEMs versus an untreated "control" AEM, thus providing insight into the compositional changes that occur during membrane fouling, and the nature of elements present on the membrane. All membranes were rinsed with deionized water three times and dried to remove any surface ions before running SEM. The control membrane **Figure 3.37a** exhibits traces of Br as this is the supporting ion that the membrane comes with. Once the membrane has been exposed to electrolytes (viologen or FCN) as in the static system there is clear diffusion through the three-dimensional network which is evidenced in **Figure 3.37b**. The morphology of the treated membrane looks quite different in comparison to the control and untreated AEM, lacking the distinct channel network, and at higher magnification the evidence of solid is apparent. The notable presence of Cl and Fe are confirmed in the EDX which supports the idea that the channels of the AEM become blocked during pre-treatment, that limiting diffusion of species through the membrane.

#### **Dynamic untreated AEM**

The first dynamic flow cell test was conducted without any current and the electrolytes were circulated for 48 hours. Visual observation of the electrolytes confirmed ferrocyanide crossover after 48 h as the NaCl electrolyte had a faint yellow tinge like the colour of the FCN electrolyte. This was affirmed by CV analysis **Figure 3.35** on both electrolytes and a distinct ferro/ferricyanide redox peak was seen in the final electrolyte. In contrast, when the same system was analysed under a fixed current, 60 mA "charge" and -60 mA "discharge", there was no trace of FCN crossover observed in the CV.

Unsurprisingly, the pH of both electrolytes changed during these experiments, and in both cases, the pH of the NaCl electrolyte became more basic, whilst the FCN electrolyte became less basic. In the absence of current, the pH change was quite small: NaCl changed from pH 6.5 to 7.0, and FCN changed from 8.5 to 7.4. However, after having applied a current, the final pH values were 9.1 and 7.3 for NaCl and FCN, respectively. The increase in pH of the NaCl electrolyte is likely due to water splitting which in the absence of redox active species in solution, thus releasing free OH<sup>-</sup> and subsequently making the pH more basic.

SEM micrographs showed that the membrane maintained its morphology in both tests, and while both show traces of Fe and Cl on the membrane, it is clear that the 48 hour dynamic test without current **Figure 3.37d** has higher traces of Fe which is consistent with the crossover that was observed in the post-cycling CV. Despite the lack of crossover, membrane fouling still persisted in the dynamic test with current, and the evidence of Fe in the XEDS **Figure 3.37e** for this sample indicates that Fe was present within the membrane channels.

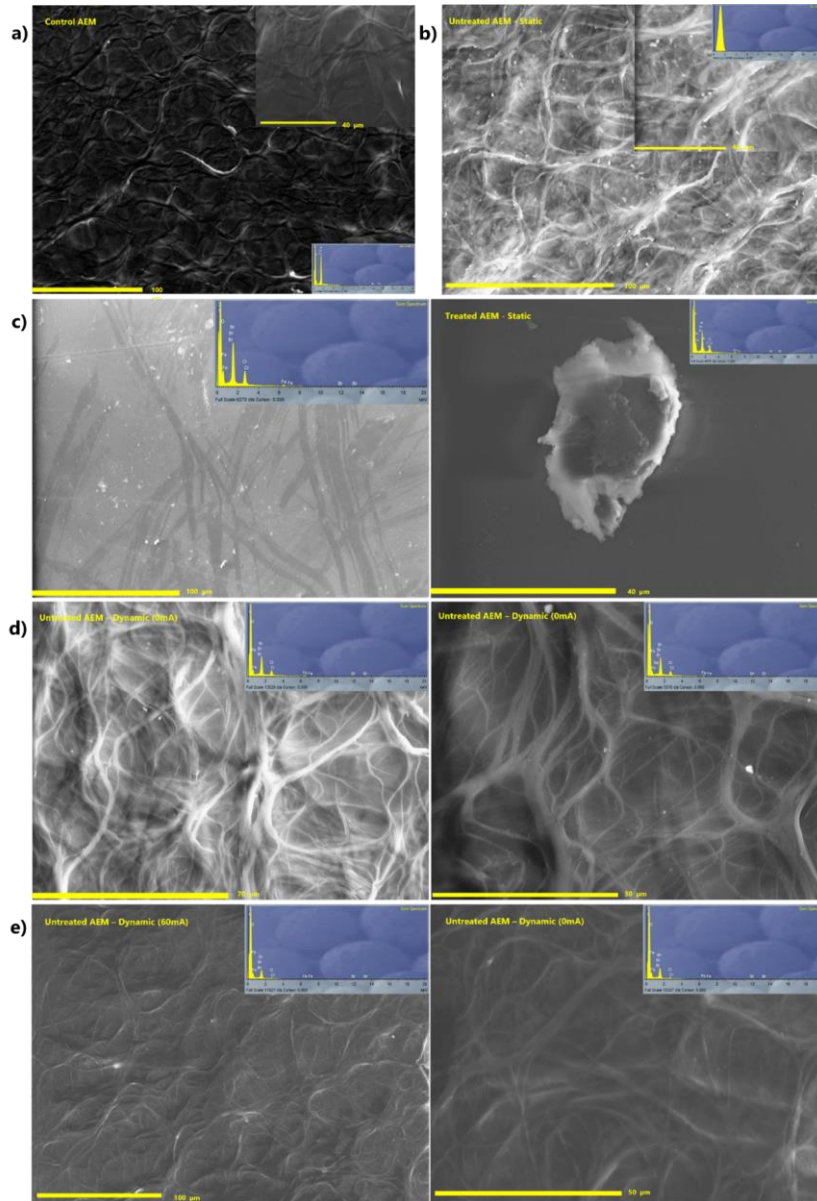


**Figure 3.37** SEM micrographs of a) control AEM.; b) Untreated AEM from the osmotic chamber.; c) Treated SEM from the osmotic chamber.; d) Untreated AEM from the dynamic flow cell at 0 mA.; e) Untreated AEM from the dynamic flow cell at 60mA.

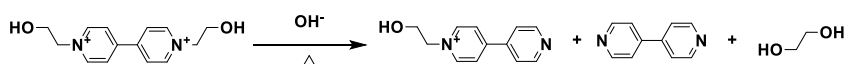
These membrane permeability tests have provided some insight into the utility of the fumasep® FAA-3-PE-30 AEM in this flow-cell system containing **1** and FCN. Regardless of the treatment status of the membrane, no crossover was observed in the CV for the static tests despite the visual evidence of membrane fouling. However, when the untreated membrane was tested in the dynamic system without current, FCN crossover was evident by visual inspection and affirmed by CV analysis. This indicates that the simple act of circulating the electrolytes leads to crossover and that this may be an artefact of the system related to internal pressure and surface contact during the circulation. Conversely, when a current was applied to the dynamic system to mimic charging and discharging, no crossover was detected, and this may be correlated to the short cycle time during this experiment which leads to the further postulation that FCN crossover in this RFB system is a time-dependent artefact and that higher levels of FCN crossover is proportional to longer cycle time. This speculation is consistent with post-cycling data for other runs wherein shorter runs had little to no evidence of crossover, but longer runs were consistently plagued by crossover.

#### ***Capacity fade and electrolyte stability***

Whilst the thermal pre-treatment of carbon felts enhanced stability of the flow cell, however, dealkylation of the viologen, as confirmed by <sup>1</sup>H NMR, was a common outcome from all flow cell tests. Furthermore, a systematic rise in pH of the viologen electrolyte was repeatedly observed. Since Hofmann Elimination<sup>39</sup> is a possible mechanism of degradation for viologens, and thereby compound **1**, it is probable that the alkyl chains were cleaved off of the viologen to produce the mono-substituted viologen, 4,4'-bipyridine and ethylene glycol. This indicates that stability of the electrolytes themselves may be a limiting factor in battery stability.



The extent of dealkylation varies between each of the flow cell runs, and this may be a time-dependent factor which is driven by overcharging which splits water, releasing free  $\text{OH}^-$  which can cleave off the alkyl chains.<sup>39</sup> Jin *et al.*<sup>40</sup> developed a phosphonate-functionalized viologen which was run at near neutral pH, and they reported that at high pH (14), one of the alkyl side chains were cleaved as confirmed by  $^1\text{H}$  NMR and CV.



**Scheme 3.3** Proposed dealkylation pathway of **1** which occurred during flow-cell cycling.

As such, a control experiment was performed to gauge the extent of dealkylation of **1** at different concentrations of base (0.1 M and 0.01 M) over 6 hours in the absence of an applied current. Two separate samples containing 6 mmol of **1** were prepared using 0.01 M KOH and 0.1 M KOH as the electrolyte, and the samples were analysed by  $^1\text{H}$  NMR at specified time intervals for a total duration of 6 hours. No degradation and dealkylation was detected for either sample over the 6-hour period, rather surprising considering that dealkylation was frequently detected under flowcell operating conditions in similar timeframes but at lower pH. This implies that dealkylation occurs in significant rate in the reduced form(s) of **1**, and therefore, dealkylation of the dication, as in the  $^1\text{H}$  NMR base degradation experiment, could not be detected due to a substantially slower rate of dealkylation.

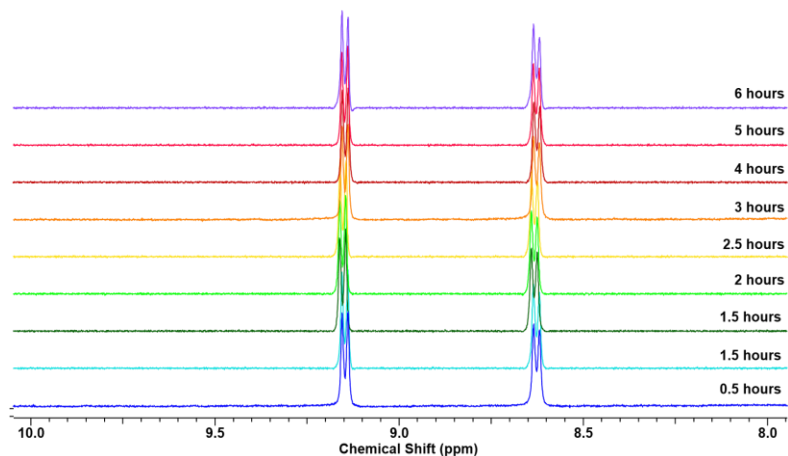


**Figure 3.38**  $^1\text{H}$  NMR of **1** in 0.1 M KOH monitored over 6 hours.

Dealkylation of **1** is a consistent issue during this work. The rate of dealkylation was never fully evaluated, but it was confirmed by post-cycling  $^1\text{H}$  NMR of the viologen electrolyte. Aziz *et al.*<sup>22</sup> assessed factors controlling electrolyte lifetime and have argued that decomposition is the dominant factor affecting capacity fade in AORFBs. Bimolecular decomposition, dimerization, disproportionation, and dealkylation are common decomposition mechanisms seen in literature.<sup>22,38,41</sup> For example, dimerization of viologens is a common occurrence which leads to the formation of an internal charge transfer complex which may disproportionate and result in a decrease or loss of redox activity in the battery. Viologens are known to be chemically unstable under corrosive conditions such as high or low pH and therefore they are frequently used at neutral or near neutral conditions in AORFBs.

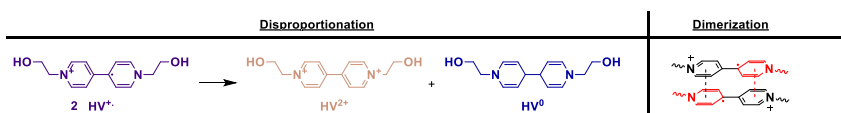


**Figure 3.39** Common degradation routes of viologens.

By functionalizing both viologen negolyte and ferrocene posolyte with positively charged quaternary ammonium groups, Beh *et al.*<sup>21</sup> achieved batteries with extremely low capacity fade rates of ( $\leq 0.1\%$ / day), and found that galvanostatic charging decreased the capacity more than potentiostatic charging which was attributed to a slower increase in the membrane resistance in the latter case. The group also reported a 29% decomposition of [BTMAP-Vi](#) after 300 cycles (approximately 15 days) as confirmed by <sup>1</sup>H NMR. Similar functionalization of [MV and TEMPO](#) was performed by DeBruler *et al.*<sup>42</sup> with the intention of preventing viologen dimerization and precipitation by incorporating charged substituents. Given the limited solubility of the radical cation, most research on viologens is limited to the first reduction, however, this group was able to access the second reduction of the viologen at -0.75 V vs SHE which resulted in higher specific capacity and average cell voltage than typically seen but unfortunately, the capacity fade rate reported was approximately ~50%/day which further affirms the notion that accessing the 2<sup>nd</sup> reduction during cell cycling leads to instability. These results clearly mirror the results obtained in this project wherein dealkylation of **1** occurred frequently, and therefore, a large proportion of capacity fade observed within this work is attributed to decomposition of the viologen by means of dealkylation, dimerization, and disproportionation.

Ferro/ferricyanide and their derivatives are commonly used as positive couples in aqueous flow batteries,<sup>10,13,43</sup> most commonly with either sodium or potassium counter cations, but their solubility may be improved by varying the nature of the counter cation.<sup>10</sup> It is well known that the stability of the ferrocyanide anion is pH dependent, and thus the change in pH during cell cycling may have an effect on the stability of cycling capacity;<sup>10,13,44</sup>

ferro/ferricyanide are particularly unstable in acidic environments where they decompose to generate toxic hydrocyanic acid.

Whilst no direct studies on the stability of ferrocyanide in this system were conducted, post-mortem analysis of ferro/ferricyanide electrolytes from the cell often revealed that the electrochemical properties were unchanged showing the expected distinct redox peak centred at 0.23 V vs SHE.

One of the most common and widely discussed issue with RFBs is crossover, which is what makes symmetrical systems so attractive: they contain a common electrolyte and therefore the consequences of crossover are minimized or ultimately eliminated. In this work, the symmetrical system proved to have several issues, particularly, the formation of a Charge Transfer Complex (CTC) between the viologen and ferro/ferricyanide and so crossover in the asymmetrical system is therefore something that should be avoided as matter of priority. Nevertheless, post-cycling CV analysis consistently revealed FCN crossover which likely resulted in the formation of the undesired CTC, ultimately decreasing the amount of redox active agents in solution and decreasing the capacity of the battery.

Typically, RFBs using the ferro/ferricyanide couple are cycled with a cation exchange membrane and the counter cation of the ferrocyanide crosses the membrane to balance the charge; in these conditions it is unlikely that the anionic FCN would cross the membrane. For example, in 2019, DeBruler *et al.*<sup>16</sup> reported the use of an ammonium ferrocyanide catholyte and propyl-viologen [(SPR)<sub>2</sub>V] anolyte which was cycled at neutral pH using a Selemion CSO cation-exchange membrane.

The group reported no chemical degradation of either species, however CV analysis confirmed 6% and 15% crossover of  $(\text{SPr})_2\text{V}$  and  $(\text{NH}_4)_4[\text{Fe}(\text{CN})_6]$ , respectively which corresponded closely to their observed capacity loss of 12%.

To overcome crossover, the group analysed a symmetrical system comprised of 0.9 M  $(\text{NH}_4)_4[\text{Fe}(\text{CN})_6]/(\text{SPr})_2\text{V}$  which was cycled for 1000 cycles, amounting to a total of 1,100 hours, and which achieved nearly 100% capacity retention with 62.6% average energy efficiency. Similarly, Jin *et al.*<sup>40</sup> coupled a symmetrical viologen containing a phosphate group with potassium ferrocyanide in an AORFB at near neutral pH using a CEM. Given that the viologen was negatively charged, it was less susceptible to decomposition and interaction with the FCN and would not cross the membrane.

Several crossover mitigation strategies have been reported in the literature, including the use of ion-selective membranes, optimization of flow rate, appropriate flow channel design, and the use of additives.<sup>45,46</sup> Work by Yan *et al.*<sup>24</sup> employed the use of a novel bipolar membrane (BPM)-enabled acid-base redox flow batteries where the positive and negative redox couples were dissolved in alkaline and acidic electrolytes, respectively.<sup>24</sup> Here, potassium ferrocyanide dissolved in 2 M KOH was used as the positive couple facing the anion exchange layer whilst the acidic electrolyte for the negative couple was exposed to the cation exchange layer of the BPM. Despite membrane fouling, and some crossover, this gave a proof-of-concept RFB relying on acid-base neutralization facilitated by using a BPM, and this might serve as a reliable way to use moderately stable redox couples such as ferro/ferricyanide.

Consistent membrane fouling was also observed throughout flow cell testing in this work. Visual observation showed increased discolouration was proportional to an increase in concentration of redox active species, in particular FCN. Fouling occurs due to attractive interactions between the membrane and the electrolyte causing the accumulation of redox active species on the surface which may block the membrane channels, decreasing the ion conductivity and thus decreasing capacity and hindering battery performance.<sup>47</sup>

In depth analysis into membrane fouling in aqueous RFBs showed that fouling was mainly attributed to “clogging” of ion exchange sites in the membrane and accumulation of redox active species at the membrane-electrolyte interface.<sup>48</sup> Uptake of FCN was observed in this work as both ferrocyanide and ferricyanide are anionic, with the uptake of ferro/ferricyanide anions driven by the electrochemical potential gradient, and the diffusion of FCN through and into the membrane is thermodynamically favoured.<sup>48</sup> SEM and EDX confirmed a higher uptake of ferro/ferricyanide when using a dynamic system as opposed to a static system. The accumulation of FCN in the membrane blocks the ion exchange sites and creates a barrier layer preventing Cl<sup>-</sup> migration across the membrane which increases the internal resistance of the cell leading to poor performance and lower capacity.<sup>48</sup>

The change in pH during cycling was another consistent issue in this work, and in most flow cell tests, the pH of the viologen electrolyte would often increase to approximately 9 or 10. This may be caused by dealkylation of the viologen, releasing bipyridine as a free base, which in turn may have resulted in the release of free hydroxy anions in solutions, or parasitic water splitting when charging.

The current collectors used in this project are porous graphite plates and consistent and prolonged use of these current collectors will naturally lead to a build-up of ions within the pores. This was confirmed by occasional efflorescence of green-blue deposits on the current collectors after washing and sonication. Given that the surface is porous, ions in solution may become imbedded in the current collectors during operation, which will decrease, albeit slightly, the concentration of active species in solutions. Furthermore, during cycling, adsorbed species may leech out of the current collectors, and interact with the electrolyte, impeding battery performance and lead to unusual charging results. This has been diagnosed as an operational failure in VRFBs as the unwashed electrode resulted in low discharge energy density and low capacity.<sup>49</sup>

The optimization of the flow rate is often overlooked when designing RFBs. Studies on flow rates and their effects on performance of VRFBs indicate that lower flow rates increase resistivity at the electrode fibres due to decreasing concentration gradients of vanadium species resulting in poor cell performance due to "fuel starvation"(insufficient amounts of redox active agent in the cell).<sup>50</sup> Hagemann *et al.*<sup>17</sup> investigated the influence of flow rate in an all organic RFB by varying the flow rate of each electrolyte both simultaneously, and then independently of each other. For that system, higher flow rates ( $16 \text{ mL}\cdot\text{min}^{-1}$ ) only increased the discharge capacity by 2.9 C when compared to the flow test run at  $4 \text{ mL}\cdot\text{min}^{-1}$  which only amounts to a 1.79% increase in the capacity. Although only minor effect was seen for this system, nevertheless the flow rate does affect the performance of the battery and therefore is it important to evaluate the effect of the flow rate on a battery's performance, especially considering the flow dependent cross-over observed.

Operating condition will unavoidably have an effect on the performance of the battery, and temperature is a particular factor reported to affect the performance of industrial VRFBs, leading to scattered results on performance and stability of the VRFB.<sup>51</sup> In addition to the scattered results, Whitehead and co-workers<sup>51</sup> cycled a cell repeatedly over a range of electrolyte temperatures from 16-41°C and found that an increase in temperature correlated to the increase in self-discharge capacity,  $j_{sd}$ , and a decrease in the coulombic efficiency, and there was a strong dependence between cell resistivity and voltage efficiency.

Results presented in this work, particularly between **Run γ12** and **Run γ14**, show large discrepancies between results and this is attributed to variations in lab temperature. Unfortunately, there was little control on the operating temperatures within the lab at the University of Kent and the flow cell was operated at a wide array of temperatures during the course of this work which will have affected the performance of the system.

### 3.3 Conclusions

During this PhD project, great strides were made towards the development and optimization of a sturdy, reliable, lab-scale flow cell testing rig for further development and optimization of an AORFB. Despite the numerous hurdles that were encountered including the loss of research time due to COVID-19, equipment failure, and improper tubing, this work has shown that a hydroxy substituted water-soluble viologen can be used in a neutral, aqueous RFB using an inexpensive couple such as FCN as the positive couple. A symmetrical viologen, **1**, was synthesized and tested in a symmetrical, neutral, AORFB using FCN as the positive couple. Precipitation of redox active agents was a recurring issue and is attributed to the formation of a CTC which are known to form between viologens and FCN, and whose the



rate of formation is accelerated when exposed to UV-light.<sup>27</sup> Therefore, despite significant issues from crossover, the asymmetrical design of this system showed better charge and discharge profiles.

As evidenced in this work, the use of correct transfer and peristaltic tubing is imperative for the success of the RFB system. Tubing should not only be chemically stable and resistant, but also impermeable to oxygen as this may lead to cell death.

Various combinations of pre-treated graphite felt and/or membrane were evaluated during cell cycling. Thermal pre-treatment in air was the only method tested for the pre-treatment of graphite felts and was found to improve the stability of the AORFB tested in this work by activating the surface of the electrodes. However, the membrane pre-treatment method used to exchange the Br<sup>-</sup> ions for Cl<sup>-</sup> ions appeared to be detrimental to the cell often leading to quick cell death which might be attributed to blocked membrane channels and confirmed by SEM and EDX analysis.

Supporting electrolyte concentration influences the internal resistance of the cell and while in this work, 1.0 M NaCl was initially used as the electrolyte of choice, when 1.5 M NaCl was used, the stability of the battery increased, and the internal resistance decreased. Therefore, for this AEM, 1.5 M NaCl appears to be better than 1.0 M NaCl when using viologens and FCN at neutral pH.

### **3.4 Future Work**

The work detailed in this chapter lays the foundations for the further development and optimization of a neutral, AORFB using a simple organic redox active agent as the negative couple, but much further work needs to be carried out to fully optimize this system.

Given the clear impact of electrolyte on overall cell behaviour, additional flow cell tests will need to be conducted using different electrolytes such as ammonium chloride and potassium chloride at varying concentrations. Considering the consistent pH swing which was observed in the symmetrical and asymmetrical design, mixed electrolytes or buffered electrolytes may offer additional support by resisting the pH change and stabilizing the pH for the duration of the flow cell test.<sup>21</sup> Similarly, although  $70 \text{ mL}\cdot\text{min}^{-1}$  was selected as the flow rate for the final experiments, testing needs to be done to find the optimum flow rate for the system.

Humidity, pressure, and temperature have all been reported to affect the transport coefficients of the redox active species used in flow cell systems and therefore, in order to maintain environmental homogeneity, future experiments should be conducted in a controlled environment such as a glove box. This will limit exposure to oxygen and ambient UV light, both of which are detrimental to long-term cycling of the flow cell.

Crossover of FCN into the viologen reservoir persisted throughout all tests, and it is therefore necessary to find a suitable AEM which can inhibit FCN crossover, and this may include modifications to the current AEM. Ceramic membrane or ion-selective dialysis membranes may provide the necessary selectivity to prevent FCN crossover and the incorporation of these into the system is worth investigating. It is hoped that these changes should, in part, address the capacity fade which was consistently observed during flow cell testing.

## 3.5 Experimental Methodology & Materials

### 3.5.1 Materials used

All reagents used were purchased from commercial suppliers and were used without further purification.

### 3.5.2 Physical Measurements

NMR (400 MHz) spectra were recorded on a Bruker AV2-400 instrument. All chemical shifts are given in ppm with respect to residual solvent peaks. Coupling constants (J values) are quoted to one decimal place with values given in Hertz (Hz). SEM images were recorded on a Hitachi S3400-N SEM which was equipped with Oxford Instruments EDX systems, running INCA software (version 7). pH of solutions was measured using a LAQUAtwin PH-11 pH meter with two-point calibration.

### 3.5.3 Electrochemical Measurements

Cyclic voltammetry experiments were carried out on a BioLogic VSP-3 potentiostat using a three-electrode system comprising a glassy carbon working electrode, a platinum wire counter electrode, and a Ag/AgCl reference electrode which was stored in 3 M KCl solution. The working electrode was polished using microfibre pads by fine polishing with 6  $\mu\text{m}$  diamond polish, 1  $\mu\text{m}$  diamond polish, and 0.05  $\mu\text{m}$  alumina polish, then rinsed with deionized water and air dried before use. CV solutions were prepared by dissolving the compound of interest (10 mg) in 0.1 M NaCl solution which was prepared in bulk. Solutions were sparged using  $\text{N}_2$  gas and then cyclic voltammetry was performed over a range of scan rates.

Where viologen/anolyte mixed studies were performed, these were first performed on only the viologen and then, following the addition of anolyte material (FCN), the solution was sparged again with N<sub>2</sub> and then mixed studies performed.

#### 3.5.4 Flow Cell Tests

Flow cell testing was conducted using a flat cell type consisting of two stainless steel end plates, two graphite current collectors, and 6 EPDM, FPM sealing gaskets (ElectroCell, Denmark); See [Figure 3.1](#) for a detailed overview. The anion exchange membrane, FAA-3-PE-30 (thickness, 120 μm, pore size 10 Å, Fumatech, Germany) and carbon felt (6.35 mm thick, 99.0%, Alfa Aesar) were cut to appropriate size with 10 cm<sup>2</sup> active area of the electrode and the separator. Originally, a Masterflex® L/S® Digital Miniflex® Pump System (Cole-Parmer) was used to circulate the electrolytes through the electrodes at varying flow rates. This was later replaced with a Longer L100-IE peristaltic pump with 4 channels. Tubing was connected using Asynt® polypropylene fittings for 1/8" tubing diameter. Each reservoir held 15-20 mL of the electrolyte containing a supporting electrolyte of either NaCl, KCl, or NH<sub>4</sub>Cl, and various concentrations of active materials. Both reservoirs were purged with nitrogen and sealed before cell cycling. The flow cell was galvanostatically charged/discharged at room temperature on a BioLogic VSP-3 potentiostat in a specified voltage range at current densities ranging from 2 to 10 mA.cm<sup>-2</sup>. Electrochemical impedance spectroscopy (EIS) was carried out to measure resistance of the system before and after cycling.

The EIS tests were carried out at approximately 100% SOC between the positive and negative electrodes over a frequency range from 10 MHz to 10 kHz, distributed evenly on a logarithmic scale. Post-cycling analysis of the electrolytes was conducted using CV and <sup>1</sup>H NMR. <sup>1</sup>H NMR spectra were recorded using a DMSO capillary and 0.5 mL of electrolyte.

### 3.5.5 Membrane Permeability Tests

Static permeability tests were carried out in a homemade osmotic chamber. The left side of the osmosis chamber was filled with 0.1 M **1** in 1.0 M NaCl (25 mL), and the right side was filled with 0.2 M FCN in 1.0 M NaCl (25 mL). The half-cells were separated by a fumasep® FAA-3-PE-30 AEM and were monitored over 48 hours. The density was measured by weighing 10 µL of each electrolyte at set-up and again after 48 hours. The electrolyte solutions were analysed by <sup>1</sup>H NMR and CV, and the pH of the initial and final solutions was recorded. This method was repeated for a pre-treated fumasep® FAA-3-PE-30 AEM which had been pre-treated for 24 h in 1 M NaCl before being used in the osmotic chamber. Dynamic tests were carried out in the flow cell, under standard conditions. One electrolyte reservoir was filled with 1 M NaCl (20 mL), and the other reservoir contained a solution of 0.2 M FCN which was made up with 1M NaCl supporting electrolyte (20 mL). The electrolytes were sparged with N<sub>2</sub>, and then circulated, without current, at 70 mL.min<sup>-1</sup>. The flow cell was assembled under standard conditions. Chronopotentiometry was run at 60 mA, -0.4 -0.4 V for 1 hour and 50 minutes with a corresponding capacity limit ( $|\Delta Q|$ ) of 110.160 mAh. Thereafter, a 0.5 mL aliquot of the NaCl electrolyte was collected, the electrolyte was resparged, and chronopotentiometry was run at -60mA, -0.4-0.4 V for 1 hour and 30 minutes with a corresponding capacity limit ( $|\Delta Q|$ ) of 90.167 mAh.

### 3.5.6 Pre-treatment Methods

Two pieces of carbon felt were cut to size (3.3 x 3.3 cm) and were placed in the oven at 200 °C for 24 hours under oxygen atmosphere. The felts were removed from the oven and placed in the flow cell which was immediately assembled for use. The AEM were pre-treated by submerging the membrane in 1 M NaCl solution and fixing it between two watch-glasses to

prevent the membrane from curling. Before use in the flow cell, the membrane was rinsed with deionized water for 2 minutes to remove any excess ions on the surface. Thereafter, the membrane was placed in the flow cell which was assembled as normal.

### 3.6 References

- 1 H. Chen, G. Cong and Y. C. Lu, *J. Energy Chem.*, 2018, **27**, 1304–1325.
- 2 A. Clemente and R. Costa-Castelló, *Energies*, 2020, **13**, 1–31.
- 3 A. Colthorpe, China's largest solar-plus-flow battery project will be accompanied by VRFB 'gigafactory', <https://www.energy-storage.news/chinas-largest-solar-plus-flow-battery-project-will-be-accompanied-by-vrfb-gigafactory/>, (accessed 22 February 2022).
- 4 B. Santos, *PV Mag.*, 2022.
- 5 BloombergNEF, <https://about.bnef.com/blog/top-10-energy-storage-trends-in-2023/>, (accessed 22 February 2023).
- 6 L. F. Arenas, C. Ponce de León and F. C. Walsh, *J. Energy Storage*, 2017, **11**, 119–153.
- 7 M. Arbabzadeh, J. X. Johnson, G. A. Keoleian, P. G. Rasmussen and L. T. Thompson, *Environ. Sci. Technol.*, 2016, **50**, 1046–1055.
- 8 W. Liu, Y. Liu, H. Zhang, C. Xie, L. Shi, Y. G. Zhou and X. Li, *Chem. Commun.*, 2019, **55**, 4801–4804.
- 9 J. Luo, B. Hu, C. Debruler and T. L. Liu, *Angew. Chemie - Int. Ed.*, 2018, **57**, 231–235.
- 10 D. Reber, J. R. Thurston, M. Becker and M. P. Marshak, *Cell Reports Phys. Sci.*, 2023, **4**, 101215.
- 11 J. Luo, A. Sam, B. Hu, C. DeBruler, X. Wei, W. Wang and T. L. Liu, *Nano Energy*, 2017, **42**, 215–221.
- 12 M. H. Chakrabarti and E. P. L. Roberts, *J. Chem. Soc. Pakistan*, 2008, **30**, 817–823.
- 13 E. Fell, D. De Porcellinis, Y. Jing, V. Gutierrez-Venegas, R. Gordon, S. Granados-Focil and M. Aziz, *Long-term stability of ferri-/ferrocyanide as an electroactive component for redox flow battery applications: on the origin of apparent capacity fade*, 2022.
- 14 J. Asenjo-Pascual, I. Salmeron-Sanchez, J. R. Avilés-Moreno, P. Mauleón, P. Mazur and P. Ocón, *Batteries*, 2022, **8**, 193.
- 15 Y. Liu, Y. Li, P. Zuo, Q. Chen, G. Tang, P. Sun, Z. Yang and T. Xu, *ChemSusChem*, 2020, **13**, 2245–2249.
- 16 J. Luo, B. Hu, C. Debruler, Y. Bi, Y. Zhao, B. Yuan, M. Hu, W. Wu and T. L. Liu, *Joule*, 2019, **3**, 149–163.

- 17 T. Hagemann, J. Winsberg, M. Grube, I. Nischang, T. Janoschka, N. Martin, M. D. Hager and U. S. Schubert, *J. Power Sources*, 2018, **378**, 546–554.
- 18 V. Singh, S. Kim, J. Kang and H. R. Byon, *Nano Res.*, 2019, **12**, 1988–2001.
- 19 J. Winsberg, T. Hagemann, T. Janoschka, M. D. Hager and U. S. Schubert, *Angew. Chemie - Int. Ed.*, 2017, **56**, 686–711.
- 20 Z. Li, Y. C. Lu, Z. Rhodes, J. R. Cabrera-Pardo, M. Li, S. D. Minteer, P. Leung, T. Martin, Q. Xu, C. Flox, M. R. Mohamad, J. Palma, A. Rodchanarowan, X. Zhu, W. W. Xing, A. A. Shah, Z. Li, Y. C. Lu, E. Sánchez-Díez, E. Ventosa, M. Guarnieri, A. Trovò, C. Flox, R. Marcilla, F. Soavi, P. Mazur, E. Aranzabe and R. Ferret, *Appl. Energy*, 2021, **32**, 101–112.
- 21 E. S. Beh, D. De Porcellinis, R. L. Gracia, K. T. Xia, R. G. Gordon and M. J. Aziz, *ACS Energy Lett.*, 2017, **2**, 639–644.
- 22 D. G. Kwabi, Y. Ji and M. J. Aziz, *Chem. Rev.*, 2020, **120**, 6467–6489.
- 23 S. Liu, M. Zhou, T. Ma, J. Liu, Q. Zhang, Z. Tao and J. Liang, *Chinese Chem. Lett.*, 2020, **31**, 1690–1693.
- 24 Z. Yan, R. J. Wycisk, A. S. Metlay, L. Xiao, Y. Yoon, P. N. Pintauro and T. E. Mallouk, *ACS Cent. Sci.*, 2021, **7**, 1028–1035.
- 25 T. Janoschka, C. Friebe, M. D. Hager, N. Martin and U. S. Schubert, *ChemistryOpen*, 2017, **6**, 216–220.
- 26 R. Papadakis, I. Deligkiozi, M. Giorgi, B. Faure and A. Tsolomitis, *RSC Adv.*, 2015, **6**, 575–585.
- 27 V. F. Ivanov, D. N. Kiselev and V. A. Tverskoi, *Russ. Chem. Bull.*, 1995, **44**, 87–90.
- 28 E. Sánchez-Díez, E. Ventosa, M. Guarnieri, A. Trovò, C. Flox, R. Marcilla, F. Soavi, P. Mazur, E. Aranzabe and R. Ferret, *J. Power Sources*, 2021, **481**, 228804.
- 29 L. F. Castañeda, F. C. Walsh, J. L. Nava and C. Ponce de León, *Electrochim. Acta*, 2017, **258**, 1115–1139.
- 30 L. Eifert, R. Banerjee, Z. Jusys and R. Zeis, *J. Electrochem. Soc.*, 2018, **165**, A2577.
- 31 E. Sebti, M. M. Besli, M. Metzger, S. Hellstrom, M. J. Schultz-Neu, J. Alvarado, J. Christensen, M. Doeff, S. Kuppen and C. V Subban, *Desalination*, 2020, **487**, 114479.
- 32 Y. Zhou, Y. Sun, C. Zhu, Y. Liu, X. Dai, J. Zhong, Q. Chen, H. Tian, R. Zhou and Z. Kang, *J. Mater. Chem. A*, 2018, **6**, 8955–8961.
- 33 B. Satola, L. Komsiyiska and G. Wittstock, *J. Electrochem. Soc.*, 2017, **164**, A2566.
- 34 E. M. Hammer, B. Berger and L. Komsiyiska, *Int. J. Renew. Energy Dev.*, 2014, **3**, 7–12.
- 35 B. Jiang, L. Yu, L. Wu, D. Mu, L. Liu, J. Xi and X. Qiu, *ACS Appl. Mater. Interfaces*, 2016, **8**, 12228–12238.
- 36 F. Gao, X. Li, Y. Zhang, C. Huang and W. Zhang, *ACS Omega*, 2019, **4**, 13721–13732.

- 37 J. Zeng, C. Jiang, Y. Wang, J. Chen, S. Zhu, B. Zhao and R. Wang, *Electrochem. commun.*, 2008, **10**, 372–375.
- 38 T. Janoschka, N. Martin, M. D. Hager and U. S. Schubert, *Angew. Chemie - Int. Ed.*, 2016, **55**, 14427–14430.
- 39 A. W. Hofmann, *Philos. Trans. R. Soc. London*, 1851, **141**, 357–398.
- 40 S. Jin, E. M. Fell, L. Vina-Lopez, Y. Jing, P. W. Michalak, R. G. Gordon and M. J. Aziz, *Adv. Energy Mater.*, 2020, **10**, 1–10.
- 41 M. H. Chakrabarti, R. A. W. Dryfe and E. P. L. Roberts, *J. Chem. Soc. Pakistan*, 2007, **29**, 294–300.
- 42 C. DeBruler, B. Hu, J. Moss, X. Liu, J. Luo, Y. Sun and T. L. Liu, *Chem*, 2017, **3**, 961–978.
- 43 J. Chai, X. Wang, A. Lashgari, C. K. Williams and J. Jiang, *ChemSusChem*, 2020, **13**, 4069–4077.
- 44 Y. Kim, S. Jeon, D. Ahn, H. Kim, C. Kim and Y. Lee, *Desalination*, 2023, **550**, 116406.
- 45 M. L. Perry, J. D. Saraidaridis and R. M. Darling, *Curr. Opin. Electrochem.*, 2020, **21**, 311–318.
- 46 R. Darling, K. Gallagher, W. Xie, L. Su and F. Brushett, *J. Electrochem. Soc.*, 2016, **163**, A5029–A5040.
- 47 M. Vijayakumar, M. S. Bhuvanewari, P. Nachimuthu, B. Schwenzer, S. Kim, Z. Yang, J. Liu, G. L. Graff, S. Thevuthasan and J. Hu, *J. Memb. Sci.*, 2011, **366**, 325–334.
- 48 M. Gao, M. Salla, F. Zhang, Y. Zhi and Q. Wang, *J. Power Sources*, 2022, **527**, 231180.
- 49 R. Gundlapalli and S. Jayanti, *J. Energy Storage*, 2021, **33**, 102078.
- 50 G. Qiu, C. R. Dennison, K. W. Knehr, E. C. Kumbur and Y. Sun, *J. Power Sources*, 2012, **219**, 223–234.
- 51 A. H. Whitehead, A. Robertson, B. Martin, E. Martin and E. Wilson, *Batteries*, 2022, **8**, 207.



**CHAPTER 4**

**OLEFIN SYNTHESIS BY REDUCTIVE DEHALOGENATION**

**USING PHASE TRANSFER ELECTROCATALYSIS.**

---

*"And my God will meet all your needs according to the riches of His glory in Christ Jesus."*

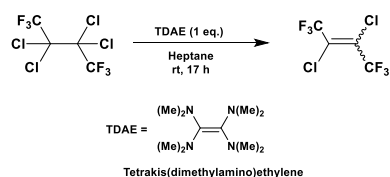
*Philippians 4:19*

## 4.1 Introduction

### 4.1.1 Debromination of vicinal dibromides

Vicinal dibromides (*vic*-dibromides) are valuable intermediates in the synthesis of dyes, pharmaceuticals, agrochemicals and plasticizers.<sup>1</sup> In organic synthesis, carbon-carbon (C-C) double bonds can be “protected” by vicinal bromination however, harsh reaction conditions such as the use of acidic medium at high temperatures and metal-based reductants, are often required for the deprotection of said C-C double bonds.<sup>2</sup> The efficiency of this deprotection/debromination step is limited by sterics and the compatibility of the reductant with C=C double bond formation.<sup>3</sup> Common reductants include zinc, copper, samarium and magnesium, but these have narrow or limited functional group compatibility and are prone to further reducing other functional groups present on the *vic*-dibromide.<sup>3,4</sup> Nevertheless, some organic reductants and methods have been developed for the debromination of *vic*-dibromides.<sup>2-6</sup>

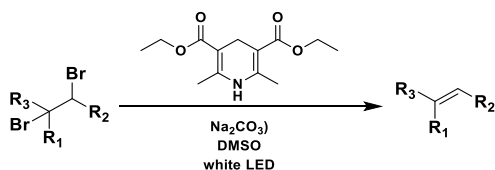
Tetrakis(dimethylamino)ethylene was used by Carpenter,<sup>7</sup> in 1965, for the dehalogenation of 2,2,3,3-tetrachloro-1,1,1,4,4,4-hexafluorobutane to produce 2,3-dichloro-1,1,1,4,4,4-hexafluoro-2-butene. The relative ease of dehalogenation was reported as I > Br > Cl > F.



**Scheme 4.1** Debromination using TDAE as proposed by Carpenter.<sup>7</sup>

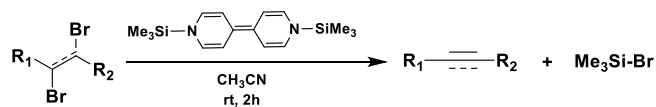
A Hantzsch Ester was used as a combined photosensitizer/reducing agent for visible-light-induced debromination of vicinal dibromides,<sup>2</sup> which boasted the lack of a catalyst used in this method in comparison to former debromination methods.<sup>7,8</sup>

This was possible because the Hantzsch Ester was used as light harvester, electron donor, and hydrogen donor.<sup>2</sup> Aided by Na<sub>2</sub>CO<sub>3</sub> and visible light, the self-activated Hantzsch ester successfully debrominated α,β-unsaturated compounds and unfunctionalized alkenes spanning a wide range of functional groups.



**Scheme 4.2** Debromination of vic-dibromides using Hantzsch Ester.<sup>2</sup>

Shortly thereafter, Mashima *et al.*<sup>5</sup> published a transition metal-free and salt free method to dehalogenate vicinal dihalo compounds. The group investigated different organosilicon reductants and found 1,10-bis(trimethylsilyl)-1H,1'H-4,4'-bipyridinylidene to be the best, affording a 98% yield of styrene from 1,2-dibromoethylbenzene. They concluded that this method had a wide substrate applicability whilst keeping various functional groups intact and that under mild-neutral conditions corresponding alkenes and alkynes were afforded without salt waste, which was an added advantage to known dehalogenation routes.



**Scheme 4.3** Salt-free and transition free debromination by Mashima *et al.*<sup>9</sup>

#### 4.1.2 Electrogenerated species

During an electrosynthetic process, several *in situ* reagents, such as acids, bases, and superoxides may be generated.<sup>10,11</sup> Trace amounts of water in the system may be oxidized, creating an acidic environment, and this *in situ* generation of protons may result in the formation of *electrogenerated acids* (EGAs) which catalyse reactions at the electrode surface.<sup>11</sup>

This has been observed for multiple reaction types including: protection or deprotection of alcohols, acetalization of carbonyls, cyclization of isoprenoids, and allylation of acetals.<sup>10</sup> In addition, electrogenerated Lewis acids formed *in situ* from the metal ions of sacrificial electrodes may activate the reactants or mediate the reaction.<sup>12</sup>

Similarly, *electrogenerated bases* (EGBs) may also be generated in electrosynthetic reactions when anion radicals or anions are formed due to electroreduction and can deprotonate or initiate base-catalysed reactions, which can prove useful by minimizing the use of strong bases within the system.<sup>10</sup> However, specific conditions are required in order to generate these EGBs. Specifically, the reduction potential of the substrate in the solution must be higher than that of the EGB, and the EGB must both have a low nucleophilicity and be a weak reducing agent to prevent unwanted side reactions.<sup>11</sup> Using EGBs, organic compounds such as oxazolidinones, carbamates, and lactams can be synthesized.<sup>10,11</sup>

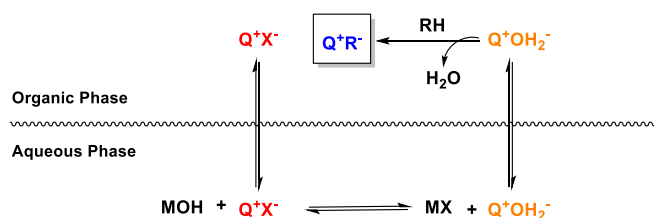
Electrogenerated superoxides ( $O_2^{\cdot-}$ ) may be used as a reducing agent, base, or nucleophile during electrosynthesis. In the presence of carbon dioxide it is able to form peroxodicarbonate, and affords further use in the field of carbon capture,<sup>11</sup> as demonstrated by Moracci and Inesi<sup>13</sup> when they converted primary and secondary amines into carbamides using electrochemically synthesized peroxodicarbonate.<sup>13</sup>

### 4.1.3 Phase-transfer catalysis

The concept of phase-transfer catalysis has been extensively explored as a way of utilizing water-soluble reagents for hydrophobic substrates in organic synthesis.<sup>14</sup> This methodology involves facilitating the movement of a reagent across an interface, often aided by a catalyst such as an organic-soluble quaternary ammonium cation.<sup>14-16</sup>

The term "phase-transfer" catalysis was coined by Starks<sup>15</sup> in 1971 when they published work using quaternary salts as catalysts for displacement reactions and the preparation of dichlorocyclopropanes from olefins. One of the reactions explored in this work was the reaction between 1-bromooctane and aqueous sodium cyanide resulting in the formation of 1-cyanooctane. The mechanism of this reaction, as proposed by Starks, can be seen in

**Scheme 4.4.** Other examples of phase-transfer include intermolecular alkylation, asymmetric alkylation of Glycine Ester Schiff Base, and intramolecular Oxo-Michael Addition.



**Scheme 4.4** Starks Extraction Mechanism of Phase-Transfer Catalysis.<sup>15</sup>

Organic electrosynthesis offers a greener method to perform redox reactions under milder and safer conditions using electrons to drive the reaction.<sup>17</sup> Biphasic electrocatalysis encompasses the safety and ease of organic electrosynthesis or electrocatalysis, coupled with the advantage of rate enhancement between substrates/reagents that may be partitioned between immiscible phases.

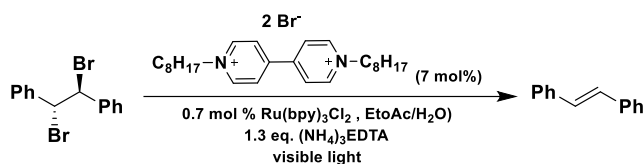
In this way, the catalyst may be consistently replenished in a different phase from the substrate which would afford smaller amounts of reagents required. One such example of this is the electrosynthesis of hydrogen peroxide using molecular redox mediation and phase-transfer catalysis wherein proton-electron reducing equivalents were shuttled between three immiscible phases to produce hydrogen peroxide in flow without precious metal catalysis.<sup>18</sup>

Typical phase transfer catalysts include quaternary ammonium salts, crown ethers and phosphonium compounds,<sup>19</sup> and these are often selected based on their solubility and stability under reaction conditions.<sup>15</sup> Starks reported salts containing phenyl, allyl and benzyl groups were unstable under the chosen reaction conditions.<sup>15</sup>

Viologens are a type of quaternary pyridinium salts (QPS) containing conjugated bipyridyl groups, and have several properties making them suitable for both electrocatalysis and phase transfer catalysis.<sup>20</sup> However, viologens are predominantly considered as undergoing simple outer-sphere electron transfer, so their potential for catalysis has generally been considered relatively low. Nevertheless, some examples of viologen-driven reductive redox catalysis do exist, including reductions of nitro compounds<sup>21,22</sup>, azo compounds<sup>23</sup>, and activated alkyl halides.<sup>24,25</sup> which use a variety of chemical terminal reductants such as samarium iodide, sodium dithionite, and zinc.

In 1986, Willner and Maidan<sup>8</sup> reported a photochemical and chemical enzyme catalysed method of debromination using ruthenium(II) tris(bipyridine) ( $\text{Ru}(\text{bpy})_3$ ) as the catalyst and NADH as the terminal reductant. The reaction was carried out using enzyme-catalysed systems which were supported on Sepharose beads and ethanol, lactic acid, alanine, and formate acted as electron donors for the debromination.

The group highlighted the hydrophilic-hydrophobic balance of the redox couple  $C_8V^{2+}/C_8V^+$  which allowed electrons to be released in the organic phase.

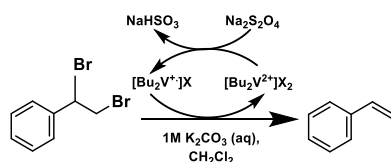


**Scheme 4.5** Biphasic phase transfer catalysis by Willner and Maidan.<sup>26</sup>

## 4.2 Biphasic electrocatalysis

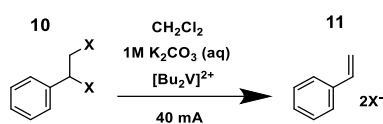
### 4.2.1 Viologens as phase-transfer catalysts

Viologens can be used as phase-transfer catalysts for biphasic catalysis as demonstrated by Endo *et al.*<sup>27</sup> in 1983, using varied chain length viologens (methyl, ethyl, propyl, heptyl, and dodecyl) coupled with different solvent systems. The dication forms of short-chain alkyl viologens,  $[R_2V]^{2+}$ , are water soluble but may be singly reduced to radical cation states,  $[R_2V]^+$  and are highly soluble in organic solvents. Their (alkyl viologens) differing solubility makes for an ideal candidate in phase transfer redox reactions wherein electrons are transferred from an aqueous reducing agent, *via* the viologen, to a substrate dissolved in an organic medium. Endo showed that this could be used to effect the efficacy of the reaction by using excess reducing agent, sodium dithionite, with the overall reaction given in **Scheme 4.6**.



**Scheme 4.6** Biphasic catalytic dehalogenation by Endo.<sup>27</sup>

With this in mind, we sought to exploit the principle of phase-transfer catalysis by using viologens,  $[5]X_2$  salts, as catalysts for electro-debromination. Specifically, the use of viologens as phase-transfer electrocatalysts for the reductive dehalogenation of various brominated species to produce an array of styrene derivatives. Using a biphasic system comprised of dichloromethane and water, we predicted that  $[5]^{2+}$  would undergo electro reduction in the aqueous phase forming the radical cation,  $[5]^{\cdot+}$ , which would move into the organic layer and reduce the substrate, regenerating the dication which would return to the aqueous phase, thus effectively catalysing substrate debromination.



**Scheme 4.7** Biphasic electrocatalytic dehalogenation as proposed in this work.

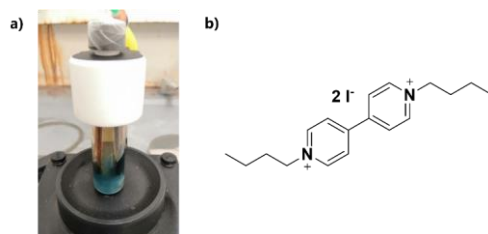
As a result of technological advancements, the IKA Electrasyn offered a means to potentially further the work of Endo<sup>27</sup> by conducting the electrocatalytic studies in an undivided cell with graphite electrodes. 1,2-Dibromoethylbenzene, **10**, was selected as the initial test substrate, with hexamethylbenzene as an internal standard, and using 1 M  $K_2CO_3$  as supporting electrolyte for the aqueous phase. The diiodide salt, **5a**, was selected as the initial test catalyst due to its ease of synthesis. The test reaction was performed on 1.5 mmol substrate scale using 15 mol% catalyst based on literature precedent using a chemical reductant at this loading.<sup>21,22,27</sup> The cell was constructed such that the electrodes were not in contact with the organic layer, which was 2 mL DCM and 10 mL of electrolyte was used. A schematic of the cell set-up and overall expected reaction process is shown in **Figure 4.1**. These conditions allow the use of cheap electrolytes, water, and DCM, without stoichiometric amounts of catalyst like Willner<sup>8</sup> or Park.<sup>21,22</sup>





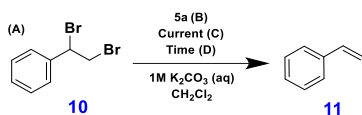
**Scheme 4.8** Proposed mechanism for biphasic electrocatalysis using an IKA Electrasyn.

Preliminary tests kept the following parameters constant; catalyst loading, electrolyte volume, DCM volume, and the nature of supporting electrolyte (1.0 M  $K_2CO_3$ ). Based on this success, subsequent optimization of the system was carried out, varying the applied current and reaction time and this allowed us to develop a system which yielded 100% conversion from **10** to form **11** after 18 hours at 15% catalyst loading (**Table 4.1, Run 8**).



**Figure 4.1** a) Electrode fouling due to  $I_2$  deposition on the electrode.; b) Structure of catalyst (**5a**) with iodoine as the counter anion.

During testing, it was found that despite being cheap, and easy to synthesise in comparison to other catalysts, we found that reactions with **5a** rapidly discoloured due to simultaneous oxidation of  $I^-$  to  $I_2$  at the anode under operating conditions. The presence of  $I^-$  in the reaction was due to the counter-ion for the catalyst, **5a**. This posed a grave issue: rapidly fouling electrodes which decreased the active surface area of the electrode, which varied the rate of conversion from **10** to **11** substantially between optimisation runs due to inconsistent electrode fouling.

**Table 4.1** Preliminary results for biphasic electrocatalysis.\*

| Run            | A (mmol) | B (mmol) | C (mA) | D (hours) | NMR Yield (%) |
|----------------|----------|----------|--------|-----------|---------------|
| 1              | 1.63     | 0.195    | 10     | 18        | 80            |
| 2              | 1.63     | 0.195    | 20     | 16        | 89            |
| 3              | 1.53     | 0.196    | 40     | 18        | 96            |
| 4              | 1.56     | 0.2      | 60     | 18        | 59            |
| 5              | 1.56     | 0.19     | 60     | 18        | 31            |
| 6 <sup>a</sup> | 1.6      | 0.194    | 40     | 18        | 36            |
| 7 <sup>b</sup> | 1.56     | 0.2      | 40     | 18        | 89            |
| 8 <sup>c</sup> | 1.53     | 0.194    | 40     | 18        | 100           |

\*New Electrodes used. <sup>b</sup>Switching polarity of the electrodes every 59 minutes. <sup>c</sup>Switching polarity of the electrodes every 30 minutes. Reaction was run in triplicates.\*No internal standard was used.

Inspired by Kawamata and co-workers,<sup>28</sup> who used alternating polarity to enhance chemoselectivity in their reactions, the polarity of the ElectraSyn electrodes was alternated during the reactions on two different occasions ([Run 7](#) and [Run 8](#)), switching the polarity every 59 minutes, and every 30 minutes, respectively. This mitigated the issue of electrode fouling, removing *macro*-deposits on the electrodes, and thus maintaining a relatively steady rate of conversion to form **11**. However, the electrodes were found to decay rapidly under these conditions and the parasitic side reactions of iodide reduction and reoxidation were associated with extremely poor NMR yield as seen between [Run 3](#) and [Run 6](#).

As a result of these observations, we tested the use of **5b** as catalyst and found that it offered improved results with fewer *macro*-deposits on the electrodes during the reaction, thus improving the longevity of the electrodes. The initial rate of reaction was comparable with that of **5a** and, given that it was less damaging to the electrodes, the dibromide was selected for further optimization, maintaining a catalyst 15 mol%.

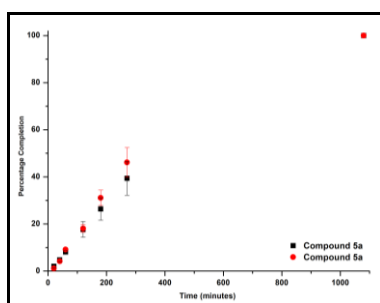
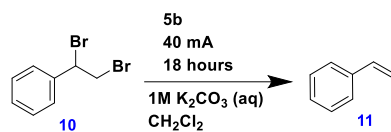


**Figure 4.2** Comparing rate of conversion using **5a** or **5b** as catalyst.

Once initial test reactions had confirmed that it was possible to convert **10** to **11** using biphasic electrocatalysis, an internal standard, hexamethylbenzene, was added to allow an accurate NMR yield to be determined during further optimization reactions. Since 40 mA had shown the best conversion when using **5a**, this was selected as the operational current for further optimization reactions using **5b**.

As mentioned, initial work was run at a 15 mol% catalyst loading given that this was the limit frequently imposed in the literature.<sup>21,22,27</sup> Keeping all other parameters constant, and changing only the catalyst loading, a short investigation was conducted into the effect of catalyst loading on the rate of conversion of **10** to **11**.



**Scheme 4.9** The electrocatalytic conditions used to investigate the effect of catalyst loading on the reaction progress. \*Polarity was alternated every 30 minutes.

As evidenced by the sluggish rate of conversion yielding only 28% conversion after 10 hours, observed at 6 mol% catalyst loading **Figure 4.3**, the catalyst is essential to this reaction. Additionally, the 100% conversion after approximately 4.5 hours at 50% catalyst loading confirmed that the rate of conversion is proportional to the catalyst loading.

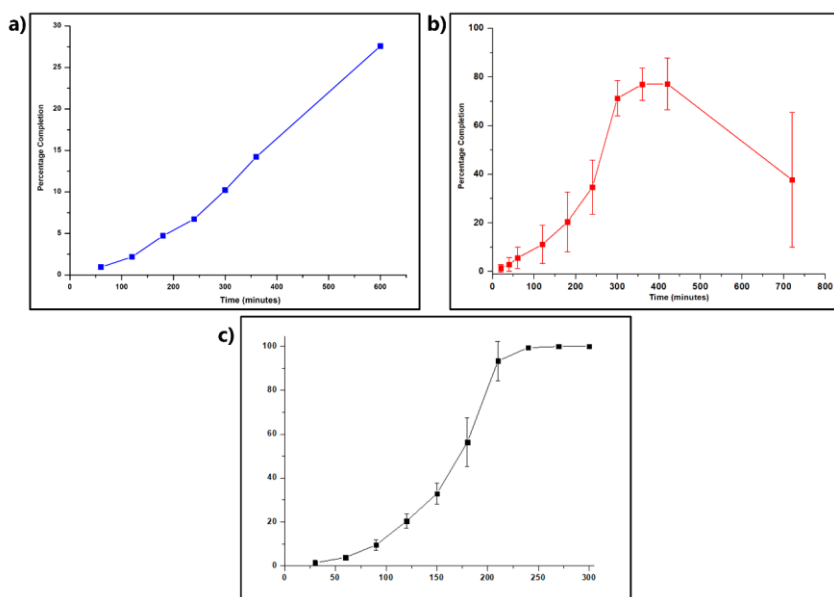


**Figure 4.3** Effect of catalyst loading at a) 6 mol%, b) 15 mol% and c) 50 mol%, versus percentage conversion to **11**, determined by  $^1\text{H}$  NMR.

Having confirmed the need for the catalyst, **5b**, further optimization efforts were directed at the reaction time. While keeping all other parameters constant, and alternating electrode polarity every 30 minutes, the reaction time was investigated, running the system for 14

hours and a second attempt at 12 hours, the results can be seen in **Figure 4.4**. Despite the conversion for 14 hour reaction being quite low, these results provided new insight into the reaction mechanism as it appeared that the reaction was moving in a reverse direction as seen by the decrease in percentage conversion between the last two data points **Figure 4.4**.

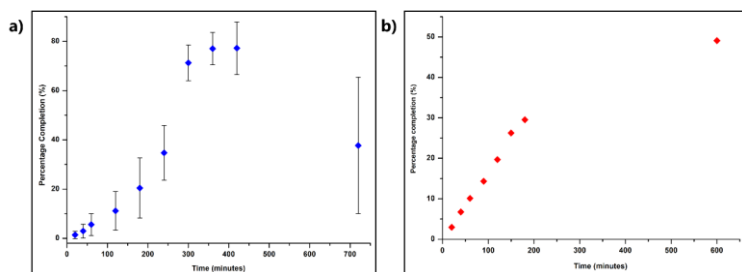


**Figure 4.4** Comparing rate of conversion using **5b** as catalyst for a total reaction time of a) 14 hours, and b) 12 hours.

#### 4.2.2 Induction Time and Use of Br Scavenger

Based on the acceleration in rate seen at higher catalyst loadings, we hypothesized that the system required an induction period to form adequate amounts of radical cation **[5b]<sup>+</sup>**; the presumed active catalyst for the system. Visual monitoring of the system indicated the need for a certain amount of time, without substrate, to form significant amounts of the catalyst, as indicated by the formation of an intensely blue-coloured DCM layer due to the formation of the radical cation **[5b]<sup>+</sup>** shown in **Figure 4.5**. This hypothesis was tested by rerunning the system for a total of 14 hours, keeping all other parameters constant, and implementing an induction period. The conditions were as follows; 15 mol% catalyst loading, 1M  $K_2CO_3$ , 10 mL of electrolyte, 1 mL DCM, 40 mA, hexamethyl benzene as the internal standard and the polarity was switched every 30 minutes. The system was run for the first 4 hours without any substrate: after 4 hours a 1 mL solution of DCM containing 1.52 mmol of substrate was added to the reaction vial.

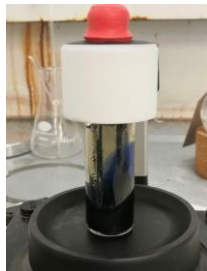


**Figure 4.5** Visual confirmation of the generation of  $[5b]^+$  in the DCM layer.

Aliquots of the DCM layer were collected over the duration of the experiment and were analysed by  $^1H$  NMR, and the results of NMR yield as a function of time are shown in **Figure 4.6**. Preliminary data had showed that the reaction had reached maximum conversion of 98% after ~5 hours but had decreased to 72% at the end point. Whilst the use of **5b** had proved initially favourable over the diiodide, a new issue was identified. After an extended period, 5 hours, the reaction seemed to be driven in reverse which was attributed to the formation of excess  $Br_2$  in the system which could easily “re-halogenate” the newly formed olefin.

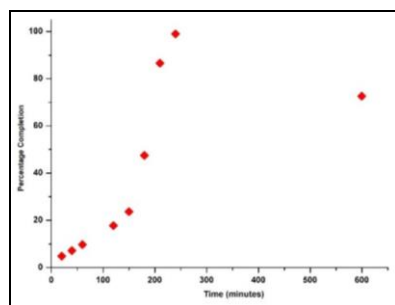


**Figure 4.6** Pre-liminary testing showing the percentage conversion with a 4 hour induction time implemented at the start; normalized to the internal standard.

Based on this, we recognised that the presence of a Br<sub>2</sub> scavenger was of paramount importance. Cyclohexene was chosen as a cheap, electron rich alkene as compared to styrene, and conversion in the presence and absence of cyclohexene as a Br<sub>2</sub> scavenger was compared. Not only did the cyclohexene increase the rate of reaction as seen by the steeper gradient of the curve within the first 3 hours, but the final NMR conversion was also 85% in comparison to the 72% previously obtained in the absence of the scavenger. Periodic monitoring of the reaction by <sup>1</sup>H NMR clearly showed the formation of 1,2-dibromocyclohexane, whilst facilitating adequate conversion of the substrate to form styrene. (Appendix 2, Figure A2.1)

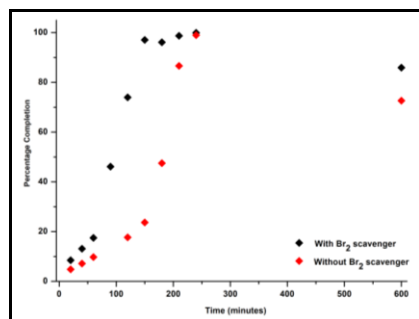


**Figure 4.7** NMR conversion in the presence and absence of cyclohexene as a Br<sub>2</sub> scavenger.

With the use of cyclohexene as the Br<sub>2</sub> scavenger, we continued with the optimization of the induction period as this seemed to be most favourable in improving the conversion from substrate to desired styrene. **Table 4.2** shows the variations of induction and reaction time that were investigated.

**Table 4.2** Variations of reaction time and induction time for biphasic debromination.

| Trial | Induction time<br>(Hours) | Total time <sup>a</sup><br>(Hours) | NMR Yield (%) |       | Faradaic<br>Efficiency<br>(%) |
|-------|---------------------------|------------------------------------|---------------|-------|-------------------------------|
|       |                           |                                    | Max           | Final |                               |
| 1     | 4                         | 14                                 | 99            | 75    | 31                            |
| 2     | 4                         | 9                                  | 44            | 44    | 6                             |
| 3     | 2                         | 14                                 | 95            | 67    | 11                            |
| 4     | 2                         | 9                                  | 98            | 81    | 9                             |
| 5     | 2                         | 7                                  | 100           | 100   | 68                            |

<sup>a</sup>Reaction time refers to the entire duration of the reaction including the induction time.

As seen in **Table 4.2**, decreasing the reaction time to 9 hours whilst maintaining a 4 hour induction period proved to be the worst variation that was tested as this only resulted in a 44% yield of **11**. In comparison, the 2 hour induction period afforded higher yields for both the 14 hour and 9 hour reactions.

When comparing the faradaic efficiency for either run, it was evident that **trial 4** was the better choice given the higher faradaic efficiency and ultimately a higher final yield of **11**. However, despite the higher yield, the reaction still proceeded in the reverse direction, and this appeared to have occurred after 5 hours. Based on this finding, **trial 5** was run for a shorter reaction time – 7 hours, maintaining the 2 hour induction period - which resulted in the highest yield obtained at an end point (97%), coupled with the highest Faradaic efficiency. **Figure 4.8** shows the results obtained relative to internal standard as per the variations detailed in **Table 4.2**.



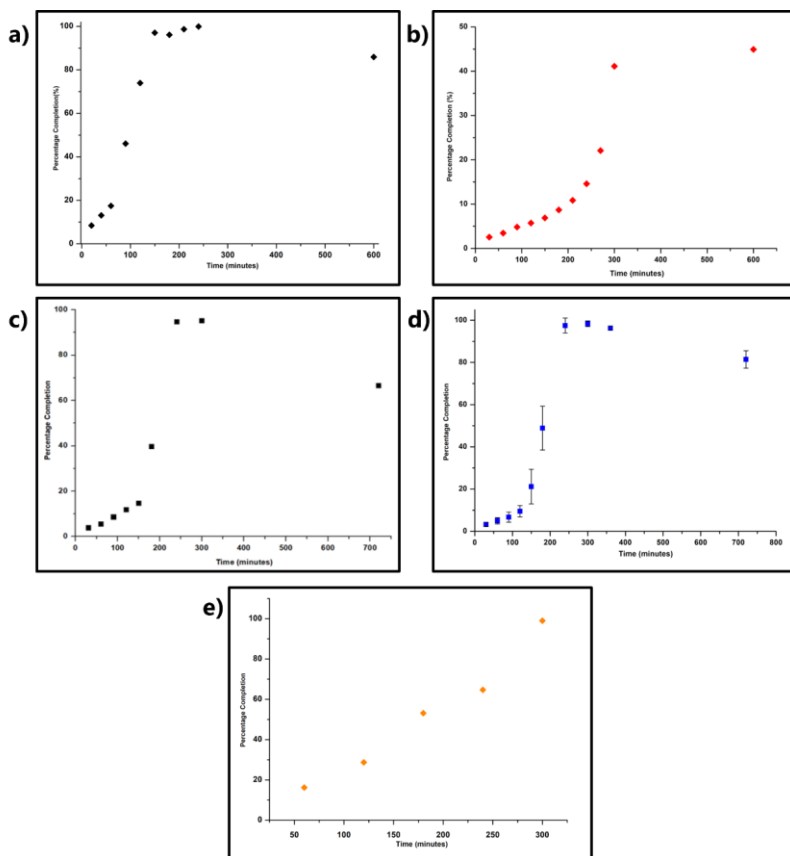


**Figure 4.8** Results of varying the induction and reaction time; a) Trial 1 ; b) Trial 2, c) Trial 3 ; d) Trial 4 ; and e) Trial 5. \* $T_0$  on the graphs represents the time when the substrate was added after the induction time had elapsed.

#### 4.2.3 Electrolyte composition

Up to this point, the nature of aqueous layer had remained 1 M  $K_2CO_3$  as inspired by Endos<sup>27</sup> work, however, changing the aqueous layer of the reaction provided further insight into the complexity of the reaction process. Initially, NaBr was investigated as an electrolyte as it was hoped it would act as a  $Br_2$  scavenger through formation of less reactive  $[Br_3]^-$  which would be retained in the aqueous phase, removing the need for alkene halogen scavenger

additives. However, the  $[\text{Br}_3]^-$  was not successful at trapping the  $\text{Br}_2$  as hoped, giving no conversion, and furthermore, there was visible formation of gas (suspected hydrogen formation) at the electrodes as a further unwanted reaction **Figure 4.9a**. Post-mortem analysis of the electrodes revealed *macro* deposits, and the Proton NMR results, shown in **Figure 4.9b** confirmed 0% conversion to **11**, and so it was concluded that NaBr was not a suitable choice for an aqueous layer.

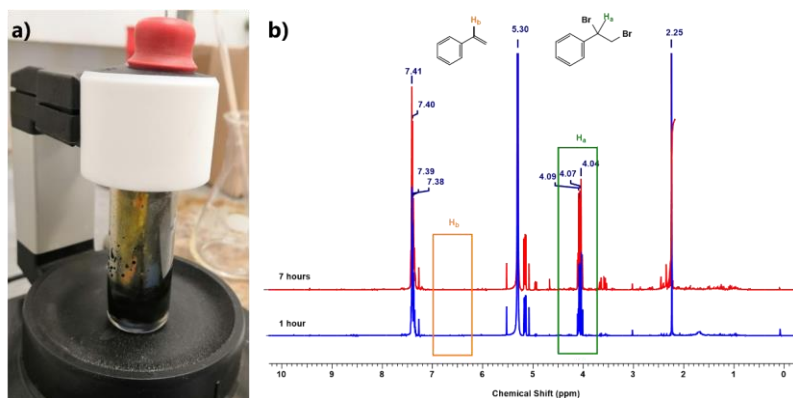
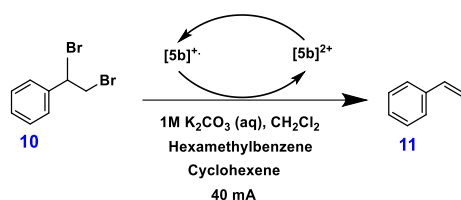


**Figure 4.9** Biphasic electrocatalysis using NaBr as the aqueous layer; a) Evidence of deposits on electrodes. b) Proton NMR spectra comparing the conversion to **11** during the ElectraSyn reaction using NaBr which confirms that no product was formed.

Conversely, despite the use of cyclohexene as a  $\text{Br}_2$  scavenger, the reaction with KCl electrolyte proceeded at a sluggish rate with a maximum NMR yield of 12 % after 5 hours. Previous work is limited, but similar chemistry by Endo<sup>29</sup> and Park<sup>22</sup> both made use of  $\text{K}_2\text{CO}_3$  as a co-reagent. Given the outcome of the reaction in different aqueous medium, it may be concluded that the mildly basic  $\text{K}_2\text{CO}_3$  electrolyte helps to drive the forward reaction, minimizing parasitic  $\text{H}_2$  evolution at the cathode surface, which makes it a good choice for the aqueous electrolyte.

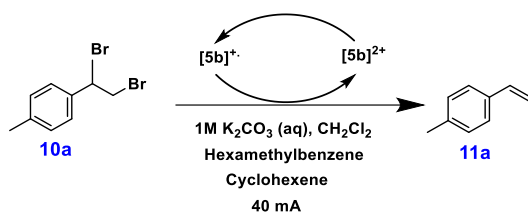
#### 4.2.4 Scavenger Optimization

After optimization, we identified conditions which resulted in > 97% conversion (**Table 4.2** – entry 5), which are shown in **Scheme 4.10**. With good working conditions at hand, we sought to ensure reproducibility and generality of this mechanism before further exploring the substrate scope of this approach. Reproducible repeats were obtained for **11** offering 100% conversion to the desired product by  $^1\text{H}$  NMR.



**Scheme 4.10** Optimized electrocatalytic dehalogenation reactions using a  $\text{Br}_2$  scavenger.

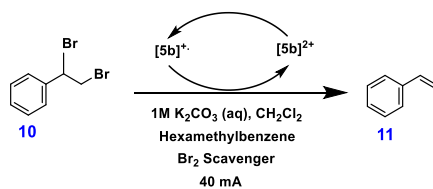
Subsequently, the reduction of 1,2-dibromo-4-methylstyrene (**10a**), was investigated. To our surprise and dismay, the system showed 100% conversion to **11a** on only two occasions and, thereafter reproducible results could not be obtained. The reaction was repeated multiple times to rule out human error and/or technical issues before concluding that there was evidently a serious issue with the set-up.



**Scheme 4.11** Electrocatalytic dehalogenation of **11a**.

Given that the system had worked previously for **11a**, there was great confusion as to why the set-up had simply stopped working. There were several speculations regarding the reason for this: 1) wear and tear on the equipment, 2) the use of graphite electrodes of inferior quality, 3) the efficacy and/or purity of the bromine scavenger, and 4) cell-design (holistic). A systematic approach was followed to eliminate each concern individually. Given the data previously obtained regarding the poor conversion due to excess bromine, the efficacy of the Br<sub>2</sub> scavenger was thoroughly examined. Firstly, the cyclohexene in use was analysed by <sup>1</sup>H NMR which confirmed its purity. However, despite this, the cyclohexene in use appeared to be failing to scavenge the excess bromine. The use of a different source of cyclohexene did not improve the conversion, and in fact, the percentage conversion decreased. A range of alternative possible Br<sub>2</sub> scavengers were thus examined, and the corresponding conversion percentages are listed in **Table 4.3**. 2-cyclohexen-1-one initially seemed to have performed well as a Br<sub>2</sub> scavenger, but unfortunately, this result was not reproducible.

**Table 4.3** <sup>1</sup>H NMR yield (%) of **11** using different Br Scavengers.



| No. | Br Scavenger          | <sup>1</sup> H NMR yield (%) |
|-----|-----------------------|------------------------------|
| 1   | 2-cyclohexen-1-one    | 71.2                         |
| 2   | 3-methyl-2-buten-1-ol | 70.53 ± 12.4                 |
| 3   | Methyl Vinyl Ketone   | 24.7 ± 10.7                  |
| 4   | Cyclohexene           | 25.7                         |

Having eliminated the Br<sub>2</sub> scavenger as the flaw in the reaction, efforts were directed to the electrodes. At the time, the graphite electrodes in use were homemade - low-grade graphite sheets that were then cut to size for the system. It was speculated that the electrodes might have been the cause of the poor conversion from substrate to product, and so to test this, the electrodes were treated to potentially enhance their performance. In the first instance, this was achieved by sonicating the electrodes in very mild acid treatment, 0.1M H<sub>2</sub>SO<sub>4</sub>, and then drying them overnight on a Schlenk line. Another pair of electrodes was filed very gently to remove any surface debris though this also damaged the surface of the electrodes, producing small groves which left the surface uneven. Electrode treatment proved to be unsuccessful and new graphite electrodes were purchased from IKA, unfortunately, this had no effect on the success of the reaction.

As previously described, the original set-up employed two, long, graphite electrodes, and a notionally 10 mL vial. However, this vial was being filled with 12 mL of solvent as well as the electrodes, stirrer bar, and reagents, reaching maximum capacity with no free volume causing the electrolyte to splash the roof of the vial. The next main working hypothesis was therefore that the equipment had endured a substantial amount of wear and tear over time, and this may have resulted in poor contact with the electrodes which would then ultimately affect the rate of conversion. **Figure 4.10** shows the original lid which was in use. There is significant damage to the contacts which has even caused one of the contacts to become severely worn and decrease in size necessitating a wedge to hold the electrodes in place. To investigate the impact of this damage, new vials and lids were purchased from IKA.

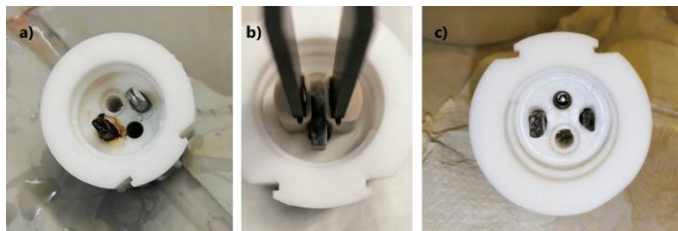


**Figure 4.10** Equipment wear and tear. a) February 2021. Damage to one contact which decreased the size. b) Damaged lid with PTFE wedge which was required to hold electrodes in place. c) March 2022. Severely damaged contacts.

#### 4.2.5 System Redesign

##### 4.2.5.1 Sacrificial Electrode: Zinc (Zn)

Given all the issues experienced with the system and the lack of success following several mitigation strategies, and considering the experience gained, a full evaluation was done on the entire set-up. This included revisiting and considering every aspect of the reaction, including nature of electrodes, solvent ratios, and catalyst loading, *via* a return to first principles and basic understanding of electrocatalysis.

The work by Schotten *et al.*<sup>30</sup> provided great insight into the design of an electrocatalytic system – in particular, the nature of the electrodes used and counter reaction occurring at the anode. Results had indicated that parasitic counter reactions were reducing the Faradaic efficiency of the system as the reaction would move in a reverse direction due to excess bromine, thus warranting the need for a scavenger, and whilst cyclohexene had successfully scavenged  $\text{Br}_2$  during the reaction, this increased the overall reaction costs and further complicated purification of the organic layer. Drawing inspiration from the “Survival Guide” by Baran *et al.*<sup>31</sup> the idea of a sacrificial metal anode, an anode that may be oxidized during the reaction which can ultimately negate the need for a divided cell, was considered.<sup>17</sup>

The only disadvantage of this method is that the anode is non-recyclable, however, given that generated metal ions can occasionally suppress overoxidation of substrates, the oxidation of the anode is not a complete "loss".<sup>12</sup> Therefore, a sacrificial anode becomes attractive as an alternative to an organic halogen scavenger. The use a sacrificial anode was felt to be ideal for a cathodic process because the anode would itself be oxidized instead of species in solution. In the initial system, the two possible counter reactions identified were  $\text{Br}^-$  oxidation and solvent degradation; in the case of a biphasic system containing water, this meant water splitting to evolve extra oxygen and decrease the pH of the aqueous phase which was hypothesised to be detrimental to the system. For a sacrificial anode, anode oxidation would be more favourable than both  $\text{Br}^-$  and water oxidation and so prevent these unwanted processes. Inexpensive metals such as magnesium, zinc, aluminium, and iron are often used as sacrificial anodes owing to their very low oxidation potentials,<sup>12</sup> relatively low toxicity,<sup>32</sup> and ability the to generate Lewis acids *in situ*.<sup>17</sup> Zinc was chosen as a potential sacrificial electrode material, and **Figure 4.11** shows the design of homemade Zn electrodes which were made by folding Zn sheets to appropriate size.

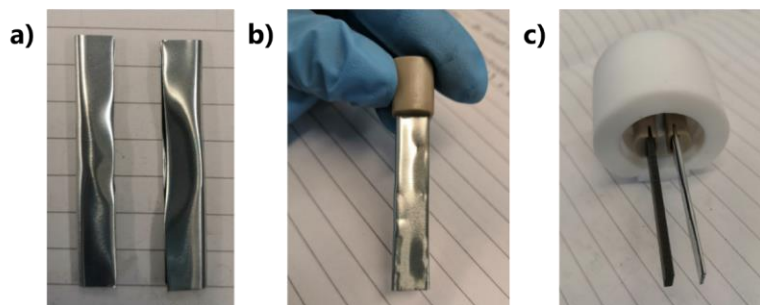


**Figure 4.11** a) Zinc sheets cut to appropriate size for electrodes.; b) Homemade Zn electrodes made from Zinc sheets.; c) Homemade Zn and commercial graphite electrodes in IKA ElectroSyn set-up.

Considering that the reaction design had been overhauled, the induction period was discarded for these initial tests. However, the catalyst mol % loading, volume of DCM, volume of electrolyte and current were maintained as per previous experiments.

As Zn itself is a reducing agent, a control reaction was carried out to confirm whether it could reduce the viologen to the first reduction to form the radical cation, **[5b]<sup>+</sup>**, and the extent to which this would influence the reaction and its outcome. The following symbols will be used henceforth to denote the orientation and nature of the electrodes used: (+) indicates the anode, and (-) indicates the cathode. “|” indicates that the cell was undivided. Hence, from **Scheme 4.12** below, it can be deduced that the reaction ran in an undivided cell with a Zn electrode as the cathode, and a carbon/graphite electrode as the anode. **Figure 4.12** shows that this configuration gave a 96 % conversion of **10** after five hours, after which the reaction moved backwards giving 92% conversion overall.



**Scheme 4.12** Biphasic electrocatalysis using Zn as a sacrificial cathode.

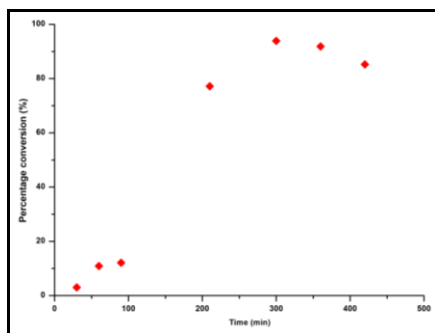


**Figure 4.12** Reaction progression using Zn as a sacrificial cathode.



An additional control reaction was then run to ensure that the Zn electrodes had minimal effect on the rate of conversion in the absence of an applied current. Using all the standard conditions as per **Scheme 4.12**, the reaction was set up for 7 hours in the absence of current, and the  $^1\text{H}$  NMR (**Figure 4.13**) shows 1% conversion, demonstrating that the Zn electrodes were not significantly chemically reducing the viologen and that it remained an electrode mediated process.

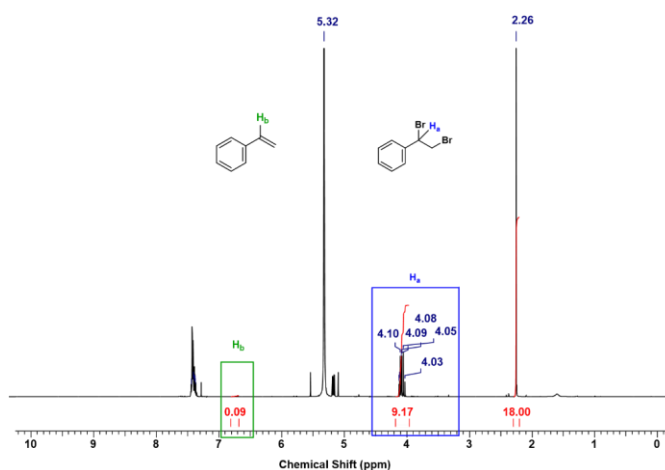


**Figure 4.13** Proton NMR spectrum (recorded in  $\text{CDCl}_3$ ) of the organic layer, after 7 hours, from the control experiment, without current, showing ~1 % conversion to **11**, which confirms that the reaction is an electrode mediated process.; Zn (-).

The initial test using Zn as the anode, needed to be halted after 2.5 hours due to the formation of solid on the surface of the electrode – likely  $\text{Zn}(\text{CO}_3)$ .  $^1\text{H}$  NMR of the organic layer revealed that there had only been 16% conversion of substrate to product in 210 minutes (**Table 4.5, Entry 1**). The formation of solid on the Zn anode is believed to have decreased the active surface area of the electrode and potentially affected the rate of conversion for the reaction.

Given the insolubility of  $\text{ZnCO}_3$  and  $\text{Zn(OH)}_2$ , it was thus necessary to change the nature of the aqueous layer to facilitate adequate conversion to the product when using a Zn anode. Up to this point, 1M  $\text{K}_2\text{CO}_3$  had been used as the mildly basic nature of the aqueous layer favoured the reaction and lead to higher rates of conversion and was in accordance with previous work in literature.<sup>21,22,27</sup> However, the formation of solid on the electrode surface now posed a new obstacle.

It was at this point in the experimental strategy that a crucial discovery was made. Up until this point, the experimental design assumed that the radical cation  $[\mathbf{5b}]^{\bullet+}$  was the catalyst for the reaction, and thus the generation of this species in the aqueous layer was necessary for the success of the reaction, thus necessitating the greater volume of aqueous phase used in the reaction (10 mL) to maximise electrolyte/electrode surface contact. This assumption was based on the work of Endo,<sup>27</sup> Park,<sup>21,22</sup> and Starks.<sup>15</sup>

As part of the deliberate return to first principles, cyclic voltammetry studies were carried out on  $\mathbf{5b}$  using MeCN as the solvent and Tetrabutylammonium hexafluorophosphate  $[(\text{NBu})_4(\text{PF}_6)]$  as the supporting electrolyte. Similar studies were also carried out in 1M NaCl solution to better understand the two separate phases of the reaction process. **Figure 4.14** shows the results obtained in MeCN and 1M NaCl respectively. These results proved that contrary to literature sources,  $[\mathbf{5b}]^0$ , the neutral form, was the active reducing agent rather than  $[\mathbf{5b}]^{\bullet+}$ , as expected. In the absence of the substrate, 1,2-dibromoethylbenzene ( $\mathbf{10}$ ), (**Figure 4.14b – solid blue line**),  $[\mathbf{5b}]^{2+}$  in MeCN shows two reversible peaks corresponding to the first and second electron reduction located at -0.42 V and -0.87 V, respectively. However, the presence of the substrate, 1,2-dibromoethylbenzene ( $\mathbf{10}$ ), (**Figure 4.14b – dotted red line**), results in the depletion of the second reduction peak.

This indicates that it is  $[\mathbf{5b}]^0$ , the neutral form, which interacts with the substrate to dehalogenate it and is itself then oxidised to  $[\mathbf{5b}]^+$ .

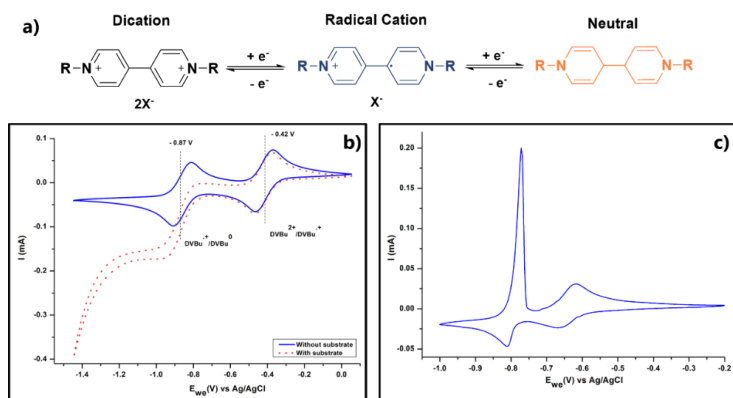


**Figure 4.14** a) The three redox states of **5b**. Cyclic voltammogram of **5b** in b) MeCN, and c) 1 M NaCl. Addition of substrate (b) depletes the 2nd reduction peak, revealing  $[\mathbf{5b}]^0$  as active catalyst contrary to literature.<sup>27</sup>

Conversely, the results obtained in **Figure 4.14c** confirmed the knowledge of the different solubilities for the different redox states of **5b** in accordance with literature.<sup>8,21,22,27</sup> Given that  $[\mathbf{5b}]^{2+}$  is soluble in aqueous electrolytes, **5b** is able to undergo the first electron reduction forming  $[\mathbf{5b}]^+$  at the electrode surface. The first reduction corresponds to a reversible redox event because both  $[\mathbf{5b}]^{2+}$  and  $[\mathbf{5b}]^+$  are soluble in aqueous electrolytes, albeit  $[\mathbf{5b}]^+$  has more limited solubility in aqueous electrolytes but is soluble in organic solvents such as MeCN and DCM. The second redox event is greatly limited by solubility which accounts for the unsymmetrical redox peak observed. The neutral form,  $[\mathbf{5b}]^0$  is insoluble in aqueous electrolytes which causes it to plate on the surface of the electrode, increasing the relative concentration at the electrode.

As the potential sweeps, becoming increasingly positive, it approaches the oxidation potential for the conversion from  $[5b]^0$  to  $[5b]^+$  allowing the radical cation species to rapidly diffuse into the electrolyte thus creating a sudden peak in the current response. When translated into the context of the electrocatalytic cell/biphasic system, it can be concluded that generation of  $[5b]^+$  begins in the aqueous layer. The increasing concentration drives the radical cation into the organic layer where it can then be further reduced to form  $[5b]^0$  which interacts with the dibromide substrate, dehalogenating it, and forming the corresponding olefin.

Due to the differences in solubility and this newly acquired information regarding the nature of the catalyst, it was imperative to alter the cell design. As mentioned, previously more aqueous electrolyte was used to accommodate a higher concentration of  $[5b]^+$ , which is soluble in both the aqueous and organic layer. However, the neutral form is only soluble in the organic layer. As such, the previous design containing greater proportions of aqueous electrolyte likely resulted in the deposition of  $[5b]^+$  on the surface of the electrode and further sequestration from the aqueous layer rather than accumulating in the DCM affording further accumulation of the neutral form after subsequent reduction on the electrode rather than dissolving into the organic phase. Furthermore, were  $[5b]^+$  the catalyst then a lower potential would be required to generate enough of the catalyst, but the neutral form requires a larger potential to be applied to ensure the success of the reaction.

As a result of this, different electrode/solvent interfaces were required to generate the active catalyst in the organic phase. In addition to a larger volume of organic electrolyte being required, the cathode must extend into the organic layer as it is there that the useful reduction to the neutral form,  $[5b]^0$ , must occur.

Conversely, the anode must be isolated from the organic layer to prevent catalyst re-oxidation and inhibition of conversion – the new cell design is shown in **Figure 4.15**.

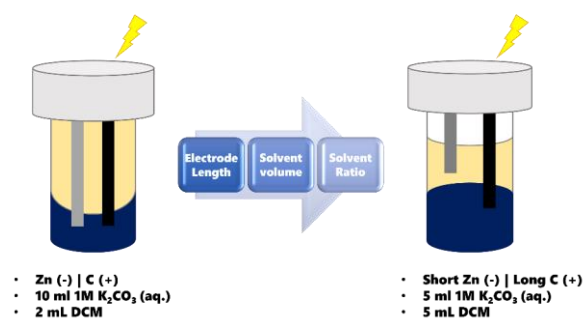


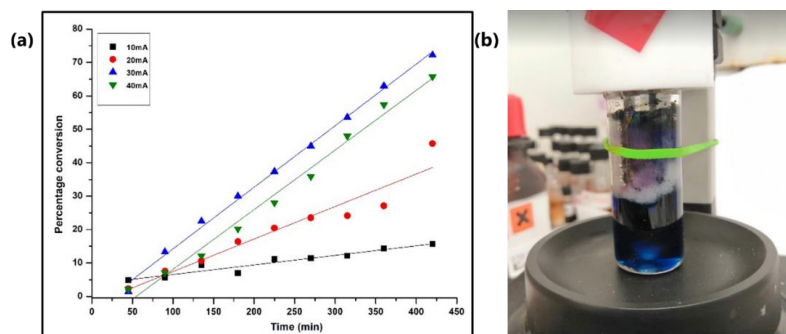
**Figure 4.15** The design overhaul for the biphasic system which incorporated different nature and lengths of electrodes and varied the solvent ratios.

Evaluation of the solubility of Zn salts revealed that NaCl might be a suitable replacement for the aqueous electrolyte as this would result in the formation of ZnCl<sub>2</sub> which is highly soluble in water. The new conditions were as follows; 15 % catalyst loading, 5 mL 1M NaCl, 5 mL DCM and 7 hour reaction time, at 10 mA. During this run it was observed that solid began to form at the interface of the organic and aqueous layer. **Table 4.4** shows the recorded potential on the ElectroSyn at each sampling interval and the corresponding visual observations made at each time point.

**Table 4.4** Data and visual observations recorded during the first experiment using 1 M NaCl as the supporting electrolyte in conjunction with Zn (-).

| Time (minutes) | Potential (V) | Comments                                    | <sup>1</sup> H NMR yield (%) |
|----------------|---------------|---|------------------------------|
| 45             | 0.83          | Droplets formed at the cathode.             | 4                            |
| 90             | 0.88          | Some solid formed at the solvent interface. | 5                            |
| 135            | 0.86          | More debris forming at interface.           | 9                            |
| 180            | 0.85          | -   | 7                            |
| 225            | 0.83          | Organic layer looks light green,            | 11                           |
| 270            | 0.87          | -   | 11                           |
| 315            | 0.82          | Solid now present in the aqueous layer.     | 12                           |
| 360            | 0.79          | -   | 14                           |

Comparing the different applied currents, shown in **Figure 4.16**, it was found that with the increase of applied current, the quantity of solid, and the rate at which it was formed, also increased linearly. This is likely due to aggregation of solid at the solvent interface that hindered cycling of  $[5b]^+$  between the aqueous and organic phase, limiting the reduction to  $[5b]^0$ , the active catalyst, thereby reducing the conversion to styrene (**4.1b**).

**Figure 4.16** a) A comparison of conversion at different applied currents using Zn anode. b) Formation of debris at solvent interface when using Zn anode with NaCl electrolyte.

It was suspected that the solid formed was likely ZnO or Zn(OH)<sub>2</sub> due to oxidation of the Zn anode. Perusal of literature sources revealed that the formation of either may be controlled by changing the pH of the reaction.<sup>33,34</sup> It was reported that under acid conditions, the rate of formation of ZnO and Zn(OH)<sub>2</sub> may be reduced,<sup>34</sup> therefore, it was decided that the aqueous electrolyte would be changed from NaCl to HCl to limit and/or inhibit the formation of Zn-solids at the electrolyte interface, and the details are listed in **Table 4.5**.

Whilst the use of acid for an aqueous electrolyte reduced the formation of solid at the solvent interface, somewhat improving the faradaic efficiency of the reaction, this resulted in a new issue: the unwanted polymerization of the styrene. This was physically observed within the vial and was further confirmed by <sup>1</sup>H NMR. (**Appendix 2, Figure A2.2**) As such, the use of HCl (and likely other acidic species) as the aqueous electrolyte would not be viable for further experiments as this would damage the product.

Whilst the formation of solid at the liquid-liquid interface had hindered the cycling of **[5b]<sup>+</sup>** between the phases, the <sup>1</sup>H NMR yield of 72% when using 30 mA was the most promising conversion to styrene that had been observed with the new system design. However, faradaic efficiency was poor, with significant parasitic side reactions observed, and it was thus proposed that the amount of catalyst, **5b**, be tripled to allow a higher concentration of **[5b]<sup>+</sup>** to be generated in the aqueous layer which may then permeate through the solid more effectively, ultimately resulting in a higher conversion. Unfortunately, as seen from (**Table 4.5, Entry 8-10**) the increase in the amount of catalyst did not improve the conversion as hoped.

**Table 4.5** Results obtained when using Zn as a sacrificial anode.

| Entry           | Electrodes |         |              | Solvent Ratio (Water : DCM) | Electrolyte                       | Current (mA) | <sup>1</sup> H NMR Yield (%) |
|-----------------|------------|---------|--------------|-----------------------------|-----------------------------------|--------------|------------------------------|
|                 | Anode      | Cathode | Anode Length |                             |                                   |              |                              |
| 1               | Zinc       | Carbon  | Long         | 10 : 2                      | 1M K <sub>2</sub> CO <sub>3</sub> | 30           | 16*                          |
| 2               | Zinc       | Carbon  | Short        | 10 : 1                      | 1M NaCl                           | 20           | 28                           |
| 3               | Zinc       | Carbon  | Short        | 5 : 5                       | 1M NaCl                           | 10           | 15                           |
| 4               | Zinc       | Carbon  | Short        | 5 : 5                       | 1M NaCl                           | 20           | 45                           |
| 5               | Zinc       | Carbon  | Short        | 5 : 5                       | 1M NaCl                           | 30           | 72                           |
| 6               | Zinc       | Carbon  | Short        | 5 : 5                       | 1M NaCl                           | 40           | 65                           |
| 7               | Zinc       | Carbon  | Short        | 5 : 5                       | 1M HCl in NaCl                    | 30           | 51                           |
| 8 <sup>a</sup>  | Zinc       | Carbon  | Short        | 5 : 5                       | 1M NaCl                           | 30           | 60                           |
| 9 <sup>a</sup>  | Zinc       | Carbon  | Short        | 5 : 5                       | 1M HCl in NaCl                    | 30           | 28                           |
| 10 <sup>a</sup> | Zinc       | Carbon  | Short        | 5 : 5                       | 0.1M HCl in NaCl                  | 30           | 50                           |

\*Reaction was stopped after 2.5% due to electrode fouling.<sup>a</sup>3x the amount of catalyst used.

#### 4.2.5.2 Nickel (Ni) Anode

Unfortunately, the use of Zn sacrificial anode was not the hoped for solution, and in fact it seemed that it resulted in further complications in the system. This meant that a new anode was needed. In the literature,<sup>17,35,36</sup> Ni is established as a possible anode material when reduction is the required reaction owing to its ability to form NiOOH, a strongly oxidizing agent, in basic conditions,<sup>17</sup> and its lower cost in comparison to other metals such as palladium.<sup>37</sup> Furthermore, Ni is an appealing choice as an anode because it can provide metal ions to the solution which will allow for a controlled rate of the oxidation of this electrode surface. Therefore, the Ni anode can act in a sacrificial manner without hindering the conversion of substrate to product.<sup>36,37</sup>



Starting at 10 mA, utility of Ni anode was tested with 1 M NaCl aqueous supporting electrolyte. The system fared well under these conditions and minimal solid was observed on the surface of the anode, which did not seem to hinder the movement of  $[5b]^+$  from the aqueous layer into the organic layer. Reaction progress was once again analysed by  $^1H$  NMR and this revealed that after 7h there was 31% conversion from substrate to product. Under the same conditions, the Ni anode had performed approximately twice as well as the Zn anode with double the percentage conversion. With this in mind, we investigated how the change of aqueous layer might influence the rate of conversion. Therefore, the next experiment was completed using 1 M  $K_2CO_3$  as the aqueous electrolyte, and this improved the conversion from 31 % to 42 %.

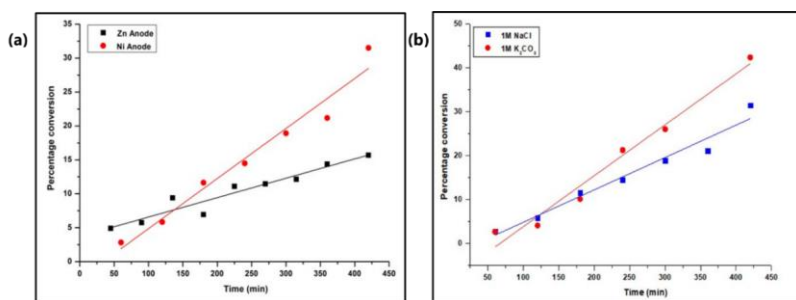


**Figure 4.17** Trend in conversion a) between Zn and Ni anode at 10 mA, and b) the effect of the aqueous electrolyte on the Ni anode performance.

These results clearly indicated that a Ni anode enhanced the overall performance of the system and further optimization reactions were carried out using a Ni anode and 1 M  $K_2CO_3$  as the aqueous electrolyte, and the parameters are detailed in **Table 4.6**. Despite the improvement in the conversion to **11** with the increase in applied current, this was seen as less favourable owing to the rate of oxidation of the Ni anode and the low Faradaic efficiency, and thus it was decided that lower current would be better.

At low current, the moderate rate of conversion was attributed to a lower concentration of active catalyst in the organic layer. However, it became apparent that catalyst loading did not necessarily equate to catalyst concentration as the rate was dependent on the current applied. Furthermore, the faradaic efficiency was low in all cases, with significant side reactions observed (as evidenced by gas formation on the cathode). This suggested that at the initial viologen concentration, the rate of viologen reduction was too low, leading to wasted current, and poor Faradaic efficiency. The amount of catalyst used was increased by a factor of three, and the reaction time was increased to 16 hours to accommodate for the low applied current. This combination worked well as it allowed for greater accumulation of the catalyst in the organic layer which led a successful debromination of the substrate, whilst also giving a lower rate of decomposition of the surface of the anode with a longer reaction time.

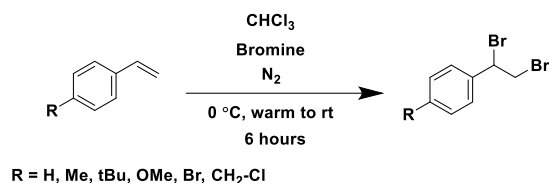
**Table 4.6** Optimization of debromination reaction using a Ni Anode.

| Entry          | Electrodes |         | Solvent Ratio (Water : DCM) | Electrolyte                       | Current (mA) | <sup>1</sup> H NMR Yield (%) | Faradaic Efficiency (%) |
|----------------|------------|---------|-----------------------------|-----------------------------------|--------------|------------------------------|-------------------------|
|                | Anode      | Cathode |                             |                                   |              |                              |                         |
| 1              | Nickel     | Carbon  | 10 : 2                      | 1M NaCl                           | 10           | 32                           | 37.6                    |
| 2              | Nickel     | Carbon  | 10 : 1                      | 1M K <sub>2</sub> CO <sub>3</sub> | 10           | 42                           | 49                      |
| 3              | Nickel     | Carbon  | 5 : 5                       | 1M K <sub>2</sub> CO <sub>3</sub> | 30           | 30                           | 15                      |
| 4 <sup>a</sup> | Nickel     | Carbon  | 5 : 5                       | 1M K <sub>2</sub> CO <sub>3</sub> | 30           | 100                          | 18                      |
| 5 <sup>a</sup> | Nickel     | Carbon  | 5 : 5                       | 1M K <sub>2</sub> CO <sub>3</sub> | 20           | 100                          | 51                      |
| 6 <sup>b</sup> | Nickel     | Carbon  | 5 : 5                       | 1M K <sub>2</sub> CO <sub>3</sub> | 20           | 53                           | 94.4                    |
| 7 <sup>a</sup> | Nickel     | Carbon  | 5 : 5                       | 1M K <sub>2</sub> CO <sub>3</sub> | 10           | 100                          | 100                     |
| 8 <sup>c</sup> | Nickel     | Carbon  | 5 : 5                       | 1M K <sub>2</sub> CO <sub>3</sub> | 10           | 100*                         | 100                     |

<sup>a</sup>3x catalyst used. <sup>b</sup>3x catalyst and 3x substrate used. <sup>c</sup>3x catalyst used. 16 hour reaction time.\*Reaction was run triplicate.

## 4.2.6 Substrate Scope

### 4.2.6.1 Synthesis of substrates



Scheme 4.13 Bromination of alkenes to form *vic*-dibromides.

The *vic*-dibromides necessary to perform the biphasic electrocatalysis were synthesized from corresponding alkenes and were obtained in high yields (> 90%).

### 4.2.7.2 Successful substrates

Having rigorously tested the design of the system and the different parameters, and thus arrived at optimized conditions for the dehalogenation of styrene, this method was applied to a range of styrene derivatives which are detailed in **Table 4.7**. All reactions were run in triplicate, and yields were determined using quantitative <sup>1</sup>H NMR analysis against an internal standard; isolated yields after purification using flash column chromatography are also reported. Most results are comparative with other dehalogenation methods in literature,<sup>2,5</sup> including the original work by Endo *et al.*<sup>27</sup>

In most cases, the styrene derivatives were easily dehalogenated. **Entries 1-3** bear electron donating substituents para to the dibromo functionality, and <sup>1</sup>H NMR showed that **Entry 1-3** were dehalogenated in high yield (100%) under these conditions. These products were purified using flash column chromatography with non-optimized conditions, giving the lower reported isolated yield as seen for **11a**. However, the yield was improved for isolated compounds as further purification attempts were made. Compound **10e**, a sterically hindered bromine adduct, was successfully dehalogenated using this method as confirmed

by  $^1\text{H}$  NMR and thus the high reported NMR yield. However, it must be noted that these experiments were conducted during a heat wave in the UK in July 2022, and there was great difficulty in isolating this compound after purification owing to its high volatility. This accounts for the low isolated yield (55 %) which is reported for **11e**. The results obtained for 1,2-dibromocyclohexane (**11f**) show great promise for this method of dehalogenation as these results are an improvement on those previously reported by Endo<sup>27</sup> and Rej.<sup>2</sup> The former reported that after 27 hours, their catalyst was completely decomposed, and the substrate was only partially (42 %) dehalogenated.<sup>27</sup> Using an organosilicon reductant, a longer reaction time (8 hours) was also required, however, this group was able to obtain cyclohexene in higher yield (86 %).<sup>2</sup> In both cases it was reported that the product could not be isolated after purification. Similar difficulty was experienced in this work and is due to the low boiling point and high volatility of cyclohexene which makes it difficult to isolate under non-optimized conditions at such a small scale.

This method was also applied to  $\alpha,\beta$ -unsaturated products and ketones (**Entries 7-9**). Fortunately, entry 7-9 (**11g**, **11h** and **11i**) were successfully dehalogenated as confirmed by  $^1\text{H}$  NMR proving further success of this method. Purification of these compounds, albeit, still unoptimized, may be highlighted as the reason for the lower isolated in good yields, however, these still remain comparable with previously reported results.<sup>2,5</sup> Finally, dehalogenation of a terminal *vic*-dibromide (**10j**) produced the corresponding alkene, **11j**, in low yield of ~ 19 %, but the product was not isolated using flash chromatography. Endo and co-workers<sup>27</sup> reported similar conversion results for 1-octene (24 %), but, their catalyst was degraded after 12 hours, therefore, the result obtained is an improvement of previous work, and affirms the success of this method.

**Table 4.7** Substrate scope for biphasic electrocatalytic debromination of vic-dibromo compounds using a Ni anode.<sup>a</sup>

| Entry | Substrate | Product | Yield [%] <sup>b</sup> |
|-------|-----------|---------|------------------------|
| 1     | 10a       | 11a     | 100 (65)               |
| 2     | 10b       | 11b     | 99 (85)                |
| 3     | 10c       | 11c     | 100 (85)               |
| 4     | 10d       | 11d     | 87 (31)                |
| 5     | 10e       | 11e     | 99 (55)                |
| 6     | 10f       | 11f     | 85 (-)                 |
| 7     | 10g       | 11g     | 94 (31)                |
| 8     | 10h       | 11h     | 92 (65)                |
| 9     | 10i       | 11i     | 99 (75)                |
| 10    | 10j       | 11j     | 19 (-)                 |

<sup>a</sup>All reactions were run in triplicates; <sup>b</sup> Yields were calculated by <sup>1</sup>H NMR spectroscopy in the presence of hexamethylbenzene as an internal standard. The isolated yield is shown in parentheses.

### 4.2.7.3 Unsuccessful substrates

In addition to the substrates listed above, other substrates were explored during this work and the reasons for their lack of success and incorporation into the final substrate scope varies and is discussed below.

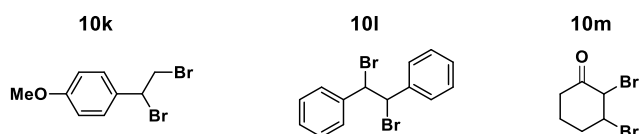


**Figure 4.18** Structures of substrates which were not debrominated successfully.

Unfortunately, 1-(1,2-dibromoethyl)-4-methoxybenzene (**10k**) was unstable and could not be isolated for testing in this substrate scope. After bromination, the product rapidly turned pink which might be indicative of the methoxy radical which makes this compound unstable. Given more time, this compound may be synthesized successfully, however, due to time constraints, it was simply discarded for further attempts.

Contrary to reports by Endo *et al.*<sup>27</sup> 1,2-dibromo-1,2-diphenylethane (**10l**) was not soluble in the organic layer at the desired concentration for this method. Even after decreasing the concentration 5-fold, a slurry rather than a homogenous mixture was obtained, and therefore, this method could not be applied to this substrate.

The greatest challenge was posed by 2,3-dibromocyclohexan-1-one (**10m**) which proved to be exceptionally unstable. In the first attempt, the product was isolated and allowed to dry on the Schlenk line for 72 hours. The <sup>1</sup>H NMR was inconclusive, revealing traces of polymerization and a mixture of broad peaks which could not be easily deciphered. A repeat synthesis was conducted with special attention being paid to the reaction temperature and limit the exposure to light, producing a yellow oil.

A concentrated aliquot was submitted for  $^1\text{H}$  NMR analysis, and the sample was left in the NMR machine overnight. The following morning it was discovered that the sample had decomposed and, in the process, generated excess pressure in the NMR tube which had caused the lid of the NMR tube to be blown off. It is believed that the decomposition results in the production of HBr which might have caused the substantial increase in pressure. Therefore, this substrate was eliminated from the substrate scope and 1-hexene was selected as the final substrate.

### 4.3 Conclusion

After extensive screening and studying the effects of applied current, reaction time, solvent ratios, and electrode materials and length, we have developed electrocatalytic conditions for debromination of *vic*-dibromides and  $\alpha,\beta$ -unsaturated products with good to excellent yields and have demonstrated the success on a range of substrates.

Electrochemical studies on the catalyst revealed the true nature of the catalytically active redox state is different from earlier literature reports.<sup>21,22,27</sup> A deeper understanding of the catalytic system nature launched the reevaluation of system design which showed that electrode material and length of the electrode are a critical aspect of electrosynthetic design protocol. Bromide re-oxidation posed a significant issue, but this can be mitigated by use of a  $\text{Br}_2$  scavenger, or choice of anode material. The choice of aqueous electrolyte can decrease active surface area of the sacrificial anode by halting the formation of unwanted solid such as  $\text{Zn}(\text{CO}_3)$  on the electrode surface or  $\text{ZnO}/\text{Zn}(\text{OH})_2$  at the electrolyte interface, hampering the optimal conversion of **10** to **11**.

Through rigorous testing and design, a method of biphasic electrocatalytic dehalogenation has been developed using low-cost materials and solvents, and kit. Using *N,N'*-dibutylviologen, [5b]<sup>2+</sup> as both phase-transfer and electrocatalyst, (1,2-dibromoethyl)benzene derivatives can be reduced to alkenes in an undivided cell and using inexpensive electrodes in the cheap and accessible IKA ElectraSyn® platform, thereby eliminating the use for stoichiometric amounts which leads to higher costs. This method is an efficient means to debrominate several classes of substrates with high yields, and confirms the initial hypothesis regarding the improvement of previously published work<sup>21,22,27</sup> through electrochemistry.

#### 4.4 Future Work

The purification and isolation method used during this work was not optimized, and thus a good starting point for future work would be to optimize the purification of the organic layer which may afford higher isolated yields. An expanded substrate scope is required to fully understand the capabilities of this method. This may be extended to dehalogenation of other halides and pseudohalides such as chloride, iodide, tosylates, and ethers, respectively. Further work may include the deoxygenation of amides to amines using a sacrificial hydride donor such as a silane. The chemical reduction of nitro groups using sodium dithionite has previously been explored,<sup>21,22</sup> and therefore, it would be good to expand this method of phase transfer electrocatalysis to the reduction of similar species, and perhaps include different functional group conversions - nitro to nitroso, diazo, and amine.



## 4.5 Experimental: Materials and Methods

### 4.5.1 Materials

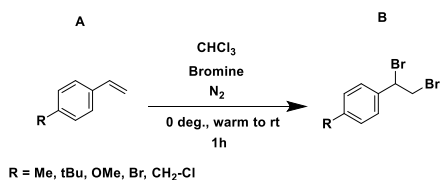
Unless otherwise stated, all materials were used as supplied from Acros Organics, Alfa Aesar, Fisher Scientific, and Fluorochem. Home-made graphite electrodes were made from graphite sheets which were purchased from Amazon UK and then cut to appropriate size without any other modifications. Zinc sheets and Nickel strips were purchased from Amazon UK and used without further surface modifications.

### 4.5.2 Synthesis of catalyst (A)

Full details are listed in [Chapter 2 – Section 2.5.6](#).

### 4.5.3 General procedure for bromination of styrene derivatives (B):

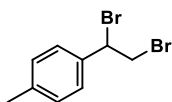
In a N<sub>2</sub> purged, 3-necked round bottom flask, a solution of alkene **A** (5 mmol) in chloroform (10 mL) was cooled to 0 °C. Bromine (1.2 equiv.) in chloroform (10 mL) was added dropwise at 0 °C. The resulting solution was stirred at 0 °C for a further 5 minutes before warming to room temperature and stirring under N<sub>2</sub> for 24 hours. The reaction was quenched with saturated Na<sub>2</sub>S<sub>2</sub>O<sub>3</sub> (2.0 g in 20 mL water) and stirred vigorously. The reaction mixture was diluted with DCM (20 mL). Thereafter, the organic phase was retained, washed with water (20 mL x 3) and brine (20 mL x 3), and the filtrate was concentrated under reduced pressure to yield final product **B**.



**Scheme 4.14** Bromination of styrene derivatives using method B.

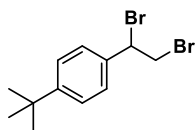
## 4.5.3.1 Characterisation of di-bromo compounds

## 1-(1,2-dibromoethyl)-4-methylbenzene (10a)



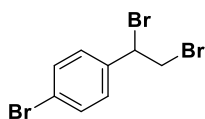
The title compound was prepared according to the general procedure and obtained as an off-white solid (4.36 g, 93.3%); NMR data match previously published values.<sup>38,39</sup> **<sup>1</sup>H NMR** (400 MHz, 298.15 K, CDCl<sub>3</sub>) δ 7.28 (d, J = 8.2 Hz, 2H), 7.17 (d, J = 8.0 Hz, 2H), 5.12 (dd, J = 5.5, 10.2 Hz, 1H), 4.04 (m, 2H), 2.34 (s, 3H); **<sup>13</sup>C NMR** (101 MHz, 298.15 K, CDCl<sub>3</sub>) δ 139.27, 135.71, 129.62, 127.56, 51.18, 35.12, 21.33.

## 1-(tert-butyl)-4-(1,2-dibromoethyl) benzene (10b)



The title compound was prepared according to the general procedure and obtained as a white solid (3.93 g, 99%); NMR data match previously published values.<sup>40</sup> **<sup>1</sup>H NMR** (400 MHz, 298.15 K, CDCl<sub>3</sub>) δ 7.41 (m, 2H), 7.35 (m, 2H), 5.18 (dd, J = 5.7, 10.1 Hz, 1H), 4.07 (m, 2H), 1.34 (s, 9H); **<sup>13</sup>C NMR** (101 MHz, 298.15 K, CDCl<sub>3</sub>) δ 151.28, 134.5, 126.26, 124.8, 50.22, 34.12, 33.99, 30.21.

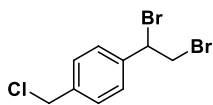
## 1-bromo-4-(1,2-dibromoethyl)benzene (10c)



The title compound was prepared according to the general procedure (C). The product was obtained a pale-yellow crystalline solid. Yield: 4.26 g, 54%; NMR was found to match previously published values.<sup>41,42</sup> **<sup>1</sup>H NMR** (400MHz, 298.15 K, CDCl<sub>3</sub>) δ 7.54-

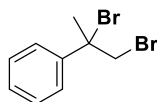
7.50 (2H, m), 7.30-7.26 (2H, m), 5.09 (1H, dd,  $J = 11.1$  Hz, 5.1 Hz), 4.08-4.04 (2H, m), 3.96 (1H, dd,  $J = 11.0$  Hz, 10.3 Hz);  $^{13}\text{C NMR}$  (101 MHz, 298.15 K,  $\text{CDCl}_3$ )  $\delta$  137.94, 132.34, 129.59, 123.45, 49.84, 34.87.

#### 1-(chloromethyl)-4-(1,2-dibromoethyl) benzene (10d)



The title compound was prepared according to the general procedure and obtained as a white crystalline solid (2.43 g, 37%); NMR data match previously published values.<sup>43,44</sup>  $^1\text{H NMR}$  (400 MHz, 298.15 K,  $\text{CDCl}_3$ )  $\delta$  7.42 (4H, s), 5.17-5.13 (1H, dd,  $J = 10.8$  Hz, 8.3 Hz), 4.6 (2H, s), 3.99 – 4.11 (2H, m);  $^{13}\text{C NMR}$  (101 MHz, 298.15 K,  $\text{CDCl}_3$ )  $\delta$  138.75, 138.57, 129.04, 128.05, 50.01, 45.53, 34.72.

#### (1,2-dibromopropan-2-yl)benzene (10e)



The title compound was prepared according to the general procedure and obtained as a colourless oil (7.51 g, 71 %); NMR data match previously published values.<sup>42</sup>  $^1\text{H NMR}$  (400 MHz, 298.15 K,  $\text{CDCl}_3$ )  $\delta$  7.65-7.62 (2H, m), 7.46-7.38 (3H, m), 4.46-4.43 (1H, m), 4.23-4.21 (1H, m), 2.40 (3H, s);  $^{13}\text{C NMR}$  (101 MHz, 298.15 K,  $\text{CDCl}_3$ )  $\delta$  141.78, 128.42, 128.38, 126.46, 63.7.

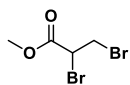
#### 1,2-dibromocyclohexane (10f)



The title compound was prepared according to the general procedure and obtained as a colourless oil (9.84g, 83%); NMR data match previously published values.<sup>42</sup>  $^1\text{H}$

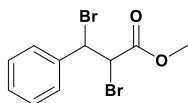
**NMR** (400MHz, 298.15 K, CDCl<sub>3</sub>)  $\delta$  4.45 (2H, s), 4.23-4.21 (2H, m), 2.49-2.43 (2H, m), 1.91-1.78 (4H, m), 1.58-1.50 (2H, m).

#### Methyl 2,3-dibromopropanoate (10g)



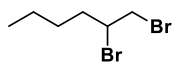
The title compound was purchased. **<sup>1</sup>H NMR** (400MHz, 298.15 K, CDCl<sub>3</sub>)  $\delta$  4.39 (dd,  $J=11.2$  Hz, 4.5 Hz, 1H), 3.83 (t,  $J=10.5$  Hz,  $J= 11.3$  Hz, 1H), 3.74 (s, 3H), 3.62 (dd,  $J= 10.5$  Hz, 4.5 Hz, 1H).

#### Methyl 2,3-dibromo-3-phenylpropanoate, (10i)



The title compound was prepared according to the general procedure and obtained as an off-white crystalline solid (5.84g, 64.8%); NMR data match previously published values.<sup>45</sup> **<sup>1</sup>H NMR** (400MHz, 298.15 K, CDCl<sub>3</sub>)  $\delta$  7.43-7.33 (5H, m), 5.35 (1H, d,  $J = 11.8$  Hz), 4.86 (1H, d,  $J = 11.7$  Hz), 3.14 (3H, s); **<sup>13</sup>C NMR** (101 MHz, 298.15 K, CDCl<sub>3</sub>)  $\delta$  168.4, 137.47, 129.4, 128.9, 128.03, 53.48, 50.59, 46.63.

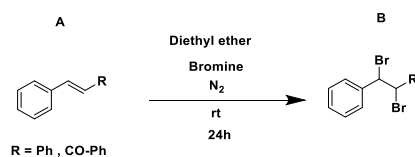
#### 1,2-dibromohexane (10j)



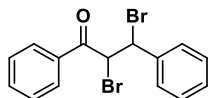
The title compound was prepared according to the general procedure and obtained as a pale, yellow oil (1.28g, 98%); NMR data match previously published values.<sup>46</sup> **<sup>1</sup>H NMR** (400MHz, 298.15 K, CDCl<sub>3</sub>)  $\delta$  4.2-4.24 (1H, m), 3.87-3.82 (1H, m), 3.65-3.59 (1H, m), 2.19-2.10 (1H, m), 1.83-1.74 (1H, m), 1.50-1.29 (4H, m), 0.97-0.88 (3H, m).

**4.5.4 Bromination of alkene derivatives (C):**

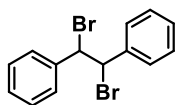
In a N<sub>2</sub> purged 3-necked round bottom flask, alkene **A** (9.72 mmol) was dissolved in diethyl Ether (40 mL), and cooled to 0 °C. Bromine (1.16 equiv) in diethyl Ether (20 mL), was added dropwise at 0 °C. The resulting solution was stirred at 0 °C for a further 5 minutes before warming to room temperature and stirring under N<sub>2</sub> for 24h. The resultant precipitate was washed with hot ethanol (40 mL) filtered and dried to yield final product **B**.



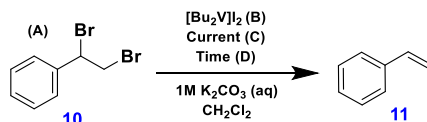
**Scheme 4.15** Synthesis of di-bromo compounds using method C.

**4.5.4.1 Characterisation of di-bromo compounds****2,3-dibromo-1,3-diphenylpropan-1-one, (11h)**

The title compound was prepared according to the general procedure and obtained as a fine, white solid (2.9g, 81.2% yield); NMR data match previously published values.<sup>40</sup> **<sup>1</sup>H NMR** (400 MHz, 298.15 K, CDCl<sub>3</sub>) δ 8.14-8.11 (m, 2H), 7.70-7.66 (m, 1H), 7.59-7.53 (m, 4H), 7.47-7.38 (m, 3H), 5.85 (d, *J* = 11.3 Hz, 1H), 5.66 (d, *J*=11.3 Hz, 1H); **<sup>13</sup>C NMR** (101 MHz, 298.15 K, CDCl<sub>3</sub>) δ 191.21, 138.27, 131.47, 134.2, 129.32, 129.09, 128.93, 128.38, 49.78, 46.86.

**1,2-dibromo-1,2-diphenylethane, (10)**

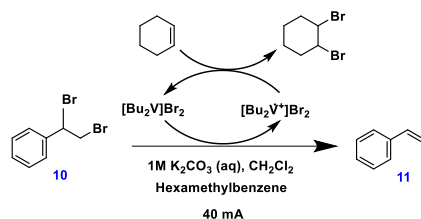
The title compound was prepared according to the general procedure and obtained as a fine, white solid (1.67 g, 45%); NMR data match previously published values.<sup>9,47</sup> **<sup>1</sup>H NMR** (400 MHz, 298.15 K, CDCl<sub>3</sub>) δ 7.54 – 7.51 (m, 4H), 7.45-7.36 (m, 6H), 5.49 (s, 2H); **<sup>13</sup>C NMR** (101 MHz, 298.15 K, CDCl<sub>3</sub>) δ 140.02, 129.01, 128.77, 127.90, 56.07.

**4.5.5 General procedure for Electrasyn® reaction (D):****i) Dehalogenation of 1,2-dibromo(ethyl)benzene (preliminary tests)****Scheme 4.16** Biphasic electrocatalytic dehalogenation using IKA ElectraSyn.

In an IKA Electrasyn platform using two graphite electrodes, [Bu<sub>2</sub>V]<sup>2+</sup> (0.19 mmol), **10** (1.52 mmol), potassium carbonate (10.1 mmol), hexamethyl benzene (0.26 mmol) were dissolved in water (10 mL) and dichloromethane (2 mL). The mixture was stirred under inert environment for 5 minutes. Thereafter, the reaction was started using the IKA Electrasyn® with the following parameters: 40 mA constant current, 18 hour reaction time, switching polarity every 30 minutes and 450 rpm stirring. <sup>1</sup>H NMR aliquots (0.1 mL) were collected at specified intervals and run in CDCl<sub>3</sub> (0.5 mL).

**ii) Dehalogenation of 10 using a Br<sup>-</sup> Scavenger**

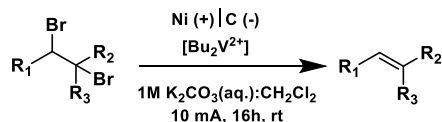
[Bu<sub>2</sub>V]<sup>2+</sup> (0.2 mmol), potassium carbonate (10.1 mmol), hexamethyl benzene (0.26 mol) were dissolved in water (10 mL) and dichloromethane (1 mL). The mixture was stirred under inert environment for 5 minutes. Reaction was started using the IKA Electrasyn® with the following parameters: 40 mA constant current, 7 hour reaction time, switching polarity every 30 minutes and 450 rpm stirring. After 2 hours, a purged solution of **10** (1.52 mmol) and cyclohexene (0.18 mL, 1.87 mmol), dissolved in DCM (1 mL), were added. <sup>1</sup>H NMR aliquots (- 0.1 mL) were collected at specified intervals and run in CDCl<sub>3</sub> (0.5 mL).



**Scheme 4.17** Biphasic electrocatalytic dehalogenation using Br<sup>-</sup> scavenger. Hexamethylbenzene was used as internal standard.

**iii) Optimized conditions for dehalogenation of vic-dibromides**

[Bu<sub>2</sub>V]<sup>2+</sup> (0.629 mmol), potassium carbonate (5 mmol), hexamethyl benzene (0.36 mmol), and vic-dibromide (1.63 mmol) were dissolved in water (5 mL) and dichloromethane (5 mL). The mixture was stirred under inert environment for 5 minutes. Thereafter, reaction was started using the IKA Electrasyn with the following parameters: 10 mA constant current, 16 hour reaction time, and 450 rpm stirring. <sup>1</sup>H NMR aliquot (- 0.1 mL) of the organic layer was analysed post-reaction and run in CDCl<sub>3</sub> (0.5 mL). The organic phase was filtered and concentrated under pressure. The product was purified by flash column chromatography on silica gel.

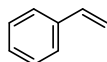


**Scheme 4.18** Optimized biphasic dehalogenation reaction.

### Spectral data of dehalogenated compounds

All compounds were obtained using procedure D-iii.  $^1\text{H}$  NMR spectra are in **Appendix 2**.

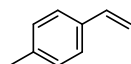
#### Styrene, (11)



Purified by flash chromatography (hexane). Colourless liquid (6.1 mg, 99 %);  $^1\text{H}$

**NMR** (400 MHz, 298.15 K,  $\text{CDCl}_3$ )  $\delta$  7.52 (dd,  $J=7.3$  Hz,  $J=0.8$  Hz, 2H), 7.43 (t,  $J=7.3$  Hz, 2H), 7.33 (t,  $J=7.2$  Hz, 4H), 6.79 (d,  $J=17.6$  Hz,  $J=10.8$ Hz, 3H), 5.85 (d,  $J = 17.6$  Hz, 1H), 5.33 (d,  $J=10.2$  Hz, 1H). Spectrum in accordance with literature.<sup>2,9</sup>

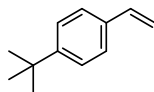
#### 4 - methyl styrene (11a)



Purified by flash chromatography (hexane). Colourless liquid (86 mg, 68 %);  $^1\text{H}$

**NMR** (400 MHz, 298.15 K,  $\text{CDCl}_3$ )  $\delta$  7.42 (s, 4H), 7.43 (t,  $J=7.3$  Hz, 2H), 7.33 (t,  $J=7.2$  Hz, 4H), 6.77 (d,  $J=17.6$  Hz,  $J=10.8$ Hz, 1H), 5.78 (d,  $J = 17.6$  Hz, 1H), 5.26 (d,  $J=10.8$  Hz, 1H). Spectrum in accordance with literature.<sup>2,9</sup>

#### 4 - $^t$ butyl styrene (11b)



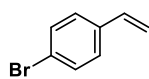
Purified by flash chromatography (silica gel, hexane). Colourless liquid (0.208

g, 84%);  $^1\text{H}$  **NMR** (400 MHz, 298.15 K,  $\text{CDCl}_3$ )  $\delta$  7.52 (dd,  $J=7.3$  Hz,  $J=0.8$  Hz, 2H), 7.43 (t,



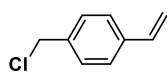
$J=7.3$  Hz, 2H), 7.33 (t,  $J=7.2$  Hz, 4H), 6.79 (d,  $J=17.6$  Hz,  $J=10.8$ Hz, 3H), 5.85 (d,  $J = 17.6$  Hz, 1H), 5.33 (d,  $J=10.2$  Hz, 1H). Spectrum in accordance with literature.<sup>44</sup>

#### 4 - bromostyrene, (11c)



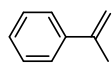
Purified by flash chromatography (silica gel, hexane). Colourless liquid (6.1 mg, 99 %); **<sup>1</sup>H NMR** (400 MHz, 298.15 K, CDCl<sub>3</sub>)  $\delta$  7.5 (m, 2H), 7.32 (m, 2H), 7.33 (t,  $J=7.2$  Hz, 4H), 6.71 (dd,  $J=17.6$  Hz,  $J=10.9$  Hz, 1H), 5.8 (d,  $J = 17.6$  Hz, 1H), 5.34 (d,  $J=10.9$  Hz, 1H); **<sup>13</sup>C NMR** (101 MHz, 298.15 K, CDCl<sub>3</sub>)  $\delta$  136.53, 135.80, 131.68, 127.79, 121.67, 128.38, 114.57. Spectrum in accordance with literature.<sup>41,42</sup>

#### 4- Vinyl benzyl Chloride (11d)



Purified by flash chromatography (silica gel, hexane). Colourless liquid (87 mg, 35 %); **<sup>1</sup>H NMR** (400 MHz, 298.15 K, CDCl<sub>3</sub>)  $\delta$  7.48-7.55 (m, 4H), 7.32 (m, 2H), 6.88 (dd,  $J=17.7$  Hz,  $J=11$  Hz, 1H), 5.94 (d,  $J = 17.6$  Hz, 1H), 5.45 (d,  $J=11$  Hz, 1H), 4.69 (s, 2H). Spectrum in accordance with literature.<sup>43,44</sup>

#### $\alpha$ -methyl styrene (11e)



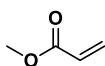
Purified by flash chromatography (silica gel, hexane). Colourless liquid (0.103 g, 55 %); **<sup>1</sup>H NMR** (400 MHz, 298.15 K, CDCl<sub>3</sub>)  $\delta$  7.52 (d,  $J=7.5$  Hz, 2H), 7.38 (t,  $J=7.5$  Hz, 2H), 7.31 (m, 1H), 5.42 (m, 1H), 5.14 (m, 1H), 2.21 (dd,  $J=1.3$  Hz,  $J=0.7$  Hz, 3H). Spectrum in accordance with literature.<sup>2</sup>

**Cyclohexene, (11f)**



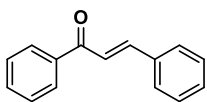
Product was not isolated after flash chromatography.

**Methyl Acrylate (11g)**



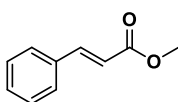
Purified by flash chromatography (95% Hexane: 5 % EtOAc). Colourless liquid (44 mg, 31 %);  $^1\text{H NMR}$  (400 MHz, 298.15 K,  $\text{CDCl}_3$ )  $\delta$  6.05 (d,  $J = 17.4$  Hz, 1H), 5.8 (dd,  $J = 17.3$  Hz, 10.5 Hz, 1H), 5.49 (d,  $J = 10.5$  Hz, 1H), 3.4 (s, 3H). Spectrum in accordance with literature.<sup>48</sup>

**Trans - chalcone, (11h)**



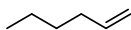
Purified by flash chromatography (10.0% EtOAc in petroleum ether) as a pale-yellow solid (81 mg, 23.8%).  $^1\text{H NMR}$  (400 MHz,  $\text{CDCl}_3$ )  $\delta$  8.04-8.06 (d,  $J = 7.4$  Hz, 2H), 7.82-7.86 (d,  $J = 15.7$  Hz, 1H), 7.50-7.68 (m, 6H), 7.43 (m, 3H). Spectrum in accordance with literature.<sup>2</sup>

**Methyl Cinnamate, (11i)**



Purified by flash chromatography (90 % Hexane : 10% EtOAc). Colourless liquid (0.22 g, 74 %). ;  $^1\text{H NMR}$  (400 MHz, 298.15 K,  $\text{CDCl}_3$ )  $\delta$  7.71 (d,  $J = 16.1$  Hz, 1H), 7.55-7.52 (dd,  $J = 6.5$  Hz,  $J = 2.9$  Hz, 2H), 7.39-7.40 (m, 3H), 6.44-6.48 (d,  $J = 15.9$  Hz, 1H), 3.82 (s, 3H). Spectrum in accordance with literature.<sup>49</sup>

**1-hexene, (11j)**



Product was not isolated after flash chromatography.

## 4.6 References

- 1 S. A. Snyder, Z.-Y. Tang and R. Gupta, *J. Am. Chem. Soc.*, 2009, **131**, 5744–5745.
- 2 W. Chen, H. Tao, W. Huang, G. Wang, S. Li, X. Cheng and G. Li, *Chem. - A Eur. J.*, 2016, **22**, 9546–9550.
- 3 B. C. Ranu, S. K. Guchhait and A. Sarkar, *Chem. Commun.*, 1998, 2113–2114.
- 4 W. M. Schubert, B. S. Rabinovitch, N. R. Larson and V. A. Sims, *J. Am. Chem. Soc.*, 1952, **74**, 4590–4592.
- 5 S. Rej, S. Pramanik, H. Tsurugi and K. Mashima, *Chem. Commun.*, 2017, **53**, 13157–13160.
- 6 A. G. Vijayashree, N. and Samuelson, *Tetrahedron*, 1992, **33**, 559–560.
- 7 W. Carpenter, *J. Org. Chem.*, 1965, **30**, 3082–3084.
- 8 R. W. Itamar and Maidan, *J. Am. Chem. Soc.*, 1986, **108**, 1080–1082.
- 9 S. Rej, S. Pramanik, H. Tsurugi and K. Mashima, *Chem. Commun.*, 2017, **53**, 13157–13160.
- 10 D. S. P. Cardoso, B. Šljukić, D. M. F. Santos and C. A. C. Sequeira, *Org. Process Res. Dev.*, 2017, **21**, 1213–1226.
- 11 M. C. Leech, A. D. Garcia, A. Petti, A. P. Dobbs and K. Lam, *React. Chem. Eng.*, 2020, **5**, 977–990.
- 12 Y. Li, L. Wen and W. Guo, *Chem. Soc. Rev.*, 2023, **52**, 1168–1188.
- 13 M. A. Casadei, F. M. Moracci, G. Zappia, A. Inesi and L. Rossi, *J. Org. Chem.*, 1997, **62**, 6754–6759.
- 14 T. Hashimoto and K. Maruoka, in *Asymmetric Phase Transfer Catalysis*, 2008, pp. 1–8.
- 15 C. M. Starks, *J. Am. Chem. Soc.*, 1971, **93**, 195–199.
- 16 J. Tan and N. Yasuda, *Org. Process Res. Dev.*, 2015, **19**, 1731–1746.
- 17 M. C. Leech and K. Lam, *Nat. Rev. Chem.*, 2022, **6**, 275–286.
- 18 A. T. Murray, S. Voskian, M. Schreier, T. A. Hatton and Y. Surendranath, *Joule*, 2019, **3**, 2942–2954.
- 19 S. Kaneko, Y. Kumatabara and S. Shirakawa, *Org. Biomol. Chem.*, 2016, **14**, 5367–5376.
- 20 J. Ding, C. Zheng, L. Wang, C. Lu, B. Zhang, Y. Chen, M. Li, G. Zhai and X. Zhuang, *J. Mater. Chem. A*, 2019, **7**, 23337–23360.
- 21 K. K. Park, C. H. Oh and W. Sim, *J. Org. Chem.*, 1995, **60**, 6202–6204.
- 22 K. K. Park, C. H. Oh and W. K. Joung, *Tetrahedron Lett.*, 1993, **34**, 7445–7446.

- 23 G.-Q. Gao and A.-W. Xu, *New J. Chem.*, 2014, **38**, 4661–4665.
- 24 C. K. Prier, D. A. Rankic and D. W. C. MacMillan, *Chem. Rev.*, 2013, **113**, 5322–5363.
- 25 L. F. T. Novaes, J. Liu, Y. Shen, L. Lu, J. M. Meinhardt and S. Lin, *Chem. Soc. Rev.*, 2021, **50**, 7941–8002.
- 26 I. Willner, N. Lapidot, A. Riklin, R. Kasher, E. Zahavy and E. Katz, *J. Am. Chem. Soc.*, 1994, **116**, 1428–1441.
- 27 T. Endo, Y. Saotome and M. Okawara, *J. Am. Chem. Soc.*, 1984, **106**, 1124–1125.
- 28 Y. Kawamata, K. Hayashi, E. Carlson, S. Shaji, D. Waldmann, B. J. Simmons, J. T. Edwards, C. W. Zapf, M. Saito and P. S. Baran, *J. Am. Chem. Soc.*, 2021, **143**, 16580–16588.
- 29 D. H. Gibson, K. Owens and T. S. Ong, *J. Am. Chem. Soc.*, 1984, **106**, 1125–1127.
- 30 C. Schotten, T. P. Nicholls, R. A. Bourne, N. Kapur, B. N. Nguyen and C. E. Willans, *Green Chem.*, 2020, **22**, 3358–3375.
- 31 C. Kingston, M. D. Palkowitz, Y. Takahira, J. C. Vantourout, B. K. Peters, Y. Kawamata and P. S. Baran, *Acc. Chem. Res.*, 2020, **53**, 72–83.
- 32 D. M. Heard and A. J. J. Lennox, *Angew. Chemie*, 2020, **132**, 19026–19044.
- 33 A. N. Moskvichev, Y. L. Gunko, M. G. Mikhalenko, A. A. Sletov, V. A. Kozyrin and O. L. Kozina, *Russ. J. Electrochem.*, 2019, **55**, 322–332.
- 34 F. El-Taib Heikal, W. R. Abd-Ellatif, N. S. Tantawy and A. A. Taha, *RSC Adv.*, 2018, **8**, 3816–3827.
- 35 B. K. Peters, K. X. Rodriguez, S. H. Reisberg, S. B. Beil, D. P. Hickey, Y. Kawamata, M. Collins, J. Starr, L. Chen, S. Udyavara, K. Klunder, T. J. Gorey, S. L. Anderson, M. Neurock, S. D. Minter and P. S. Baran, *Science (80-. )*, 2019, **363**, 838–845.
- 36 Z. Li, S. Kelkar, C. H. Lam, K. Luczek, J. E. Jackson, D. J. Miller and C. M. Saffron, *Electrochim. Acta*, 2012, **64**, 87–93.
- 37 D. S. Santana, G. O. Melo, M. V. F. Lima, J. R. R. Daniel, M. C. C. Areias and M. Navarro, *J. Electroanal. Chem.*, 2004, **569**, 71–78.
- 38 Y. Li, L. Tang, W. Zhou and X. Wang, *Chinese Chem. Lett.*, 2016, **27**, 1495–1499.
- 39 N. S. Y. Loy, S. Kim and C.-M. Park, *Org. Lett.*, 2015, **17**, 395–397.
- 40 N. S. Martins and E. E. Alberto, *New J. Chem.*, 2018, **42**, 161–167.
- 41 R. Rubio-Presa, O. García-Pedrero, P. López-Matanza, P. Barrio and F. Rodríguez, *European J. Org. Chem.*, 2021, **2021**, 4762–4766.
- 42 S. Song, X. Li, X. Sun, Y. Yuan and N. Jiao, *Green Chem.*, 2015, **17**, 3285–3289.
- 43 G. K. Dewkar, S. V. Narina and A. Sudalai, *Org. Lett.*, 2003, **5**, 4501–4504.
- 44 L. Zhang, G. Zhang, P. Wang, Y. Li and A. Lei, *Org. Lett.*, 2018, **20**, 7396–7399.

| Chapter 4 : Phase-transfer Electrocatalysis

- 45 X. Ma, W. Li, X. Li, X. Tao, W. Fan, X. Xie, T. Ayad, V. Ratovelomanana-Vidal and Z. Zhang, *Chem. Commun.*, 2012, **48**, 5352–5354.
- 46 G. W. Kabalka, K. Yang, N. K. Reddy and C. Narayana, *Synth. Commun.*, 1998, **28**, 925–929.
- 47 T. Hirose, Y. Miyazaki, M. Watabe, S. Akimoto, T. Tachikawa, K. Kodama and M. Yasutake, *Tetrahedron*, 2015, **71**, 4714–4721.
- 48 K. Lowpetch and D. W. Young, *Org. Biomol. Chem*, 2005, **3**, 3348–3356.
- 49 B. Zhang, P. Feng, Y. Cui and N. Jiao, *Chem. Commun.*, 2012, **48**, 7280–7282.

**CHAPTER 5**

**FLAVIN DERIVATIVES:**

**SYNTHESIS AND ALTERED PROPERTIES.**

---

*"Be strong and courageous. Do not be afraid or terrified because of them, for the Lord your  
God goes with you; He will never leave you nor forsake you."*

*Deuteronomy 31:6*

## 5.1 Introduction

The flavin structure is a three-ring isoalloxazine structural motif which serves as the main backbone for all the of the most well-known flavin species: flavin mononucleotide (FMN), flavin adeninedinucleotide (FAD), riboflavin and lumichrome.<sup>1</sup> (**Figure 5.1**) Each of these molecules have a 7,8-dimethyl substitution on the main benzene ring, however the side chains on the *N10* positions are different.

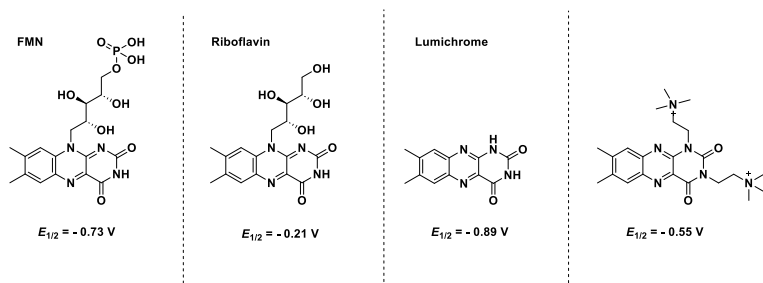
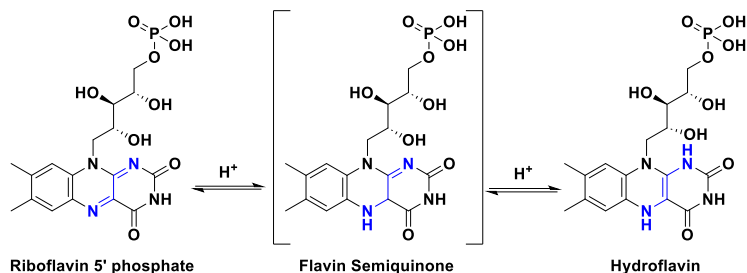


**Figure 5.1** Known flavin derivatives and their redox potentials vs Ag/AgCl.<sup>1,2</sup>

Riboflavin 5' phosphate, commonly known as (FMN), is a highly water-soluble biomolecule produced from Riboflavin (vitamin B2).<sup>3</sup> In alkaline solution FMN has a low reduction potential and as seen in **Scheme 5.1**, can undergo a two-electron reduction on its isoalloxazine backbone which occurs *via* a flavin semiquinone radical.



**Scheme 5.1** The two-electron reduction of FMN.

Flavins had proven to be suitable electrolyte materials for RFBs and like other organic molecules, their properties could be tuned by changing substituents and/or varying the substitution pattern.<sup>1,4,5</sup> Typically, flavin substitution occurs at position 7 and 8 because this can regulate the reduction potential of the flavins.<sup>5</sup> Riboflavin, FAD, FMN and lumiflavin have been studied extensively due to their biological significance. However, there are limited literature reports regarding the substituent effects on synthetic flavins, and the available used a combination of theoretical and experimental methods.<sup>4-6</sup> The development of RFBs based on aza-aromatics such as phenazine<sup>7</sup> and alloxazine<sup>8</sup> suggest the potential of these molecules for energy storage based on naturally occurring products.<sup>7,9-11</sup>

In a 2016 article in *Nature Energy*,<sup>8</sup> the Aziz group demonstrated the use of an alloxazine-based electrolyte in an AORFB, inspired by the naturally occurring flavin co-factors. Using a computational study, they screened different functional groups and their effects on the redox potentials of alloxazine, and they found that functionalization of the alloxazine with a carboxylic group afforded high solubility (2M) in pH 14 KOH. The alloxazine was paired with ferri/ferrocyanide and this resulted in a RFB with an open-circuit voltage of 1.2 V with 99.7% and 99.98% current efficiency and capacity retention per cycle, respectively.



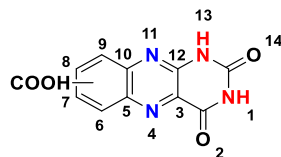


**Figure 5.2** Structure of alloxazine 7/8-carboxylic acid (ACA).<sup>8</sup>

In the field of RFBs, there is little information about the substitution at position *N*-1 and *N*-3, but the work by Kormányos *et al.*<sup>1</sup> provides the most comprehensive insight into the effect of substitution at *N*-1 and *N*-3 on the redox and electrochemical properties of the flavin derivatives.

These derivatives were synthesized through disubstitution at position *N*-1 and *N*-3. Their primary analogue was 2,2'-(2,4-dioxobenzo[*g*]pteridine-1,3(2*H*,4*H*)-diyl)bis(*N,N,N*-trimethylethan-1-aminium)bromide (**Figure 5.3**) contained terminal quaternary ammonium groups and was selected because it had a more thermodynamically favourable interactions with dioxygen than isoalloxazines.

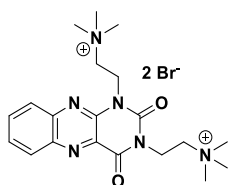


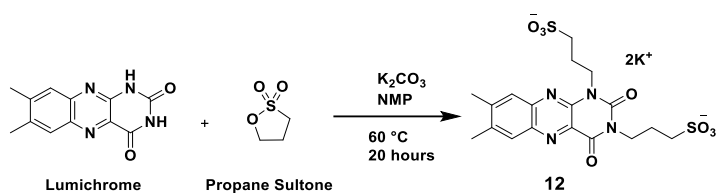
**Figure 5.3** Structure of 2,2'-(2,4-dioxobenzo[*g*]pteridine-1,3(2*H*,4*H*)-diyl)bis(*N,N,N*-trimethylethan-1-aminium) bromide, as synthesized by Kormányos *et al.*<sup>1</sup>

The work in the Clark group was inspired by the work by Kormanyos *et al.*<sup>1</sup> who showed that water-soluble flavin derivatives show reversible redox behaviour and good electrochemical kinetics. So, a flavin with terminal sulphonate groups was developed because it would be water-soluble, with stable electrochemical properties making it an ideal redox active species for AORFBs and be synthesized from a cheap and plentiful natural product: riboflavin.

## 5.2 Developing Flavin Derivatives

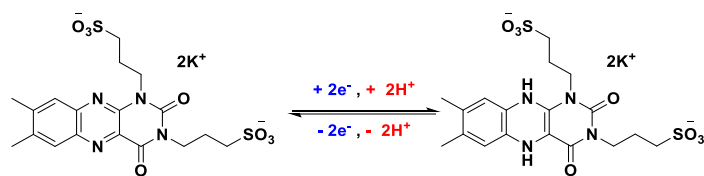
### 5.2.1 Sulphonate-flavin

The water-soluble Flavin containing a sulphonate terminal group, **12**, was successfully synthesized by another member of the Clark group, Koray Gumus as per **Scheme 5.1**.



**Scheme 5.1** Synthesis of **12**.

Initial redox screening had revealed that **12** undergoes a two-proton, two-electron, proton coupled electron transfer (PCET) which is in accordance with the literature.<sup>3,12</sup> Given that the redox process was proton-coupled, this requires two protons to be donated from the electrolyte to the flavin, and the process is shown in **Scheme 5.2**.



**Scheme 5.2** PCET redox pathway that **12** undergoes.

Cycling voltammetry of **12** was carried out in 1.0 M H<sub>2</sub>SO<sub>4</sub> (~pH 0), and a reduction potential of -0.183 V vs Ag/AgCl was recorded (**Appendix 1, Figure A1.7**). The redox event was highly reversible in this electrolyte, with symmetrical redox peaks with a peak separation of 34 mV, close to the ideal two-electron redox process 28 mV peak separation.

Since cell pH is an important criterion in determining potential coupled reactions, the pH dependence of **12** was studied *via* preliminary CV analysis at different pH values was conducted. The supporting electrolytes used were 1 M H<sub>2</sub>SO<sub>4</sub> in 1 M NaCl(aq), brine (1 M NaCl(aq)) and base (1 M NaOH in 1 M NaCl(aq)). Data showed that **12** was not redox active at neutral pH (1 M NaCl(aq)) nor under basic conditions (1 M NaOH in 1 M NaCl(aq)) given the absence of a redox peak in the CV. This warranted further investigation into the chemical stability of **12** across a large pH range (1-14) and analysis of the decomposition at high pH.

#### ***pH studies – physical & electrochemical results***

Generally speaking, in biochemical reactions, flavins have been reported to undergo reversible two electron reduction reactions which results in the protonation of the *N1* and *N5*.<sup>12</sup> This is a two-step process *via* the formation of a semiquinoid free radical intermediate, and finally the formation of the protonated flavin. These findings are based on the results obtained for the redox properties of riboflavin, FAD and FMN, and the redox potentials of these flavins are dependent on their sidechains, the pH of the electrolyte, and the presence of metal ions in solution. Unlike **12**, riboflavin, FMN, and FAD have been reported to be electrochemically stable at high pH (12-13) with a typical redox potential of approximately -0.20 V vs Ag/AgCl.

Flavins have often been studied in a biological context and the pH conditions of these mediums has limited the research done on flavins at high pH (pH > 12).<sup>10</sup> The drastically different behaviour seen between pH 1 and pH 7, where the compound is known to be stable, indicated that speciation may be to blame. It was hypothesised that at acidic pH, the dominant species is a protonated molecule, while at basic pH, free pyrazine is found.

Based on the preliminary redox data collected on **12** in electrolytes at varying pH, it was expected that the redox behaviour would be pH dependent. As such, the electrochemical properties of **12** were studied over a range of pH 1 to pH 14 in unbuffered aqueous solutions made up from serial dilution of 1 M HCl and 1 M NaOH with 1 M NaCl to maintain ionic strength. **Figure 5.4** shows the cyclic voltammograms of **12** in aqueous solutions from pH 1 to pH 14 and owing to the proton-coupled redox nature of flavins, it was expected that the reduction potential would shift to a more negative value because of the pH change.

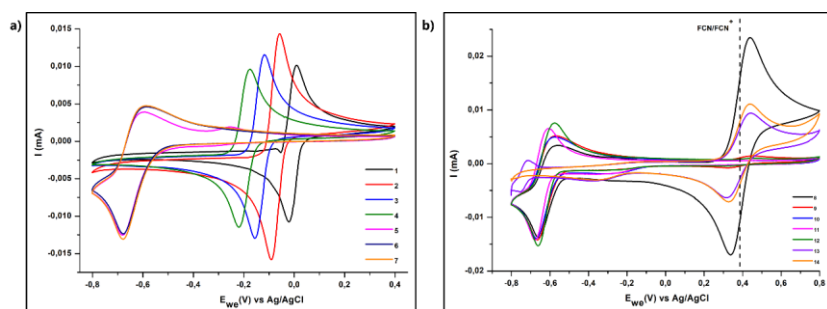


**Figure 5.4** Cyclic voltammograms of **12** in unbuffered aqueous electrolytes as a function of pH : a) pH 1-7, and b) pH 8-14 with FCN as an internal reference.

Consistent with previous results, and literature regarding flavins,<sup>1,3,8,12-14</sup> the reduction potential of **12** did become more negative as the pH of the electrolyte increased from pH 1 to pH 4 with the reduction potential decreasing from -0.005 V at pH 1 to -0.203 V for pH 4. However, as seen in **Figure 5.5**, the voltammogram at pH 5 shows only a small peak at -0.250 V and a new event is seen at the more negative value of -0.648 V which then remains unchanged between pH 5 and pH 12 as seen in **Figure 5.4 a&b**.

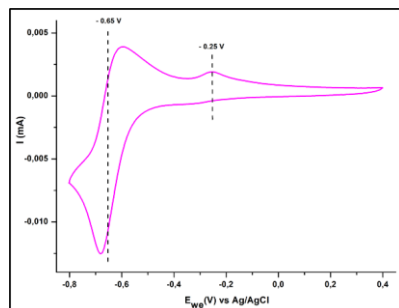


**Figure 5.5** Cyclic voltammogram of **12** in an unbuffered aqueous electrolyte at pH 5.

This shift of redox potential can be related to the protonation state and  $pK_a$  of **12** whereby it is protonated between pH 1 and pH 4, and in this state, it can be reduced at a higher redox potential. However, from pH 5 onwards, the flavin is neutral and therefore this requires a lower (more negative) redox potential for the flavin to be reduced, causing the shift in redox potential.<sup>3,12,15</sup>

At pH 13 the reduction potential is shifted more negative yet again, resulting in an  $E_{1/2}$  value of -0.742 V. This voltammogram had a slightly distorted shape in comparison to the other voltammograms obtained in this work, and at pH 14, **12** loses its electrochemical capabilities as indicated by the lack of a redox peak for the voltammogram ran at pH 14.

Following the CV analysis,  $^1\text{H}$  NMR analysis using the CV solutions with a DMSO capillary, was carried out at pH 1, 4, 8, 11 and 14. The NMR shift observed at pH 1 can be related to the  $pK_a$  of **12**: at pH 1 the compound is fully protonated, however, as the pH increases to 4, compound **12** becomes deprotonated and thus the NMR shifts are related to the hydrogen bonding between the flavin and the solvent molecules. The  $^1\text{H}$  NMR spectra, **Figure 5.6**, shows that the structure of **12** remains intact from pH 1-11, but at pH 14 some decomposition occurs, as evidenced by the appearance of 4 new peaks in the aryl region.

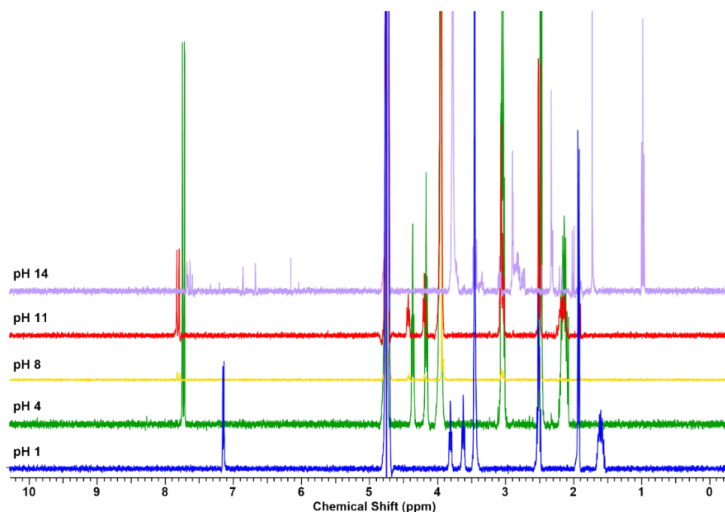


**Figure 5.6** <sup>1</sup>H NMR of **12** in electrolyte solutions of various pH with DMSO capillary at 298.15 K showing the structural change of the flavin as a function of pH.

In addition, the peaks in the alkyl region (1-4 ppm) have also undergone changes, in which the two CH<sub>2</sub> peaks relating to the CH<sub>2</sub> of the sulphonate chains have shifted as a result of the degradation (**Figure 5.6**). A zoomed view of the <sup>1</sup>H NMR spectrum, shown in **Figure 5.7**, highlights the extent of the decomposition which indicates an undesirable chemical change such as dealkylation and cleavage of terminal sulphonate chains due to the interaction with base (*e.g.* Hofmann elimination).<sup>16</sup> Comparison to the <sup>1</sup>H NMR spectrum of lumichrome (**Appendix 1, Figure A1.8**), the starting material, confirmed that the compound had not undergone degradation by cleavage of the terminal chains to revert to lumichrome but rather, some other decomposition pathway.

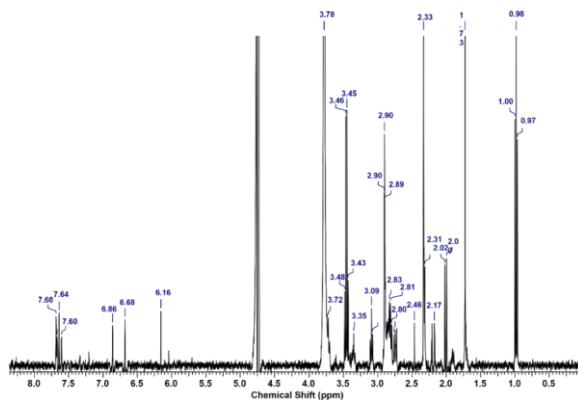


**Figure 5.7**  $^1\text{H}$  NMR of **12** at pH 14 with DMSO capillary at 298.15 K confirming decomposition of the flavin at high pH.

The results obtained from these studies show strong correlation to the base hydrolysis investigation on **12** which was carried out by Dr. Clark. Given the irreversible electrochemical behaviour at high pH observed in the cyclic voltammetry, further evaluation of the degradation of the flavin was required. Therefore, parallel hydrolysis studies were attempted on NMR samples of 0.1 M **12** in a range of electrolytes: 1 M NaCl(aq), 1 M NaOH (aq), and 0.01 M NaOH in 1 M NaCl to retain consistent ionic strength.

No degradation and/or structural change is observed for the weaker base electrolyte or the 1 M NaCl over 8 hours at room temperature. (**Figure 5.8a**) However, there was extensive degradation for the sample in 1 M NaOH for this time. In the minutes between adding the analyte to 1 M NaOH and recording the spectrum. It can be seen in the  $^1\text{H}$  NMR spectrum, **Figure 5.8b**, that there is a marked degree of degradation, corresponding to the new signals observed in the aromatic and aliphatic regions.

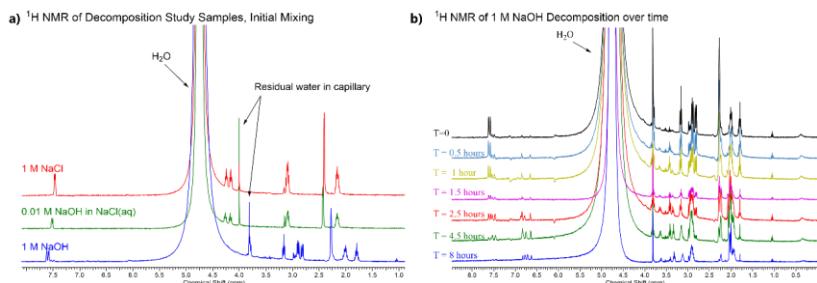


**Figure 5.8** <sup>1</sup>H NMR spectra of **12**: a) After initial mixing in different electrolytes [ 1 M NaCl(aq), 1 M NaOH (aq), and 0.01 M NaOH in 1 M NaCl] ; and b) Decomposition of **12** in 1 M NaOH over 8 hours. \*NMR spectra published with permission from Dr. Clark.

This warranted further investigation into the base-hydrolysis products and bulk hydrolysis was carried out by Dr. Clark. The results ultimately revealed that **12** was not degraded by Hofmann elimination as expected, but rather by a ring-opening of the terminal ring and imide hydrolysis, the sulphonate groups remained bound to the ring. The isolated hydrolysis product depended on whether the product was isolated from unquenched reaction mixture (**13**) or quenched with 10 M HCl first (**14**), and these differences were confirmed by Single Crystal X-Ray Diffraction, the evidence of which can be seen in **Figure 5.9**.



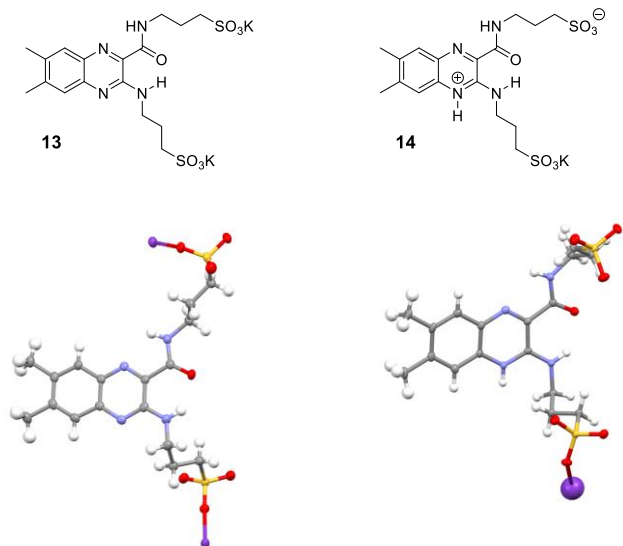


**Figure 5.9** Molecular and crystal structures of hydrolysis products **13** and **14**.  
\*Published with permission from Dr. Clark.

The electrochemical kinetics of **12** were measured using rotating disk electrode (RDE) voltammetry. Linear sweep voltammetry experiments were performed using 1M H<sub>2</sub>SO<sub>4</sub> in 1 M NaCl as the electrolyte, and the average data obtained from these experiments which were run in triplicates is shown in **Figure 5.10**.

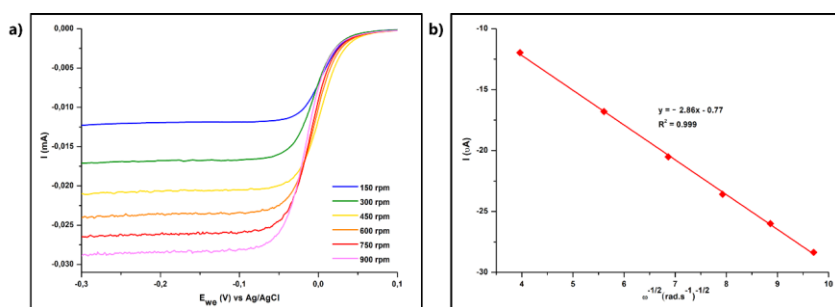


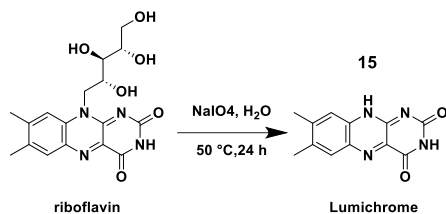
**Figure 5.10** Rotating Disk electrode experiment on **12** (1 mM in 1M H<sub>2</sub>SO<sub>4</sub> made up with 1 M NaCl). a) Current vs potential at different rotation rate with potential sweep of 5 mV/s.; b) Levich-plot of limiting current versus square root of rotation rate.

Since **12** is stable at acidic pH, and determination of kinetic properties was limited to an acidic environment at ~ pH 1. The sigmoidal shape of the RDE curve is indicative of a simple and reversible half-reaction at this pH which is further affirmed by the linear relationship observed in the Levich plot. The diffusion coefficient ( $D$ ) of **12** was determined from the Levich plot to be  $4.77 \times 10^{-7} \text{ cm}^2/\text{s}$ , and as a novel compound this value could not be confirmed in literature.

### 5.2.2 Water-soluble flavin derivatives

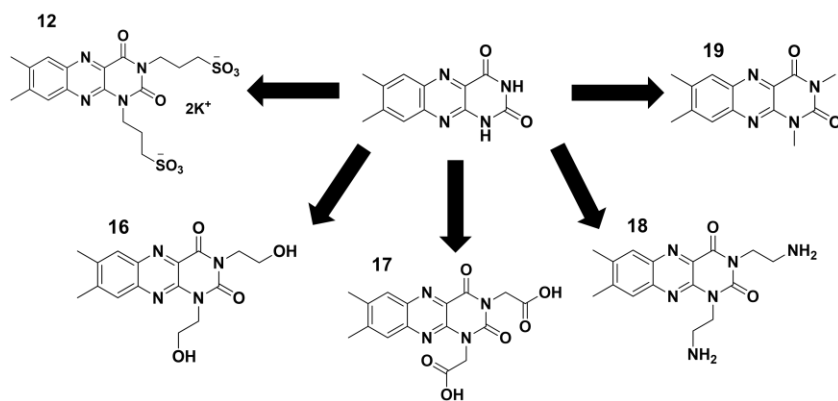
Other than the work by the Aziz group<sup>8</sup>, and a report in 2016 by Orita *et al.*<sup>10</sup> utilizing a flavin mononucleotide as the negative couple in an AORFB with 99% capacity retention, flavins have not been used in redox flow batteries. Water-soluble flavin derivatives such as **12** are therefore a low-cost alternative negative couple for AORFBs which may be paired with positive couples such as Tiron<sup>®</sup> or HBr.

The work in this section was aimed at expanding the development of a water-soluble flavins. The lumichrome core is stable and easy to synthesize from riboflavin, and therefore, additional analogues were planned around the substitution of water-solubilising side chains at positions *N1* and *N3*. Cost and synthetic efficiency evaluations regarding the synthesis of lumichrome were previously performed within the research group and it was found that lumichrome was obtained in higher yield by oxidative cleavage of the sugar chain from riboflavin than by conventional coupling of 3,4-diamino-*o*-xylene and alloxan.<sup>17</sup> Given that the commercial price of lumichrome is approximately £ 26.65/mole, lumichrome was synthesized from riboflavin (£ 131/ mole) (**Scheme 5.2**) and used as the key synthetic intermediate for flavin derivatives.



**Scheme 5.2** Synthesis of lumichrome (**15**) via sugar chain cleavage of riboflavin.

Based on reports in literature<sup>1,18</sup> and previous synthesis methods described in this work (Chapter 2), the initial synthesis of the desired flavin derivatives was attempted *via*  $S_N2$  substitution at positions *N1* and *N3*.



**Scheme 5.3** Schematic of Flavin derivatives which were investigated in this work.

#### **1,3-bis(2-hydroxyethyl)-7,8-dimethylbenzo[g]pteridine-2,4(1H,3H)-dione (**16**)**

Lacking literature precedent, *N*-methyl pyrrolidone (NMP) was used as the reaction solvent following its successful use in the synthesis of **12**, and the synthesis was attempted as per

**Scheme 5.4.**

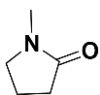
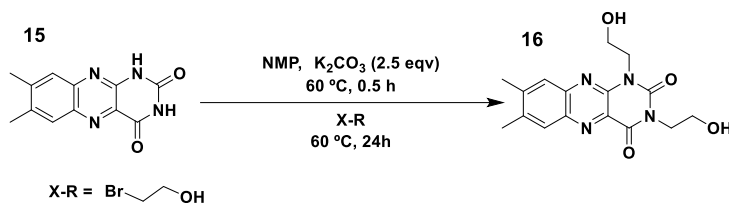


**Figure 5.11** Structure of *N*-methyl pyrrolidone (NMP).



**Scheme 5.4** Synthesis of 1,3-bis(2-hydroxyethyl)-7,8-dimethylbenzo[g]pteridine-2,4(1H,3H)-dione (**16**).

The initial synthesis attempt was relatively successful and resulted in the formation of the di-substituted flavin as desired. Neither lumichrome nor  $K_2CO_3$  fully dissolve in NMP and therefore, it is difficult to visibly monitor the progress of the reaction or observe formation of any solid in the reaction flask, as such, the reaction was monitored by NMR. The desired product proved to be highly soluble in alcohol solvents but could be precipitated as a yellow solid on addition of diethyl ether, however  $^1H$  NMR showed persistent NMP and diethyl ether. Further efforts to remove residual solvents by re-crystallization were unsuccessful.

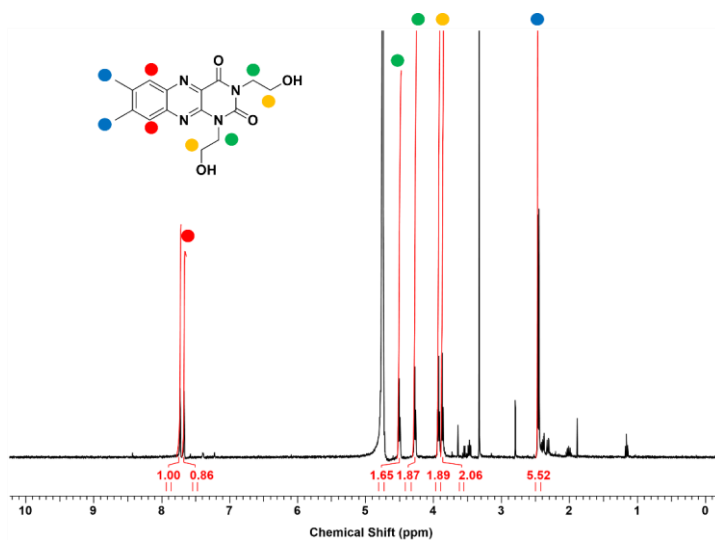
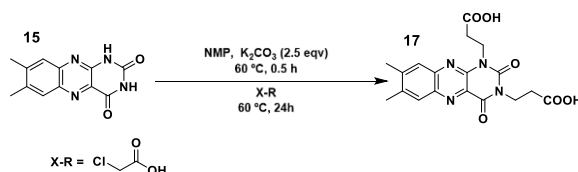


**Figure 5.12**  $^1H$  NMR spectrum of **16** after precipitation from diethyl ether in  $D_2O$  at 298.15 K.

Subsequent synthesis attempts encompassed various factors such as reaction time for deprotonation, overall reaction time and nature of solvent, and complete reaction details can be found in [Table 5.1](#). Despite copious efforts, **16** was not successfully isolated and due to its arduous and costly optimization, research focus was redirected.

### 2,2'-(7,8-dimethyl-2,4-dioxobenzo[g]pteridine-1,3(2H,4H)-diyl)diacetic acid (**17**)

The Aziz group successfully employed the addition of a carboxylic acid group at position C7 or C8 to improve solubility at pH 14 and lower the reduction potential.<sup>8</sup> Compound **17** was targeted to introduce carboxylic acid functionality through position N1 and N3, but these carboxylates are not directly conjugated into the aromatic backbone and so it cannot be assumed that the substitution would have the same effect.



**Scheme 5.5** Synthesis of 2,2'-(7,8-dimethyl-2,4-dioxobenzo[g]pteridine-1,3(2H,4H)-diyl)diacetic acid (**17**).

Again, NMP was used as the reaction solvent for the initial synthesis attempt and the same reaction procedure followed as for compound **11**. It was clear from the initial NMR that the reaction was unsuccessful and there was no trace of the product. The reaction was then repeated using 3 equivalents of base, DMF which resulted in the formation of deep yellow solid that was isolated by filtration however the NMR showed only possible formation of the monosubstituted product. For the third and final synthesis attempt of **17**, 5.5 equivalents of base were used to ensure complete deprotonation of N1 and N3, and the reaction ran for 48 hours to drive the reaction to completion.

The  $^1\text{H}$  NMR spectrum (**Figure 5.12**) showed strong peaks for the aromatic protons and terminal hydrogens on the methyl groups at C7 and C8 but only traces of side-chain peak. Given how tedious the synthesis had proven to be, with minimal positive results, the synthesis of this flavin was not pursued any further, and synthetic details are listed in [Table 5.2](#).

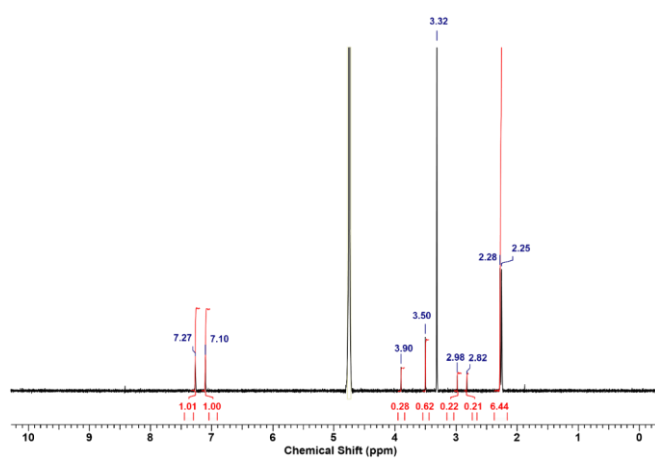
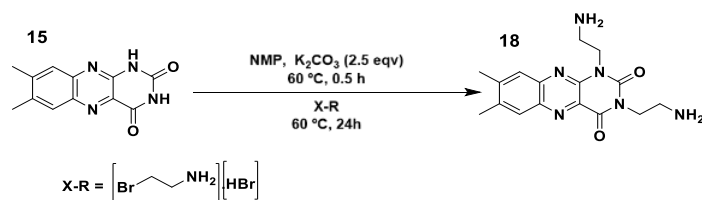


**Figure 5.13**  $^1\text{H}$  NMR spectrum of (**17**) in  $\text{D}_2\text{O}$  at 298.15 K.

### **1,3-bis(2-aminoethyl)-7,8-dimethylbenzo[g]pteridine-2,4(1H,3H)-dione (**18**)**

As the addition of a terminal quaternary ammonium cation had already been investigated using alloxazine, this work sought a disubstituted lumichrome with an ethyl amine chain.



**Scheme 5.6** Synthesis of 1,3-bis(2-aminoethyl)-7,8-dimethylbenzo[g]pteridine-2,4(1H,3H)-dione (**18**).

As with the previous compounds, NMP was selected as the reaction solvent. The initial reaction of **15** with 2-bromoethylamine-hydrobromic acid was unsuccessful as confirmed by  $^1\text{H}$  NMR on the final product obtained after the workup (**Appendix 1, Figure A1.9**). The NMR showed major peaks for the alkylating agent, 2-bromoethylamine-hydrobromic acid, but rather minor peaks for the flavin which is likely because the reaction had not reached completion.

Therefore, the product was resubjected in DMF with a larger quantity of base to completely deprotonate both species, as the presence of hydrobromic acid from the alkylating agent may have been deprotonated before the *N1* and *N3* positions on **15**. Therefore, more  $\text{K}_2\text{CO}_3$  (5 equivalents) was required to drive the reaction to completion. Attempts to isolate this product in pure form were unsuccessful, with the signal-to-noise ratio of the  $^1\text{H}$  NMR obtained on the final product being too large to properly integrate the peaks. Ultimately, this compound appeared to be less soluble than **16** in aqueous solutions and therefore further attempts to repeat and optimize the synthesis were discarded.

### 5.2.3 1,3,7,8-tetramethylbenzo[g]pteridine-2,4(1H,3H)-dione (**19**)

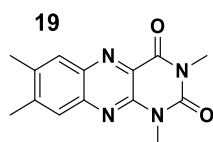


**Figure 5.14** Structure of **19**.

For comparison, a known flavin: 1,3,7,8-tetramethylbenzo[g]pteridine-2,4(1H,3H)-dione, **19**, was synthesized. Unlike the other flavin derivatives presented in this chapter, **19** has limited water solubility and therefore, the electrochemical analysis was conducted in MeCN as the solvent and  $[\text{TBA}][\text{PF}_6]$  as the supporting electrolyte.

In MeCN, **14** exhibits irreversible electrochemical behaviour as the CV shows a single oxidation peak at - 0.58V. (**Figure 5.15a**) Since flavins reductions are proton-coupled electron transfer reactions, **14** does not exhibit reversible electrochemical capabilities in MeCN due to the absence of free protons.

However, as seen in **Figure 5.15b** after the addition of excess trifluoroacetic acid (TFA), the redox behaviour changes, and a reversible redox peak at -0.84 V appears which is more negative than the redox peak in the absence of acid.

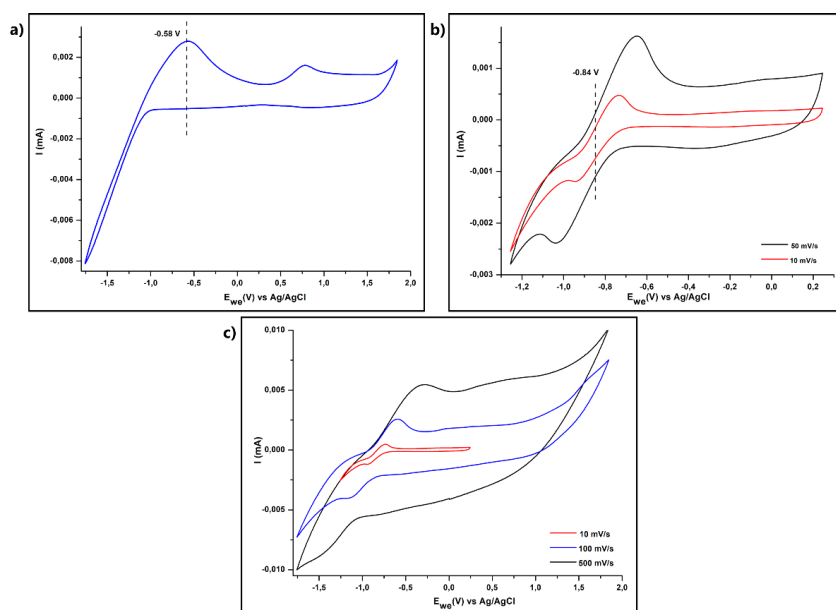


**Figure 5.15** Cyclic voltammograms of **19** in MeCN with 0.1 M ([TBA][PF<sub>6</sub>]) as supporting electrolyte. a) Scan rate of 100 mV/s.; b) CV of **19** after the addition of TFA.; c) CVs at varying scan rates.

This is due to the electrochemical nature of PCET processes which **19** undergoes during redox reactions and their relationship to the Nernst equation (**Equation 1.2**).



Therefore, as per this equation it can be deduced that the redox potential of a reaction with  $m$  protons and  $n$  electrons will shift the redox potential by 0.059 V per 10-fold change in proton activity (per pH unit).<sup>19</sup> The addition of TFA changed the pH of the solution making it more acidic, and as a result, this correlated to a shift in the redox potential as expected by the Nernst equation. The electrochemical processes of **19** were further investigated using variable-scan-rate CV (**Figure 5.15a & b**) which shows considerable merging of the redox peaks as the scan rates increase. It may be deduced that at higher scan rates, the rate of reduction from the fully protonated form to the neutral form was outrun, resulting in a lower local concentration of flavin at the electrode surface, which caused a broadened peak.<sup>14</sup>

Rotating disk electrode experiments were performed to investigate the reduction kinetics of **14**, using linear sweep voltammetry to sweep negatively from 0.01 V to -1.3 V vs Ag/AgCl using MeCN and 0.1 M [TBA][PF<sub>6</sub>] as the supporting electrolyte and the results are shown in **Figure 5.16**. The Levich plot obtained showed good linearity, giving a diffusion coefficient ( $D$ ) of **14** of  $7.56 \times 10^{-8}$  cm<sup>2</sup>/s. This may be indicative of poor/slow electron-transfer kinetics for a two-electron transfer, however, further detailed investigation using different solvents would be necessary to fully conclude this.<sup>14,20,21</sup>

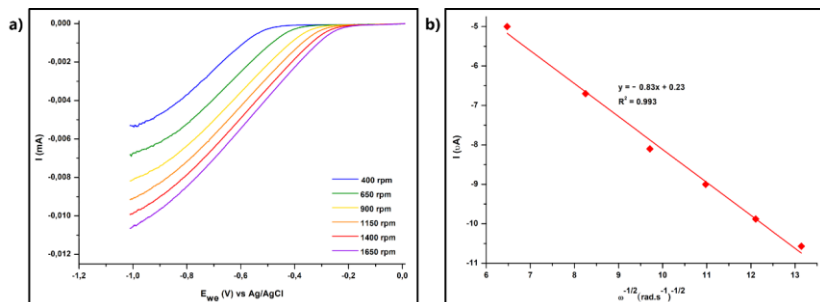


**Figure 5.16** Rotating Disk electrode experiment on **19** (MeCN with 0.1 M ([TBA][PF<sub>6</sub>]) as supporting electrolyte.). a) Current vs potential at different rotation rate with potential sweep of 5 mV/s.; b) Levich-plot of limiting current versus square root of rotation rate.

### 5.3 Conclusions

The synthesis of three water-soluble flavin-derivatives was attempted but the syntheses were not successful. Electrochemical analysis of **12** across a pH range determined the stability window for **12** which was between pH 1 – pH 4, and the nature of the base hydrolysis products, of **12**, was elucidated.

Correlating the CV results with the <sup>1</sup>H NMR results, it is evident that the electrochemical properties of **12** are pH dependent, and that at very basic pH, that the molecule is degraded which renders it electrochemically inactive and therefore, unsuitable for use in alkaline AORFBs.

### 5.4 Future Work

Given the previous success of a water-soluble flavin (**12**), further flow cell testing should be conducted to confirm the usability of this flavin as a negolyte for AORFBs. Further investigation should also be done into the hydrolysis product obtained during the stability studies as there may themselves be viable for use in alkaline AORFBs.

## 5.5 Experimental Methodology & Materials

### 5.5.1 Materials used and Physical Measurements

All reagents used were purchased from several commercial suppliers and were used without further purification.  $^1\text{H}$  NMR (400 MHz) spectra were recorded on a Bruker AV2-400 instrument. All chemical shifts are given in ppm with respect to residual solvent peaks. Coupling constants ( $J$  values) are quoted to one decimal place with values given in Hertz (Hz). pH of solutions was measured using a LAQUAtwin PH-11 pH meter with two-point calibration.

Commented [EC1]: You do have the  $^{13}\text{C}$  as well, yes?

### 5.5.2 Electrochemical Measurements

Cyclic voltammetry experiments were carried out on a BioLogic VSP-3 potentiostat using a three-electrode system comprising a glassy carbon working electrode, a platinum wire counter electrode, and a Ag/AgCl reference electrode which was stored in 3M KCl solution. The working electrode was polished using microfibre pads by fine polishing with 6  $\mu\text{m}$  diamond polish, 1  $\mu\text{m}$  diamond polish, and 0.05  $\mu\text{m}$  alumina polish, then rinsed with deionized water and air dried before use. CV solutions were prepared by dissolving the compound of interest (10 mg) in the specified electrolyte which was prepared in bulk. Solutions were purged using  $\text{N}_2$  gas and then CV was run at varying scan rates. Where pH-dependence studies were performed, these were first performed on only the flavin and then, following the addition of FCN as an internal standard, the solution was purged again with  $\text{N}_2$  and then the CV was run.

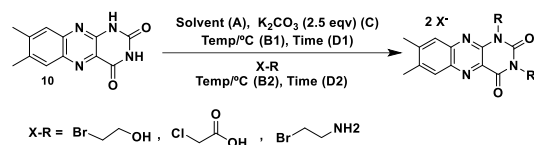
Rotating-disc electrode (RDE) measurements were conducted using a Metrohm Autolab RDE (AUT.RDE.S) instrument equipped with an Ultra Trace carbon working electrode, a Ag/AgCl reference electrode (pre-soaked in 3M KCl solution) and a platinum wire counter electrode.

Linear sweep voltammetry (LSV) scans were recorded at a scan rate of  $5 \text{ mV.s}^{-1}$  from 0.0 V to -1.4 V vs. SHE, with rotational speed between 100-1500 rpm. Three scans were recorded and averaged to ensure reproducible results at each rotation rate. A Levich plot was constructed of the limited current versus the square root of the rotation speed, and the diffusion coefficient was calculated from the linear slope of the plot according to the Levich equation:  $i = 0.620nFAcD^{2/3}\nu^{-1/6}\omega^{1/2}$ , where  $n = 1$ , Faraday's constant  $F = 96485 \text{ C.mol}^{-1}$ , electrode area  $A = 0.196 \text{ cm}^2$ , molar concentration  $c = 2 \times 10^{-6} \text{ mol.cm}^{-3}$ , the kinematic viscosity  $\nu = 0.0114 \text{ cm}^2.\text{s}^{-1}$  (1M  $\text{H}_2\text{SO}_4$  in 1M NaCl aqueous solution), and kinematic viscosity  $\nu = 4.2 \times 10^{-3} \text{ cm}^2.\text{s}^{-1}$  (0.1 M [TBA][PF<sub>6</sub>] in MeCN), and  $D$  represents the diffusion coefficient.

### 5.5.3 Synthesis of Lumichrome

Lumichrome (**15**) was prepared using a modified literature method.<sup>18</sup> Riboflavin (15.02 g, 39 mmol) and  $\text{NaIO}_4$  (23.90 g, 112 mmol) in  $\text{H}_2\text{O}$  (350 mL) were stirred at 50 °C for 24 hours. The reaction mixture was left to cool and sodium sulphite (approx. 20 g) was added portion wise to the stirred dark brown solution until the colour changed to a bright orange. The solid was isolated by filtration, washed with  $\text{H}_2\text{O}$  (60 mL) and MeOH (50 mL), and dried to give lumichrome (**15**) as a yellow powder (7.64 g, 79 %). Unlike the literature method, this method removes excess iodine using sodium sulphite rather than washing with large quantities of MeOH. **<sup>1</sup>H NMR** (300 MHz, 298.15 K; DMSO)  $\delta_{\text{H}} = 11.54$  (2H), 7.86 (1H, s, Ar-H), 7.65 (2H, s, Ar-H), 2.33 (3H, s, CH<sub>3</sub>), 2.17 (3H, s, CH<sub>3</sub>) ppm. <sup>1</sup>H NMR and <sup>13</sup>C analytical data in accordance with literature.<sup>18</sup> (see **Figure A1.7** for <sup>1</sup>H spectrum).

### 5.5.4 Synthesis of water soluble flavin derivatives (General procedure A)



**Scheme 5.7** Alkylation of **15** to form water-soluble flavin derivatives.

**15** (1.007 g, 3.4 mmol) and K<sub>2</sub>CO<sub>3</sub> (1.25 g, 9 mmol) were combined in NMP (25 mL) and stirred at 60 °C for 30 minutes. Butyl halide (14 mmol) was added to the stirred reaction mixture and stirring continued at 60 °C for a further 24 hours. The reaction mixture was quenched with MeOH (25 mL), filtered, and the isolated solid washed with hot MeOH (10 mL). The MeOH filtrate, containing the reaction solvent, was added portion-wise to vigorously stirred diethyl ether (200 mL) and the mixture was stirred vigorously for 2 more hours, then filtered and the isolated solid dried before NMR analysis.

#### 5.5.4.1 Preparation of **16**:

**Table 5.1** Synthesis conditions for 1,3-bis(2-hydroxyethyl)-7,8-dimethylbenzo[g]pteridine-2,4(1H,3H)-dione (**16**).

| Trial | Solvent (A) | Temp. / °C        |                   | K <sub>2</sub> CO <sub>3</sub> (eqv.) | Time / hours (D) | Outcome  |
|-------|-------------|-------------------|-------------------|---------------------------------------|------------------|--|
|       |             | (B <sub>1</sub> ) | (B <sub>2</sub> ) |                                       |                  |  |
| 1     | NMP         | 60                | 60                | 2.5                                   | 0.5 ; 24         | Product not purified successfully. Additional purification led to loss of product.     |
| 2     | DMF         | 60                | 60                | ~2.6                                  | 0.75 ; 24        | Unsuccessful. Product was not isolated.  |
| 3     | DMF         | 60                | 60                | ~2.6                                  | 0.75 ; 48        | Unsuccessful. A product was isolated from this reaction but was lost at a later stage. |
| 4     | NMP         | 60                | 60                | 2.5                                   | 2 ; 96           | Unsuccessful. Product not isolated.  |

**5.5.4.2 Preparation of 17:****Table 5.2** Synthesis conditions for 2,2'-(7,8-dimethyl-2,4-dioxobenzo[g]pteridine-1,3(2H,4H)-diyl)diacetic acid (**17**).

| Trial | Solvent (A) | Temp. / °C        |                   | K <sub>2</sub> CO <sub>3</sub> (eqv.) | Time / hours (D) | Outcome  |
|-------|-------------|-------------------|-------------------|---------------------------------------|------------------|--|
|       |             | (B <sub>1</sub> ) | (B <sub>2</sub> ) |                                       |                  |  |
| 1     | NMP         | 60                | 60                | 3                                     | 0.5 ; 24         | Unsuccessful. The reaction did not reach completion, no product formed.            |
| 2     | DMF         | 60                | 60                | ~2.6                                  | 0.75 ; 24        | Unsuccessful. Monosubstituted product may have formed.                             |
| 3     | DMF         | 60                | 60                | 5.5                                   | 0.75 ; 48        | Unsuccessful. A product was isolated from this reaction and lost at a later stage. |

**5.5.4.2 Preparation of 18:**

Only one synthesis attempt was made, and this was conducted as per **Scheme 5.6**.

**5.5.5 Synthesis of 1,3,7,8-tetramethylbenzo[g]pteridine-2,4(1H,3H)-dione (19)**

Compound **19** was prepared using a modified version of **procedure A**, and a synthetic method in literature.<sup>18</sup> **15** (0.726 g, 3 mmol) and K<sub>2</sub>CO<sub>3</sub> (1.38 g, 10 mmol) were suspended in DMF (20 mL), giving a yellow reaction mixture to which was added methyl iodide (0.6 mL, 10 mmol). The flask was covered with aluminium foil to exclude light, and the reaction stirred overnight, whereupon <sup>1</sup>H NMR showed complete conversion to the desired product. The reaction mixture was filtered, and volatiles removed under vacuum to give crude yellow solid. To this was added brine (10 mL) and the aqueous phase was extracted with DCM (4 x 10 mL); the organic phase was dried with MgSO<sub>4</sub>, and the solvent removed to give crude **19** as a yellow solid (0.573 g) which <sup>1</sup>H NMR showed to contain significant residual DMF. A portion (0.2 g) was purified by flash column chromatography to give pure **19** as a yellow solid. (0.07 g, 0.29 mmol) which was used for subsequent electrochemical analysis.

## 5.6 References

- 1 A. Kormányos, M. S. Hossain, G. Ghadimkhani, J. J. Johnson, C. Janáky, N. R. de Tacconi, F. W. Foss, Y. Paz and K. Rajeshwar, *Chem. - A Eur. J.*, 2016, **22**, 9209–9217.
- 2 E. Silva and A. M. Edwards, *Flavins: photochemistry and photobiology*, Royal Society of Chemistry, 2006, vol. 6.
- 3 O. S. Ksenzhek, S. A. Petrova and I. D. Pinielle, *Bioelectrochemistry Bioenerg.*, 1979, **6**, 405–412.
- 4 W. S. Li, N. Zhang and L. M. Sayre, *Tetrahedron*, 2001, **57**, 4507–4522.
- 5 X. L. Li and Y. Fu, *J. Mol. Struct. THEOCHEM*, 2008, **856**, 112–118.
- 6 A. Niemz, J. Imbriglio and V. M. Rotello, *J. Am. Chem. Soc.*, 1997, **119**, 887–892.
- 7 A. Hollas, X. Wei, V. Murugesan, Z. Nie, B. Li, D. Reed, J. Liu, V. Sprenkle and W. Wang, *Nat. Energy*, 2018, **3**, 508–514.
- 8 K. Lin, R. Gómez-Bombarelli, E. S. Beh, L. Tong, Q. Chen, A. Valle, A. Aspuru-Guzik, M. J. Aziz, R. G. Gordon, A. A. Lindén, M. Johansson, N. Hermanns, J. E. Bäckvall, X. L. Li, Y. Fu, A. Niemz, J. Imbriglio, V. M. Rotello, J. B. Gerken, C. W. Anson, Y. Preger, P. G. Symons, J. D. Genders, Y. Qiu, W. W. Li, T. W. Root, S. S. Stahl, A. C. S. De Souza, L. Kodach, F. R. Gadelha, C. L. Bos, A. D. M. Cavagis, H. Aoyama, M. P. Peppelenbosch, C. V. Ferreira, A. W. Hofmann, A. Permatasari, W. Lee, Y. Kwon, S. S. Chen, M. S. Hossain, F. W. Foss, Y. Chen, S. A. Freunberger, Z. Peng, O. Fontaine, P. G. Bruce, K. Lin, R. Gómez-Bombarelli, E. S. Beh, L. Tong, Q. Chen, A. Valle, A. Aspuru-Guzik, M. J. Aziz, R. G. Gordon, K. Yamamoto, Y. Asano, Y. Xu, Y. H. Wen, J. Cheng, G. P. Cao, Y. S. Yang, V. Sichula, Y. Hu, E. Mirzakulova, S. F. Manzer, S. Vyas, C. M. Hadad, K. D. Glusac, E. Behavior, J. B. Gerken, A. Stamoulis, S. E. Suh, N. D. Fischer, Y. J. Kim, I. A. Guzei, S. S. Stahl, W. W. Li, N. Zhang, L. M. Sayre, H. J. Powers, R. Huang, J. K. Hyun, D. B. Min, H. Grajek, A. Orita, M. G. Verde, M. Sakai, Y. S. Meng, F. da Silva Miranda, A. M. Signori, J. Vicente, B. de Souza, J. P. Priebe, B. Szpoganicz, N. S. Gonçalves, A. Neves, S. S. Chen, F. W. Foss, Y. Liu, S. Lu, S. S. Chen, H. Wang, J. Zhang, Y. Xiang, R. Ohkado, T. Ishikawa, H. Iida, E. Silva, A. M. Edwards, R. Ariana, J. Asenjo-Pascual, I. Salmeron-Sanchez, J. R. Avilés-Moreno, P. Mauleón, P. Mazur, P. Ocón, J. T. Pinto, J. Zempeni, Y.-J. Zheng, D. B. Jordan, D.-I. Liao, K. Kis, R. Volk, A. Bacher, L. B. A. Johansson, A. Davidsson, G. Lindblom, K. R. Naqvi, B. J. Fritz, K. Matsui, S. Kasai, A. Yoshimura, J. Y. D'Aoust, W. G. Martin, J. Giroux, H. Schneider, J. Knight, C. Caseldine, M. T. Boykoff, K. Hoenes, U. Wenzel, B. Spellerberg, M. Hessling, B. J. Fritz, S. Kasai, K. Matsui, W. Kaim, B. Schwederski, O. Heilmann, F. M. Hornung, C. Frier, J. L. Décout, M. Fontecave, A. Kormányos, M. S. Hossain, G. Ghadimkhani, J. J. Johnson, C. Janáky, N. R. de Tacconi, F. W. Foss, Y. Paz, K. Rajeshwar, K. Lin, R. Gómez-Bombarelli, E. S. Beh, L. Tong, Q. Chen, A. Valle, A. Aspuru-Guzik, M. J. Aziz, R. G. Gordon, T. Sakai, T. Kumoi, T. Ishikawa, T. Nitta, H. Iida, P. F. Heelis, B. J. Parsons, G. O. Phillips, E. J. Land, A. J. Swallow, A. Orita, M. G. Verde, M. Sakai, Y. S. Meng, X. Wu, W. Hao, K. Y. Ye, B. Jiang, G. Pombar, Z. Song, S. Lin, T. Sakai, T. Kumoi, T. Ishikawa, T. Nitta, H. Iida, Y. Liu, S. Lu, S. S. Chen, H. Wang, J. Zhang, Y. Xiang, G. Tang, Z. Yang, T. Xu, C. Zhang, Z. Niu, S. Peng, Y. Ding, L. Zhang, X. Guo, Y. Zhao, G. Yu, K. Lin, R. Gómez-Bombarelli, E. S. Beh, L. Tong, Q. Chen, A. Valle, A. Aspuru-Guzik, M. J. Aziz, R. G. Gordon, A. T. Murray, P. Matton, N. W. G. Fairhurst, M. P. John, D. R. Carbery, A. Hollas, X. Wei, V. Murugesan, Z. Nie, B. Li, D. Reed, J. Liu, V. Sprenkle, W. Wang, L. Hooper-Burkhardt, S. Krishnamoorthy, B. Yang, A. Murali, A.

- Nirmalchandar, G. K. S. Prakash, S. R. Narayanan, B. Huskinson, M. P. Marshak, C. Suh, S. Er, M. R. Gerhardt, C. J. Galvin, X. Chen, A. Aspuru-Guzik, R. G. Gordon and M. J. Aziz, *Nat. Energy*, 2016, **1**, 1–8.
- 9 W. Raza, F. Ali, N. Raza, Y. Luo, K. H. Kim, J. Yang, S. Kumar, A. Mehmood and E. E. Kwon, *Nano Energy*, 2018, **52**, 441–473.
- 10 A. Orita, M. G. Verde, M. Sakai and Y. S. Meng, *Nat. Commun.*, 2016, **7**, 1–8.
- 11 B. Lee, Y. Ko, G. Kwon, S. Lee, K. Ku, J. Kim and K. Kang, *Joule*, 2018, **2**, 61–75.
- 12 E. S. S. A, O. S. Ksenzhek and S. A. Petrova, 1983, **156**, 105–127.
- 13 Y. Liu, Y. Li, P. Zuo, Q. Chen, G. Tang, P. Sun, Z. Yang and T. Xu, *ChemSusChem*, 2020, **13**, 2245–2249.
- 14 S. L. J. Tan, J. M. Kan and R. D. Webster, *J. Phys. Chem. B*, 2013, **117**, 13755–13766.
- 15 D. R. Weinberg, C. J. Gagliardi, J. F. Hull, C. F. Murphy, C. A. Kent, B. C. Westlake, A. Paul, D. H. Ess, D. Granville and T. J. Meyer, *Chem. Rev.*, 2012, **112**, 4016–4093.
- 16 A. W. Hofmann, *Philos. Trans. R. Soc. London*, 1851, **141**, 357–398.
- 17 K. Gumus, University of Kent, 2022.
- 18 T. Sakai, T. Kumoi, T. Ishikawa, T. Nitta and H. Iida, *Org. Biomol. Chem.*, 2018, **16**, 3999–4007.
- 19 J. M. Mayer, *Annu. Rev. Phys. Chem.*, 2004, **55**, 363–390.
- 20 S. L. J. Tan, M. L. Novianti and R. D. Webster, *J. Phys. Chem. B*, 2015, **119**, 14053–14064.
- 21 Z. Yang, L. Tong, D. P. Tabor, E. S. Beh, M. A. Goulet, D. De Porcellinis, A. Aspuru-Guzik, R. G. Gordon and M. J. Aziz, *Adv. Energy Mater.*, 2018, **8**, 1702056.



## CHAPTER 6

### CONCLUSIONS & FUTURE WORK

---

*"For I know the plans I have for you," declares the Lord. "plans to prosper you and not to harm you, plans to give you hope and a future."*

*Jeremiah 29:11*

## 6.1 Conclusions

The results obtained during this PhD and discussed in this thesis show that viologens can be easily synthesized using an  $S_N2$  reaction. Based on the desired application wherein the viologen will be utilized, properties such as reduction potential, ion conductivity, and water solubility may be fine-tuned during the synthetic procedure.

It was found that enhanced water solubility (~6 M) may be achieved by the addition of hydrophilic substituents such as hydroxyl (-OH) and sulphonic acid groups (-SO<sub>3</sub>), as seen in compound **1** and compound **4**, respectively. Given the high water solubility, **1** was tested in a neutral pH, asymmetric AORFB set-up, and showed promise for further optimization and development.

In the pursuit of scientific discovery, it is imperative that the results obtained are reproducible. As such, a large focus of this research was on the development of a sturdy, lab-scale testing rig to ensure reproducibility, and integrity during flow cell testing. This optimization procedure revealed the importance of using the correct tubing to support cell longevity.

The addition of an alkyl chain to the 4,4'-bipyridine core produced a stable, symmetrical viologen, compound **5**, which served as a valuable, biphasic electrocatalyst. By exploiting the different solubilities of the three, stable, redox states of this viologen, this research showed an efficient and cost-effective method for the synthesis of valuable olefins using reductive dehalogenation.

Like viologens, flavins offer a unique set of properties which make them attractive for electrochemical applications. However, previously, flavins have typically been explored for

their biological significance and their feasibility therein. This work has further explored the possibility of using a flavin with terminal sulphonate groups, compound **12**, in an AORFB at low pH (pH 1-4).

## 6.2 Future Work

This work has led to an improved understanding of the use of viologens in various electrochemical applications.

Whilst unsuccessful in this research, bulky, conjugated molecules, similar to compounds **7** & **9** may lead to the development of a stable AORFB with little to no crossover. These bulkier molecules offer much promise in minimizing a critical, and persistent issue in the RFB community: crossover. Therefore, future efforts will be directed at optimizing a synthetic route to successfully synthesize bulkier, conjugated molecules for RFB applications.

Looking ahead, there is an inevitable need for more sustainable, and environmentally friendly energy storage devices. Both viologens and flavins offer this possibility, and efforts should be dedicated to advancing the development of stable, water-soluble, redox active agents for use in AORFBs., in particular, focused should be directed at preventing electrolyte degradation due to viologen decomposition.

Lastly, given the success of the biphasic electrocatalytic dehalogenation method explored in this research, efforts will be directed to expand the substrate scope. This may include the dehalogenation of halides, and reduction of other functional groups.

## APPENDIX 1

---

## Additional characterization techniques

### *Electrochemical Impedance Spectroscopy (EIS)*

Electrochemical impedance spectroscopy (EIS) or impedance spectroscopy (IS) is an electrochemical technique that provides information about the conductivity of a sample and/or surface.<sup>1,2</sup> EIS investigates the correlation between the properties of electrode materials and controllable variables such as temperature, applied static voltage, and oxygen partial pressure. For flow cell applications, EIS rapidly characterizes the system, and provides information regarding the resistance of the cell at specified currents, and at different times (Before or after cell cycling).

There are 3 different approaches to EIS: galvanostatic (GEIS), potentiostatic (PEIS), and galvanostatic adaptive amplitude (GEIS-AA),<sup>3</sup> but for this work only Galvanostatic EIS, wherein a single frequency voltage or current is applied to the interface and the phase shift and amplitude measured, is relevant. During a GEIS experiment, the DC current is fixed and a sinusoidal current perturbation is imposed on the DC current which produces a corresponding potential that determines the impedance of the system.<sup>1,3</sup> The sinusoidal output potential curve may be offset from the sinusoidal input current and this is referred to as a "phase difference" or "phase angle" which would arise due to the nature of the analyte, its conductivity, and the internal resistance of the system (flow cell). The flow rate of the charged particles (current) is dependent on the ohmic resistance of the electrolyte, and electrodes, and the rate of reaction at the electrode-electrolyte interfaces. As such, the contribution of impedance due to energy loss is called the *real component of the impedance*,  $Z_{Re}$  or  $Z'$ , and the imaginary contribution is labelled  $Z''$ .<sup>4</sup>

## | Appendix 1

The impedance of the system can be calculated from the ratio of the frequency dependent potential over the frequency of the frequency dependent current.<sup>3</sup>

Impedance data may be represented using a Bode plot or a Nyquist plot, and in this work, only Nyquist plots were used. Nyquist plots are a typical method of representing impedance data and this relates the major impedance ( $Z$ ) components which are the real/in-phase ( $Z'$ ) and imaginary/out-of-phase ( $Z''$ ) components, and these are plotted to their limits.<sup>3,5</sup> EIS plots allow for the determination of the real resistances of the system (point x), and the capacitance of the double layer can be modelled from this data.<sup>5</sup>

**Figure A1.1** shows a typical Nyquist plot obtained during a flow cell test for impedance experiments run before and after cell cycling. Point A and point B represent the x-intercept which provides the value for the impedance or internal resistance, in  $\Omega$ , at that point.

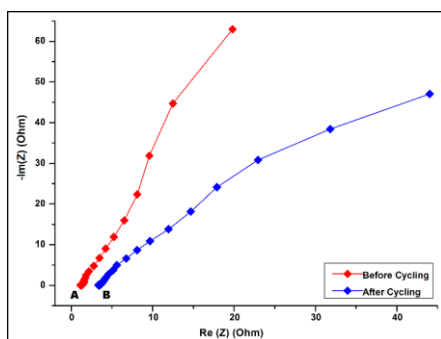


**Figure 01.1** EIS curves for Run y8.

### ***Nuclear Magnetic Resonance (NMR)***

Nuclear Magnetic Resonance (NMR) spectroscopy is one of the most widely used techniques in modern chemistry given its various applications in different research fields including biology, chemistry, food science and medicine. The wide use is given that this non-destructive technique can provide a wide range of information about the sample in question including hydrogen bonding properties, hydration state, configurational and conformational changes, and weak molecular interactions.<sup>6</sup> NMR experiments are performed on the nuclei of atoms rather than the electrons, and as such, the typical environment of certain nuclei can be mapped using NMR spectroscopy.<sup>7</sup>

All nuclei are electrically charged with multiple spins, and in the presence of an external magnetic field an energy transfer from a lower energy level to a higher energy level is possible when a nuclei absorbs radio frequency energy.<sup>6</sup> A typical NMR experiment produces a spectrum which is displayed on a plot showing the applied field strength which increases from left to right. Due to the different local chemical environments around each nuclei, the nuclei will resonate at different frequencies, resulting in the chemical shift, which allows for the determination of different chemical structures.

In this work, only  $^1\text{H}$  and  $^{13}\text{C}$  NMR spectroscopy were used for the determination of different chemical structures. For flow battery samples (Chapter 4), NMR spectra were recorded in *protio*-solvents with an inset DMSO  $d_6$ -capillary and referenced to residual solvent peaks in ppm.

### Additional data

#### Chapter 3

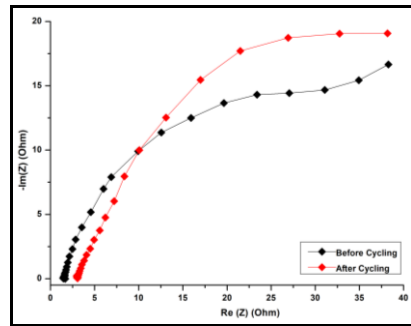


Figure 01.2 EIS curves for Run y8.

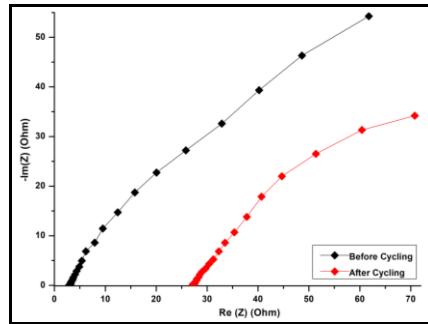


Figure 01.3 EIS curves for Run y9.

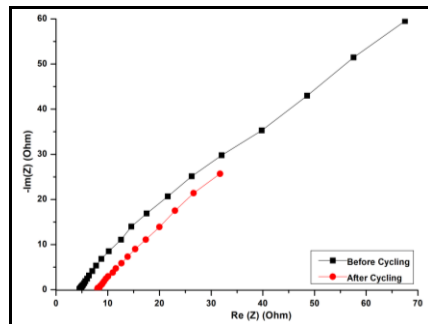
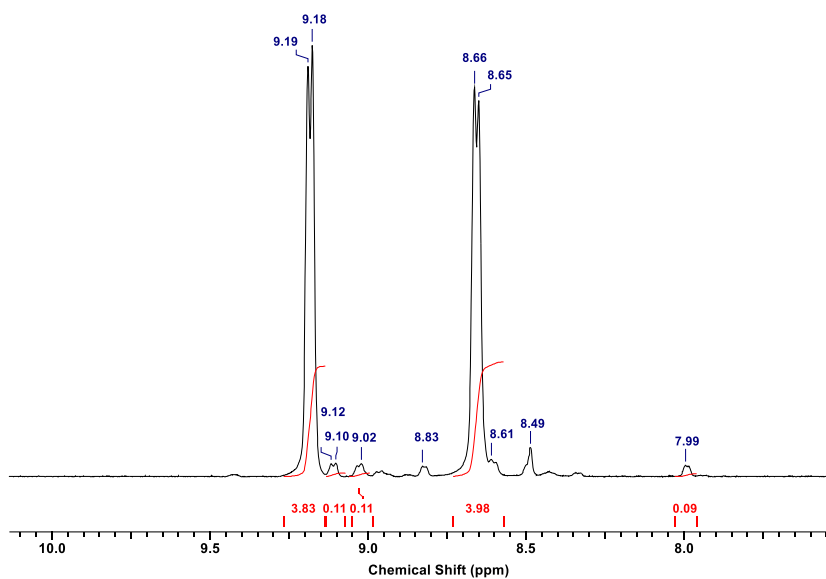
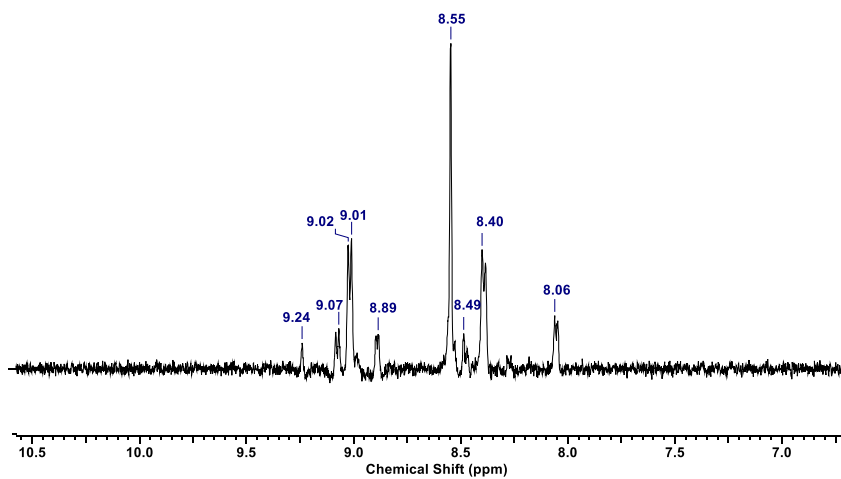


Figure 01.4 EIS curves for Run y10.





**Figure 01.5** Truncated  $^1\text{H}$  NMR with DMSO capillary at 298.15K of **Run y11** viologen electrolyte post-cycling confirming dealkylation of **1**.



**Figure 01.6** Truncated  $^1\text{H}$  NMR with DMSO capillary at 298.15K of **Run y13** viologen electrolyte post-cycling confirming dealkylation of **1**.

## Chapter 5

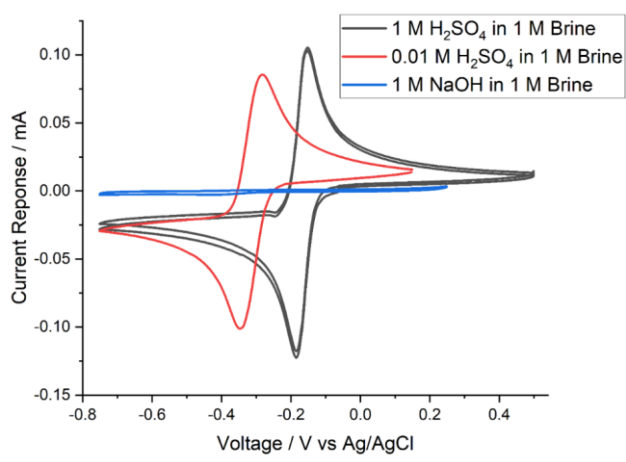


**Figure A1.7** Multiple CV graph, all containing 0.005 M **14** (0.028 g) degassed with  $N_{2(g)}$ , taken at 100 mV/s scan rate. Reproduced with permission.<sup>8</sup>

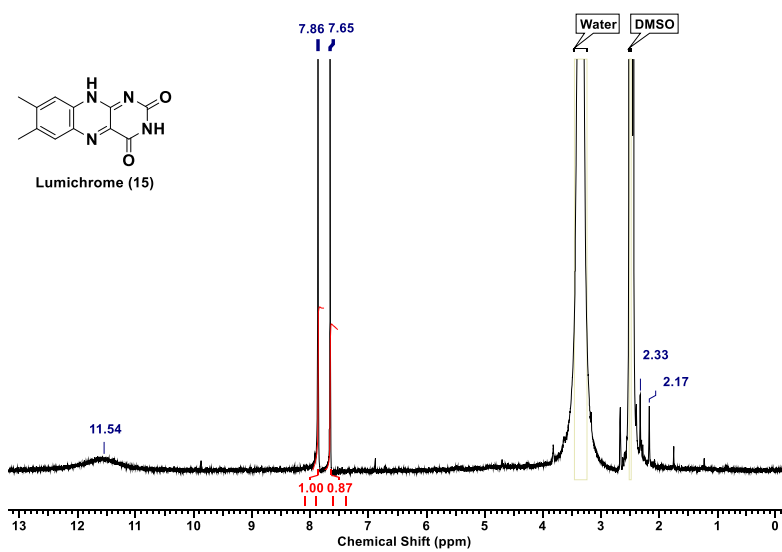


**Figure 01.8**  $^1\text{H}$  NMR spectrum of **15** in DMSO at 298.15 K.

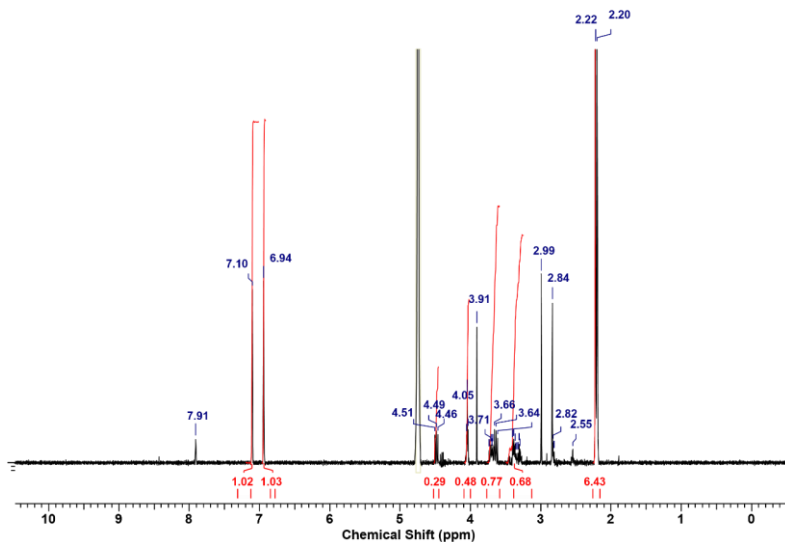


**Figure 01.9**  $^1\text{H}$  NMR spectrum of **18** in  $\text{D}_2\text{O}$  at 298.15 K.

## References

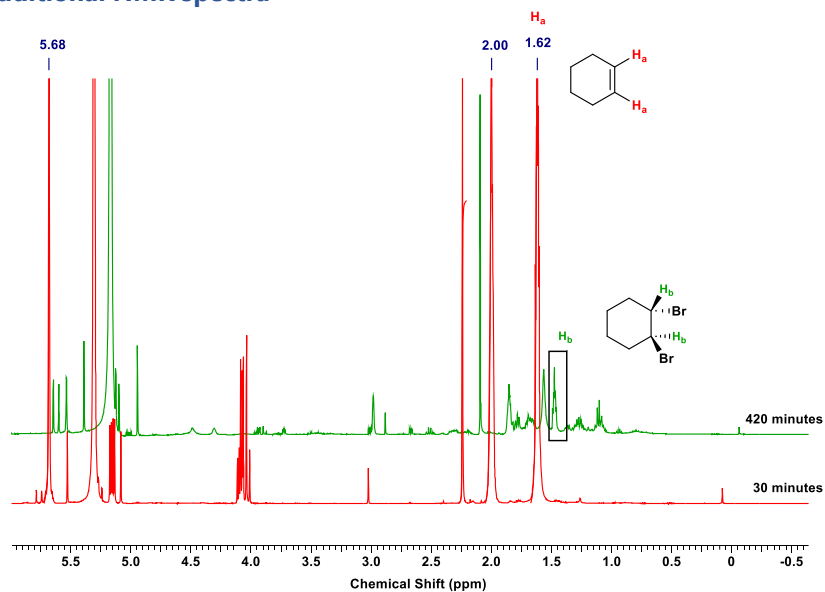
- 1 B. Y. Chang and S. M. Park, *Annu. Rev. Anal. Chem.*, 2010, **3**, 207–229.
- 2 J. R. Macdonald and E. Barsoukov, Eds., *Impedance spectroscopy: theory, experiment, and applications*, John Wiley & Sons, Second., 2018.
- 3 What is Electrochemical Impedance Spectroscopy (EIS)? (Electrochemistry Basics Series) - BioLogic Learning Center, <https://www.biologic.net/topics/what-is-eis/>, (accessed 18 April 2023).
- 4 W. R. Browne, *Electrochemistry*, Oxford University Press, 2018.
- 5 EIS Data Plotting – Pine Research Instrumentation Store, <https://pineresearch.com/shop/kb/theory/eis-theory/eis-data-plotting/>, (accessed 18 April 2023).
- 6 J. B. Lambert, E. P. Mazzola and C. D. Ridge, *Nuclear magnetic resonance spectroscopy: an introduction to principles, applications, and experimental methods*, John Wiley & Sons, 2019.
- 7 M. K. Singh and A. Singh, in *The Textile Institute Book Series*, eds. M. K. Singh and A. B. T.-C. of P. and F. Singh, Woodhead Publishing, 2022, pp. 321–339.
- 8 K. Gumus, University of Kent, 2022.

## **APPENDIX 2**

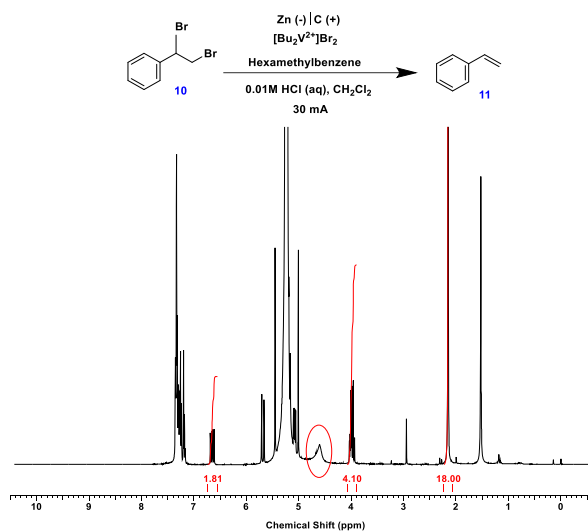
### **Additional Data for Chapter 4**

---

## Additional NMR spectra

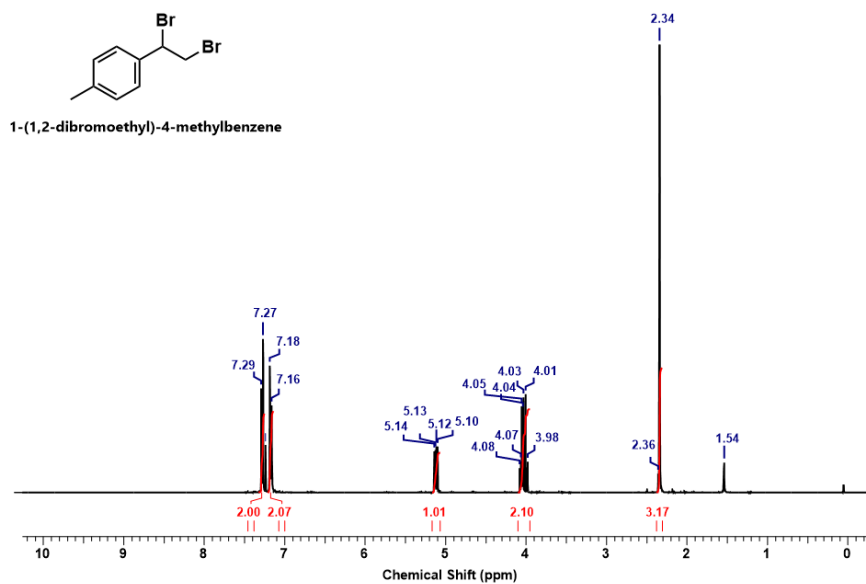
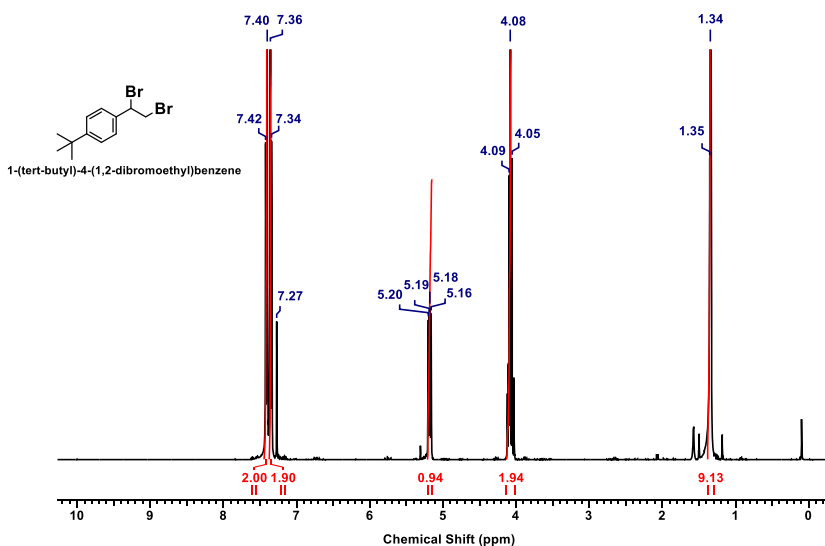


**Figure A2.1**  $^1\text{H}$  NMR spectrum in  $\text{CDCl}_3$  at 298.15 K of the organic layer confirming the consumption of cyclohexene to 1,2-dibromocyclohexane.



**Figure A2.2**  $^1\text{H}$  NMR spectrum in  $\text{CDCl}_3$  at 298.15 K of the organic layer for the reaction with 0.01M HCl as the aqueous layer which confirms the polymerization of styrene as seen by the encircled peak.

## NMR Spectra of vic-dibromides

Figure A2.3  $^1\text{H}$  NMR spectrum of **10a** in  $\text{CDCl}_3$  conducted at 298.15 K.Figure A2.4  $^1\text{H}$  NMR spectrum of **10b** in  $\text{CDCl}_3$  conducted at 298.15 K.

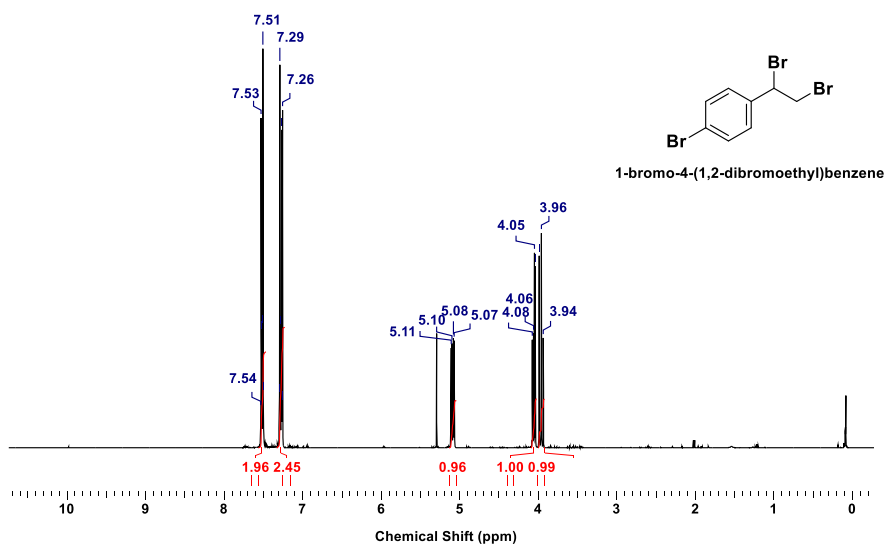


Figure A2.5 <sup>1</sup>H NMR spectrum of **10c** in CDCl<sub>3</sub> conducted at 298.15 K.

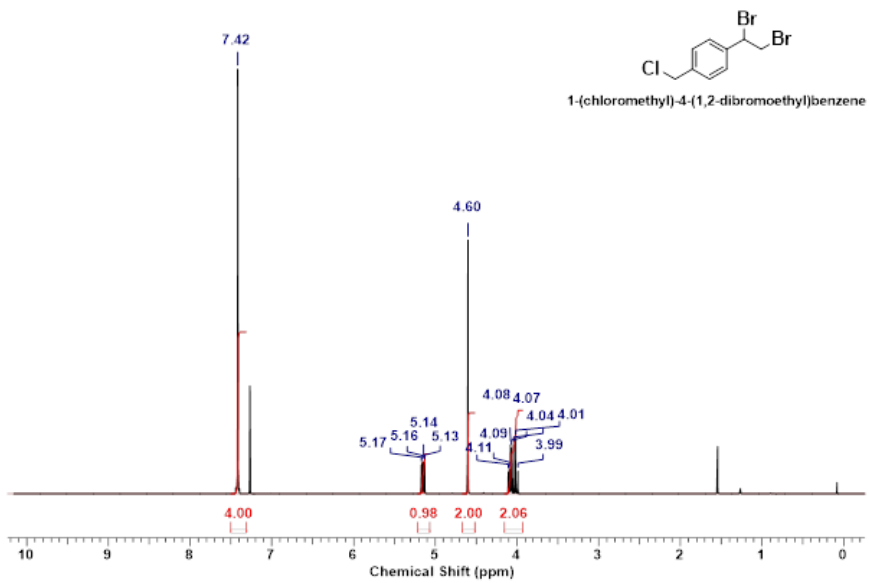


Figure A2.6 <sup>1</sup>H NMR spectrum of **10d** in CDCl<sub>3</sub> conducted at 298.15 K.

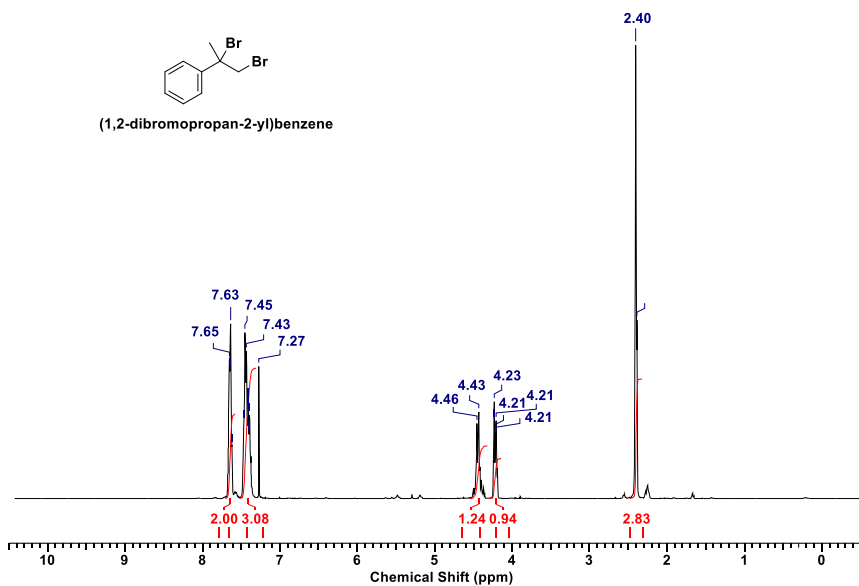


Figure A2.7  $^1\text{H}$  NMR spectrum of **10e** in  $\text{CDCl}_3$  conducted at 298.15 K.

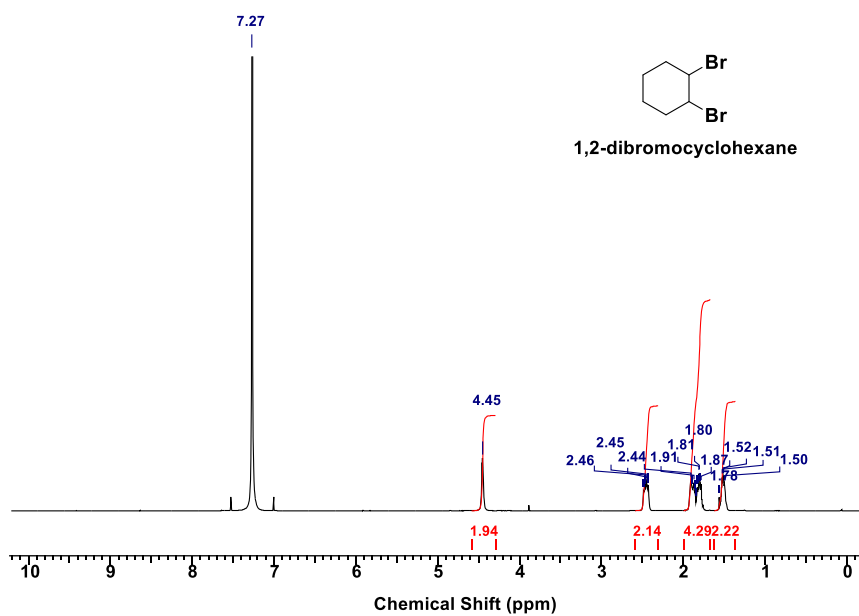


Figure A2.8  $^1\text{H}$  NMR spectrum of **10f** in  $\text{CDCl}_3$  conducted at 298.15 K.



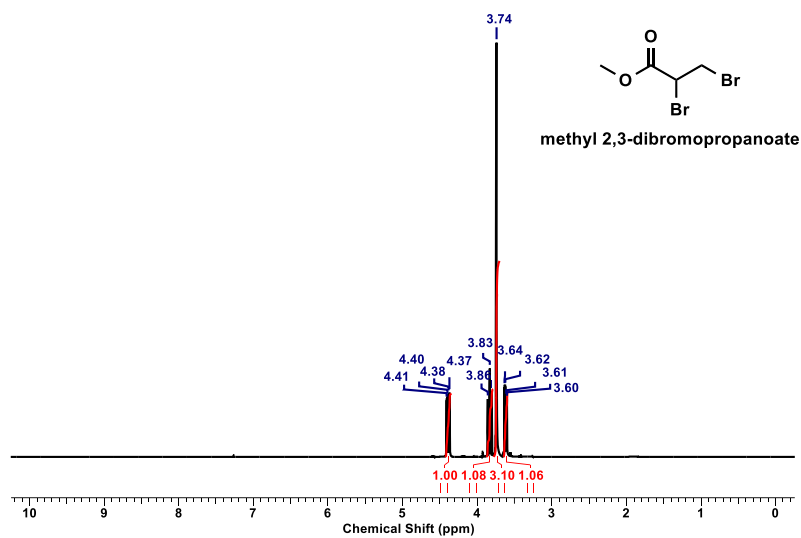


Figure A2.9 <sup>1</sup>H NMR spectrum of **10g** in CDCl<sub>3</sub> conducted at 298.15 K.

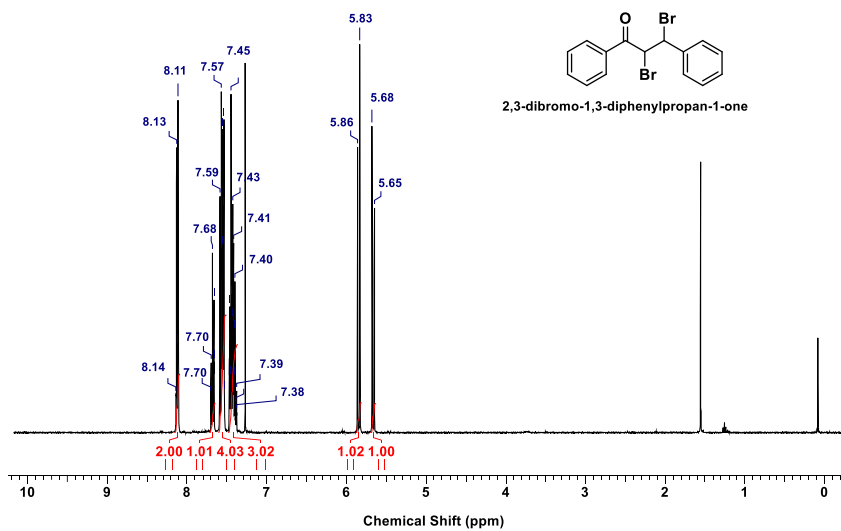


Figure A2.10 <sup>1</sup>H NMR spectrum of **10h** in CDCl<sub>3</sub> conducted at 298.15 K.

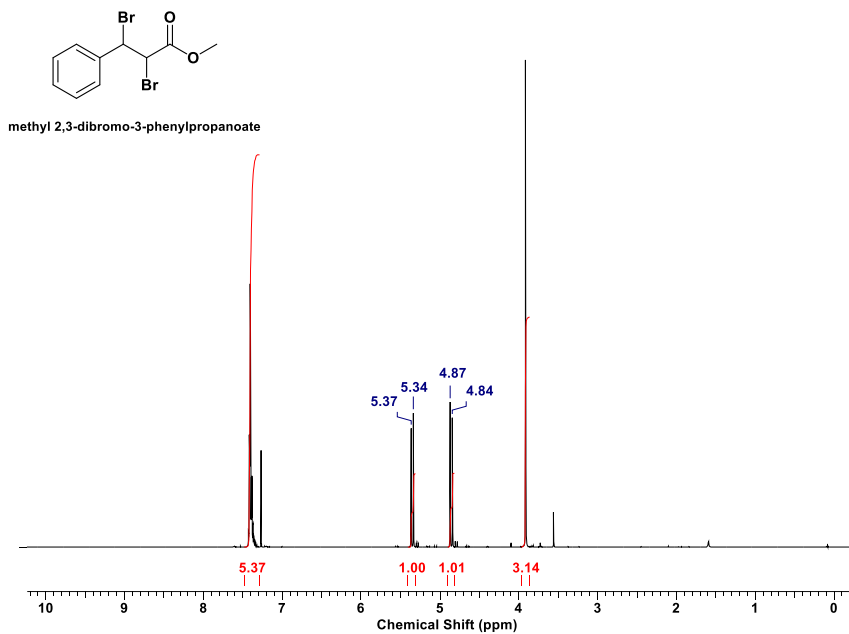


Figure A2.11  $^1\text{H}$  NMR spectrum of **10i** in  $\text{CDCl}_3$  conducted at 298.15 K.

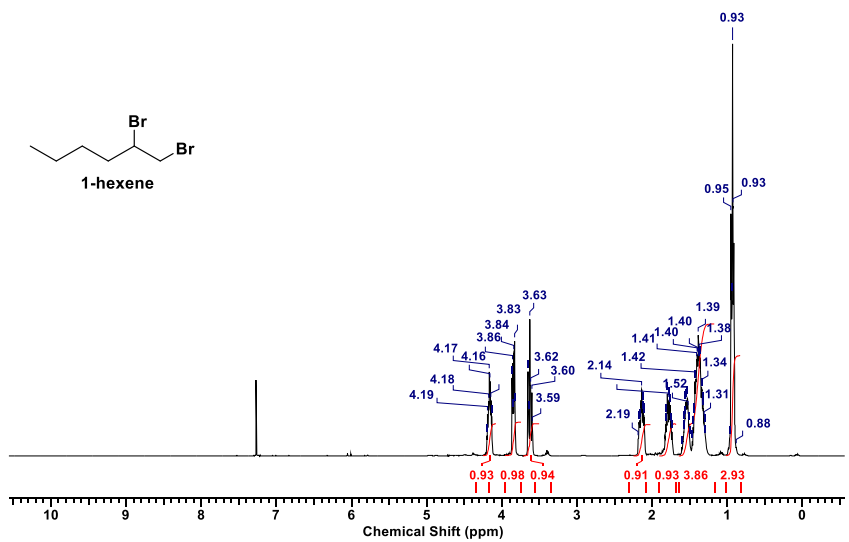


Figure A2.12  $^1\text{H}$  NMR spectrum of **10j** in  $\text{CDCl}_3$  conducted at 298.15 K.

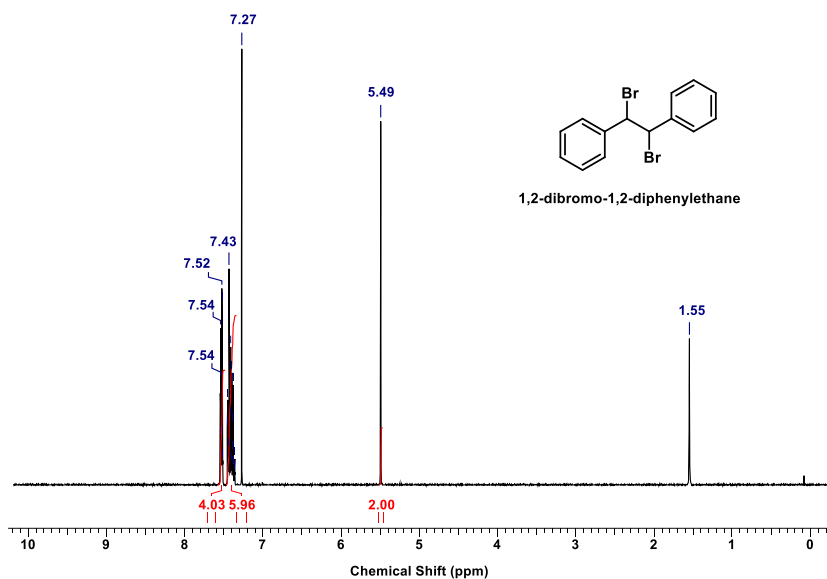


Figure A2.13  $^1\text{H}$  NMR spectrum of **10l** in  $\text{CDCl}_3$  conducted at 298.15 K.

### NMR Spectra of alkenes

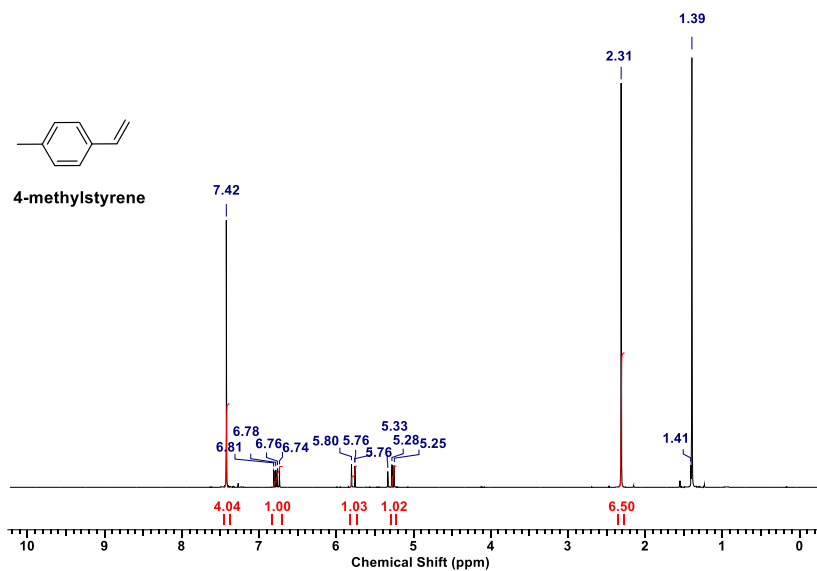


Figure A2.14  $^1\text{H}$  NMR spectrum of **11a** in  $\text{CDCl}_3$  conducted at 298.15 K.

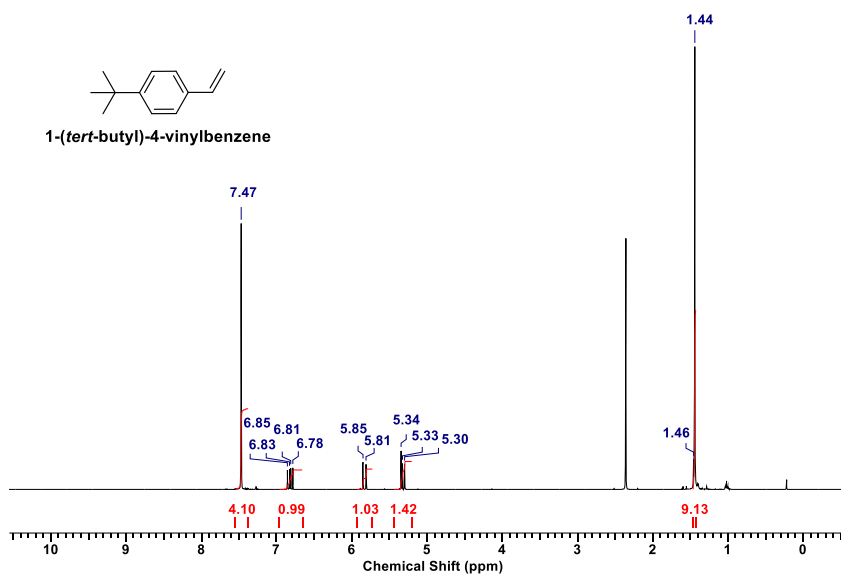


Figure A2.15  $^1\text{H}$  NMR spectrum of **11b** in  $\text{CDCl}_3$  conducted at 298.15 K.

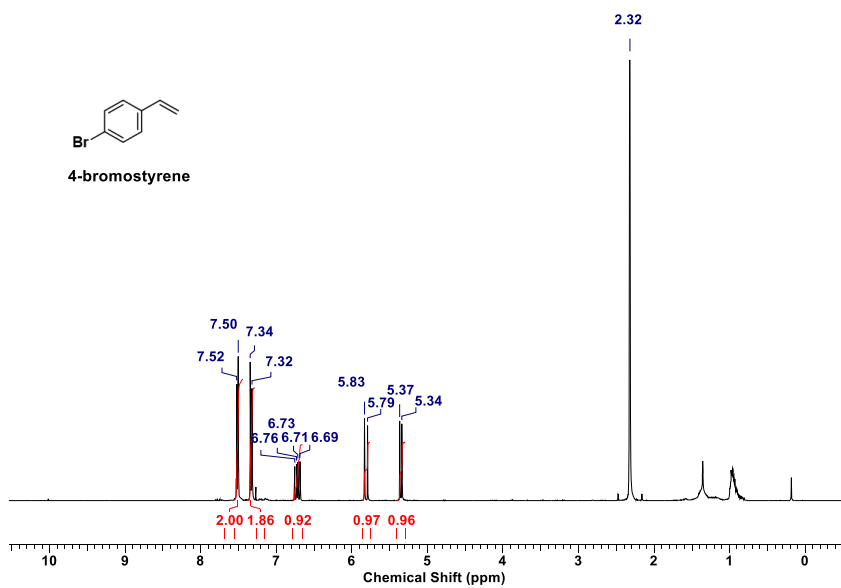


Figure A2.16  $^1\text{H}$  NMR spectrum of **11c** in  $\text{CDCl}_3$  conducted at 298.15 K.

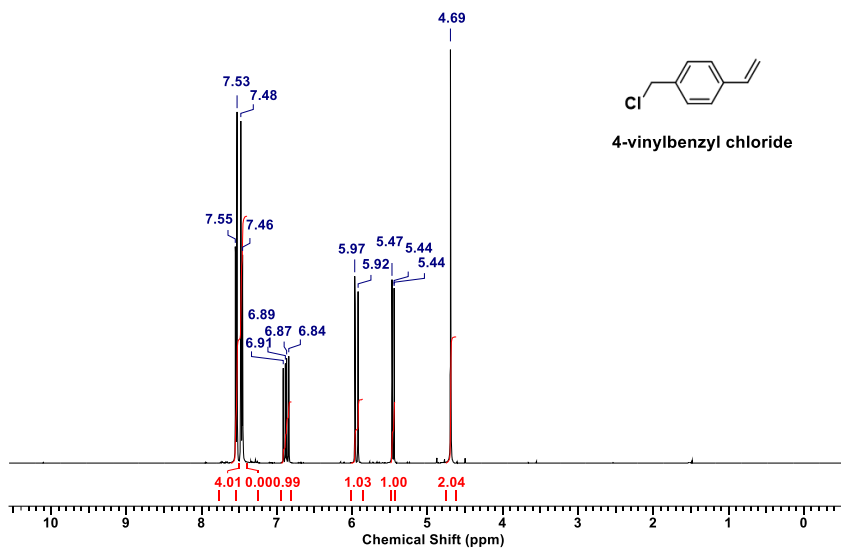


Figure A2.17  $^1\text{H}$  NMR spectrum of **11d** in  $\text{CDCl}_3$  conducted at 298.15 K.

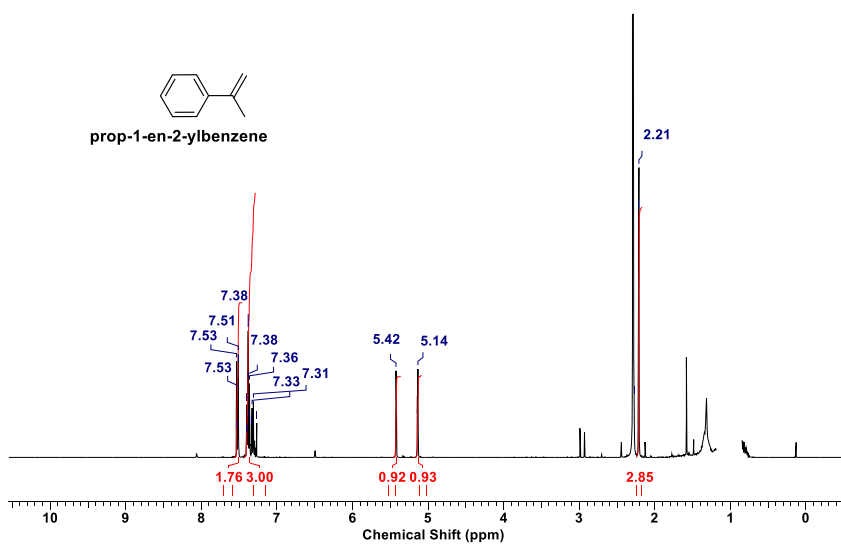


Figure A2.18  $^1\text{H}$  NMR spectrum of **11e** in  $\text{CDCl}_3$  conducted at 298.15 K.

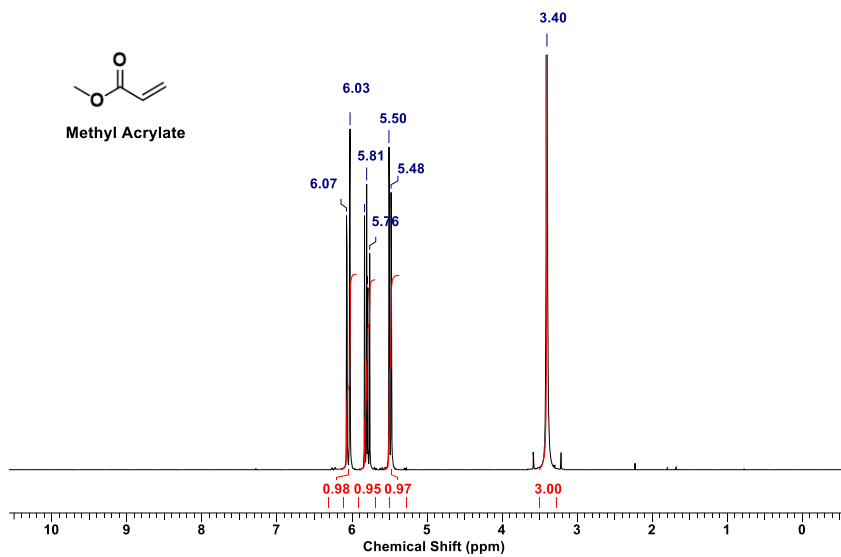


Figure A2.19 <sup>1</sup>H NMR spectrum of **11g** in CDCl<sub>3</sub> conducted at 298.15 K.

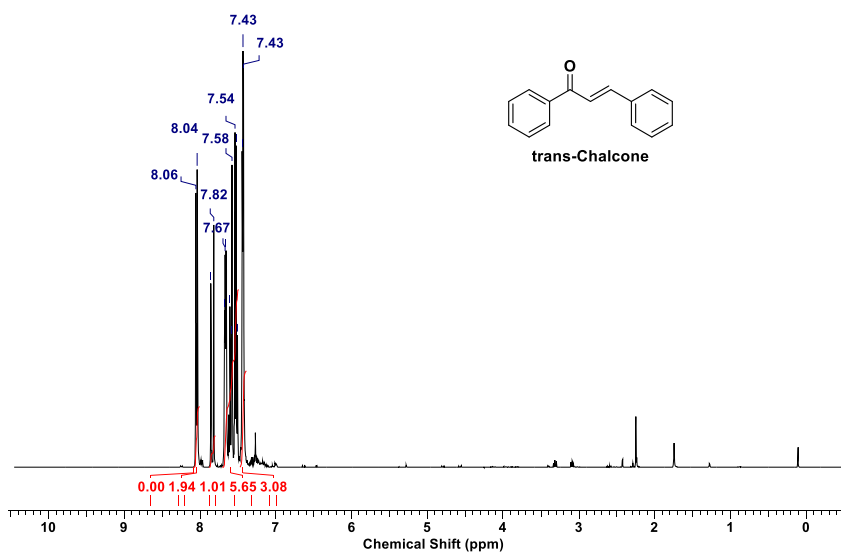
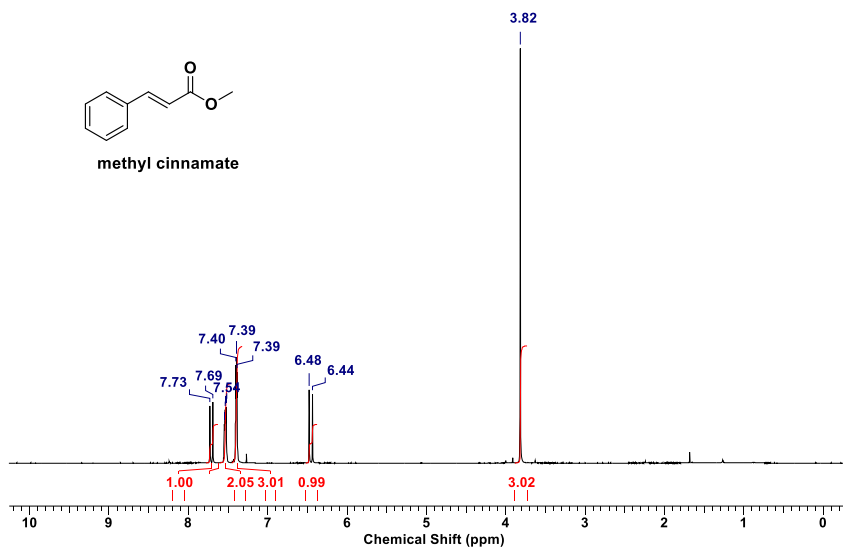


Figure A2.20 <sup>1</sup>H NMR spectrum of **11h** in CDCl<sub>3</sub> conducted at 298.15 K.



**Figure A2.21**  $^1\text{H}$  NMR spectrum of **11i** in  $\text{CDCl}_3$  conducted at 298.15 K.